

Diss. ETH Nr. 19266

**Development of direct atmospheric
sampling for laser ablation-inductively
coupled plasma-mass spectrometry**

DISSERTATION

Submitted to

ETH Zurich

for the degree of

DOCTOR OF SCIENCES

by

ROBERT KOVACS

Dipl. Env. Sci., University of Debrecen, Hungary

born 6th October 1981

citizen of Hungary

accepted on the recommendation of

Prof. Dr. Detlef Günther, examiner

Prof. Dr. Wendelin J. Stark, co-examiner

Prof. Dr. Jozsef Posta, co-examiner

2010

Acknowledgements

I would like to thank Prof. Detlef Günther for the great opportunity to carry out this work in his research group. I am grateful for the freedom in research, the motivating numerous discussions and the support to set up the collaboration with the partners involved in my studies.

I would like to thank Prof. Wendelin Stark and Prof. Jozsef Posta for accepting to be the co-referent of my thesis and their careful review.

I am grateful to Kohei Nishiguchi and co-workers (Sumitomo Seika Chemicals Co., Japan) for the collaboration and support, moreover for the very pleasant atmosphere not only during technical discussions. I also thank Sandra Schlosser for her contribution to the numerous analyses we performed together and the knowledge I gained in archaeology. Besides, many thanks go to Samuel P. Staub, 'my master student' for his preliminary work on the calibration approaches applied within the gold study.

I thank the members of the 'Günther group' who supported me during the years and for the exciting table soccer games.

ETH Zurich for the unique infrastructure and the Swiss National Science Foundation for the financial support are greatly acknowledged.

A big thank you goes to my brother Joe who inspired me for the interest in chemistry during and after my master studies and for his continuous support and encouragement through the years.

Furthermore, special thanks go to my Parents for their support and Andrea for her care, patience and love.

Contents

Acknowledgements	3
Contents	5
Abstract	7
Zusammenfassung	11
Publications, presentations, awards	15
1. Introduction	17
1.1 The ICP-MS	17
1.1.1 The working principle of ICP-MS	18
1.1.2 Sample introduction systems for ICP-MS	28
1.2 Laser ablation as a sample introduction system for ICP-MS	32
1.2.1 Laser beam properties.....	33
1.2.2 Aerosol generation.....	35
1.2.3 Ablation cells and aerosol transport	36
1.2.4 Carrier gases used for ablation	38
1.2.5 Non stoichiometric effects.....	39
1.2.6 Calibration strategies in LA-ICP-MS.....	40
1.3 Aim of the study	43
2. Influence of tube materials on plasma conditions	45
2.1 Introduction	45
2.2 Experimental	47
2.3 Results and discussion.....	49
2.3.1 Influence of PVC tube material	49
2.3.2 Comparison of the influence of PVC, nylon, Teflon and copper tube materials....	54
2.4 Conclusion	57
3. Air as a new gas environment for ablation using LA-ICP-MS	59
3.1 Introduction	59
3.2 Experimental	60
3.3 Results and discussion.....	64
3.3.1 Air as a new gas environment for LA-ICP-MS	64
3.3.2 Experiments using an open cell configuration	67
3.3.3 Experiments using the novel sampling approach	69
3.4 Conclusion	72
4. Fundamental studies on gas exchange experiments for LA-ICP-MS	75
4.1 Overview of performed experiments	75

4.2 Influence of humidity of air on signal response by LA-ICP-MS.....	77
4.3 Elemental fractionation studies during ablation in air	81
4.4 Comparison of aerosol particle sizes generated in He, Ar and air	86
4.5 Investigation of ion diffusion within the ICP	93
4.5.1 Evaluation of radial ion profiles obtained using He or Ar as carrier gases.....	94
4.5.2 Studies on mass dependent ion intensity changes when exchanging He to Ar.....	99
4.6 Application of GED to remove gas impurities from the transport system	106
4.7 Direct liquid ablation in ambient air using aerosol suction	109
4.8 Conclusion.....	114
5. Trace analysis of gold using new calibration materials.....	117
5.1 Introduction	117
5.2 Experimental	119
5.3 Results and discussion	122
5.3.1 Evaluation of the solid calibration materials	122
5.3.2 Quantitative analysis of various gold objects	127
5.4 Conclusion.....	134
6. Conclusions and outlook	135
6.1 Conclusions	135
6.2 Outlook.....	137
7. Appendix.....	139
7.1 Quantitative results of Peruvian gold samples	139
7.2 Abbreviations.....	150
7.3 List of figures	153
7.4 List of tables	159
7.5 References	162
7.6 Curriculum Vitae.....	179

Abstract

Laser Ablation-Inductively Coupled Plasma-Mass Spectrometry (LA-ICP-MS) represents one of the most popular techniques for direct analysis of solid samples. The 'ease of use' of the technique has attracted particular attention in the past decades, since it offers rapid access to qualitative and quantitative information of components contained within solid samples without the need for sample preparation. However, it requires thorough understanding of the numerous processes involved to improve its capabilities and reduce its limitations. Therefore, the focus of this work was directed towards fundamental studies using LA-ICP-MS and consists of four main topics.

- A) Development of a unique direct atmospheric sampling method for LA-ICP-MS
- B) Investigation of the influence of gas exchange experiments on various fundamental processes in LA-ICP-MS
- C) Investigation of the influence of tube materials on ICP operating conditions
- D) Investigation of new solid gold calibration materials using liquid and solid calibration approaches and their applicability for gold analysis

As the main focus of this work, the novel sampling method describes laser ablation sampling in ambient air, utilizing aerosol suction and gas exchange prior to the ICP-MS without losing significant amounts of particles. With the use of a recently developed Gas Exchange Device (GED), various gases can be online exchanged to argon. The gas exchange is based on gas diffusion through a silica membrane. The present prototype of GED is applicable to exchange air at a flow rate of 0.25 L min^{-1} by Ar at 0.21 L min^{-1} . This gas flow is significantly lower than the commonly applied flow rate of carrier gases used for LA, however the results obtained are very promising. The efficiency of air exchange to Ar was studied using various factors monitored during measurements. Oxide formation, background count rates and potential spectral interferences generally caused by polyatomic ions were found to be in the same order when exchanging air to argon like in case of the general setup utilizing helium as carrier gas. Quantification of various gold, brass and steel samples provided results of similar accuracy and precision as commonly obtained using closed cell configurations and helium as aerosol carrier gas.

The capabilities of air as a new gas environment for LA were studied in terms of sensitivity, signal and aerosol structure, elemental fractionation, and the influence of humidity conditions. The sensitivity using air was approximately 50 % lower than that using helium

based on the ablation of a silicate glass NIST 610 (National Institute of Standards and Technology) standard reference material. Air provided significantly higher sensitivity than Ar (factor of 2) and only the sensitivity of boron was found to be significantly influenced by the humidity of air. Aerosol generation and transport led to a lower elemental fractionation for the ablation of NIST 610 in air in contrast to He. The particle size distribution of aerosols (NIST 610) generated in Ar and air was more stable over longer period of ablation than in He. During ablation in Ar and air, larger spherical particles (up to 1 μm) are also formed (few % of the total aerosol) during ablation at a wavelength of 193 nm. Scanning electron microscopy (SEM) proved that relatively large (around 1 μm) spherical particles are present in the aerosol generated by air and Ar, while the aerosol generated in He consists of agglomerates. Both optical particle counting experiments and scanning electron microscope images proved that the aerosol structure and particle sizes are not affected by the gas exchange process. However, as indicated by the sensitivity measured by ICP-MS, 20 % loss of aerosol was observed when the aerosol is introduced into the gas exchanger. Additionally, experiments on He exchange to Ar were performed to investigate ion diffusion losses within the ICP when He is introduced into the plasma. The obtained results indicate that the low helium gas flow rate (approximately 0.2 L min^{-1} determined by the outlet gas flow rate of the gas exchange device) introduced into the plasma in the present study does not contribute to higher ion diffusion losses in comparison to argon only.

Another important result of this work is the influence of gas impurities from the transport tubes on ICP operating conditions. The molecules (presumably in the form of H_2O) degassing from the inner surface of polyvinyl chloride (PVC) and nylon tubes are entering the carrier gas flow and subsequently the ICP. Although, the amount of these degassing components is low in the He carrier gas, the ICP operating conditions were altered significantly. The presence of the degassing components resulted in signal enhancement (up to 70 %), especially for elements with high 1st ionization potentials during the ablation of NIST 610. Since the amount of oxygen and hydrogen in the carrier gas was decreased over time owing to degassing (desorption of molecules from the tube walls into the gas stream), a drift in element-to-Ca ratios of up to 25 % was observed. This drift can take as long as 1.5 – 2 h and exceeds typical warm up times of ICP-MS instruments. This degassing process using PVC and nylon tubes is both time and tube length dependent. The use of solution nebulization (loading the ICP with H_2O) or performing gas exchange was found to diminish the influence of gas impurities from the transport system on the ICP. In contrast to PVC and nylon, low permeability Teflon and copper tubes provided most stable plasma conditions.

The last topic consists of the characterization of two solid gold calibration materials (NA1 and NA2) in terms of element composition using liquid and solid calibration. To ensure stable element concentrations within the calibration solutions containing Ag, Au and other elements, Ag was first stabilized by transferring it into a chloro-complex. Thus, the multi-element solutions could be diluted with hydrochloric-acid. The applicability of this calibration approach was validated by femtosecond laser ablation of NIST 8053 and 8062 reference materials, which provided accuracy and precision in the order of 8 % and 5 %, respectively, for most of the determined elements. The element concentrations determined by liquid calibration were confirmed by solid calibration using NIST 8053 and 8062. The two solid calibration materials (NA1, NA2) provide access to elements, which are important for archaeological investigations and trace element fingerprint studies of gold. Furthermore, these calibration materials contain Ag as a major element, which provide matrix-matched calibration for the analysis of gold artifacts. Investigations of various gold objects showed the applicability of the produced calibration materials. The analysis of large gold objects were carried out using an open-design ablation cell attached to the surface of the large samples. Since the sealing process caused microscopic contamination on the sample surface, only a few large objects were analyzed. This problem might be overcome in the future with the application of the developed atmospheric sampling approach omitting the need for an ablation cell.

Zusammenfassung

Laserablations-Massenspektrometrie mit induktiv gekoppeltem Plasma als Anregungsquelle (laser ablation-inductively coupled plasma-mass spectrometry, LA-ICP-MS) ist eine der erfolgreichsten Techniken für die direkte Analyse fester Proben. Besonders die ‚einfache Handhabung‘ der Technik sorgte in den vergangenen Jahrzehnten für ihre Attraktivität, da sie ohne Bedarf an Probenvorbereitung schnellen Zugang zu sowohl qualitativer als auch quantitativer Information über die in Festkörperproben enthaltenen Elemente bietet. Trotzdem ist ein tiefgehendes Verständnis der einzelnen Prozesse notwendig, um die Möglichkeiten der Methode zu verbessern und ihre Nachteile zu reduzieren. Deshalb liegt der Fokus dieser Arbeit auf Grundlagenstudien zur Anwendung von LA-ICP-MS und besteht aus vier Hauptteilen:

- A) Entwicklung einer neuen atmosphärischen Beprobungsmethode für LA-ICP-MS,
- B) Grundlagenstudien zum Gasaustausch in der LA-ICP-MS,
- C) Untersuchung des Einflusses des Schlauchmaterials auf die Anregungsbedingungen im ICP,
- D) Evaluation neuer fester Goldkalibrationsmaterialien mittels Flüssig- und Festkörper-Kalibrationsstrategien und ihrer Anwendbarkeit für die Goldanalyse.

Das Hauptthema dieser Arbeit beschreibt die neuartige Beprobungsmethode für Laserablation in Umgebungsluft durch Aerosolansaugung und Gasaustausch vor dem ICP-MS, ohne dass signifikanter Partikelverlust stattfindet. Der Einsatz eines kürzlich entwickelten Gasaustauscher (gas exchange device, GED) erlaubt den direkten Austausch verschiedener Gase gegen Argon. Der Gasaustausch basiert auf Gasdiffusion durch eine Silicamembran. Der momentane Prototyp des GED kann eine Flussrate von 0.25 L min^{-1} Luft durch Argon mit einer Flussrate von 0.21 L min^{-1} austauschen. Dieser Gasfluss ist signifikant niedriger als die übliche Flussrate für in der LA verwendete Trägergase. Trotzdem sind die erhaltenen Ergebnisse sehr vielversprechend. Die Effizienz des Luft-zu-Argon-Austausches wurde anhand zahlreicher Faktoren ermittelt, die während der Messungen überwacht wurden. Oxidraten, Untergrundzählraten und das Auftreten möglicher spektraler Interferenzen, die generell durch polyatomare Ionen verursacht werden, entsprachen beim Austausch von Luft durch Argon der Grössenordnung der bisher erreichten Kenndaten unter Verwendung von Helium als Trägergas. Quantifizierung verschiedener Gold-, Messing- und Stahlproben lieferten Ergebnisse ähnlicher Richtigkeit

und Präzision, wie sie mit geschlossener Ablationszellenkonfiguration und Helium als Trägergas erreicht werden können.

Die Einsatzmöglichkeit von Luft als neue Gasumgebung für LA wurden in Bezug auf Empfindlichkeit, Signal- und Aerosolstruktur, Elementfraktionierung und den Einfluss der Feuchtigkeitsbedingungen untersucht. Basierend auf der Ablation des Referenzmaterials NIST 610 (National Institute of Standards and Technology), eines Silikatglases, lag die Empfindlichkeit bei der Verwendung von Luft ca. 50 % tiefer als für Helium. Luft sorgte für eine signifikant höhere Empfindlichkeit als Ar (Faktor 2), und nur die Empfindlichkeit für Bor wurde signifikant durch die Feuchtigkeit der Luft beeinflusst. Aerosolgenerierung und -transport führten bei der Ablation von NIST 610 in Luft im Vergleich zu Helium zu geringerer Elementfraktionierung. Die Partikelgrößenverteilung des in Ar oder Luft generierten Aerosols von NIST 610 war über eine längere Zeit stabiler als in He. Bei Ablation bei einer Wellenlänge von 193 nm besteht das Aerosol in Ar und Luft zu ein paar Prozent auch aus grösseren kugelförmigen Partikeln (bis zu 1 μm). Rasterelektronenmikroskopie belegte, dass relativ grosse (ca. 1 μm) sphärische Partikel im unter Luft und Argon generierten Aerosol vorliegen, während das in He gebildete Aerosol aus Nanoagglomeraten besteht. Sowohl optische Partikelzählexperimente als auch Rasterelektronenmikroskopiebilder zeigten, dass weder die Struktur noch die Partikelgrößenverteilung des Aerosols durch den Gasaustauschprozess beeinflusst werden. Trotzdem deutet der Empfindlichkeitsverlust der ICP-MS-Messung auf einen Aerosolverlust von 20 %, wenn das Aerosol den Gasaustauscher passiert. Zusätzlich wurden He-zu-Ar-Austauschexperimente durchgeführt, um Diffusionsverluste der Ionen im ICP zu untersuchen, wenn He im Plasma vorliegt. Die Resultate weisen darauf hin, dass die niedrige Heliumgasflussrate (ca. 0.2 L min^{-1} , bestimmt über die Auslassgasflussrate des Gasaustauschers) nicht zu höheren Diffusionsverlusten der Ionen, im Vergleich zu einem reinen Argonplasma, führen.

Ein weiteres wichtiges Ergebnis dieser Arbeit bezog sich auf den Einfluss von Gasunreinheiten aus Transportschläuchen auf die ICP-Anregungsbedingungen. Die aus den inneren Oberflächen von Polyvinylchlorid- (PVC-) und Nylon-Schläuchen entgasenden Moleküle (wahrscheinlich in der Form von H_2O) treten in den Trägergasfluss ein und werden in das ICP transportiert. Obwohl der Beitrag dieser entgasenden Bestandteile im He-Trägergas sehr gering sind, werden die ICP-Anregungsbedingungen massgeblich verändert. Die Anwesenheit der Ausgasungskomponenten schlug sich in erhöhten Signalintensitäten (bis zu 70 %) nieder. Bei der Ablation von NIST 610 war dieser Effekt besonders ausgeprägt für Elemente mit hohem 1. Ionisierungspotential. Da der Gehalt an

Sauerstoff und Wasserstoff im Trägergas sich mit der Zeit durch Entgasung verringert (Desorption von Molekülen von den Schlauchwänden in den Gasstrom), wurde in den Element-zu-Ca-Verhältnissen eine zeitliche Änderung von bis zu 25 % beobachtet. Die Drift kann bis zu 1.5 – 2 h andauern und übersteigt damit normale Aufwärmzeiten von ICP-Instrumenten. Der Entgasungsprozess bei der Verwendung von PVC- und Nylonschläuchen hängt dabei sowohl von der Zeit als auch von der Schlauchlänge ab. Flüssiger Probeneintrag mit Zerstäubern (Laden des ICPs mit H₂O) oder Gasautausch verringerten den Einfluss der aus dem Transportsystem stammenden Gasunreinheiten auf das ICP. Die stabilsten Plasmabedingungen liessen sich jedoch durch Verwendung wenig durchlässigen Teflons oder von Kupferrohren erreichen.

Der letzte Teil der Arbeit bestand in der Charakterisierung zweier fester Goldkalibrationsmaterialien (NA1 und NA2) in Bezug auf ihre Elementzusammensetzung mit Hilfe von Flüssig- und Festkörper kalibration. Zur Stabilisierung der Elementkonzentrationen in den Ag, Au und andere Elemente enthaltenden Kalibrationslösungen wurde Ag zuerst durch Überführung in einen Chloro-Komplex stabilisiert. Daraufhin konnte die Multielementlösung mit Salzsäure verdünnt werden. Die Anwendbarkeit dieses Kalibrationsansatzes wurde durch Femtosekunden-Laserablation der Referenzmaterialien NIST 8053 und 8062 validiert. Für die meisten der bestimmten Elemente wurden Richtigkeiten und Präzisionen im Bereich von 8 % bzw. 5 % erreicht. Die durch Flüssigkalibration bestimmten Elementkonzentrationen wurden durch Festkörper-Kalibration mit NIST 8053 und 8062 bestätigt. Die zwei festen Kalibrationsmaterialien (NA1, NA2) bieten Zugang zu Elementen, die für archäologische Untersuchungen und Spurenelementfingerabdruckstudien von Gold von hohem Wert sind. Da diese Kalibrationsmaterialien Ag als Hauptelement enthalten, eignen sie sich zur matrixangepassten Kalibration bei der Analyse von Goldartefakten. Untersuchungen an unterschiedlichen Goldobjekten zeigten die Verwendbarkeit der hergestellten Kalibrationsmaterialien. Die Analyse grosser Goldobjekte wurde mit Hilfe einer offenen Ablationszelle durchgeführt, die auf die Oberfläche grosser Proben geheftet wurde. Da der Abdichtungsprozess mikroskopische Verunreinigungen auf der Probenoberfläche zurückliess, wurden nur einige wenige grosse Objekte analysiert. Dieses Problem könnte in Zukunft mit Anwendung der entwickelten atmosphärischen Beprobungsstrategie überwunden werden, für die keine Ablationszelle mehr notwendig ist.

Publications, presentations, awards

Publications

- R. Kovacs and D. Günther, Influence of transport tube materials on signal response and drift in laser ablation – inductively coupled plasma – mass spectrometry, *J. Anal. At. Spectrom.*, 2008, **23**, 1247.
- S. Schlosser, R. Kovacs, E. Pernicka, D. Günther and M. Tellenbach, Fingerprints in gold, *New technologies for Archaeology: Multidisciplinary investigations in Palpa and Nasca, Peru*; eds. M. Reindel and G. Wagner, Springer Verlag, 2009, Ch. **24**, 409.
- R. Kovacs, S. Schlosser, S. P. Staub, A. Schmiderer, E. Pernicka and D. Günther, Characterization of calibration materials for trace element analysis and fingerprint studies of gold using LA-ICP-MS, *J. Anal. At. Spectrom.*, 2009, **24**, 476.
- R. Kovacs, K. Nishiguchi, K. Utani and D. Günther, Development of direct atmospheric sampling for laser ablation – inductively coupled plasma – mass spectrometry, *J. Anal. At. Spectrom.*, 2010, **25**, 142.

Presentations

- R. Kovacs and D. Günther, Investigation of aerosol transport parameters on signal response in laser ablation – inductively coupled plasma – mass spectrometry, *2008 Winter Conference on Plasma Spectrochemistry, Temecula, CA, USA*, 2008. (Poster)
- R. Kovacs, S. Schlosser, E. Pernicka, D. Günther, Investigation of new solid gold reference materials and their application for gold analysis using LA-ICP-MS, *Swiss Chemical Society Fall Meeting, Zurich, Switzerland*, 2008. (Poster)
- R. Kovacs, Characterization of calibration materials for trace element analysis and fingerprint studies of Peruvian gold artifacts using LA-ICP-MS, *Minisymposium of Laboratory of Inorganic Chemistry, ETH Zurich, Zurich, Switzerland*, 2008. (Oral)
- R. Kovacs, S. Schlosser, S. P. Staub, A. Schmiderer, E. Pernicka, D. Günther, New solid calibration materials for trace element analysis of gold artifacts using LA-ICP-MS, *Analyze That!, ETH Zurich, Zurich, Switzerland*, 2009. (Poster)
- R. Kovacs, K. Nishiguchi, K. Utani, D. Günther, A novel aerosol sampling strategy for LA-ICP-MS, *Colloquium Spectroscopicum Internationale XXXVI, Budapest, Hungary*, 2009. (Poster)
- R. Kovacs, K. Nishiguchi, K. Utani, D. Günther, Direct analysis of solid samples by LA-ICP-MS using air for aerosol transport, *2010 Winter Conference on Plasma Spectrochemistry, Fort Myers, FL, USA*, 2010. (Poster)

Awards

- R. Kovacs, K. Nishiguchi, K. Utani, D. Günther, A novel aerosol sampling strategy for LA-ICP-MS, *Colloquium Spectroscopicum Internationale XXXVI, Budapest, Hungary*, 2009. (AWARD FOR THE BEST POSTER PRESENTATION, ELSEVIER'S SPECTROCHIMICA ACTA: PART B., ATOMIC SPECTROSCOPY POSTER AWARD)
- R. Kovacs, K. Nishiguchi, K. Utani, D. Günther, Direct analysis of solid samples by LA-ICP-MS using air for aerosol transport, *2010 Winter Conference on Plasma Spectrochemistry, Fort Myers, FL, USA*, 2010. (SCNAT CHEMISTRY TRAVEL AWARD, Division of Analytical Chemistry, Swiss Chemical Society)

1. Introduction

1.1 The ICP-MS

The establishment of Inductively Coupled Plasma-Mass Spectrometry (ICP-MS) is based on a major instrumental development to couple an atmospheric pressure ICP with a mass spectrometer, which operates under high vacuum conditions. Since its introduction in the 1980s by Houk et. al.¹, ICP-MS has become a widespread technique for elemental and isotopic analysis within samples of various physical conditions. ICP-MS provides high sensitivity and low background levels providing superior limits of detection (down to ppq^{2,3,4}), relatively high precision, wide linear dynamic range, fast data acquisition and access to elemental and isotopic information of most elements within the periodic table^{5,6} in contrast to other techniques most commonly applied for elemental analysis such as FES⁷ (Flame Emission Spectrometry), FAAS⁸ (Flame Atomic Absorption Spectrometry), GFAAS⁸ (Graphite Furnace Atomic Absorption Spectrometry) and ICP-OES⁹ (Inductively Coupled Plasma-Optical Emission Spectrometry). ICP-MS has achieved great attention in the last two decades and this versatile technique has been successfully applied to a wide range of environmental, medical, biological, industrial, archaeological applications amongst others making it a popular and routine technique for elemental and isotopic analysis¹⁰.

ICP-MS instruments consist of five main parts (Figure 1). The sample, ideally in a form of a fine, dispersed wet or dry aerosol is introduced by a sample introduction system (1) into the atmospheric pressure inductively coupled plasma (ICP) (2), which functions as the ion source. In the plasma, the sample aerosol undergoes a rapid heating and first, it is getting desolvated and then evaporated. When it arrives at the analytical zone of the ICP, at approximately > 6000 K atomization takes place and the generated atoms are then further excited and finally ionized. The generated ions are representing the elemental composition of the original sample. The generated ions are transferred through the interface (3), which consists of two metallic cones (sampler and skimmer) with small orifices (normally 1.1 mm and 0.8 mm, respectively). Between the sampler and skimmer a supersonic expansion of the ion beam takes place owing to a pressure drop to approximately 1 mbar generated by a roughing pump. The ion optics is focusing the ions into the mass analyzer (4) as a narrow beam, repels the electrons and negatively charged ions, furthermore preventing the photons from entering the mass filter. The mass analyzer is operating under high vacuum (10^{-6} mbar) generated by turbo-molecular pumps. Mass separation may be performed by various

types of mass spectrometers (MS). Finally, the ions are detected (5) and the generated signals are recorded by the instrument software.

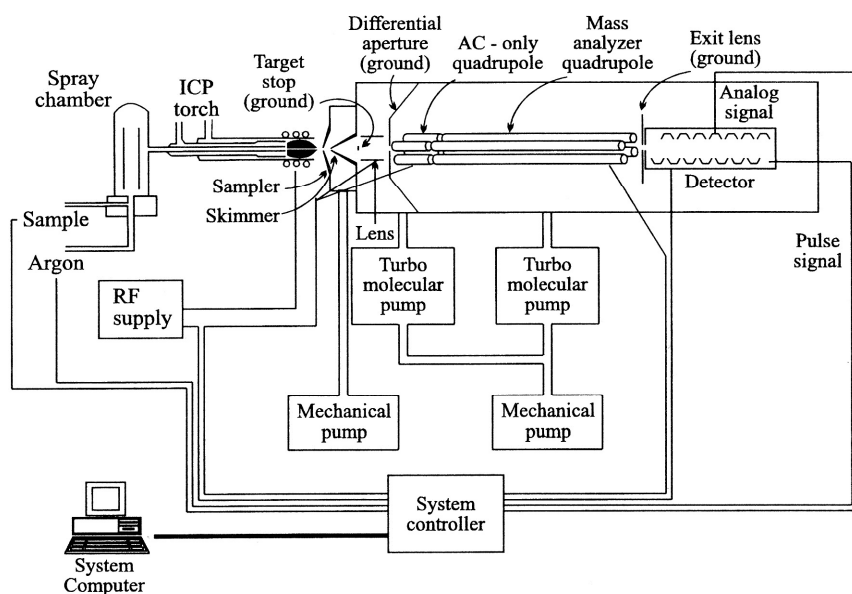


Figure 1 Schematic diagram of a quadrupole ICP-MS, the ELAN 6000 ⁶.

In the following sections, the working principles of the individual sections are discussed with respect to the aim of the studies demonstrated in this thesis.

1.1.1 The working principle of ICP-MS

Formation and operation of the Inductively Coupled Plasma

The plasma is formed from argon gas flowing through generally a conventional Fassel quartz torch consisting of three concentric tubes (Figure 2). The most outer tube introduces argon gas flow at a relatively high flow rate of up to 20 L/min to prevent the torch from melting and forms the typical shape of the plasma. The auxiliary argon gas flow (up to 1.5 L/min) introduced in the middle channel stabilizes the plasma, moreover it may be adjusted to change the position of the plasma base, which influences the sampling depth (distance between plasma and sampler cone). The most inner tube, namely the injector is responsible for introducing the sample aerosol into the plasma at an argon gas flow rate of usually up to 1.5 L/min. The torch is placed in an induction coil, which is connected to a radio frequency (RF) generator. The induction coil is made of copper and is cooled either by argon or water. The RF generator operates at 27.12 MHz or 40.68 MHz at output powers of 700-1700 W. The RF oscillations generate a magnetic field at the top of the torch. The plasma is

ignited by a high voltage spark applied to the argon gas. These electrons are accelerated in the magnetic field and collide with neutral argon atoms causing electrons to be stripped from them. These collisions cause the generation of further electrons and result in a chain reaction. The formed plasma therefore consists of argon atoms, positively charged argon ions and electrons, which represents a quasi neutral state. Furthermore, electron – argon atom collisions generate the high temperature of the plasma, which is between 6000 – 10000 K depending on the region. Since the gas flows within the various regions of the torch are different, the shape of the plasma becomes distinctively annular⁶.

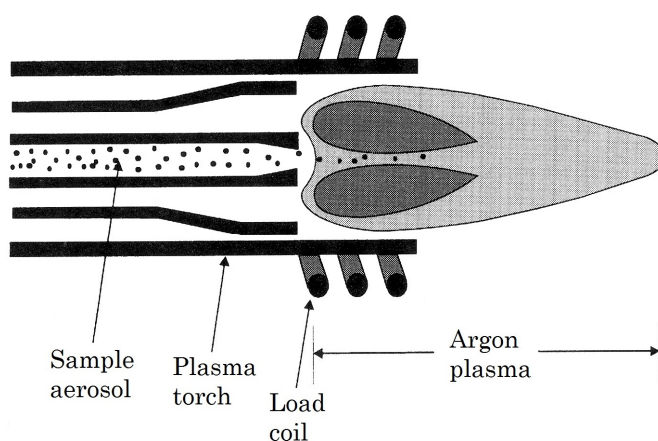


Figure 2 Schematic view of an Ar ICP in a Fassel torch⁶.

Various processes take place during the plasma – sample interaction. In case of wet aerosol, in the first instance the aerosol becomes desolvated, while it travels closer to the plasma in the Ar nebulizer gas flow. The solid particle undergoes vaporization by absorbing energy from the plasma. The vaporization is strictly matrix dependent, since the physical properties of matrix elements can be different to a high extent (e.g. Zn – mp.: 419.6 °C, bp.: 903 °C versus W – mp.: 3387 °C, bp.: 5927 °C). Particles consisting of high melting and boiling point elements require more energy to be vaporized within the ICP. Therefore, the plasma conditions need to be well optimized prior to the specific analysis. The vaporization is thus affected by the gas temperature, the heat of vaporization of solvent and solid, the particle size and the vapor transport rate from the particle surface¹¹. The gas temperature is affected by the RF power applied, the gas flow rates and indirectly by the sampling depth. The heat of vaporization of solvent and solid is defined by the sample composition and the solvent type. The particle size strictly determines the extent of vaporization of a particle, which is also influenced by its elemental composition. The mass transport rate from the particle surface is affected by the gas temperature, moreover the gas composition (gas additions, mixed-gas plasmas)¹¹. After the vaporization of the material the liquid and vapor phases no longer exist and the sample components are dissociated into neutral atoms

and molecules based on the bond-energies of elements. These are then further excited, ionized and the molecules are ideally dissociated and ionized. In the plasma, not dissociated ionized molecular species are also exist and are sampled by the interface. These ions can be molecular ions, such as Ar_2^+ or polyatomic ions originating from impurities of argon, e.g. water, air (e.g. ArO^+ , ArH^+ , OH^+ , NH^+ , etc.) or the combination of these with matrix elements (e.g. SiO^+ , CaO^+ , CaOH^+ , CaH^+ , SO_2^+ , etc.)¹². Besides, refractory elements with high element-oxygen bond energy¹³ may not be completely dissociated within the plasma or may recombine at lower temperature plasma regions close to the sampler cone¹⁴. These polyatomic ions (elemental-oxides) are normally measured and indicate the extent of oxide formation of these elements (e.g. ThO^+)¹⁵.

The ionization within the plasma depends on the ionization potential of elements and ionization mechanisms. Ionization of an element is mostly occurring via electron impact¹⁶ and charge transfer¹⁷ with Ar^+ . Electron impact is influenced by the electron temperature and the electron population. Charge transfer is affected by the gas temperature and Ar^+ number density, which is theoretically equal to the number density of electrons within the ICP. The total number density of the particles given by the gas laws at atmospheric pressure and at a temperature of 6000 K is 1.5×10^{18} , which is mostly argon. At an ionization temperature of 7500 K the degree of ionization of argon is about 0.1 %, while the population of Ar^{2+} ions is negligible as the second ionization potential of argon is very high (27 eV). The electron number density is $1 \times 10^{15} \text{ cm}^{-3}$ within a 'dry plasma'¹⁵. As described in ref.¹⁵, if water is introduced into the plasma, containing 1 % HNO_3 , then additional electrons evolve by the ionization of H^+ , O^+ and N^+ and therefore, the total electron population is increased within the ICP in contrast to dry plasma conditions. The presence of water vapor in the aerosol thus contributes significantly to the ion and electron population of the axial channel¹⁵. The flow velocity for the majority of ICP-MS instruments is between 15 – 20 m/s, which results in a residence time of approximately 2 ms for the sample aerosol introduced into the ICP¹⁵. The degree of ionization depends mainly on the first ionization potential of the analyte atoms. Since argon has a rather high first ionization potential (15.76 eV), all elements with a lower ionization potential are ionized. The calculated values for the degree of ionization demonstrated by Houk in 1986 indicate that most analyte atoms are ionized by more than 90 % (Figure 3). However, these values are assumed to be overestimated, because of the relatively high temperature applied in the calculations.

H 0.1																	He
Li 100	Be 75											B 58	C 5	N 0.1	O 0.1	F 9x10 ⁴	Ne 6x10 ⁻⁶
Na 100	Mg 98											Al 98	Si 85	P 33	S 14	Cl 0.9	Ar 0.04
K 100	Ca 99(1)	Sc 100	Ti 99	V 99	Cr 98	Mn 95	Fe 96	Co 93	Ni 91	Cu 90	Zn 75	Ga 98	Ge 90	As 52	Se 33	Br 5	Kr 0.6
Rb 100	Sr 96(4)	Y 98	Zr 99	Nb 98	Mo 98	Tc	Ru 96	Rh 94	Pd 93	Ag 93	Cd 65	In 99	Sn 96	Sb 78	Te 66	I 29	Xe 8.5
Cs 100	Ba 91(9)	La 90(10)	Hf 96	Ta 95	W 94	Re 93	Os 78	Ir	Pt 62	Au 51	Hg 38	Tl 100	Pb 97(0.1)	Bi 92	Po	At	Rn
Fr	Ra	Ac	Unq	Unp	Unh	Uns	Uno										

Ce 96(2)	Pr 90(10)	Nd 99*	Pm	Sm 97(3)	Eu 100*	Gd 93(7)	Tb 99*	Dy 100*	Ho	Er 99*	Tm 91(9)	Yb 92(8)	Lu
Th 100*	Pa	U 100*	Np	Pu	Am	Cm	Bk	Cf	Es	Fm	Md	No	Lr

Figure 3 Calculated values for degree of ionization (%) of M^+ and M^{2+} at $T_i = 7500$ K, $n_e = 1 \times 10^{15} \text{ cm}^{-3}$. Elements marked by an asterisk yield significant amounts of M^{2+} but partition functions are not available^{15,18}.

Few elements, such as noble gases, fluorine, oxygen, nitrogen and chlorine are ionized to a low degree within the Ar plasma caused by the relatively high ionization potentials of these elements. The dependence of the degree of ionization on ionization energy for singly charged ions is shown in Figure 4, which indicates that the degree of ionization falls rapidly above 9 eV. Doubly charged ions occur only for elements with a second ionization potential significantly lower than the first ionization potential of argon. Since the second ionization potential of most elements are higher than 10 eV, doubly charged ions do not represent severe problems. Table 1 indicates the distribution of ionization energies for various elements for singly and doubly charged ions at 1 eV intervals.

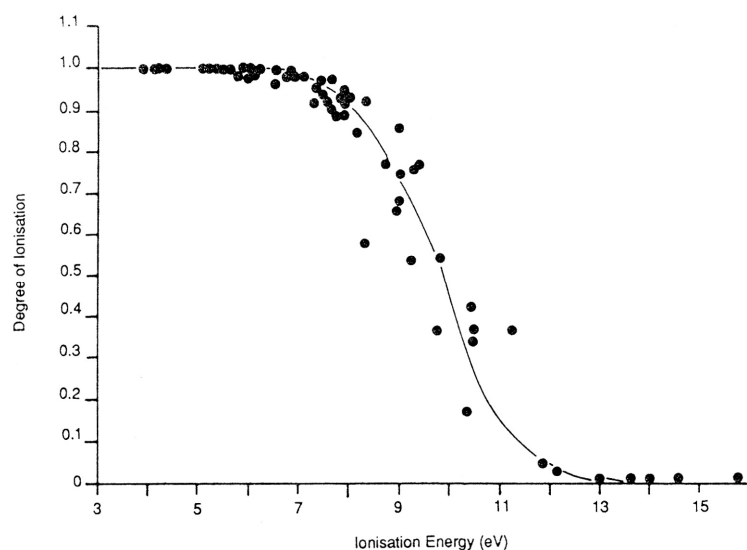


Figure 4 Degree of ionization versus ionization energy for singly charged ions in the ICP^{15,19}.

The distribution of ions within the ICP is not uniform. When no sample is introduced into the plasma, the relative response for Ar⁺ by the MS is the highest within the center of the ICP. However, during sample introduction the Ar⁺ population becomes significantly lower in the center in contrast to the sides, while the analyte response is the highest at this location (Figure 5). This phenomenon is caused by the introduced sample aerosol, which reduces the temperature of the central channel gas flow. Therefore, the ionization of argon at this location is reduced, while it is maintained in the hotter induction region¹⁵.

Table 1 Distribution of ionization potentials (IP) among the elements for singly and doubly charged ions at 1 eV intervals. Adapted from refs ^{15,19}

IP (eV)	Elements
< 7	Li, Na, Al, K, Ca, Sc, Ti, V, Cr, Ga, Rb, Sr, Y, Zr, Nb, In, Cs, Ba, La, Ce, Pr, Nd, Pm, Sm, Eu, Gd, Tb, Dy, Ho, Er, Tm, Yb, Lu, Hf, Tl, Ra, Ac, Th, U
7-8	Mg, Mn, Fe, Co, Ni, Cu, Ge, Mo, Tc, Ru, Rh, Ag, Sn, Sb, Ta, W, Re, Pb, Bi
8-9	B, Si, Pd, Cd, Os, Ir, Pt, Po
9-10	Be, Zn, As, Se, Te, Au
10-11	P, S, I, Hg, Rn
11-12	C, Br
12-13	Xe
13-14	H, O, Cl, Kr
14-15	N
15-16	Ar
> 16	He, F, Ne

<u>doubly charged ions</u>	
10-11	Ba, Ce, Pr, Nd, Ra
11-12	Ca, Sr, La, Sm, Eu, Tb, Dy, Ho, Er
12-13	Sc, Y, Gd, Tm, Yb, Th, U, Ac
13-14	Ti, Zr, Lu
14-15	V, Nb, Hf
15-16	Mg, Mn, Ge, Pb
> 16	all other elements

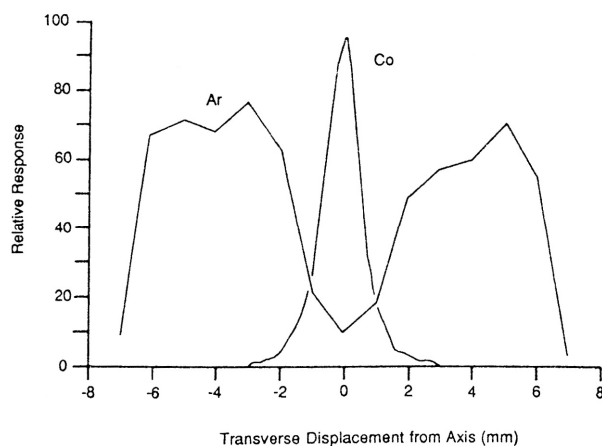


Figure 5 Transverse profiles of ions across the mouth of the plasma torch¹⁵.

Ion extraction

A schematic view of the interface region is shown in Figure 6. The ion extraction^{14,20,21} from the atmospheric pressure ICP is performed by the sampler cone of the interface. The interface owing to the high temperature is water-cooled and the material of both metallic cones is generally Ni, Pt or Al, which provide high heat conducting properties. The orifice diameter of the sampler and skimmer cones commonly applied within an ELAN 6100 DRC+ instrument is 1.1 mm and 0.8 mm, respectively. Between the two cones, a supersonic jet consisting of plasma species and ions is formed generated by the pressure drop (1 bar / 1 mbar). The plasma sampled by the sampler cone is deflected and cooled because of the water-cooled metal cones. The temperature of the boundary layer formed between the plasma and the side of the cone is lower than that of the plasma, therefore chemical reactions, such as oxide formation occur¹⁴. However, the interface design with a smaller diameter of skimmer cone prevents the majority of oxides to enter the high vacuum area. The supersonic jet²² consists of a freely expanding region, called zone of silence surrounded by shock waves, called barrel shock and Mach disk²³. The barrel shock and Mach disk are caused by collisions of fast atoms with the background gas, which reheats the atoms. The central zone of the jet passes through the skimmer cone into the second vacuum stage (10^{-6} mbar). Behind the skimmer, the ion lens is located. The function of the electrostatically controlled lens equipped with a photon stop is to steer the ions into the mass analyzer, moreover to eject particulates and neutral species out of the ion beam and prevent photons from reaching the MS. The ions of different m/z have different kinetic energies and therefore, different pathways through the lens. Thus, different voltages applied to the ion lens are required to transmit ions of different m/z . Since the electric field generated by the

lens repels electrons, the electrons are no longer present in the ion beam traveling towards the mass analyzer, thus the beam loses its quasi-neutral state. Since the ion density is high, the repulsion generates a space-charge effect^{21,24,25}, which causes a difference in the extent of transmission of ions to the MS based on their m/z . Light ions are affected most by space-charge and are deflected most extensively. This phenomenon results in poorer sensitivity for light elements in contrast to heavy ones²⁴.

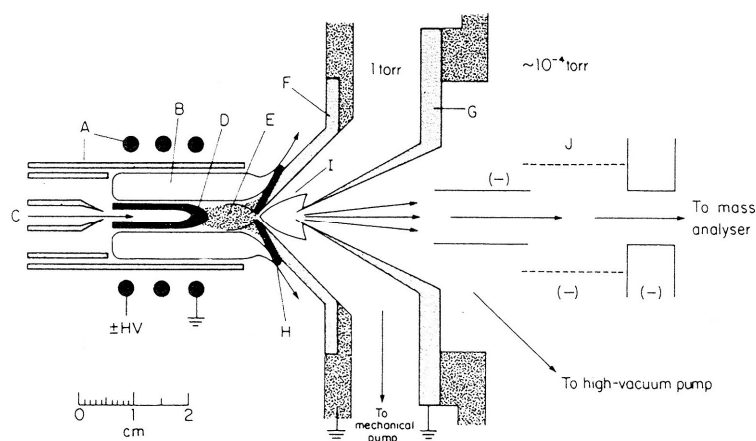


Figure 6 ICP and sampling interface for ICP-MS^{15,18}. A: torch and load coil; B: induction region; C: aerosol gas flow; D: initial radiation zone; E: normal analytical zone; F: sampler cone; G: skimmer cone; H: boundary layer of ICP gas deflected outside sampler; I: supersonic jet; J: ion lens.

Mass spectrometers

The mass spectrometer is basically a mass filter designed to separate an ion with specific m/z from the total ion beam. Different types of mass spectrometers based on specific working principles are applied for ion separation in ICP-MS. These include: quadrupole mass spectrometers (Q-MS)^{1,26}, double focusing magnetic sector field mass spectrometers (SF-MS)²⁷ with single or multiple collectors (MC)^{28,29} based on Nier-Johnson geometry or with Mattauch-Herzog geometry (MH-MS)², time of flight mass spectrometers (TOF-MS)^{30,31}, ion traps (IT)³² and Fourier transform ion cyclotron resonance (FT-ICR) mass spectrometers³³.

Quadrupole-MS offers simple and fast operation with excellent stability and relatively low manufacturing costs. Since the introduction of ICP-MS, quadrupole-based systems are the most commonly used and represent a mature, routine, high-throughput trace element technique³⁴. It consists of four precisely machined cylindrical metal rods arranged in

parallel to each other (Figure 7). Opposite pairs are connected together. DC potential (U) and RF alternating current potential ($V \cos \omega t$) are applied to the pairs of the rods. DC potential is positive for one pair and negative for the other pair, while the amplitude of RF potential is equal for each pair. Varying the potentials applied to the rods generates an electromagnetic field that interacts with the ion beam. The ions are introduced from one end of the quadrupole at velocities based on their kinetic energy and mass. The flight path of each ion is deflected in a spiral path owing to the RF potential applied. At specific RF and DC potentials only ions with a specific m/z ratio can have a stable path through the rods, while all the others collide with the rods and are removed from the mass filter¹⁵.

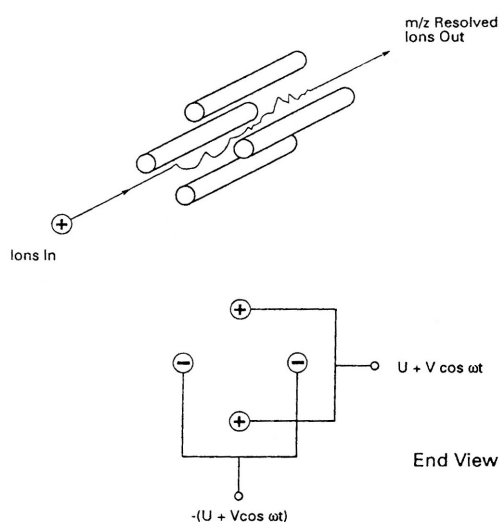


Figure 7 Schematic diagram of quadrupole rods showing ion trajectory and applied voltages¹⁵.

By rapidly changing the field generated by the quadrupole rods, the mass spectrum is scanned. Normally, scan rates of up to 3000 atomic mass units/s are achieved and cover the entire mass range in about 0.1 s. Scanning through the entire mass range (6-250 amu) easily contribute to the identification of all elements present within the sample analyzed. Moreover, for quantitative multi-element analysis, instead of scanning the entire mass range, a selected number of m/z ratios may be specified and measured using the so-called 'peak hopping' mode to save time. The resolving power of a Q-MS is relatively low ($R = 300$), which only allows to resolve most analytical species. However, this resolution does not allow to resolve isobaric (e.g. $^{110}\text{Pd}^+ - ^{110}\text{Cd}^+$) and polyatomic interferences (e.g. $^{56}\text{Fe}^+ - ^{40}\text{Ar}^{16}\text{O}^+$)¹².

The principle of a magnetic sector mass analyzer (Figure 8) is based on the fact that the flight path of a charged particle passing through a magnetic field is deflected by an angle proportional to its m/z . Double focusing instruments are combining the magnetic-sector mass analyzer with an electrostatic analyzer, which are applied to minimize directional and energy aberrations of an ion beam. This combination leads to improved resolution capabilities ($R = 10000$) in contrast to single focusing instruments. Such resolving powers can be applied routinely, greatly enhancing the ability to carry out interference-free determinations. The magnetic field applied is dispersive with respect to ion kinetic energy and m/z and focuses all ions with different flight angles. The electrostatic analyzer (ESA) is applied to filter the ions according only to their kinetic energy and focus the ions onto the exit slit, where the detector is located. By continuously varying either the accelerating voltage or the strength of the magnetic field as a function of time, the various m/z ion beams can be scanned onto the exit slit. Instruments in which a 90° ESA is combined with a 60° magnetic sector are referred to as Nier-Johnson geometry devices. This geometry is applied for multi-collector instruments, which are capable for high precision isotope ratio determinations³⁵. In the reverse Nier-Johnson geometry instruments, the ESA is placed behind the magnetic sector, which leads to subsequent energy focusing after mass separation. This geometry improves abundance sensitivity and reduce noise³⁶ and applied for single collector magnetic sector instruments.

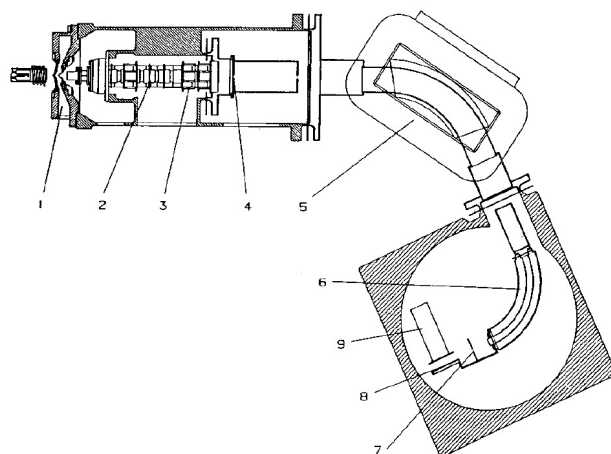


Figure 8 Reverse Nier-Johnson geometry HR-ICP-MS³⁷.

Detectors

Various types of detectors may count the number of ions emerging from the mass analyzer. The most popular ones are electron multipliers and Faraday collectors for high ion currents. Active film or discrete dynode electron multipliers (Figure 9) are used in the majority of ICP-MS systems applied for ultratrace analysis³⁸. Their working principle is based on one of the earlier designs applied, the so-called channeltron (channel electron multiplier)^{39,40}. The difference is that discrete dynodes are used for electron multiplication. The detector is positioned off axis from the MS to minimize background. The ions emerging from the MS strike the first dynode, which liberates secondary electrons that are accelerated and strike the next dynode to generate more electrons. The process is repeated many times and the multiplication factor is typically in the order of 10^8 . Finally the electrons are directed to a collector electrode. To extend the dynamic range, pulse and analog measuring modes can be performed by the same detector. Pulse counting mode measures relatively low currents (less than 2 million counts/s in case of a PE Sciex ELAN 6100 ICP-MS) with high sensitivity, while the operation in analog mode reduces the sensitivity of the detector. Therefore, this mode is capable to measure high currents. These two modes are properly calibrated against each other (normally referred to as 'dual-detector calibration') and provide an extended dynamic range of up to 9 orders of magnitude, moreover the simultaneous detection of major, minor, trace and ultra-trace element concentrations^{41,42}. While electron multipliers are commonly used for Q-MS, Faraday cup technology is applied rather for magnetic-sector instruments, particularly where high ion signals are detected for the investigation of high-precision isotope ratios using MC-ICP-MS⁴³.

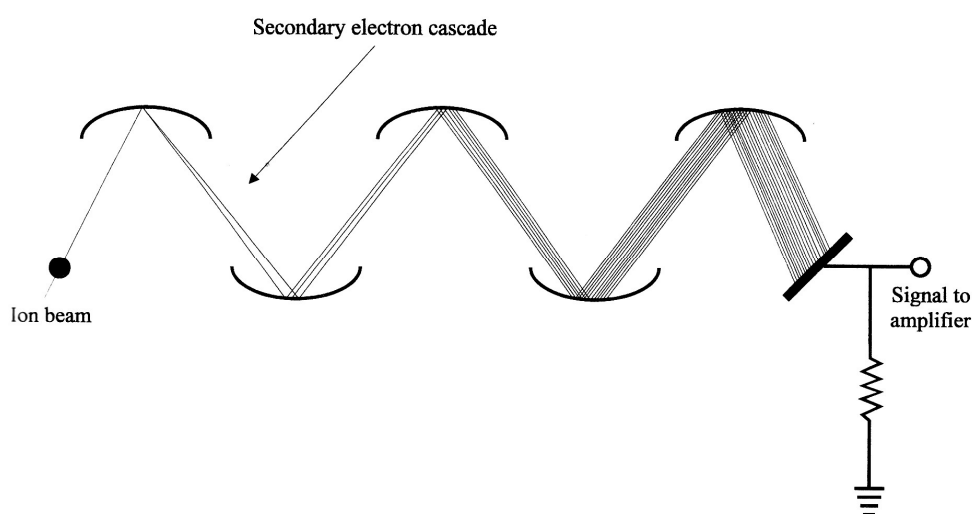


Figure 9 Schematic diagram of a discrete dynode electron multiplier⁶.

1.1.2 Sample introduction systems for ICP-MS

The common goal of sample introduction systems is to reproducibly transfer a representative portion of the sample to the ion source with the highest efficiency. Owing to the characteristics and requirements of ICP-mass spectrometers, the design and efficiency of the sample introduction system is a key point that influences the quality of the analytical results⁴⁴. Samples in different physical conditions, such as gaseous, liquid and solid may be introduced into the ICP-MS. Therefore, a wide range of sample introduction devices and methods have been developed⁶.

Gaseous samples may be introduced into the ICP-MS directly or after separation of various components by GC^{45,46,47}. On the other hand, gaseous samples may be generated from volatile element species, e.g. hydrides or other volatile chemical forms. Gas samples provide almost no matrix interferences within the ICP, since analytes in the vapor phase are separated from the matrix of the sample. The transport efficiency of gases into the ion source is the highest ($\leq 100\%$) in contrast to various solution nebulization and solid sample introduction methods. Moreover, the introduction of gaseous samples to the ICP does not require desolvation and vaporization, therefore the plasma energy contributes to more efficient atomization and ionization, which leads to improved sensitivity and lower detection limits. However, the drawback is that most samples are either liquid or solid and their analytes are often very difficult to convert to gaseous state. Hydride-generation (HG)^{48,49,50} produces volatile hydrides of elements, such as As, Bi, Ge, Pb, Sb, Se, Sn, Te at ambient temperatures. However, some of the severe drawbacks are related to interferences (caused by transition metals) and memory effects.

Liquid sample introduction is the major application of ICP-MS. The liquid samples are aspirated or pumped into the nebulizer, where it is getting dispersed into tiny droplets with the help of a high velocity Ar gas stream. The generated wet aerosol is introduced into a spray chamber where large droplets are separated and drained⁵¹. To achieve relatively high efficiency, the nebulizers must produce small droplets (10 μm in diameter), which are introduced to the ICP and being rapidly desolvated and vaporized. Various nebulizers may produce polydisperse aerosols with droplet size up to 100 μm in diameter. To enhance precision and improve plasma stability, these large droplets are removed by a spray chamber. Most popular are the barrel type and cyclonic spray chambers. The barrel-type double-pass Scott spray chamber⁵² (Figure 10) removes the large droplets by on-wall deposition caused by turbulence and gravitational forces. The inner concentric tube

diminishes the fluctuations of the aerosol density. Cyclonic spray chambers^{53,54} (Figure 11) are conical, where the nebulized aerosol enters from the side and transported in a spiral motion downwards, towards the drain and the inlet of the ICP. The characteristic motion causes a centrifugal force, which lead to collision of the large droplets with the chamber wall.

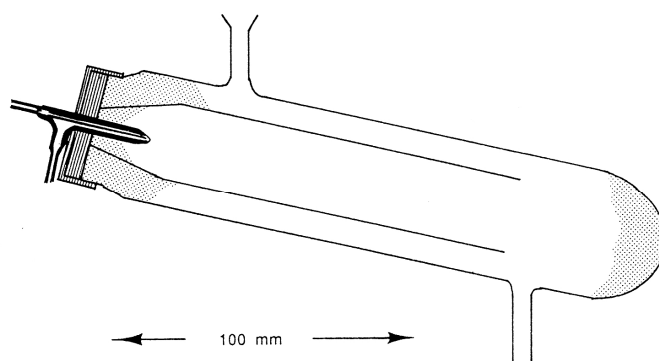


Figure 10 Double pass spray chamber¹⁵.

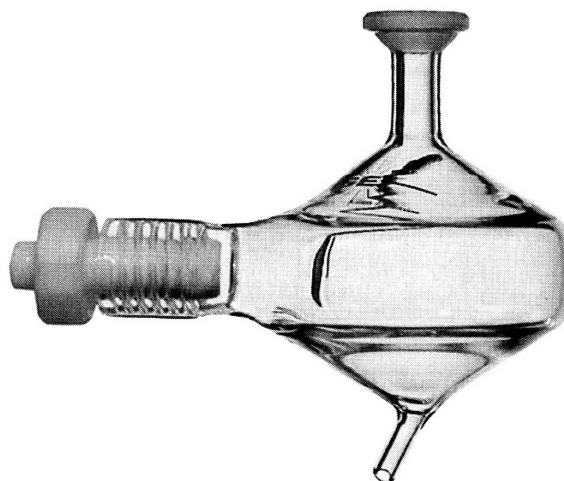


Figure 11 A typical glass cyclonic spray chamber⁵.

Selection of the nebulizer type is application dependent based on the total sample amount, the amount of dissolved solid contents and the presence of solid particles. Therefore, many different types have been developed, such as crossflow and concentric pneumatic nebulizers, hydraulic high pressure nebulizers (HHPN), babington-type nebulizers (e.g. V-groove nebulizers), ultrasonic nebulizers (USN), thermospray nebulizers, electrothermal nebulizers, etc^{55,56}. Where the sample amount is limited, e.g. direct injection nebulizers, high efficiency pneumatic nebulizers, direct injection high efficiency nebulizers, micro-

concentric nebulizers, micro-ultrasonic nebulizers, etc. can be applied for consuming relatively low sample amounts. The most common nebulizers for ICP spectrometry are pneumatic nebulizers (PN) and ultrasonic nebulizers (USN). The pneumatic micro-concentric nebulizer (MCN, Figure 12) is relatively highly efficient and produces fine aerosol and provides low RSD, moreover reasonably stable operation, even for unusually high concentrations (4 g/L) of dissolved matrix⁵⁷. Besides the early types made of glass, nowadays PFA versions are also available and they provide resistance to HF containing samples. Uptake rate normally varies between 20 – 1000 $\mu\text{L}/\text{min}$, which requires an Ar nebulizer gas flow rate of 0.5 – 1.5 L/min.

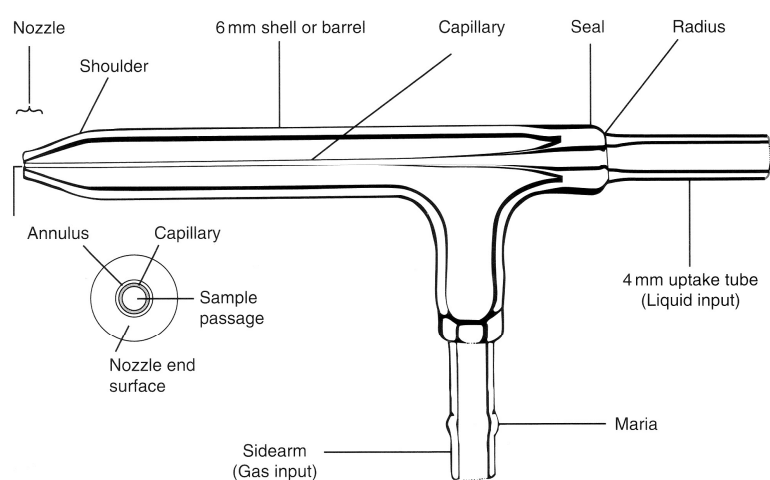


Figure 12 Schematic view of a glass concentric nebulizer⁵.

Solution nebulization is the most common way to introduce samples into an ICP-MS, however the samples to be analyzed are mostly solid. Converting solids to liquids is often problematic, since acid digestion is sometimes difficult and the digested liquid samples are prone to contamination from solvents, acids and the contact with the walls of vials and pipettes, etc. Moreover, element loss on container walls, evaporation during digestion and precipitation may also lead to the production of liquid samples not completely representing the composition of the original sample. In addition, digestion and preparation of sample solutions are relatively time consuming. Therefore, the direct introduction of solid samples into the ICP-MS represents alternative sample introduction strategies, which may contribute to overcome some of the limitations and drawbacks of sample digestion. In direct solid analysis, the preparation and handling of samples are significantly reduced and the samples are less prone to contamination. Spectral interferences caused by the solvent are greatly reduced and these methods may offer spatially resolved and/or in-depth information

as well. Specific techniques are required for successful introduction of solid samples into an ICP. Solid samples may be introduced directly into the plasma by using direct sample insertion (DSI)⁵⁸ or a fine aerosol or vapor may be produced from the solid samples using arc and spark ablation^{59,60}, electrothermal vaporization (ETV)⁶¹, laser ablation (LA)⁶² and others.

The application of DSI and ETV is similar, since both techniques offer microsampling capabilities and their operation is based on evaporation of solid samples. Since the material of the DSI probe and the furnace of ETV are generally both made of graphite, the drawbacks are similar, namely carbide formation, deterioration and memory effects make the analysis difficult. Both techniques require small amount of homogeneous sample (powders), which does not contribute to spatial or in-depth information of the original solid sample. The analytical performance is limited by the poor precision based on sample-to-sample heterogeneity, variability of sample size and the rate of vaporization. The last factor is mainly influenced by DSI, since ETV provides complete evaporation of the sample affected by the fully controlled temperature program. Another limitation is caused by the transient nature of the ion signal and the volatility differences of analytes, which do not lead to adequate multi-element capabilities by a quadrupole-ICP-MS.

Ablation by electrical discharges, such as arc (high current, low voltage discharges) and spark (low current, high voltage discharges), generates evaporation and material sputtering from the sample surface. The limitation of the techniques is that the sample matrix must be conductive or sample preparation is needed to make them conductive. This may result in contamination and costly sample preparation owing to the application of high purity conductive materials⁶.

Nowadays, laser ablation (LA) coupled to ICP-MS is representing the most attractive and versatile solid sampling technique, which enables the direct analysis of various solid samples without sample preparation and provides access to major, minor and trace element concentrations. Moreover, isotopic information with high spatial resolution and in-depth capabilities can be achieved.

1.2 Laser ablation as a sample introduction system for ICP-MS

Coupling of laser ablation as a direct solid sampling technique to ICP-MS was first realized by Gray⁶² in 1985. LA-ICP-MS offers superior capabilities for trace element analysis as well as isotope-ratio determinations in solid samples. Direct analysis of solids without the need of sample preparation, chemical dissolution and reagents provides particularly reduced risk of contamination of samples to be analyzed^{63,64,65,66}. Laser ablation may be applied for bulk analysis of samples using large crater sizes, or high spatial resolution capabilities can also be obtained while reducing the spot size of the laser radiation on the sample surface^{67,68,69,70}. LA provides rapid, quasi non-destructive sampling due to the removal of small sample amounts, and the high sensitivity offered by ICP-MS is sufficient to determine trace and ultra trace element concentrations⁷¹.

The operating principle of LA-ICP-MS has not changed significantly since its introduction. However, its capabilities have been significantly improved by the application of modern laser systems providing lower laser wavelengths in the UV range, reduced pulse duration and improved pulse to pulse stability⁷². Moreover, depending on the application almost all different types of mass spectrometers were coupled to LA, which improved the detection capabilities⁷². The general experimental setup of LA-ICP-MS is shown in Figure 13.

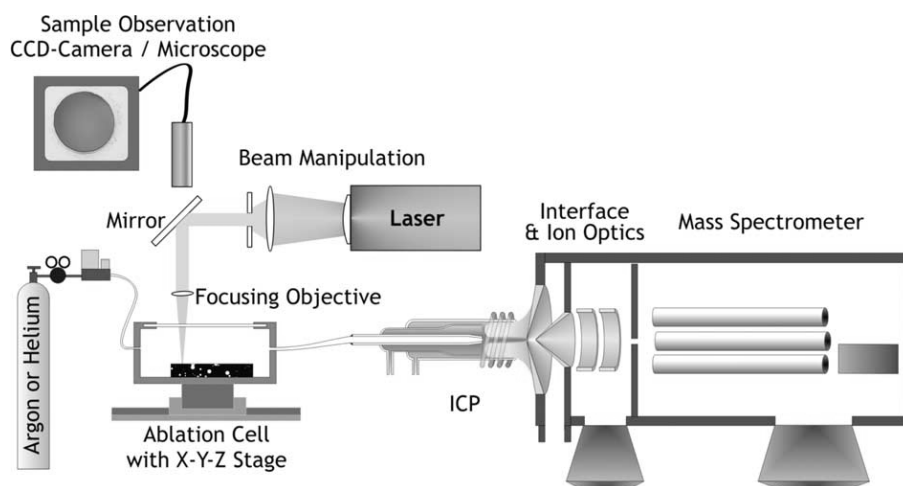


Figure 13 Schematic setup of LA-ICP-MS⁶⁵.

Pulsed laser radiation generated by a laser system is focused onto the surface of a solid sample, which is enclosed in an ablation cell. As the result of the laser-sample interaction, an aerosol cloud consisting of clusters, particles, atoms and ions is generated above the sample surface, which is continuously transported directly into the ICP-MS by an inert gas flow, such as Ar or He⁶⁵. The positioning of the sample relatively to the incident laser beam and the ablation process can be visually observed by a modified petrographic microscope or a CCD camera. The aerosol consisting of solid particles is vaporized, atomized and ionized within the ICP, and the generated ions are extracted by the vacuum interface and guided into the mass filter and finally detected.

In the following chapters, the characteristics of the individual parts are briefly summarized.

1.2.1 Laser beam properties

The laser (Light Amplification by Stimulated Emission of Radiation) source emits photons that are released from energized atoms applied. The emitted laser light is monochromatic, coherent and directional, which is well suited for interaction with samples. Based on the working principle, solid-state, gas, dye and semiconductor lasers are available⁷³. In solid-state lasers the solid matrix, which is most commonly a transparent crystal is doped with small amounts of metal ions (e.g. Nd or Cr). The most common solid state laser is the Nd-doped yttrium aluminium garnet (Nd:YAG) laser^{74,75,76,77}, having the most powerful emission at a wavelength of 1064 nm. However, other wavelengths, even in the UV region (e.g. 266 nm, 213 nm) can also be produced by harmonics generation^{78,79}. Ti:sapphire (Ti:Al₂O₃) laser systems having an output wavelength in the NIR range (~ 800 nm) are also commonly applied for fs-LA^{80,81,82}. Gas lasers representing four groups based on the kind of gases applied within the systems (He-Ne lasers, ion lasers (noble gas ions), molecular gas lasers (CO, CO₂) and excimer lasers (ArF, F₂, KrCl, KrF, XeCl, XeF providing different wavelengths depending on the gas applied)^{83,84,85,86}).

Nowadays, solid state (Nd:YAG, Ti:sapphire) and excimer (ArF, Figure 14) laser systems are mostly applied for LA⁶⁵ and are operating dominantly in UV wavelengths (266 nm, 213 nm, 193 nm) based on the benefits obtained in the ablation behavior^{77,83,79,87,88,89}. Parameters such as laser wavelength, pulse duration, irradiance based on the applied pulse energy, ablation frequency, laser beam profile and spot size have significant influence on the ablation process. The wavelength is one of the parameters most influencing the ablation

process, ablation rates, fractionation processes and the absorption characteristics of various materials (e.g. glass, fluorite, etc.)^{77,87,88}. IR wavelengths in contrast to UV lead to thermal processes that can cause melting of the material during ablation, which enhances the highly undesired elemental fractionation processes^{90,91}.

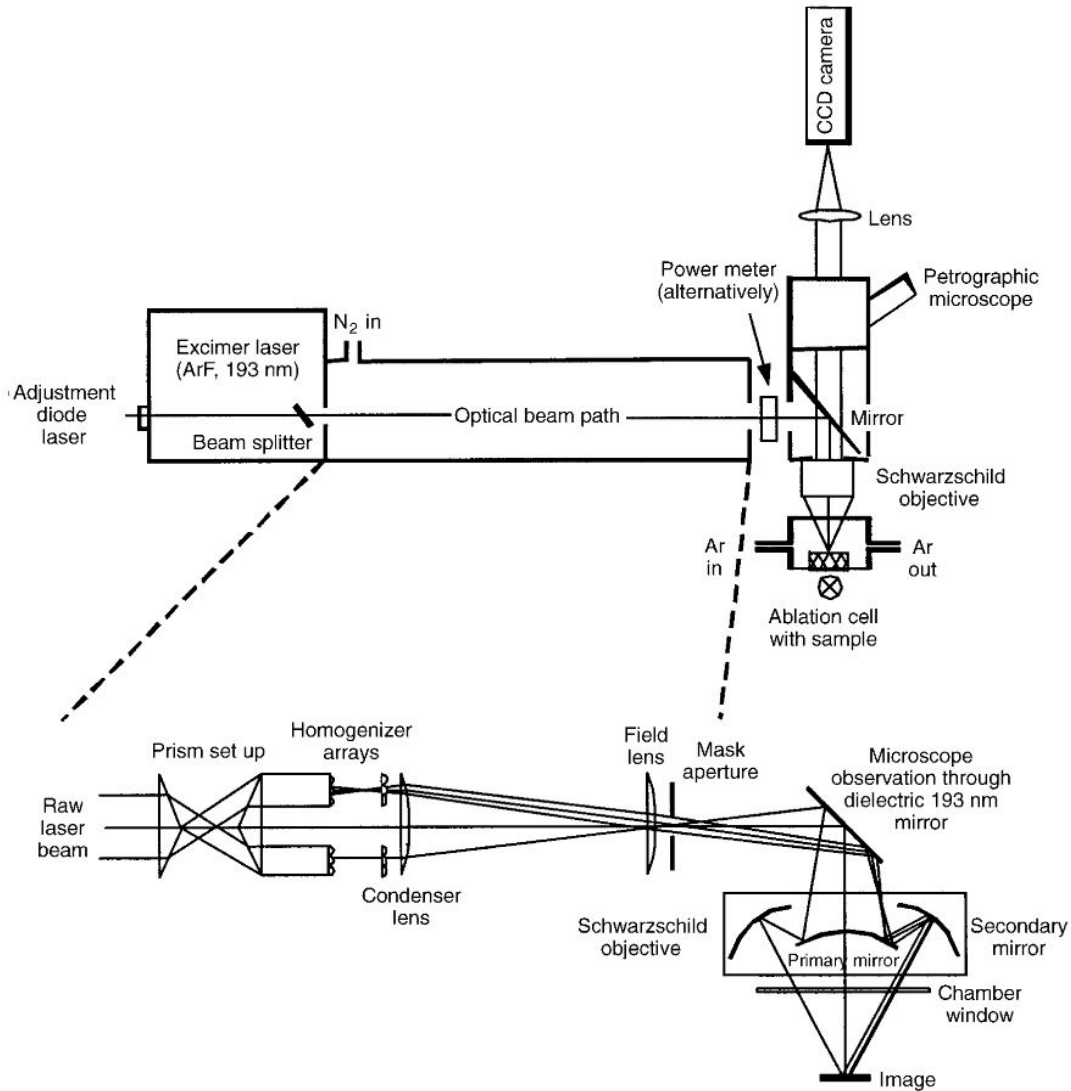


Figure 14 Schematic view of the optical beam path performing beam homogenization for an ArF excimer laser operating at a wavelength of 193 nm in combination with a petrographic microscope⁸³.

For samples with low melting points (e.g. numerous metals), the laser pulse duration appears to be more important than the wavelength applied. This is based on the thermal effects causing melting in the ablation crater, which contributes to altered vaporization

processes influenced by the melt, moreover a deterioration of the spatial and depth resolution due to the modified crater shape⁹². By reducing the pulse duration to femtoseconds from the typically applied nanoseconds, the thermal effects are greatly reduced. Therefore, a more stoichiometric sampling can be achieved^{81,93}. Besides, irradiance (power density) has also been found to influence the ablation characteristics and may contribute to non-stoichiometric effects⁹⁴. The laser beam profile may influence the spatial and depth resolution capabilities, since most lasers provide a Gaussian beam profile. Gaussian beam profile shows intensity maximum at the center of the beam, while towards the edges, the intensity is reduced. For analyses with high spatial and depth resolution, 'flat-top' beam profile is therefore preferred over the Gaussian profile. This can be achieved by beam homogenization (Figure 14) providing more uniform energy distribution across the laser spot⁷⁹. The spot size together with the irradiance have an effect on the amount of the ablated material, moreover, the crater depth to diameter ratio has been reported to be critical in terms of elemental fractionation⁹⁵.

1.2.2 Aerosol generation

The interaction of the laser beam and the sample involves processes that include heating, melting and evaporation of the sample material at extremely high temperatures and pressures⁹⁶. The conversion of the incoming energy into heat is very fast, leading to melting and boiling across the area of the laser spot⁷². Since the time required for vaporization is dependent on the thermal conductivity, mass density, heat capacity and vaporization temperature of the sample and the irradiance of the laser, the time for vaporization is sample matrix dependent. Owing to the high temperature gradient at the periphery of the crater, a segregation of elements having different boiling points may occur⁷². Mass from the sample may be released in the form of atoms, electrons, ions, molecules, vapor, droplet solid flakes, large particulates, or a mixture of these^{63,96}. The laser induced plasma can interact with the incident beam causing plasma shielding^{97,98}, which is generated by absorption or reflection of the incoming beam by the plume. Plasma shielding, which depends on the ionization potential of the gas environment, reduces laser energy coupling efficiency onto the sample⁹⁴. High ablation frequencies contribute also to more pronounced plasma shielding, which may influence the ablation rate of the sample. Depending on the laser power density and the sample matrix, mass removal can occur by desorption, thermal evaporation, surface instability of the molten mass, exfoliation, phase explosion and other mechanisms^{63,99}. The size of individual particles may change by condensation, vaporization

or agglomeration^{100,101} and a significant amount of the material is deposited as debris on the sample surface¹⁰². The structure of the agglomerates is matrix dependent¹⁰¹, while individual particles may differ in composition based on their size⁹². An extensive review is available on the physical description of laser-sample interaction⁹⁶, however the particle forming processes using various state-of-the-art laser systems operating at different wavelength, pulse duration, energy and power density and various gas atmospheres are not fully understood yet¹⁰³. Investigation of particle size distribution of aerosols generated from different samples has been studied using mainly optical particle counters or scanning electron microscopes^{101,104,105,106}. The size of the generated particles is crucial, since it may influence the transport efficiency and the vaporization efficiency inside the ICP. As demonstrated by Aeschliman et. al. many large ablated particles fly through the ICP intact contributing to signal noise, deposition on cones and elemental fractionation¹⁰⁷. Studies on visualization of aerosol expansion within various gas environments has recently been carried out using laser induced scattering to gain further insights into dispersion characteristics of laser generated aerosols within the ablation cell^{108,109} or during transport¹¹⁰.

1.2.3 Ablation cells and aerosol transport

A typical LA sampling system consists of an ablation cell, which hosts the samples to be analyzed and supports the positioning of the sample in three spatial axes relatively to the incident laser beam, moreover a tube, which transfers the laser generated aerosol from the ablation cell to the ICP.

The most important requirements for the ablation cell are to host the samples, to be air-tight, to allow fast washout and easy handling for exchanging samples. Many different ablation cells have been reported since the introduction of LA. These designs were different in terms of internal volume, geometry and gas flow dynamics. Most of the earliest cell designs were reported for LA-ICP-OES by Thompson et. al¹¹¹, Carr and Horlick¹¹², Ishizuka and Uwamino¹¹³ and for LA-ICP-MS by Arrowsmith and Hughes¹¹⁴, Mochizuki et. al.¹¹⁵. Since the introduction of a nozzle within the gas inlet of the cells, all ablation cells succeeded in having a relatively rapid washout of particles from the cells¹¹⁶. The volume, geometry, type of carrier gas and its flow pattern, moreover the properties of the transport tubing can contribute to the transport process of the laser generated aerosol, consequently to the transient signal structure. Thus, enhancing the transport efficiency with respect to fast washout leads to an increase in spatial resolution, which improves the capabilities of

LA-ICP-MS. The volume of the entire transport system (cell and tube) has almost no influence on transport efficiency^{117,118}, but it affects the transient signal structures owing to the different aerosol dispersion characteristics^{116,117}. The mass transport efficiency is rather influenced by the gas environment within the ablation cell, the laser wavelength and the irradiance. These factors can contribute to differences in particle size distribution¹¹⁴ of the aerosol depending on the sample absorption characteristics and the resulting thermal processes on the sample surface. The transport efficiency has been found to be typically low for particles smaller than 5 nm, which tend to be lost by diffusion, and also low for particles larger than 3 μm , which are prone to be settled out due to gravity and other forces^{119,114}. Transport efficiency may also be influenced by deposition of particles on the tube walls¹²⁰, especially if the tube material is electrostatic and capture some of the particles. Novel ablation cell designs have been demonstrated recently, to improve washout characteristics^{118,121} and particle extraction^{122,123,124}. Numerical simulation of mass transport has also been proposed to investigate the dispersion of the aerosol and other factors influencing analyte loss within the transport process^{125,126,127}. Since the size of the ablation cells restricts the sample size, the use of commonly applied ablation cells is not feasible, if the sample is valuable and cannot be segmented. Thus, the use of open design cells has also been proposed^{114,128}. In this case the cell is attached to the sample and sealed to the surface. This approach may be an alternative solution to analyze large and valuable samples, such as art objects or archaeological samples, etc. The sealing process has to be performed carefully in order to prevent the introduction of ambient air into the carrier gas. Moreover causing any contamination to the sample surface by the sealing material and modifying surface geometry (uneven surfaces) are usually not allowed for specific samples. For such applications an open, non contact sampling system designed in the current study can offer a feasible solution. Other severe sample requirements led to the development of cells used for special applications, such as cryogenically cooled ablation cells for the analysis of biological samples^{129,130}.

In terms of transport tubes, various studies have been focusing on the properties of aerosol dispersion and transient signal structures by varying the length or diameter of the tube used^{113,116,117}. Beside the dispersion characteristics, particle deposition causing aerosol loss within the transport tubes has also been reported¹²⁰.

1.2.4 Carrier gases used for ablation

Various studies have reported that the use of different gases within the ablation cell contribute to changes in signal intensities and background levels measured by ICP-MS. Ar was traditionally used as an aerosol carrier for LA-ICP-MS, since it can be passed through the ablation cell and directly introduced into the ICP without altering the plasma conditions. With the application of gases other than Ar, ICP operating conditions are influenced causing altered plasma temperature, electron temperature, electron number density, which affect vaporization, atomization and ionization processes within the ICP^{131,132,133,134}. Recently, instead of argon, helium is applied in most applications due to improved ablation and transport characteristics. Helium contributes to improved mass transport efficiency resulting in less deposition of the ablated material on the sample surface^{102,135}, and therefore to improved signal to noise ratios, which lead to enhanced sensitivity and lower detection limits¹³⁶. Since the different physical properties (density, ionization energy and thermal conductivity) of gases may induce differences in the PSD of aerosols, smaller particles generated in helium can be more efficiently transported¹³⁵. On the other hand, the enhanced signal response recorded by ICP-MS is also caused by the presence of helium in the plasma resulting in higher gas temperature and faster vapor transfer from the particle surface during vaporization¹³¹. However, the degree of signal to noise improvement has been reported to be wavelength dependent¹³⁵. Significant differences in ablation rates based on the type of gas applied within the ablation cell were not found¹³⁷. Mixing the aerosol generated in helium with moistened argon has also been reported¹³⁶. This leads to an additional increase in sensitivity owing to a more efficient energy transfer to the analyte by the diatomic water inside the ICP. However, the higher background caused by polyatomic interferences owing to the presence of water has reduced the multi-element capabilities especially for light elements¹³⁶. The influence of other noble gases, such as Ne, Kr and Xe has also been investigated^{138,135,139}, however, these were not found to provide improvements in sensitivity in comparison to He. Addition of other reactive gases, such as H₂, N₂ and methane has also been reported using various sample introduction systems^{140,141,142,143,144,145,146}. The addition of hydrogen, nitrogen and methane was found to contribute to enhanced ionization. This was caused by improved energy transfer from the plasma towards the particles affected by the higher thermal conductivity, moreover the partial ionization of these gases contributed to a higher electron density, which also affects ionization. The degree of signal enhancement was found to be roughly correlated with the 1st ionization potential of elements indicating an improved degree of ionization^{142,140,144}. Some studies demonstrated not significantly enhanced sensitivity when adding N₂^{140,147}, however it was found to improve stability and precision when it was

introduced within the cooling gas flow¹⁴⁷. The application of molecular gas additions is however, limited by the increased background caused by enhanced polyatomic ion formation and often represent a drawback for multi-element analysis.

1.2.5 Non stoichiometric effects

Elemental fractionation¹⁴⁸ is one of the limitations in LA-ICP-MS that is described by non-stoichiometric effects occurring during ablation, aerosol transport, vaporization, atomization and ionization of the material within the ICP and ion transfer⁶⁵. This effect can be described by the so-called ‘fractionation index’ (Figure 15), which is defined as the temporal change in the elemental ratios during a single hole drilling mode ablation. The second half of the analyte signal is divided by the first half and normalized to the signal of Ca¹⁴⁸. The processes involved in elemental fractionation have been widely investigated since 1995, and various approaches have been proposed to minimize fractionation, however it has not been completely eliminated yet^{65,94}. Fractionation is element dependent, thus a correlation has been made between fractionation effects and physical properties of elements, such as melting and boiling points, vapor pressure, atomic and ionic radii, charge, and speciation^{77,149,150,151,152,153,154}. Laser induced elemental fractionation describes non-stoichiometric effects highly depending on various laser parameters (Chapter 1.2.1). The applied wavelength, pulse width, irradiance, absorption characteristics of the sample, etc. may influence the particle forming mechanisms, consequently the particle size distribution (PSD) of the generated aerosols^{135,137,153,155,156,157,158}. For example, it was demonstrated that during ablation of a brass sample using a ns-LA system operating at 266 nm, the composition of the generated particles is size dependent. Cu was found in larger particles (> 100 nm) and Zn was enriched in the smaller particles or in the vapor phase based on the different volatility of these elements⁹². It was found that a critical crater depth to diameter ratio (> 6) may also induce elemental fractionation⁹⁵. Transport induced fractionation has been demonstrated in numerous studies. Element selective vapor condensation on tube walls or selective nucleation of species on different sized particles have been reported^{91,119,159}. Ablation gas environment may also contribute to elemental fractionation, since it may influence the transport efficiency and PSD of the aerosols¹⁰². ICP induced fractionation has also been studied. It was shown that separating large particles from the aerosol transported into the ion source leads to a more uniform and complete vaporization of particles within the ICP with reduced fractionation^{156,160}. Kuhn et. al. has studied particle-size-related fractionation within the ICP by removing large particles from

the aerosol¹⁰⁵. It was shown that solid particles produced by the ablation of a silicate glass NIST 610 sample are completely vaporized and ionized in the size range of 90 – 150 nm¹⁰⁵. Particles larger than this size range may not be completely vaporized and thus the measured ions do not completely represent the real composition of the sample. Furthermore, it was reported that the carrier gas composition may also influence fractionation effects¹⁶¹.

Beside elemental fractionation, matrix effects within the ICP caused by intense mass load have also been reported¹⁶². It was demonstrated that by introducing different amounts of aerosol into the ICP by changing the laser spot size, the intensity ratios of elements are significantly changed, especially for elements with low melting points^{80,162}.

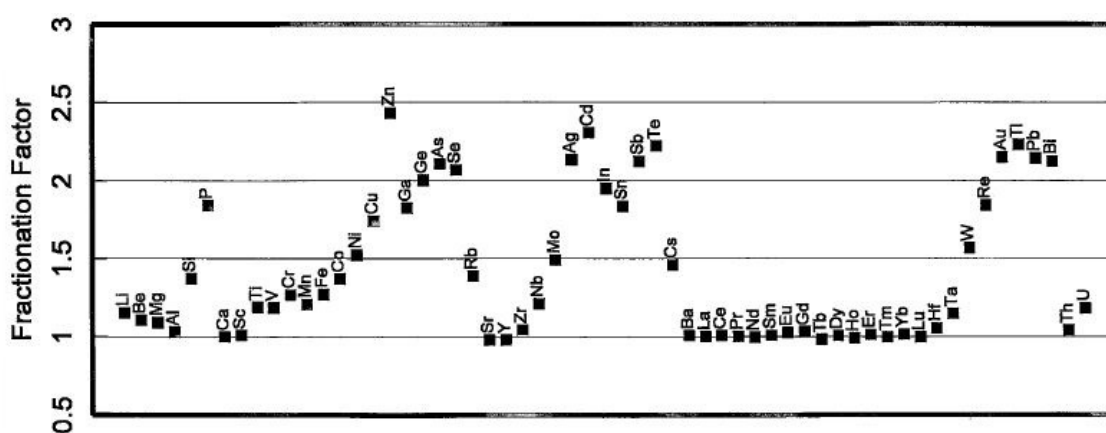


Figure 15 Fractionation indices reported by Fryer et. al. for a total of 4 minutes continuous ablation of NIST 610 silicate glass normalized to Ca¹⁴⁸.

1.2.6 Calibration strategies in LA-ICP-MS

Various calibration strategies are applied to determine element concentrations in solid samples by LA-ICP-MS⁹⁴. Since there is no universal method to perform calibration using LA-ICP-MS, a number of strategies have been proposed. These include external calibration using matrix-matched solid reference materials to perform calibration using a selected element as internal standard, or to perform calibration using the 100 % normalization approach using the entire matrix as internal standard¹⁶³. Alternative strategies are the liquid calibration using dual liquid-solid sample introduction systems or direct liquid ablation using LA only for sample introduction.

Matrix-matched external calibration is the most commonly applied quantification strategy for LA-ICP-MS. To match the matrix of a sample and a calibration standard is important in terms of ablation rate, particle size distribution and mass. A wide range of certified reference materials is available from various manufacturers (e.g. National Institute of Standards and Technology – NIST, MD, USA; MBH Analytical Limited, UK; Institute for Reference Materials and Measurements – IRMM European Commission Joint Research Centre, Belgium; Federal Institute for Materials Research and Testing – BAM, Germany; etc.). Although numerous types of reference materials are offered, these do not cover the entire range of sample types and elements that can be contained within the samples. This limitation therefore represents one of the major difficulties in LA-ICP-MS. Alternatively to commercially available reference materials, in-house produced calibration materials may be used. This can be accomplished by mixing of compounds to a powdered matrix and pressing them with or without binder materials^{164,165,166}. Furthermore, the addition of standard solutions to a powdered matrix; co-precipitation of elements into a matrix with single element solution¹⁶⁷; drying and pressing^{167,168}; glass fusion¹⁶⁹; etc have also been tested. The use of internal standards provides a robust calibration method by correcting for the different ablation yield between sample and reference material. The internal standard element in known concentration must be homogeneously distributed within the sample and should behave similarly to the analytes of the sample during sampling. In case of completely unknown samples, the 100 % normalization approach may also be applied if all constituents of the sample are measurable. This allows to use the entire matrix for internal standardization¹⁶³.

External calibration using solution standards for the analysis of solids requires a dual sample introduction system^{165,170}. This dual flow system allows the simultaneous introduction of nebulized solution standards and laser ablated material. During the ablation a blank solution is aspirated and nebulized into the plasma to maintain constant plasma conditions during the entire analysis. To prevent higher oxide formation and enhanced polyatomic ion formation, the solution standards are commonly desolvated before entering the ICP^{171,172}, if analyte loss is not caused by the desolvation process. Solution standard additions have also been reported, which offers correction for potential plasma-based matrix effects¹⁷³.

Direct liquid ablation as an alternative calibration strategy for laser generated aerosols has been demonstrated by Günther et al.¹⁷⁴. It was shown that the fractionation resulting from splashing and evaporation was minimized by covering the surface of the liquid with a plastic thin film. This approach allowed the determination of numerous element

concentrations in NIST 610 and 612 by using an ArF excimer laser operating at 193 nm. The direct liquid ablation has been improved by modifying optical absorption characteristics of the solutions with the addition of a chromophore to improve ablation characteristics¹⁷⁵.

1.3 Aim of the study

This work consists of four major topics and the aim of the individual parts was focused on the following points:

A) Development of a unique direct atmospheric sampling method for LA-ICP-MS

The aim was to develop, manage and optimize an experimental setup for LA-ICP-MS that utilizes ambient air as ablation gas atmosphere and direct suction of laser generated aerosols above the ablation spot. This flexible sampling method was planned to substitute the role of the ablation cell. To realize the compatibility of air as the ablation gas atmosphere and the Ar ICP, a recently developed gas exchange device was planned to be included and optimized within the experimental setup. The developed setup had to be optimized and its applicability had to be determined by comparing the capabilities using He, Ar and air. Moreover, the efficiency of the aerosol suction had to be investigated.

B) Investigation of the influence of gas exchange experiments on various fundamental processes in LA-ICP-MS

The aim of these studies was to investigate the potential of a number of fundamental processes when using air instead of He or Ar as ablation gas environment. These investigations included to compare elemental fractionation, aerosol structure and particle size distributions and study the effect of humidity on signal intensity. Utilizing the gas exchanger, ion diffusion loss within the ICP was planned to investigate based on the exchange of He to Ar. Furthermore, the capabilities of the developed aerosol suction method was planned to investigate for direct liquid ablation.

C) Investigation of the influence of tube materials on ICP operating conditions

The aim of this study was to prove that various tube materials used in the transport system of LA-ICP-MS has an influence on the plasma operating conditions. With respect to stable plasma conditions, suitable tube materials were planned to propose. Moreover, approaches were planned to demonstrate how to reduce the influence of tube materials on plasma conditions.

D) Investigation of new solid gold calibration materials using liquid and solid calibration approaches and their applicability for gold analysis

The aim of this study was to investigate the applicability of new calibration materials for fingerprint studies of various gold objects using LA-ICP-MS. For the application of the

calibration materials, their composition had to be determined. For this purpose, cross validation of results obtained using solid and liquid calibration were planned to utilize. For liquid calibration, a suitable approach had to be developed to stabilize Cu, Ag, Au, and other elements within one solution. The developed liquid calibration had to be validated in terms of accuracy and precision using NIST certified gold reference materials. The determined element concentrations had to be compared with data provided by the manufacturer based on acid digestion and liquid analysis by ICP-OES. The new calibration materials with the determined element concentrations were planned to apply in routine analysis of gold objects using LA-ICP-MS.

2. Influence of tube materials on plasma conditions

The content of this chapter was partially published in J. Anal. At. Spectrom., 2008, ref.¹⁷⁶

Authors: R. Kovacs and D. Günther

Influence of transport tube materials on signal response and drift in laser ablation-inductively coupled plasma-mass spectrometry

2.1 Introduction

Besides the aerosol generation and decomposition of the ablated material in the high temperature argon plasma, the transport of laser generated particles is of importance for quantitative analysis^{118,108}. The transport tube is responsible for aerosol dispersion^{116,117,177,110}, can contribute to material losses¹²⁰, and might therefore influence precision and accuracy. The effects on tube lengths and diameter in LA-ICP-MS have been studied using single shot ablations^{117,177} and it has been shown that the reduced volume of the transport system improves signal to background ratios. Similar results have been reported using ETV-ICP-MS¹⁷⁸. Bleiner and Bogaerts modeled transport systems used in LA-ICP-MS¹²⁶. It was found that longer tubes contribute to reduced signal intensities, which is most pronounced for larger tube diameters.

Recently, Luo et. al.¹⁷⁹ demonstrated that the uncertainty of the element concentrations in the standard reference materials and instrumental drift are the major contributors to the total uncertainty budget in LA-ICP-MS. However, origin and magnitude of drift remained partially unknown.

Different molecular (O₂, N₂, H₂) and other (Xe) gas additions to argon ICPs have been extensively studied. Gas additions to argon aimed to improve limits of detection and reduce matrix effects^{180,131}. The principal reason for the addition of oxygen to argon was the reduction of carbon deposition from organic materials during analysis. However, it has been reported that oxygen addition to the outer gas flow has no influence on signal intensities using wet plasma conditions¹⁸¹. Rodushkin et. al. reported that the addition of small amounts of carbon-containing substances to the carrier gas results in enhanced sensitivity, especially for elements with high first ionization potentials. Reduced oxide formation and

reduced abundance of Ar-based molecular ions have also been reported¹⁴². Similar results and reduced Xe background have been discussed by Hu et. al.¹⁸².

Additions of hydrogen, nitrogen and carbon-containing gases to the argon nebulizer gas have also been reported for LA-ICP-MS. Various amounts of these mostly diatomic gases were added to the argon plasma to improve sensitivity. Louie and Soo¹⁴⁶ found improved sensitivity when adding hydrogen or nitrogen to the plasma. Guillong and Heinrich¹⁴⁰ reported that the addition of 4-9 mL min⁻¹ hydrogen to the He carrier gas results in 2-4 times enhanced sensitivity in LA-ICP-MS when ablating NIST 610, especially for elements with high first ionization potentials. This work has shown that nitrogen and methane was less effective on sensitivity. Günther and Heinrich¹³⁶ added small amounts of water to the argon carrier gas and observed slightly enhanced signal intensities, lower backgrounds for high mass elements, but also increased polyatomic ion formation. O'Connor et. al.¹⁸³ demonstrated that wet plasma conditions are advantageous for LA-ICP-MS analysis owing to the increased tolerance with respect to different plasma loads¹⁶². Furthermore, it has been reported that water addition to laser-generated aerosols provides plasma conditions in favor of reduced matrix effects. However, the general applicability of water addition to the carrier gas in LA-ICP-MS is reduced due to an increased probability of polyatomic ion formation (oxides, hydroxides). Based on these reports the reduction of matrix effects by adding water (pro) and the occurrence of polyatomic interferences (con) need further validation before general recommendations can be made. Furthermore, Kosler et. al.¹⁶¹ have shown that the presence of small amounts of oxygen added to the carrier gas contributes to laser-induced elemental fractionation in LA-ICP-MS.

All of the mixed gas studies have demonstrated that already 'tiny' amounts of gases added to the carrier gas flow can change the operating conditions of the ICP. Furthermore, various ablation cell designs and transport tube dimensions have been studied to influence the signal shape. However, only one manuscript was focused on material loss within the transport tube¹²⁰. To our knowledge, the influence of the transport tube material and length on signal response and plasma stability has not been investigated in detail. We are well aware that some common knowledge of pros and cons of tube materials exist. However, this knowledge is not broadly applied. Therefore, the influence of four of the most commonly applied tube materials (PVC, nylon, Teflon and copper) on signal intensities and drift was investigated.

2.2 Experimental

The experiments were performed using two versions of a beam-homogenized 193 nm ArF excimer laser ablation system⁸³ (GeoLas Q and C, MicroLas, Göttingen, Germany) coupled to an ELAN 6100 DRC+ quadrupole ICP-MS instrument (Perkin Elmer Sciex, Canada). PVC (Tubclair AL, transparent, lightweight, flexible), nylon (SMC, opaque, rigid), Teflon (opaque, rigid) and copper tube materials were used upstream and downstream of the ablation cell. The length of the tubes was varied between 1 and 20 m and the inner diameters were 4 - 4.5 mm with approximately 1 mm wall thickness. To change between tubes of different length without changing the carrier gas flow rate, plastic switch taps (Semadeni AG, Ostermundigen, Switzerland; inner part: PTFE, outer part: PP) were applied. This configuration allowed passing the aerosol separately into two different transport lines, when the tubes were applied downstream of the ablation cell (Figure 16). To maintain stable plasma conditions, the laser generated aerosol transported in helium was mixed with argon (nebulizer gas) using a mixing bulb directly in front of the injector. The laser and ICP-MS operating conditions are summarized in Table 2. It is important to note that the ICP-MS instrument used is exclusively applied for laser ablation sampling. Therefore, no long-term drying procedure was necessary. However, the entire transport system (cell and every tube) was flushed with helium prior to the measurements.

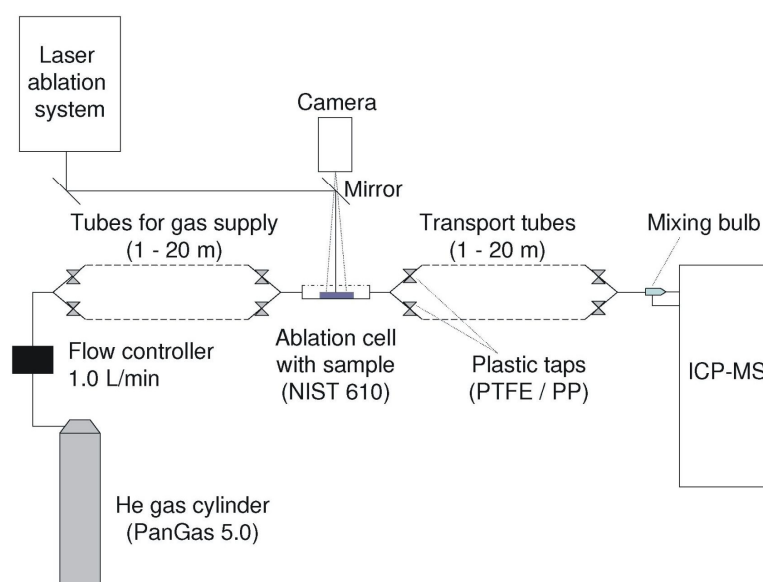


Figure 16 Schematic view of the experimental setup for the tube material studies. Plastic taps were applied to switch between different tubes without changing the carrier gas flow rate.

Table 2 Operating conditions for laser ablation and ICP-MS

Laser ablation		
Laser ablation system	GeoLas Q, ArF excimer	GeoLas C, ArF excimer
Wavelength	193 nm	193 nm
Pulse duration	15 ns	15 ns
Ablation frequency	10 Hz	10 Hz
Spot size	40 – 80 μm	94.5 μm
Laser fluence	18.6 – 21.2 J cm^{-2}	3.2 J cm^{-2}
Ablation time	60 s	60 s
Ablation mode	single hole drilling	single hole drilling
Sample	NIST 610	NIST 610
Carrier gas flow	He (PanGas 5.0 purity), 1.0 L min^{-1}	He (PanGas 5.0 purity), 1.0 L min^{-1}

ICP-MS	
Instrument	PE Sciex ELAN 6100 DRC+
Nebulizer gas flow	0.85 - 0.90 L min^{-1}
Auxiliary gas flow	0.75 L min^{-1}
Plasma gas flow	17.5 – 17.8 L min^{-1}
RF power	1340 - 1380 W
Lens setting	autolens calibrated
Detector mode	dual (pulse counting and analogue mode)
Dwell time	10 ms
Scan mode	peak hopping

After a 30 minute warm-up period of the instrument, the operating conditions were always optimized prior to the analysis using a 1 m PVC tube. The gas flows and RF power were tuned with respect to highest sensitivity, while keeping the oxide formation low (based on $\text{ThO}^+ / \text{Th}^+ \leq 0.5 \%$). After the last step of the optimization (auto lens calibration) no parameters were changed during the measurements. All experiments were carried out using NIST 610 glass SRM, since it provides access to information on concentrations for 61 elements. The transient signal recording started with the measurement of 30 s background of the He blank followed by a 60 s signal acquisition from a single crater ablation. The ablation events were continuous and the applied frequency was 10 Hz. All experiments were carried out using a fixed number of laser shots. Data reduction and signal integration (the entire signal was integrated) was adapted to the procedure described in ref.¹⁸⁴. To demonstrate the influence of the tube length for each material, the background corrected signal intensities obtained using various tube lengths (e.g. 5, 10, 20 m) were normalized to the background corrected intensities measured using a 1 m long tube. The stability of the setup was tested for one configuration (both tubes PVC of a length of 1 m) and relative standard deviations of better than 2 % were determined. Therefore, all deviations above 10 % can be attributed to the tube material and will be discussed.

2.3 Results and discussion

2.3.1 Influence of PVC tube material

Using PVC tubes of a length of 1, 5, 10 and 20 m led to signal enhancements towards longer tubes of up to 70 %. Figure 17 exemplarily summarizes the relative increase in background corrected signal intensity when compared to the shortest tube length (1 m). The lighter elements ($\leq m/z$ 111) are significantly more influenced than the heavier ones. The most significant signal enhancements were observed for Be, Si, Ni, Cu, Zn, Ag and Cd. These changes in intensity were also observed when using a 266 nm Nd:YAG and a Ti-sapphire-based femtosecond laser ablation system (data not shown) and were not caused by changes in the position of ablation within the ablation cell¹¹⁷ or changes in the background intensities for the majority of the elements listed. The enhancement factors were depending on the time applied for flushing the tubes with helium. In addition to the relative changes of the intensities, normalization to Ca was applied to investigate the influence of the tube material on drift of element ratios. The changes of the element-to-Ca ratios are summarized in Figure 18.

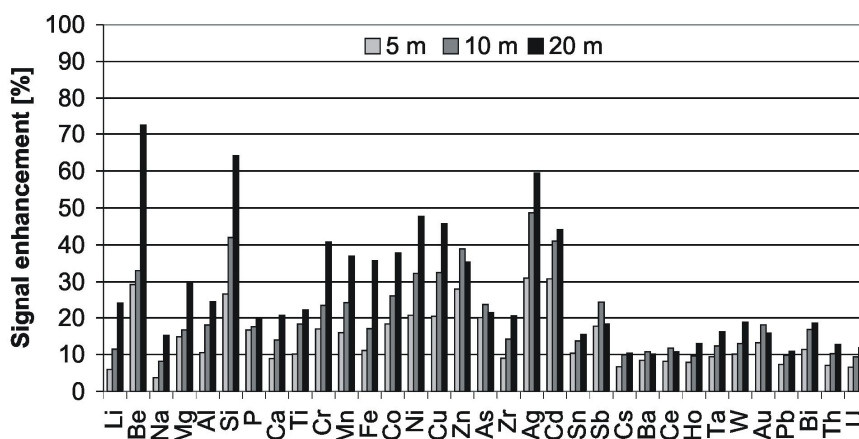


Figure 17 Enhancement in signal intensity using 5, 10, 20 m long PVC tubes normalized to 1 m. The tubes were applied as transport tubes. Laser ablation system: ArF excimer (GeoLas C, 94.5 μm , 10 Hz, 3.2 J cm^{-2}). Measured oxide formation: 0.31 % (1 m), 0.44 % (5 m), 0.56 % (10 m), 1.06 % (20 m) based on ThO^+/Th^+ .

Investigation of the background intensities indicated however, that some isotopes were influenced by increased background (e.g. $^{27}\text{Al}^+$, $^{29}\text{Si}^+$, $^{42}\text{Ca}^+$, etc.) when longer tubes were used. To monitor the element response and the plasma conditions for the different tube

lengths, mass spectra in the range of m/z 1-260 were recorded. It was found that the intensities of carbon, oxygen, water vapor and argon-hydride are a function of the tube length when using PVC (Figure 19).

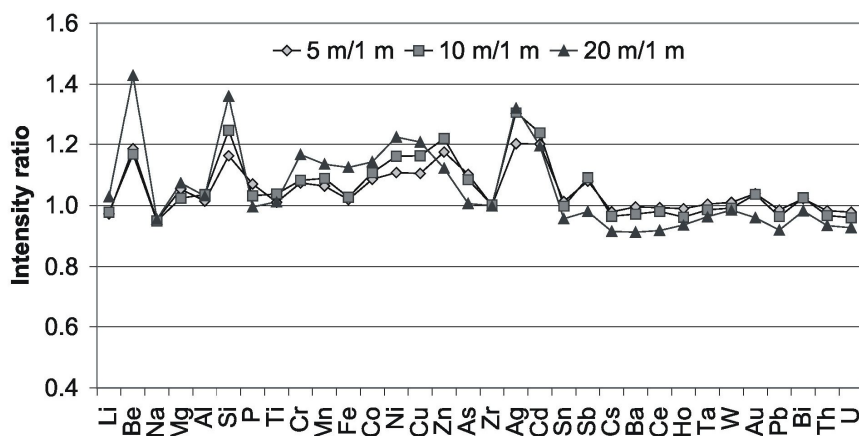


Figure 18 Element-to-Ca ratios for 5, 10 and 20 m PVC tubes, normalized to the results obtained with 1 m long tube. The tubes were applied as transport tubes.

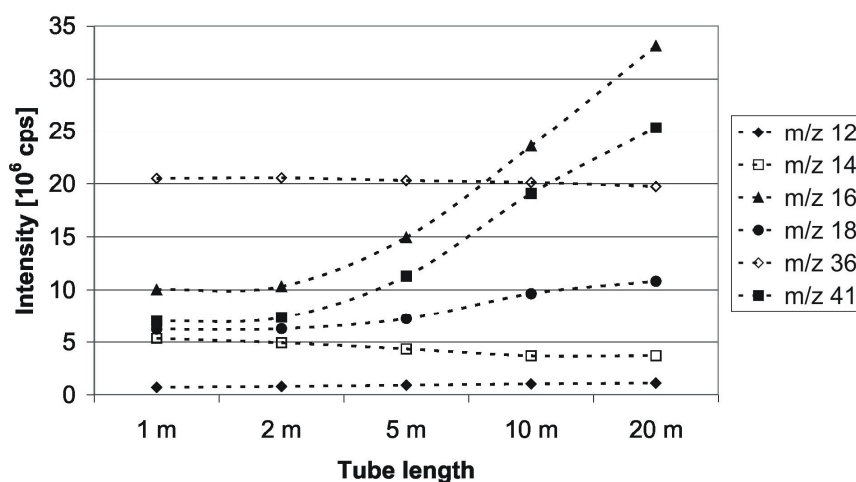


Figure 19 Differences in the He gas blank when using PVC tubes of 1, 2, 5, 10, 20 m downstream of the ablation cell ($n=3$, $RSD \approx 1\%$). The most significant differences in intensity were measured for argon-hydride (m/z 41) with a factor of 3.6, oxygen (m/z 16) with a factor of 3.3 and water (m/z 18) with a factor of 1.7 when comparing background intensities measured for a tube length of 20 m in contrast to 1 m. The increase in intensity of carbon (m/z 12) was 60 %, whereas the intensity of nitrogen (m/z 14) decreased by 30 %. Furthermore, a minor decrease of 4 % in the ion intensity of argon was also observed.

The presence of hydrogen and oxygen in the plasma leads also to more pronounced formation of polyatomic interferences (e.g. $^{27}\text{Al}^+$ ($^{15}\text{N}^{12}\text{C}^+$, $^{14}\text{N}^{13}\text{C}^+$, $^1\text{H}^{12}\text{C}^{14}\text{N}^+$), $^{29}\text{Si}^+$ ($^{13}\text{C}^{16}\text{O}^+$, $^{12}\text{C}^{17}\text{O}^+$, $^{12}\text{C}^{16}\text{O}^1\text{H}^+$, $^{15}\text{N}^{14}\text{N}^+$, $^{14}\text{N}^{14}\text{N}^1\text{H}^+$), $^{42}\text{Ca}^+$ ($^{40}\text{Ar}^1\text{H}^1\text{H}^+$)), and therefore, to changes in the background. Furthermore, the higher concentration of oxygen when using longer PVC tubes contributes to higher oxide formation as indicated in the caption of Figure 17.

The most probable explanation for the different amount of hydrogen and oxygen with respect to PVC tube length is the desorption of these gas molecules from the inner surface of the tube wall by the continuous carrier gas flow. To determine the influence of the degassing process on long-term drift, experiments were extended to 4 hours using 1 m and 10 m PVC tubes. Results (Figure 20) indicate that stable background intensities are not reached for a 1 m and 10 m tube within a period of 4.5 hours.

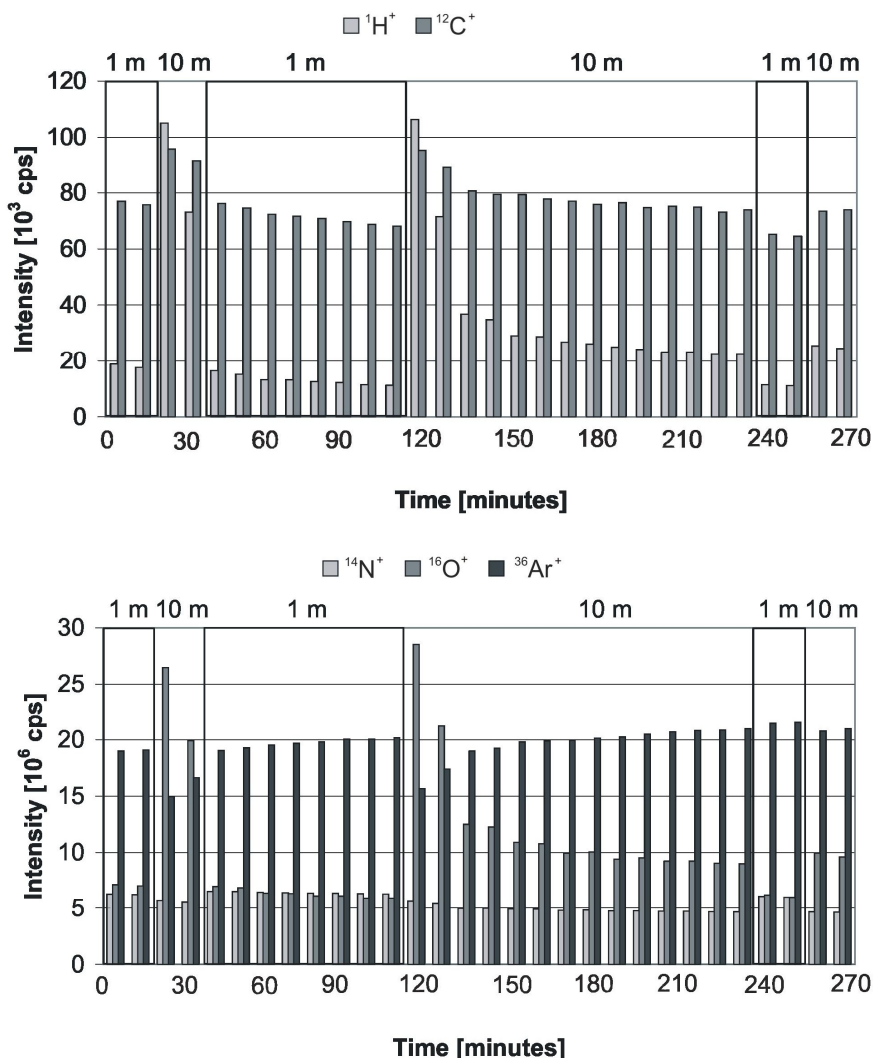


Figure 20 Temporal changes of plasma composition when using 1 and 10 m long PVC tubes over a period of 4.5 hours. To plot the analytes to the same figure, the intensity of $^{12}\text{C}^+$ was divided by 10.

During this degassing process, laser ablation analyses of NIST 610 were performed to monitor the differences in intensity and drift of element-to-Ca ratios over time. An indication for the temporal changes of up to 25 % is summarized in Table 3. As discussed above, element ratios influenced by background (e.g. Al/Ca, Si/Ca) are drifting towards lower values, especially when using longer tubes (10 m). In contrast, element ratios increasing over time are influenced by changes of the plasma conditions (e.g. As/Ca, Sb/Ca). Figure 21 demonstrates that the intensity of hydrogen and oxygen is correlated to the relative signal enhancement of certain elements (e.g. Na, Si, P, Zn).

Table 3 Changing element-to-Ca intensity ratios as a function of time (individual data points are shown) and tube (PVC) length (40 μm , 10 Hz)

Length (m)	Time (min)	Al/Ca	Si/Ca	Ni/Ca	Cu/Ca	Zn/Ca	As/Ca	Ag/Ca	Cd/Ca	Sb/Ca
1	0	5.41	4.62	0.14	0.17	0.13	0.13	0.31	0.06	0.41
10	23	6.61	5.74	0.15	0.18	0.15	0.12	0.32	0.06	0.41
1	35	5.48	4.57	0.13	0.16	0.13	0.12	0.30	0.06	0.41
1	62	5.48	4.53	0.14	0.17	0.13	0.13	0.31	0.06	0.42
1	84	5.40	4.60	0.14	0.17	0.13	0.13	0.32	0.06	0.43
1	105	5.42	4.47	0.14	0.17	0.13	0.13	0.31	0.06	0.43
10	117	6.75	5.77	0.15	0.19	0.15	0.12	0.34	0.07	0.42
10	137	5.81	5.07	0.16	0.19	0.16	0.14	0.36	0.07	0.46
10	158	5.66	4.79	0.15	0.19	0.15	0.14	0.35	0.07	0.46
10	178	5.63	4.90	0.16	0.19	0.15	0.14	0.36	0.07	0.48
10	199	5.62	4.93	0.16	0.19	0.15	0.14	0.37	0.07	0.48
10	218	5.60	4.82	0.16	0.19	0.15	0.15	0.37	0.07	0.48
10	240	5.55	4.81	0.16	0.19	0.15	0.15	0.37	0.07	0.48
1	253	5.39	4.61	0.15	0.18	0.14	0.14	0.35	0.07	0.47
10	265	5.63	4.99	0.16	0.20	0.16	0.15	0.38	0.07	0.51

To verify that the above mentioned components from the tube cause the changes in the plasma conditions leading to signal enhancements, wet plasma conditions were applied to diminish the influence of the gas impurities from the transport tubes. A cyclonic spray chamber was coupled to the injector of the ICP-MS. High purity water (Millipore, MilliQ) was nebulized into the plasma using a PFA nebulizer with an uptake rate of 100 $\mu\text{L min}^{-1}$. This generated stable wet plasma conditions, while ablation events were carried out using 2 m and 10 m PVC tubes upstream of the ablation cell. The 1 m long transport tube and the spray chamber were coupled using a glass Y-piece in front of the injector. The measured intensity ratios using this setup are summarized in Figure 22. The relative standard deviation for most of the element ratios measured were stable within 2 % when using

different tube lengths under wet plasma conditions. However, deviations of up to 10 % were observed for some high ionization potential elements such as P, Zn, As, Cd.

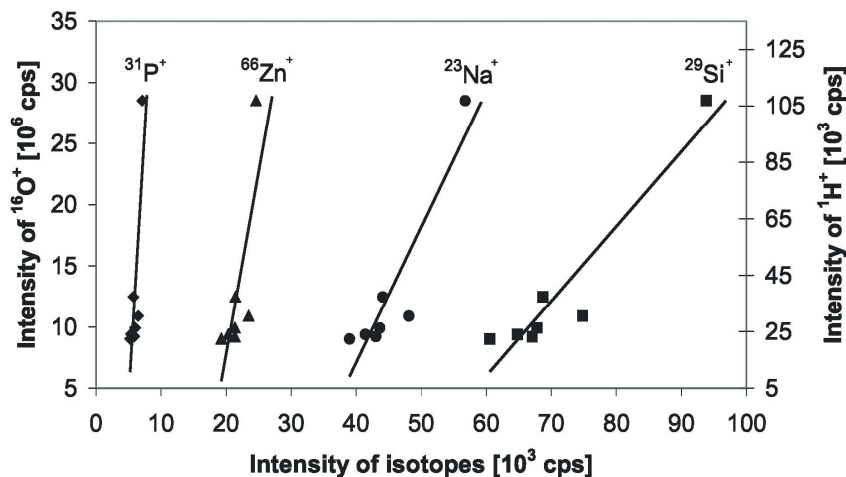


Figure 21 Correlation of the background intensity of $^1\text{H}^+$ and $^{16}\text{O}^+$ and the background corrected intensity obtained for $^{23}\text{Na}^+$, $^{29}\text{Si}^+$, $^{31}\text{P}^+$ and $^{66}\text{Zn}^+$ when using the 10 m PVC tube as transport tube (40 μm , 10 Hz). To plot the analytes to the same figure, the intensity of $^{23}\text{Na}^+$ and $^{29}\text{Si}^+$ was divided by 100 and 10, respectively.

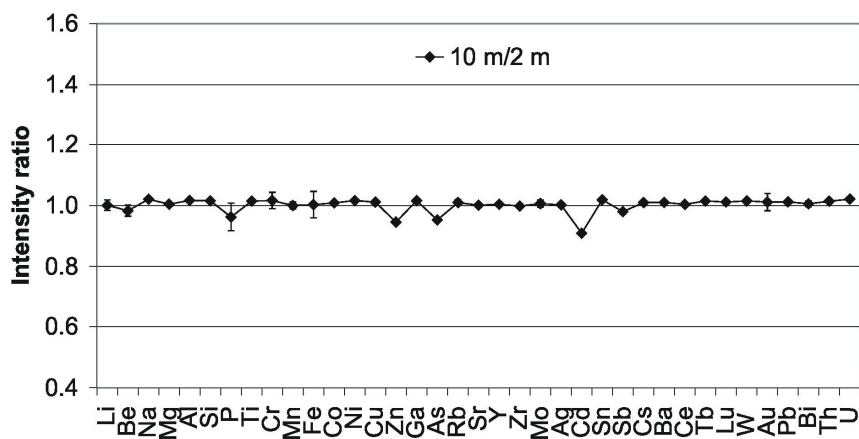


Figure 22 Element-to-Ca ratios for 10 m PVC tube normalized to the results obtained using 2 m long tube. The tubes were used upstream of the sample cell. Helium was applied as carrier gas and ultra high purity water was nebulized into the plasma. The oxide rate was determined for ThO^+/Th^+ and was 11.2 % for both tube lengths (2 m and 10 m).

2.3.2 Comparison of the influence of PVC, nylon, Teflon and copper tube materials

PVC, nylon, Teflon and copper were studied using the tubes upstream of the sample cell. The difference in sensitivity for most of the elements was less than 7 % when using all four materials of 1 m length (n=3). However, some more significant deviations (up to 13 %) were observed for Li, Be, Na, Mg, Al, Si, Ca. In contrast, when using longer tubes (10 m, except copper 9 m) differences in sensitivity became significant (up to 50 %) amongst the different tube materials. The sensitivity decreased in the order nylon > PVC > Teflon \cong Cu. For example, Figure 23 shows the abundance normalized sensitivity for Ag, background intensity of oxygen, hydrogen, argon-hydride and argon in dependence on tube material and length. It can be seen that the sensitivity of silver, oxide formation based on ThO^+/Th^+ , hydride formation on argon ($^{40}\text{Ar}^1\text{H}^+$) and doubly-charged ion rates were decreased with decreasing hydrogen and oxygen concentrations in the plasma when using PVC and nylon tubes. In contrast, the measured sensitivities using long and short Teflon and copper tubes were constant within few %.

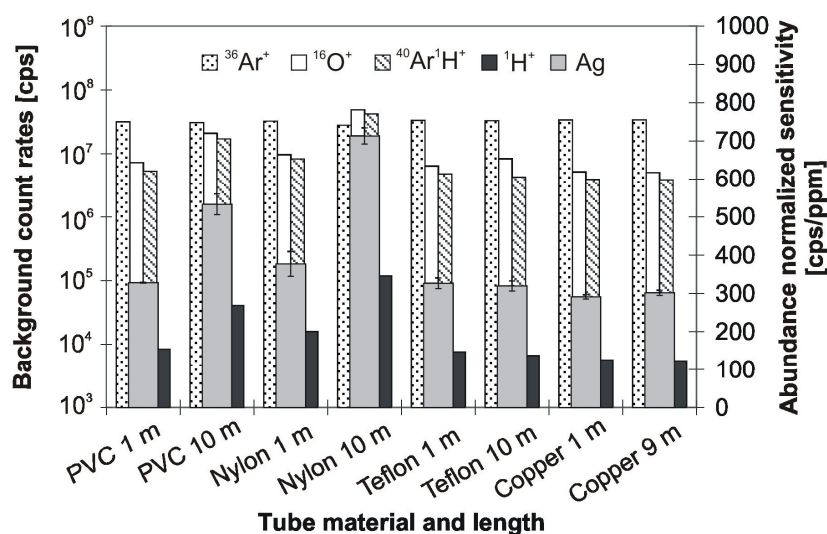


Figure 23 Correlation between the abundance normalized sensitivity for Ag and the background count rates for $^{36}\text{Ar}^+$, $^{16}\text{O}^+$, $^{40}\text{Ar}^1\text{H}^+$ and $^1\text{H}^+$, using different tube material and length. Oxide formation based on ThO^+/Th^+ : 0.36 % (1 m PVC), 0.77 % (10 m PVC), 0.45 % (1 m nylon), 2.21 % (10 m nylon), 0.38 % (1 m Teflon), 0.43 % (10 m Teflon), 0.35 % (1 m copper), 0.35 % (9 m copper). Doubly-charged ion formation based on $^{42}\text{Ca}^{++}/^{42}\text{Ca}^+$: 0.29 % (1 m PVC), 0.45 % (10 m PVC), 0.36 % (1 m nylon), 0.67 % (10 m nylon), 0.35 % (1 m Teflon), 0.38 % (10 m Teflon), 0.37 % (1 m copper), 0.36 % (9 m copper).

Figure 24 shows the calculated element ratios for each type of tube material. Owing to the strong influence of the degassing process using nylon and PVC tubes, the element ratios deviate up to 50 %. In contrast, the majority of the element-to-Ca ratios using Teflon or copper tubes remained stable within 3 %, except for Be, P, As and Au in case of Teflon tubes, which indicates a remaining, but minor influence of impurities on high ionization potential elements.

Experiments were performed using short and long copper and Teflon tubes for aerosol transport to investigate the aerosol loss within the transport tube. The reduction in sensitivity for most of the elements was less than 8 % when changing the copper tube length from 1 to 9 m (data not shown). This insignificant loss of particles can be attributed to increased deposition within the longer tube. The element-to-Ca ratios remained stable within 3 % (except As 4 %), which indicates that the loss of material leads to minor modification of the composition of the ablated material. In case of Teflon tubes the difference in sensitivity was strongly length dependent when changing towards longer tubes. This is caused by the electrostatic characteristics of Teflon, which leads to more significant loss of material.

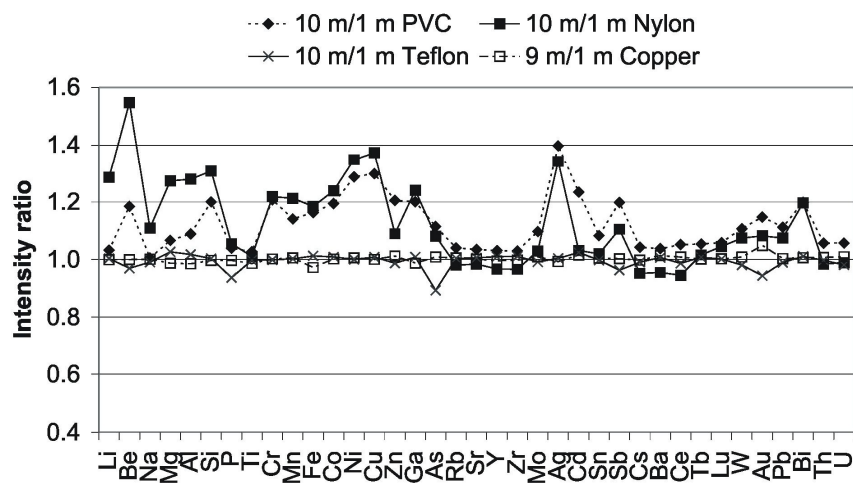


Figure 24 Element-to-Ca ratios for the four tube materials. The calculated element ratios for a longer tube (10 m except copper 9 m) were normalized to the results obtained with 1 m long tube. The tubes were applied upstream of the ablation cell.

The results of this study indicate that the degassing process of various tubes has a significant influence on the plasma conditions and therefore on drift. It can be assumed that hydrogen and oxygen presumably as water vapor are entering the carrier gas flow from the wall of the PVC and nylon tubes. Unfortunately, the exact composition of the PVC and nylon tubes used in this study is not accessible. These types of plastic materials have

many modified compositions and therefore different physical properties. It is reported that all nylons are hygroscopic and absorb moisture from the atmosphere^{185,186,187}. Moreover, nylon and PVC are both permeable to gases and water^{185,186,187}. In contrast, fluoropolymer tubes designed for laboratory use are produced by stringently controlled production conditions (e.g. selection of resin type, particle size; temperature and pressure conditions, etc.) and provide non-porous, dimensionally stable tubing with superior smooth walls (Saint Gobain Performance Plastics). FEP, PTFE and PFA tubes are chemically inert and they resist the absorption/adsorption of liquids owing to their hydrophobic characteristics, therefore these are more suitable for the delivery of natural gases.

A major role in the observed changes may be attributed to hydrogen, because it increases the gas and electron temperature in the plasma^{131,140,188}. In this study it was found that the increased concentration of hydrogen (originating from longer PVC and nylon tubes), higher doubly-charged ion rate and the greater enhancement in signal intensity for the elements with higher 1st ionization potential refer to a higher electron temperature, as described in ref.^{131,140,188}. When comparing our results to ref.¹⁴⁰, similar elements were enhanced in sensitivity. However, the extent of signal enhancement was lower owing to the significantly lower amount of hydrogen introduced into the ICP. The correlation of the 1st ionization potential to the signal enhancement (Figure 25) were similar to previously reported¹⁴⁰ mixed gas studies using H₂. However, the oxide formation was significantly higher, which indicates that oxygen and water contributes also to the changes in the plasma conditions.

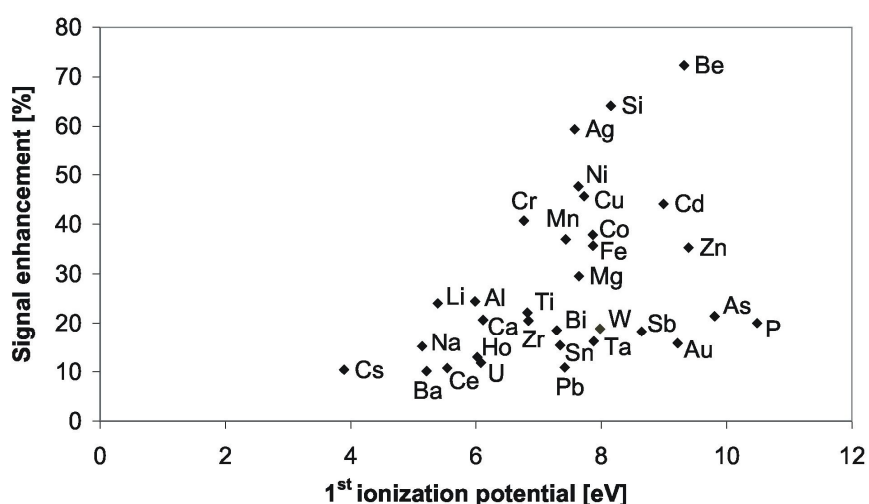


Figure 25 Correlation of the 1st ionization potential and the signal enhancement based on the data of Figure 2 (20 m PVC normalized to 1 m).

As mentioned in the introduction, Kosler et. al. studied the influence of oxygen on the formation of laser aerosols and reported elemental fractionation in dependence on the oxygen concentration¹⁶¹. To validate that our reported drift was not caused by changes in the aerosols formed during ablation, PVC tubes (1 and 10 m) were applied in front of the ablation cell to change the oxygen concentration in the sample cell. The data support that the tiny amounts of gas impurities do not induce fractionation effects.

2.4 Conclusion

This study demonstrates that the type of tube material used in LA-ICP-MS can cause drift in signal intensities and element ratios. The drift, mainly observed using PVC and nylon, is based on a degassing effect from the tube walls (hydrogen, oxygen and/or water) and were measured to be most influential when using longer tubes. The degassing components change the plasma conditions very similar to previously reported mixed gas plasma conditions. However, the changing amounts of the degassing components lead to a significant drift. Furthermore, the ‘washout time’ of the gas components or water depends on the carrier gas flow (conditioning of the tube). Owing to the complexity of changes within the ICP caused by the degassing components of some of the materials, various element-selective effects were measured (e.g., hydride, oxide and doubly charged ion formation, enhanced sensitivity). Based on these studies, fluoropolymer (e.g. FEP, PTFE, PFA) and copper tubes can be a suitable choice for gas supply, while the most suitable tube material for aerosol transport must be non-electrostatic, hydrophobic, the least permeable to ambient gases and water and preferably flexible. Specially designed Tygon tubes (Saint Gobain Performance Plastics; e.g. Tygon 2275 High purity tube, Tygon SE-200 Inert tube, etc.) may offer well suitable choice for aerosol transport from the ablation cell to the ICP-MS. With the application of non-degassing tubes, the length becomes less critical in terms of plasma stability influencing sensitivity and element-to-Ca ratios.

3. Air as a new gas environment for ablation using LA-ICP-MS

The content of this chapter was partially published in J. Anal. At. Spectrom., 2010, ref.¹⁸⁹

Authors: R. Kovacs, K. Nishiguchi, K. Utani and D. Günther

Development of direct atmospheric sampling for laser ablation – inductively coupled plasma – mass spectrometry

3.1 Introduction

Since the early study⁶² of Gray in 1985, the general experimental setup of LA-ICP-MS has not changed significantly. An inert gas, either helium or argon at a desired flow rate regulated by a mass flow controller carries the laser generated aerosol of a solid sample from the ablation cell through a transport tube into the ICP-MS. Since the early period of the technique, numerous publications were focusing on aerosol transport characteristics of various ablation cells, different in geometry and volume^{114,117,190,121,122}. Since the number and size of the samples to be analyzed are limited due to the fact that the samples need to be enclosed in the ablation cell, studies have also been carried out on open cell designs^{128,112,113}. These cells can be placed onto the sample surface and have to be sealed and need to be airtight to provide stable operating conditions within the ICP. In some cases (e.g. large sized precious gold objects, jewels, artifacts and fragile samples) the sample provides insufficient flat surface areas, which makes the sealing process difficult or impossible. Most recently the application of an open, non-contact ablation cell was also reported¹²⁸. However, the gas flow design requires flat sample surfaces, such as silicon wafers, gel plates and tissue samples, etc. Most important, however are the results that all different ablation cell geometries lead to similar high transport efficiencies, which has been recently reported by Garica et. al.¹¹⁸.

As carrier gases either helium or argon have been proposed owing to their inertness and physical properties with respect to optimum operating conditions of the ICP. In comparison to argon, helium provides up to 5 times higher transport efficiency¹⁰² of laser aerosols and reduced particle deposition around the ablation pit, lower background and therefore, improved limits of detection¹⁹¹. This can be explained by the higher thermal conductivity of helium in contrast to argon, which has a significant influence on the aerosol expansion,

vapor transport from the particle surface during vaporization and on the plasma temperature^{108,192,131}.

The current research project was focused on the development and investigation of a novel online laser ablation sampling approach for ICP-MS utilizing ambient air as ablation environment and omitting the need of an ablation cell. The in air generated aerosol was sucked by a micro-diaphragm pump into a transport tube and further carried towards the ICP. Before the ICP, the air containing the aerosol was exchanged online by argon using a gas exchange device¹⁹³, which has been successfully applied for real-time multi-element investigations of airborne particulate matter using ICP-MS. Such an experimental setup provides improved flexibility in terms of sample size and geometry for LA-ICP-MS and can be very useful in special applications. For example, in case of large art or archaeological samples, which exceed the size limit of most ablation cells, and use of open cell designs are not allowed owing to microscopic surface contamination caused by the sealing process.

3.2 Experimental

The recently reported gas exchange device¹⁹³ - developed by Sumitomo Seika Chemicals Co., Ltd., Hyogo, Japan - enables online analysis of dust and airborne particles in various gas environments using ICP based techniques. The gas exchange is accomplished in a gas converter cell, which consists of a porous inner tube made of silica within an outer tube consisting of borosilicate. Due to the fact the gas exchange process is based on diffusion, the flow rate of the sample gas (desired to exchange) is dependent on its diffusion speed relative to that of argon. The sample gas is introduced into the central channel at a flow rate of 0.25 L min⁻¹ (in case of air). A counter flow argon sweep gas, at a relatively high flow rate (3.0 L min⁻¹) is introduced to the outside of the porous wall. Consequently, the gas exchange mechanism is realized by the partial pressure difference of gases between the two sides of the porous membrane and the flow direction makes a complete decrease of the concentration of the sample gas within the central channel. The gas exchange efficiency has already been described in ref.¹⁹³. The device applied within this study contains two gas converter cells connected in series. For the experiments performed using ambient air as ablation environment, a micro diaphragm pump (NMP05L 6V, KNF Neuberger AG, Balterswil, Switzerland) was connected to the inlet tubing (Tygon 2275, Saint Gobain, Akron, OH, USA) of the gas exchange device to transport the laser aerosol through the gas exchanger into the ICP. The operation of the micro pump is based on a steadily moving

elastic diaphragm. In this way the medium is transferred using automatic valves and it provides uncontaminated flow due to oil-free operation and high level of gas tightness by means of a closed diaphragm surface and a special sealing system. By adjusting the operating voltage of the pump, the desired gas flow rate can be introduced into the gas exchanger.

The ICP operating conditions including gas flows, RF power and lens settings were always optimized prior to the measurements. Between the measurement sequences performed using various gases for transport, only the nebulizer gas flow rate was adjusted to fulfill the optimization criteria (highest sensitivity, while keeping the background count rates, oxide and doubly charged ion formation as low as possible).

Silicate samples were ablated using a beam-homogenized 193 nm ArF excimer laser ablation system⁸³ (GeoLas Q, MicroLas, Göttingen, Germany) with a pulse duration of approximately 15 ns. Metallic samples (gold, brass, steel) were ablated using a solid-state Nd:YAG laser ablation system (LSX-213, CETAC Technologies, Omaha, NE, USA) operating at a wavelength of 213 nm providing a shorter pulse duration of approximately 5 ns. The transient signals were recorded by a quadrupole ICP-MS (ELAN 6100 DRC+, Perkin Elmer Sciex, Canada). The signal acquisition started with the measurement of 30 s background of the gas blank followed by a 70 s signal acquisition from a single crater ablation. Data reduction and signal integration were adapted to the procedure described in ref.¹⁸⁴. The operating conditions of the laser systems, ICP-MS and gas exchanger are summarized in Table 4.

Three experimental configurations were applied within this study.

Closed cell configuration. The samples were enclosed by an ablation cell (cell volume ~ 7 cm³) and the cell was continuously flushed at a desired gas flow rate of helium, argon or compressed air. The gas transported the laser aerosol either through the gas exchange device or directly into the plasma. This configuration allowed investigating the potential loss of aerosol within the gas exchanger.

Open cell configuration. The samples were placed into an ablation cell (cell volume ~ 7 cm³) leaving its inlet and bottom open for free access of ambient air. The in air generated laser aerosol was sucked by a micro-diaphragm pump into the gas exchange device and from there online introduced into the ICP-MS. This setup was used to validate the applicability of ambient air as an ablation gas environment for LA-ICP-MS.

Novel sampling approach. The samples were placed on a sample holder under ambient conditions. The transport tube inlet (i.d. 4 mm) was directed as close as possible to the desired site of ablation (Figure 26) and the other end was connected to the diaphragm pump. During laser sampling, the generated aerosol was sucked directly into the transport

system and carried to the gas exchange device and further to the ICP-MS by the pump. Laser ablation sampling was always carried out within a range of 3 mm in front of the tube inlet to ensure the highest aerosol uptake. A sketch of the experimental setup for this approach is shown in Figure 27.

Table 4 Operating conditions for ICP-MS, laser ablation systems and gas exchange device

Laser ablation		
Laser ablation system	LSX-213, Nd:YAG	GeoLas Q, ArF excimer
Wavelength	213 nm	193 nm
Pulse duration	5 ns	15 ns
Ablation frequency	4, 5, 10 Hz	10 Hz
Spot size	50, 100 μm	60 μm
Laser fluence	8 J cm^{-2}	20-21 J cm^{-2}
Ablation time	70 s	70 s
Ablation mode	single hole drilling	single hole drilling
Samples	gold, brass, steel	silicate glass
ICP-MS		
Instrument	PE Sciex ELAN 6100 DRC+	
Nebulizer gas flow	0.8-0.95 L min^{-1}	
Auxiliary gas flow	0.8 L min^{-1}	
Plasma gas flow	17.5 L min^{-1}	
RF power	1380 W	
Lens setting	autolens calibrated	
Detector mode	dual (pulse counting and analogue mode)	
Dwell time	10 ms (50 ms when using the diaphragm pump)	
Scan mode	peak hopping	
Gas exchange device		
Pore size	0.1 μm	
Membrane tube dimensions	\varnothing 10 mm, wall thickness of 0.6 mm, length 2x350 mm	
Inlet gas flow rates	0.25 L min^{-1} air, 0.63 L min^{-1} He	
Outlet gas flow rate	0.21 L min^{-1} Ar	
Sweep gas flow rate	3.0 L min^{-1} Ar	

The ambient air used for the experiments was derived from the laboratory atmosphere, which was continuously dust filtered by a high performance laminar flow box (SIT AG, Montlingen, Switzerland) at a gas flow rate of 8480 $\text{m}^3 \text{h}^{-1}$ to ensure stable and low background levels for the gas blank within the ICP-MS. Humidity was not controlled, however the gas exchange device removes the moisture from the central channel gas flow and therefore, it has no influence on the ICP operating conditions.

To demonstrate the figures of merit of using air as a new choice as carrier gas for LA-ICP-MS, a few selected applications for proof of principle are discussed.

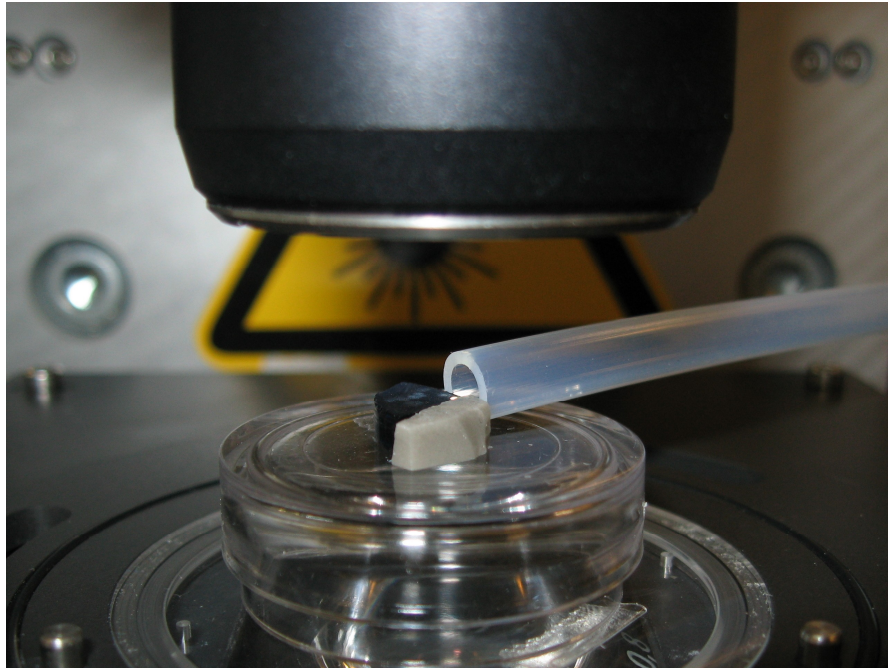


Figure 26 Atmospheric sampling approach. The laser generated aerosol is directly sucked by the tube directed relatively close (within 3 mm) to the ablated crater at an angle of either 90 ° or 45 °.

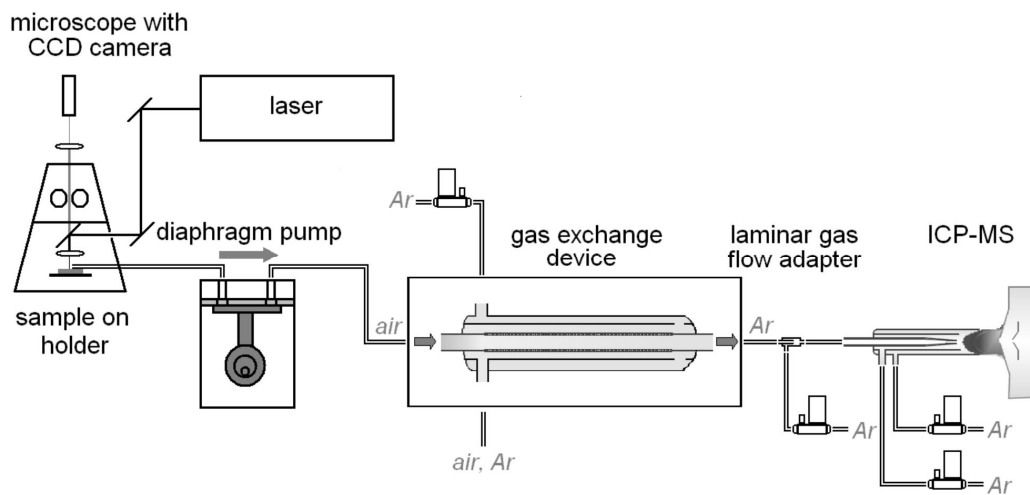


Figure 27 Sketch of the experimental setup of the novel sampling approach.

3.3 Results and discussion

3.3.1 Air as a new gas environment for LA-ICP-MS

To compare the influence on sensitivity of various carrier gases (He, Ar and compressed air) applicable for ablation and aerosol transport, the experiments were performed using the closed cell configuration on the silicate glass SRM NIST 610 (National Institute of Standards and Technology, Gaithersburg, MD, USA), which was ablated by the 193 nm ArF excimer laser. A list of the various measurements performed is given in Table 5. The oxide formation (Table 5) and background count rates (Figure 28) indicate that the exchange of air to argon was complete and almost no remains of air influenced the plasma operating conditions, which can be seen in particular in the background count rates of isotopes potentially influenced by polyatomic interferences (e.g. ^{27}Al : $^{14}\text{N}^{12}\text{C}^1\text{H}$; ^{31}P : $^{14}\text{N}^{16}\text{O}^1\text{H}$, $^{15}\text{N}^{16}\text{O}$; ^{51}V : $^{12}\text{C}^1\text{H}^{38}\text{Ar}$, $^{14}\text{N}^1\text{H}^{36}\text{Ar}$; ^{53}Cr : $^{12}\text{C}^1\text{H}^{40}\text{Ar}$, $^{36}\text{Ar}^{16}\text{O}^1\text{H}$, $^{38}\text{Ar}^{14}\text{N}^1\text{H}$; ^{55}Mn : $^{14}\text{N}^1\text{H}^{40}\text{Ar}$, $^{38}\text{Ar}^{16}\text{O}^1\text{H}$). Only a minor increase in the background count rates by 70 % and 50 % for m/z 23 and m/z 29 respectively was observed when the gas exchanger was connected to the transport system and only Ar was entering the ICP. This increase was assumed to be caused by the different operating conditions (Ar only vs. He admixed with Ar) within the ICP¹³⁶. For most isotopes potentially influenced by spectral interferences caused by polyatomic ions the background count rates were found to be significantly lower when Ar only was entering the plasma in contrast to He admixed with Ar (He without GED).

Table 5 Gas flow rates applied for the measurements performed using various gases for laser ablation and aerosol transport. The measured oxide formation based on ThO^+/Th^+ is shown for the respective measurements

Measurement sequence	GED state	Carrier gas and flow rate	Gas to ICP	Nebulizer gas flow added	ThO^+/Th^+
He without GED	Not connected	He, 0.25 L min ⁻¹	He, 0.25 L min ⁻¹	Ar, 1.1 L min ⁻¹	0.39 %
Passing the aerosol in Ar through GED	Idle	Ar, 0.25 L min ⁻¹	Ar, 0.25 L min ⁻¹	Ar, 0.9 L min ⁻¹	0.33 %
He exchange to Ar	In operation	He, 0.63 L min ⁻¹	Ar, 0.21 L min ⁻¹	Ar, 1.0 L min ⁻¹	0.30 %
Air exchange to Ar	In operation	Air, 0.25 L min ⁻¹	Ar, 0.21 L min ⁻¹	Ar, 1.0 L min ⁻¹	0.27 %

The highest sensitivity for the majority of the measured elements was obtained when using helium as transport gas without exchanging it to argon (Figure 29). When exchanging helium to argon in comparison to using helium as carrier gas without connecting the gas exchanger, boron was enhanced by 20 %, zinc and arsenic were found to provide

insignificantly higher sensitivity (2 %), while the sensitivity of beryllium remained unchanged and the sensitivity of most elements decreased by approximately 20 %.

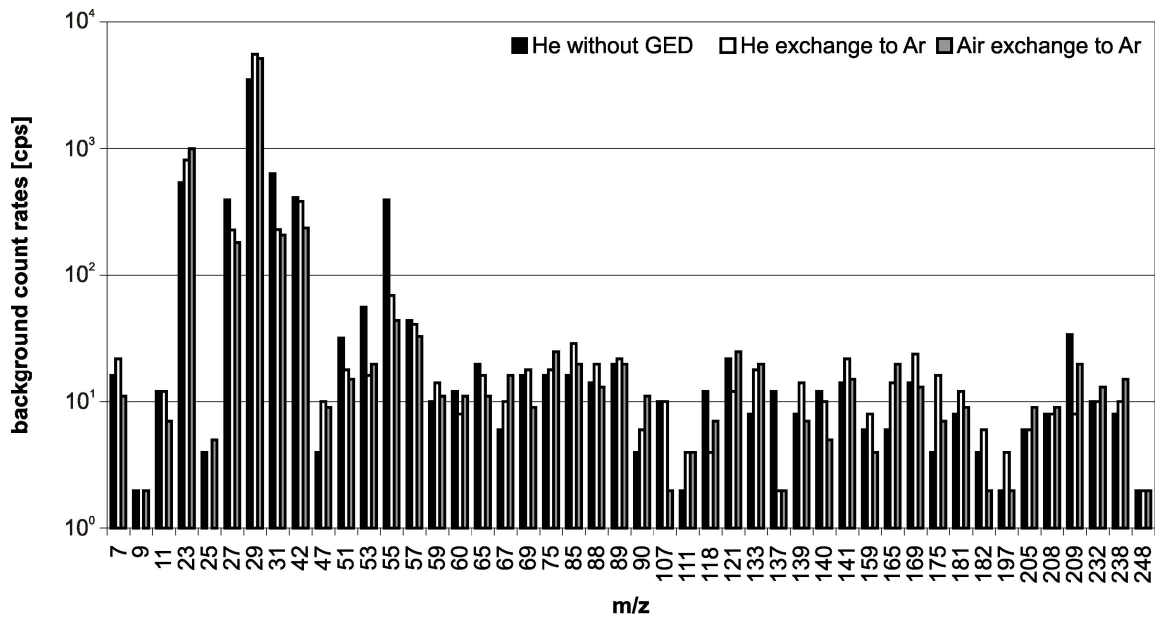


Figure 28 Average background count rates for the closed cell configuration using various gases for aerosol transport. In the experiment assigned with “He without GED”, the gas exchange device was not connected to the transport system.

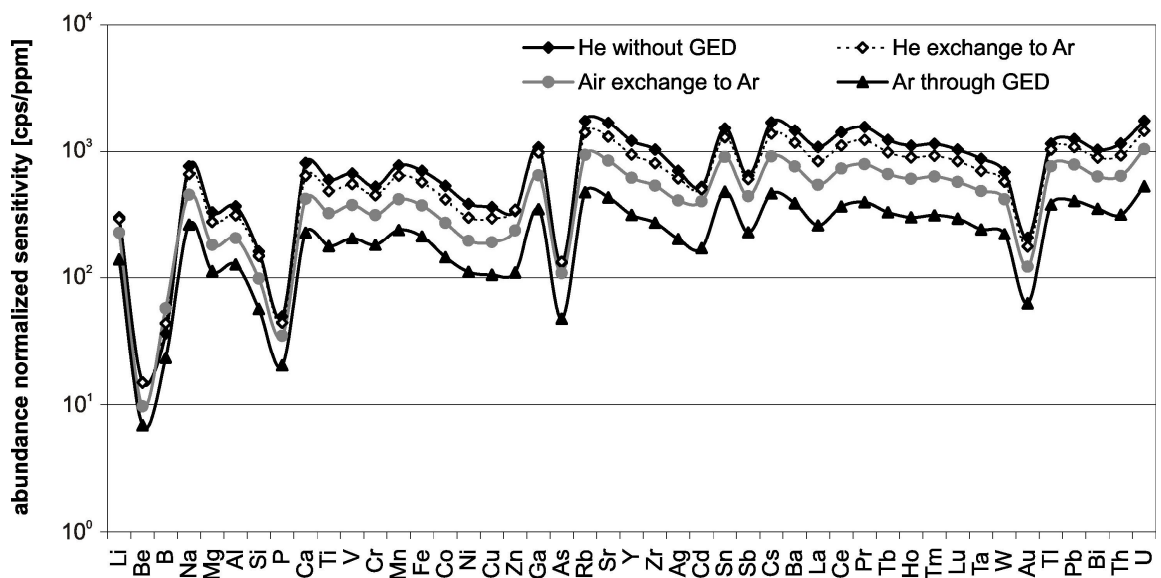


Figure 29 Comparison of the abundance normalized sensitivity obtained using various carrier gases ($\lambda = 193 \text{ nm}$, $60 \mu\text{m}$ spot size, 10 Hz ablation frequency, 20 J cm^{-2} energy density).

This decrease in sensitivity was found to be caused by a non-element dependent loss of aerosol within the gas exchange device based on the sensitivity comparison of the aerosol contained in He passing through the GED in contrast when the GED was not connected to the transport system (data not shown). The gas exchange process makes possibly a mixing of the aerosol, which leads to a representative transport through the GED. “Helium without gas exchanger” in comparison to “argon through the gas exchanger” provided higher sensitivity by a factor of 2-4 for all elements measured due to a higher efficiency of aerosol transport and potential influence of helium on the argon plasma^{102,131}. In contrast, the sensitivity obtained using compressed air for laser ablation was only a factor of 1.2-2 less when compared to the use of helium. The higher sensitivity obtained for ablation in air in contrast to ablation in argon was caused by improved transport efficiency indicated by reduced particle deposition around the crater (Figure 30).

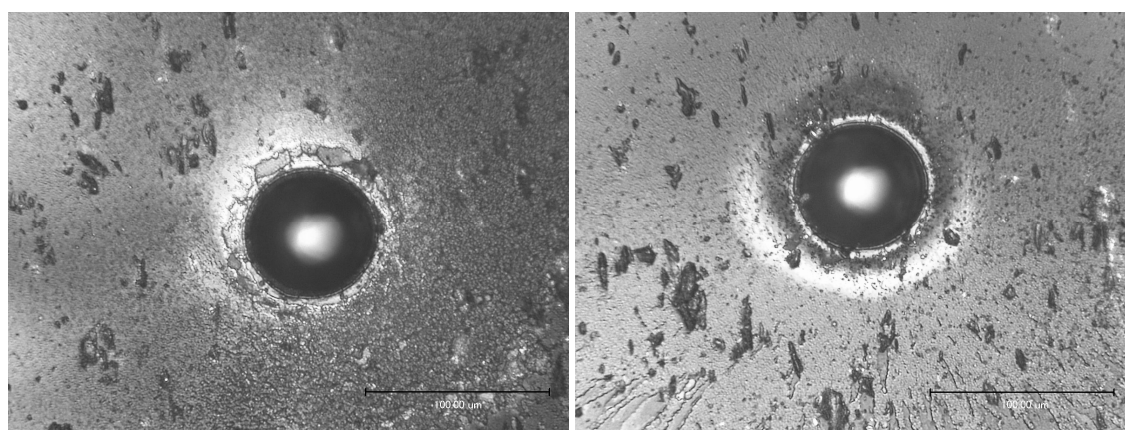


Figure 30 Light microscope images of craters generated by 150 laser pulses ($\lambda = 193$ nm, 60 μm spot size, 10 Hz ablation frequency, 21.6 J cm^{-2} energy density) on NIST 610 SRM with a magnification of 1000. During ablation the cell was flushed by Ar (left) or compressed air (right) at a flow rate of 0.25 L min^{-1} .

The capabilities of ambient air as ablation environment and transport gas for LA-ICP-MS was further investigated and figures of merit for quantitative analysis were determined. These measurements were carried out either within a partially open ablation cell or without using a cell.

3.3.2 Experiments using an open cell configuration

Two gold wire certified reference materials (NIST 8054, NIST 8063) were quantified against a gold calibration material (NA2) recently characterized and reported in ref.¹⁹⁴. Ambient air at a flow rate of 0.25 L min⁻¹ was steadily sucked through the partially open ablation cell into the transport system by the diaphragm pump. For providing the desired flow rate by the pump, its operating voltage was adjusted to 3.2V. The intensity fluctuations of the transient signals generated by the pumping were reduced by applying 50 ms dwell time for signal acquisition. Figure 31 shows representative transient signals for an aerosol passed through the gas exchange device. The typical aerosol washout time was approximately 20 s, which is mainly caused by the low gas flow rate and the entire volume of the transport and gas exchange system.

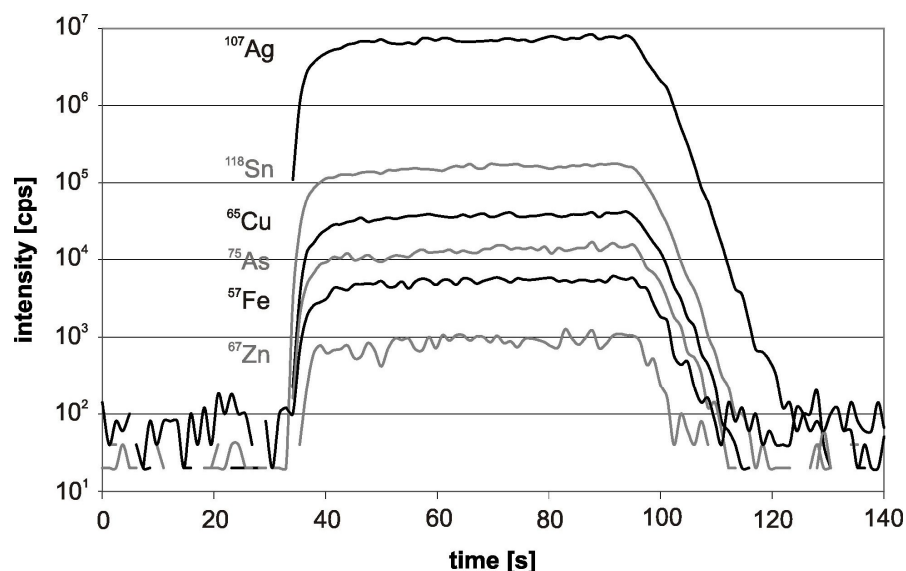


Figure 31 Typical transient signals of six analytes of NA2 gold calibration material¹⁹⁴. Laser ablation sampling was performed in ambient air using the open cell configuration and 100 μm spot size, 4 Hz ablation frequency and a fluence of 8 J cm⁻² at a wavelength of 213 nm. The ICP-MS dwell time was set to 50 ms per isotope.

Figure 32 shows a typical crater formed in ambient air without indicating excessive particle deposition in the vicinity of the crater. The rim shows molten material accumulated by ejection of particles and fragments from the crater and the dark circular area indicates laser energy spread on the sample surface around the crater. The quantitative results with uncertainties obtained using Cu as internal standard showed no significant deviations to

the reference values (Table 6) for most of the determined elements. However, in NIST 8054 approximately 15 % deviation was obtained for Zn and Sn, moreover 10 % for Pt. Determined concentrations using liquid calibration reported 7 % and 4 % deviations for Zn and Sn from the reference values respectively¹⁹⁴. In contrast, these elements were determined within the confidence interval in case of NIST 8063. In NIST 8063 the Fe concentration was 13 % lower in comparison to the reference value, however the confidence intervals of our results and the reference are overlapping, moreover the deviation of the determined Fe concentration vs. the reference value was similar when using liquid calibration¹⁹⁴. Even the concentrations of trace elements ($< 5.1 \mu\text{g g}^{-1}$) such as Ti, Cr and Pt in NIST 8063 were successfully determined, which support representative aerosol sampling in air and transport through the gas exchange device.

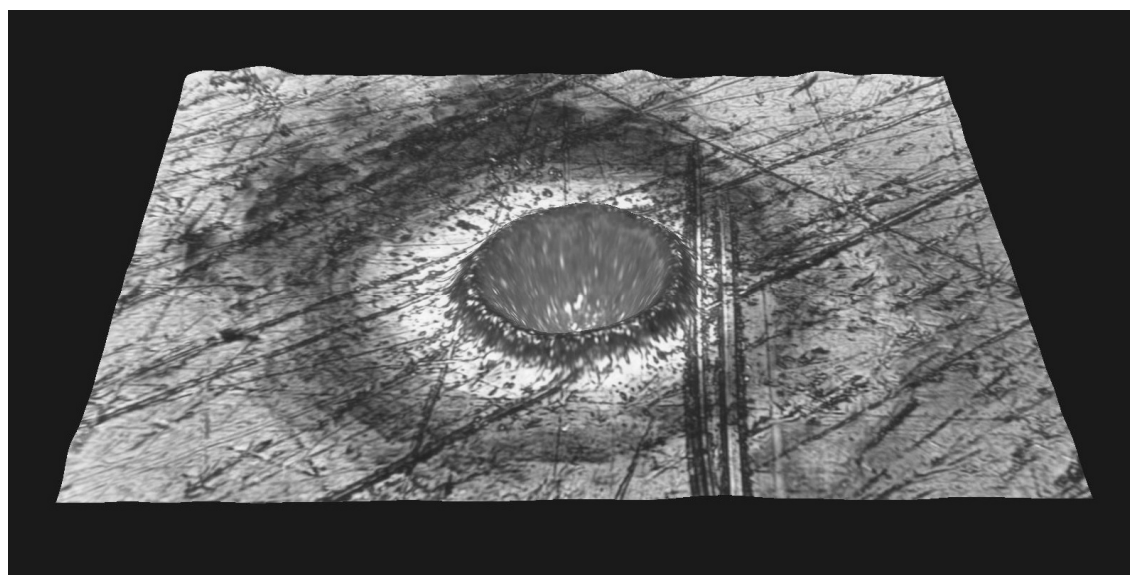


Figure 32 Light microscope image of a crater generated by 120 laser pulses ($\lambda = 213 \text{ nm}$, $50 \mu\text{m}$ spot size, 4 Hz ablation frequency, 12.0 J cm^{-2} energy density) on NA2 gold calibration material with a magnification of 1000. Laser ablation was carried out in laboratory ambient air at a flow rate of 0.25 L min^{-1} .

Table 6 Determined element concentrations and average detection limits ($\mu\text{g g}^{-1}$) for the analysis of NIST 8054 and NIST 8063 using NA2 as calibration standard and Cu as internal standard. The laser sampling was carried out in ambient air in a partially open ablation cell

	NIST 8054 c.v. ^a	determined ^b	detection limits	NIST 8063 c.v. ^a	determined ^b	detection limits
Ti	12.7 ± 0.9	14.3 ± 1.5	0.5	2.6 ± 0.5	4.4 ± 1.5	0.5
Cr	32.6 ± 2.8	34.1 ± 0.9	1.7	4.9 ± 1.1	3.2 ± 0.4	1.4
Mn	58.9 ± 5.9	64.0 ± 1.5	0.1	64.3 ± 4.9	68.2 ± 6.0	0.1
Fe	11.6 ± 1.4	10.9 ± 1.7	4.6	90.4 ± 9.4	78.8 ± 3.1	4.1
Ni	32.5 ± 2.0	33.6 ± 0.7	0.4	14.6 ± 2.3	14.3 ± 1.4	0.5
Cu	98.1 ± 3.6	98.1 (I.S.)	0.2	9.8 ± 0.8	9.8 (I.S.)	0.2
Zn	54.6 ± 3.2	62.8 ± 1.5	0.7	20.9 ± 1.0	22.8 ± 2.1	0.6
As	10.0 ± 1.2	9.6 ± 0.3	0.06	29.4 ± 2.7	26.1 ± 2.7	0.06
Pd	43.1 ± 1.5	44.5 ± 1.5	0.07	119 ± 5	110.4 ± 8.4	0.06
Ag	20.3 ± 2.4	19.2 ± 0.5	0.06	49.7 ± 3.5	46.6 ± 4.4	0.05
Sn	33.8 ± 2.0	39.2 ± 1.1	0.04	49.7 ± 2.5	53.8 ± 4.9	0.04
Pt	87.1 ± 3.4	95.7 ± 2.7	0.07	5.1 ± 2.8	4.9 ± 0.6	0.04
Pb	21.9 ± 1.7	24.2 ± 0.7	0.01	49.7 ± 2.7	47.3 ± 4.8	0.01
Bi	24.0 ± 1.4	25.5 ± 0.8	0.01	53.9 ± 3.6	55.3 ± 5.8	0.01

^a certified values, uncertainty is expressed as $2s_p$ (s_p : square root of the pooled variance)

^b n=6, uncertainty is given as \pm standard deviation

3.3.3 Experiments using the novel sampling approach

Instead of using an ablation cell, the laser aerosol generated in ambient air was directly sucked into the inlet tubing of the gas exchanger by the diaphragm pump. Since the applied gas flow rate (air: 0.25 L min^{-1}) is determined by the exchange capacity of the gas converter cell, the distance between the ablation site and the tube inlet is a crucial parameter in terms of sample uptake. The distance of the ablation spot relatively to the tube inlet was kept as close as possible to 3 mm to ensure the highest aerosol uptake. However, an optimum ablation position with respect to the tube inlet and an optimum tube diameter can not be given at present and further experiments are needed to investigate these parameters in more detail. This sampling approach provided approximately 30 % lower sensitivity for all elements except boron (Figure 33) in comparison to enclosing the sample in a cell. The lower sensitivity was determined based on the ablation of NIST 610 silicate glass and MBH-B22 brass by a Nd:YAG laser system operating at a wavelength of 266 nm (100 μm spot size, 10 Hz ablation frequency, 13 J cm^{-2} energy density). The high efficiency obtained for boron can not be explained at this stage, however later studies indicated that the sensitivity of boron is highly dependent on the actual humidity of air used for ablation (Chapter 4.2)

By comparing the gas velocity based on the gas flow rate and transport tube dimensions with aerosol expansion phenomena^{108,109}, which is influenced by the melting point of the sample matrix, absorption of the laser wavelength, energy density and gas atmosphere, it can be assumed that the entire aerosol in the current configuration is not completely sucked into the transport system. Nevertheless, this sampling approach was investigated and quantitative analyses on various metallic samples were carried out.

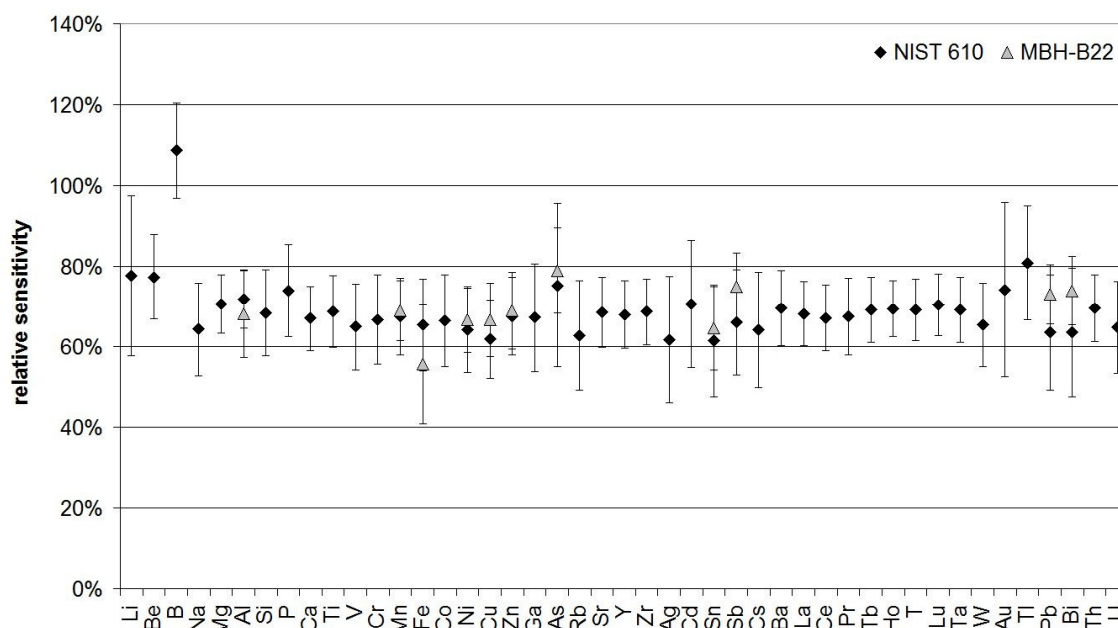


Figure 33 Relative sensitivity of various elements within NIST 610 (silicate glass) and MBH-B22 (brass) obtained for the aerosol suction approach in contrast to in cell ablation.

A brass CRM B22 (MBH Analytical Ltd., England) with a major element composition of 14.5 % zinc and 83.5 % copper was analyzed using brass CRM B26 (MBH Analytical Ltd., England), consisting of 30 % zinc and 62.9 % copper, as external calibration standard. The determined element concentrations in comparison to the certified values and the average detection limits of the analysis are summarized in Table 7. Since uncertainties are not given in the certificate, only Al and Fe were found to be deviating from the reported values by approximately 10 %. Transient signals acquired on the brass samples using the novel sampling approach are very similar to those obtained using the open cell configuration (Figure 34).

Furthermore, small chips of highly alloyed steel JK-37 (Swedish Institute for Metals Research, Stockholm, Sweden; Fe: 35.8 %, Ni: 30.8 %, Cr: 26.7 %, Mo: 3.6 %) were analyzed using ECRM-298-1 (Swedish Institute for Metals Research, Stockholm, Sweden; Fe: 63.4 %,

Cr: 24.7 %, Ni: 7.1 %, Mo: 3.8 %) stainless steel block as external standard. Although the sample and the calibration material were not matrix matched, most of the determined element concentrations were in agreement with the certified values (Table 8).

Table 7 Analytical results and obtained detection limits for MBH-B22 treating as sample using MBH-B26 brass certified reference material as calibration standard and Cu as internal standard. The laser sampling was carried out in ambient air without using an ablation cell

	MBH-B22 c.v. ^a [wt%]	determined ^b [wt%]	detection limits [$\mu\text{g g}^{-1}$]
Al	0.05	0.060 ± 0.002	1.65
Mn	0.08	0.11 ± 0.04	0.34
Fe	0.19	0.26 ± 0.04	25.5
Ni	0.20	0.206 ± 0.004	1.37
Cu	83.5	83.5 (I.S.)	6.75
Zn	14.5	14.5 ± 0.3	10.3
As	0.45	0.42 ± 0.07	1.14
Sn	0.16	0.13 ± 0.02	0.29
Sb	0.11	0.10 ± 0.03	0.25
Pb	0.18	0.20 ± 0.07	0.17
Bi	0.12	0.15 ± 0.06	0.08

^a certified values

^b n=4, uncertainty is given as \pm standard deviation

Table 8 Analytical results and obtained detection limits for JK-37 steel turnings CRM treating as samples using ECRM-298-1 as calibration standard and Cr as internal standard. The laser sampling was carried out in ambient air without using an ablation cell

	JK-37 c.v. ^a [wt%]	determined ^b [wt%]	detection limits [$\mu\text{g g}^{-1}$]
B	12 ± 2 ($\mu\text{g g}^{-1}$)	16.0 ± 0.7 ($\mu\text{g g}^{-1}$)	0.13
Al	80 ± 6 ($\mu\text{g g}^{-1}$)	69.0 ± 2.3 ($\mu\text{g g}^{-1}$)	0.76
P	160 ± 7 ($\mu\text{g g}^{-1}$)	166 ± 6 ($\mu\text{g g}^{-1}$)	4.94
V	750 ± 40 ($\mu\text{g g}^{-1}$)	750 ± 30 ($\mu\text{g g}^{-1}$)	0.12
Cr	26.72 ± 0.04	26.72 (I.S.)	4.12
Mn	1.73 ± 0.01	1.68 ± 0.06	0.20
Co	580 ± 30 ($\mu\text{g g}^{-1}$)	578 ± 25 ($\mu\text{g g}^{-1}$)	0.12
Ni	30.82 ± 0.06	25.7 ± 1.1	1.58
Cu	0.936 ± 0.005	0.882 ± 0.046	0.61
Mo	3.55 ± 0.03	3.5 ± 0.4	0.58

^a certified values, uncertainty is given for 95 % confidence interval

^b n=4, uncertainty is given as \pm standard deviation

However, a significant deviation from the reference was obtained for Ni. Therefore, experiments were carried out using the closed cell configuration and helium as carrier gas and indicated similar deviations for Ni in comparison to the certified value (data not shown), which demonstrates that the obtained deviation was not caused by the novel sampling approach. The limits of detection (Table 7 and 8) in both analyses were about $1 \mu\text{g g}^{-1}$ for most elements, which are insignificantly higher than those determined using the closed cell configuration.

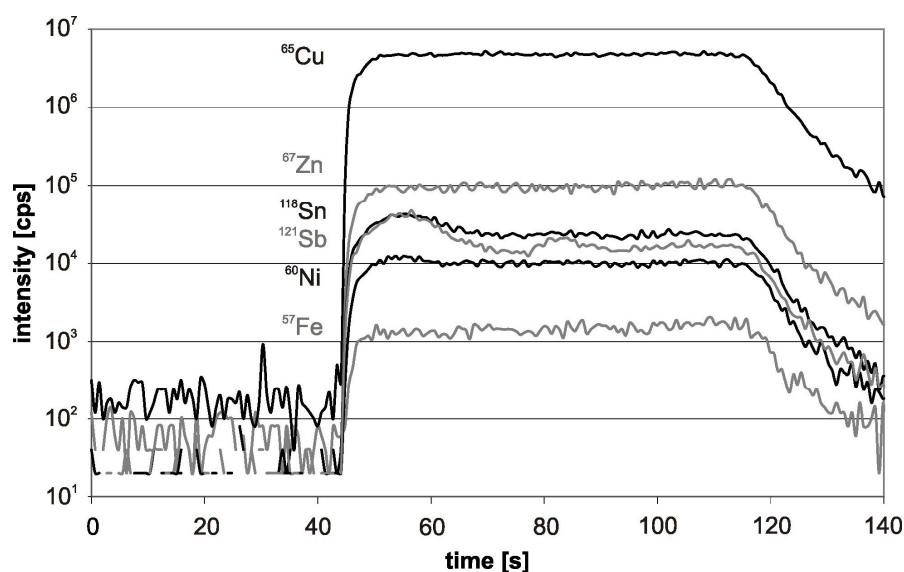


Figure 34 Transient signals of six analytes of MBH-B22 brass CRM. Laser ablation was performed in ambient air using the novel sampling approach and $50 \mu\text{m}$ spot size, 10 Hz ablation frequency, a fluence of 8 J cm^{-2} at a wavelength of 213 nm. The ICP-MS dwell time was set to 50 ms per isotope.

3.4 Conclusion

The preliminary results achieved in this initial study using a gas exchange device for LA-ICP-MS indicate the capabilities of air as an alternative gas environment for laser ablation sampling without using any ablation cell. The system used in this study is, however, limited by the low gas flow rate providing lower sensitivities in comparison to the use of a closed cell configuration under optimum gas flow conditions. Therefore, further development of a high performance gas exchange device (flow rate up to 1 L min^{-1} for air) is already in progress.

The quantitative results achieved using atmospheric ablation followed by sucking the laser generated aerosol into a transport tube and further into the gas exchange device are encouraging and it is worthwhile to carry out further optimization towards a complete aerosol sampling.

Quantification of various gold, brass and steel samples as representative examples for the typical composition of archeological samples provided results of similar accuracy and precision as commonly obtained using closed cell configurations and helium as aerosol carrier. Since the novel aerosol sampling approach has no requirements on the sample geometry, it can be a useful alternative strategy for the analysis of larger gold objects, valuable archeological and many other samples. However, to make the aerosol suction generally applicable, aerosol expansion in dependence on laser parameters (wavelength, fluence) need to be studied in detail.

4. Fundamental studies on gas exchange experiments for LA-ICP-MS

4.1 Overview of performed experiments

For the application of air as a new ablation gas atmosphere for LA-ICP-MS, the ablation and transport processes have to be studied in detail. This study demonstrates a summary on the status-quo of experiments performed and provides an overview on the influence of humidity conditions, elemental fractionation and aerosol particle size distribution when comparing the use of air to Ar and He. Particle sizes generated by 193 nm laser wavelength are dependent on the ablation cell gas atmosphere. The generated particles are transported into the ICP-MS, with different transport efficiency based on the gas used and are undergoing a decomposition process within the ICP. Since the carrier gas flow rates (around 0.2 L min^{-1}) are relatively low in the experiments of the present study determined by the gas exchanger, the influence of the aerosol carrier gas entering the ICP has a low contribution to the total central channel gas flow of the ICP. This provides a limitation on the study of various ongoing processes (e.g. particle size distribution of the transported aerosols, elemental fractionation, ion diffusion processes within the plasma). Aerosol generation and transport lead to a lower elemental fractionation of elements for the ablation of NIST 610 in air in contrast to He. The particle size distribution generated in air and Ar is more stable over longer ablation time duration than in He. However, in Ar and air, larger spherical particles (up to $1 \mu\text{m}$) are formed to a slightly higher extent ($< 0.5 - 1 \%$ of the total PSD formed) than in He. In addition, it was found that the small particle size fraction ($< 100 \text{ nm}$) is higher for ablation in air and Ar than in He, which is contradictory to literature. The particle size distribution measurements might be influenced by the inadequate operation of the optical particle counter device used, moreover no information could be obtained on the differentiation between individual particles and agglomerates during the measurements. Scanning electron microscopy proved that relatively large (around $1 \mu\text{m}$) spherical particles are present within the aerosol generated by air and Ar, while the aerosol generated in He was only consisted of agglomerates. In all three cases (He, Ar, air) the major part of the aerosol consisted of particles smaller than 150 nm , which can be fully vaporized within the ICP¹⁰⁵. Both optical particle counting experiments and

scanning electron microscope images proved that the aerosol structure and particle sizes are not affected by the gas exchange device. However, based on the measured sensitivity by the ICP-MS, 20 % loss of aerosol was observed when the aerosol was introduced into the gas exchanger. However, optical particle counting measurements were not indicating significant particle size dependent loss from the aerosol when introducing the aerosol into the gas exchange device. Maintaining the high transport efficiency offered by He and exchanging helium to argon in front of the ICP did not contribute to a significant increase in sensitivity, which suggest that the low helium gas flow rate introduced into the plasma in the present study (total central channel gas flow: 1.25 L min⁻¹: Ar: 1 L min⁻¹, He: 0.25 L min⁻¹) does not contribute to higher ion diffusion losses in the ICP than pure argon. The presence of helium in the ICP significantly changed the ICP operating conditions. Sensitivity response of a wide range of elements showed that the zone of the plasma providing the highest sensitivity for individual elements is shifted when helium is present in the ICP. However, dramatic differences in sensitivity when introducing the aerosol in He into the ICP in contrast when exchanging helium to argon were not detected. It was found that certain elements such as B, P, Zn, As, Cd and Sb are highly influenced by the ICP conditions. The common characteristics of all these elements are related to vaporization (relatively low melting and boiling points), ionization (high ionization potentials) and fractionation (highly fractionating elements). Based on the ablation gas atmosphere used, boron is greatly influenced and humidity plays an important role in the attainable sensitivity of boron.

The aerosol suction approach demonstrated in Chapter 3.3.3 was tested for direct liquid ablation in ambient air and provided limits of detection down to 1 ng g⁻¹ for most elements measured (Table 9). Variation of the matrix load up to a factor of 180 did not influence most elements. Therefore, liquid ablation can be considered as a suitable calibration technique for LA-ICP-MS even without using an ablation cell. The performed experiments proved that the introduction of laser generated aerosols by aerosol suction and gas exchange into ICP-MS can be considered as a suitable and flexible way of direct solid and liquid sampling.

Table 9 Limits of detection (ng g⁻¹) as a function of ablation frequency (NIR-fs-LA) for direct liquid ablation in ambient air utilizing aerosol suction

		Li	Al	Ca	Mn	Cu	Ag	Ba	Tl	Pb
10 Hz	AVG	22	112.7	15	14	25	6.7	3.3	3.1	13
	SD	5	2.1	3	3	6	2.1	2.3	1.7	8
100 Hz	AVG	7	18	4.1	6.0	5.5	1.4	0.71	5.1	2.5
	SD	3	4	1.1	1.0	1.6	0.6	0.03	3.4	0.3
1 kHz	AVG	1.67	4.6	0.91	1.42	1.64	1.0	0.25	0.83	0.73
	SD	0.20	0.4	0.06	0.25	0.12	0.8	0.01	0.15	0.01

4.2 Influence of humidity of air on signal response by LA-ICP-MS

As it has already been shown in Chapter 3.3.1, the intensity of boron was found to be enhanced by approximately 20 % for the ablation of NIST 610 using 193 nm wavelength in compressed air (dried, particle filtered air) in contrast to the ablation in helium. This signal enhancement was significant, especially when considering the observed 1.2-2 fold sensitivity loss for most of the 40+ elements measured between the ablation in air and helium. This enhancement was not caused by 'spikes' in the transient signals or changes in the background count rates. A relatively stable and higher transient signal was obtained for the isotopes of boron in air in contrast to helium or argon. Furthermore, Figure 33 in Chapter 3.3.3 indicated highly efficient aerosol suction efficiency in terms of boron signal intensity in contrast to other elements, which observation is not completely understood.

Since the difference between compressed air (dried, particle filtered air) and laboratory ambient air (humidity depends on the temporal laboratory climate and the ambient particles are filtered by a high performance laminar flow box) is dominated by the humidity conditions, the influence of humidity on signal intensity was studied. Therefore, all experiments were performed using air as a carrier gas with different humidity within a closed ablation cell. By comparing the transient signals during ablation of NIST 610 at 193 nm in compressed air in comparison to ambient air, a great difference was observed exclusively for boron. In the experimental data, the ratio of the boron isotopes (^{10}B , ^{11}B) was constant, therefore the data based on ^{11}B is shown in the figures. Figure 35 indicates signal enhancement for ^{11}B by a factor of approximately 11 when changing the ablation cell gas from compressed air to ambient air, while other analytes were not affected (Figure 35 and Figure 36). Experiments under extreme humid conditions were performed by sucking the air through the atmosphere of a closed glass beaker containing boiling water prior to entering the ablation cell. The results indicate (Figure 36) that the humidity severely influences the intensity of boron (increase in sensitivity by up to a factor of 80 in contrast to compressed air) measured by the ICP-MS. It must be noted that the ICP-MS operating conditions were not changed during the entire experiment, since water vapor and air are removed and exchanged to Ar within the gas exchange device before the laser generated aerosol reached the plasma. This is confirmed by the stable background count rates during the entire measurement (data not shown). In case of humid air, a significant loss in sensitivity was observed for all elements except boron. This loss might be caused by reduced transport efficiency of the aerosol based on deposition of particles on the wet sample surface and tube wall.

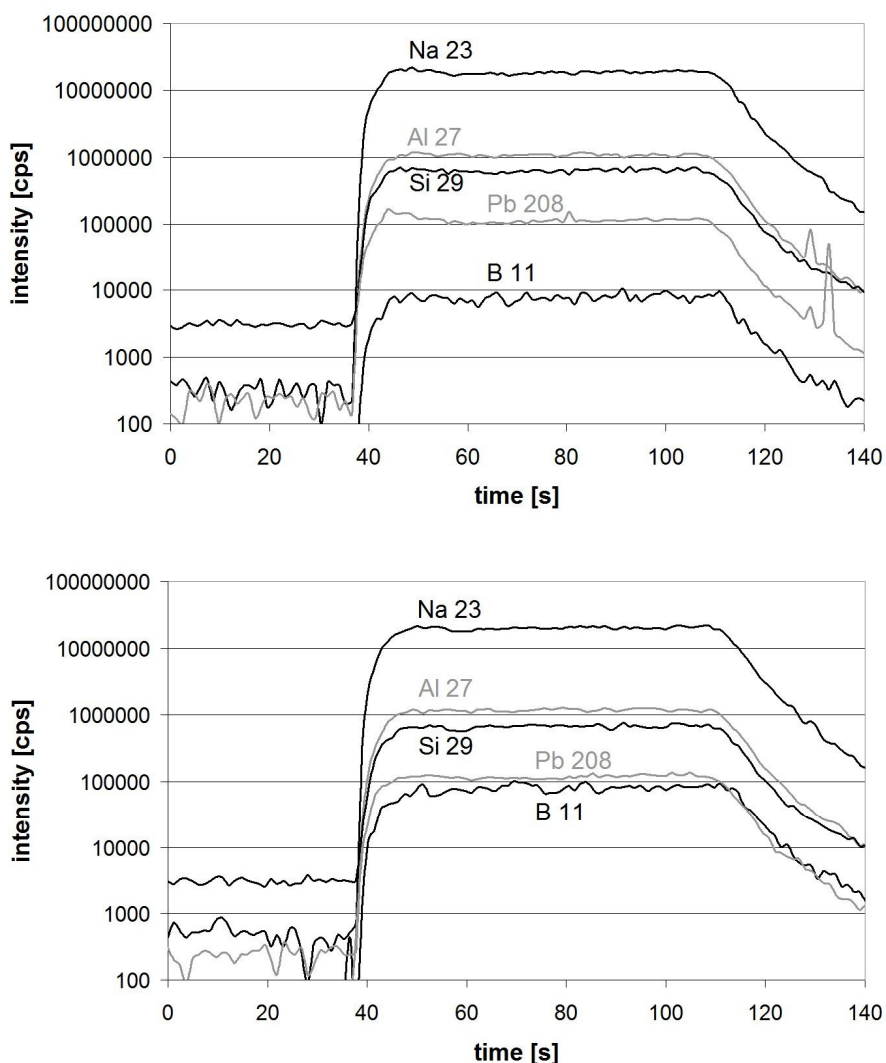


Figure 35 Transient signals of various analytes during the ablation of NIST 610 ($\lambda = 193$ nm, $60 \mu\text{m}$ spot size, 10 Hz ablation frequency, 21.9 J cm^{-2} energy density) in compressed air (top) and ambient air (bottom).

In Table 10 melting and boiling points of elemental boron, boron-oxide and various boron-hydride compounds are summarized. In comparison to other elements within the periodic table, the melting point of boron is relatively high and the boiling point ($4000 \text{ }^\circ\text{C}$) is also one of the highest among most elements. However, under specific conditions, boron may sublime around $2500 \text{ }^\circ\text{C}$ ¹⁹⁵. Boron-oxide, which is assumed to be formed during ablation in air has a significantly lower boiling point than elemental boron. However, the boron-hydride compounds, which might be formed during the ablation, especially when using humid gas atmosphere are highly volatile.

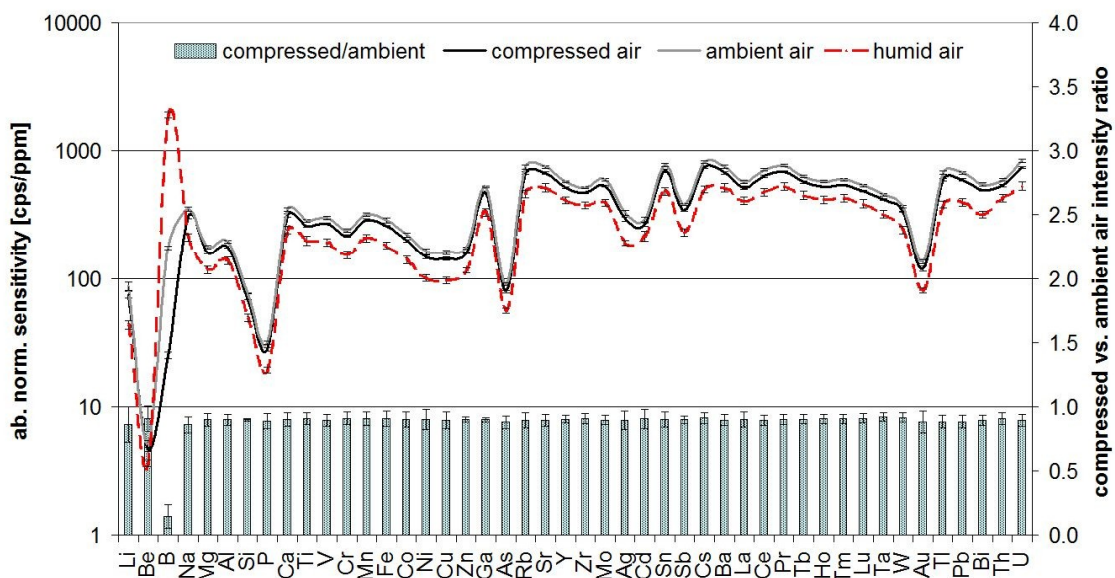


Figure 36 Abundance normalized sensitivities calculated for the ablation of NIST 610 ($\lambda = 193$ nm, $60 \mu\text{m}$ spot size, 10 Hz ablation frequency, 21.9 J cm^{-2} energy density) in compressed air, laboratory ambient air and humid air. The sensitivity ratio of compressed air and ambient air indicates that only boron is affected by humidity changes in the ablation cell.

Table 10 Melting and boiling points of boron, boron-oxide and boranes

	Melting point ($^{\circ}\text{C}$)	Boiling point ($^{\circ}\text{C}$)
Boron (B)	2075 ^a	4000 ^a (boiling point)
Boron (B)	2300 ^b	2550 ^b (point of sublimation)
Boron-oxide (B_2O_3)	450 ^{a,c}	1860 ^c
Diborane (B_2H_6)	-164.85 ^a	-92.49 ^a
Tetraborane (B_4H_{10})	-120 ^a	18 ^a
Pentaborane (B_5H_{11})	-122 ^a	65 ^a
Hexaborane (B_6H_{12})	-82.3 ^a	~ 85 ^a
Decaborane ($\text{B}_{10}\text{H}_{14}$)	98.78 ^a	213 ^a
etc.		

^a CRC Handbook of Chemistry and Physics, CRC Press, USA, 2003

^b RömPP online, <http://www.roempp.com/>

^c READE Advanced Materials, <http://www.reade.com/>

In contrast to the experiments carried out on the silicate glass NIST 610, no signal enhancement was observed for boron isotopes during the ablation of NIST 1411 (soft borosilicate glass) and NIST 1412 (multi-component glass) when comparing the transient signals acquired using compressed air and ambient air. The concentration of boron within NIST 610 is known to be 356.4 $\mu\text{g/g}$ ¹⁹⁶, while in case of NIST 1411 and NIST 1412 the certified B_2O_3 concentrations are 10.9 wt% and 4.5 wt% respectively. This implies that accurate quantification of boron cannot be performed when using NIST 610 as reference material and air as ablation gas environment.

The boranes (i.e. hydrides of boron) are gaseous at room temperature, and the simplest and most important hydride is diborane. Higher boranes are generally originating from a strong heating of diborane in the absence of air. Theoretically, if diborane is formed during laser ablation, that might be converted into higher boranes (which are still highly volatile), because of the extreme temperature within the laser plume. On the other hand, diborane undergoes spontaneous combustion in air due to the strong affinity of boron with oxygen, and boron-oxide can be formed.

Theoretically, highly volatile compounds like boranes would be lost within the ablation cell and gas exchange device due to diffusion and therefore intensity loss could be expected. Most likely, the humidity promotes the formation of boranes, which are immediately burn to boron-oxide, a compound, which is not difficult to vaporize within the ICP (b.p.: 1860 °C). Since the ablation process is performed in a relatively small area on the sample surface, most of the boron content is most likely not changed to boron-hydrides during ablation of high boron content samples, but rather vaporized and condensed into solid particles. The high difference in concentration with respect to the available moisture at the volume of the ablation plume might explain the insignificant change in sensitivity of boron during ablation of NIST 1411 and 1412.

An indication for early vaporization, atomization and ionization of boron within the ICP is discussed in Chapter 4.5.2, Table 15. However, this early vaporization, atomization and ionization of elemental boron are not consistent with the boiling point (Table 10) and 1st ionization potential (8.298 eV).

4.3 Elemental fractionation studies during ablation in air

Non-stoichiometric effects occurring during laser ablation sampling, aerosol transport and the decomposition process within the ICP are generally described as elemental fractionation^{148,90} as explained in detail in Chapter 1.2.5.

A study¹⁶¹ has recently demonstrated that oxygen added to the He aerosol carrier gas as an impurity enhances elemental fractionation. The measurement was carried out on various samples such as silicates (e.g. glass, zircon) and sulphides using a 266 nm laser wavelength. However, the influence of O₂ on the ablation process and ICP operating conditions could not be separated with the experimental setup used. In contrast, our experimental setup including a gas exchange device can remove O₂ from the carrier gas and therefore provides stable operating conditions within the ICP. Therefore, the influence of air on elemental fractionation was determined and the obtained fractionation indices were compared to those measured using He as carrier gas.

Here, the results of two experiments performed on the silicate glass NIST 610 using a 193 nm and a 266 nm laser ablation system are summarized. For all measurements using different gas combinations, the ICP-MS operating conditions were optimized separately using identical optimization criteria. Laser ablation and ICP-MS operating conditions used are summarized in Table 11.

Influence of helium within the ICP with respect to elemental fractionation

Figure 37 indicates that the changed plasma conditions (He admixed with Ar vs. Ar only in the ICP) are not influencing elemental fractionation of aerosols generated when using a 193 nm laser for ablation. The presence of helium within the plasma at the flow rates applied generates significantly higher gas temperatures within the ICP in contrast to Ar only¹⁹⁷. The results demonstrate that the temperature difference (He admixed with Ar vs. Ar only) of the ICP does not influence fractionation. This was also observed for 266 nm LA (Figure 38). In this experiment 0.25 L min⁻¹ and 0.63 L min⁻¹ He flow rates were also tested and compared to match the flow rate of argon and the flow rate of He when performing gas exchange (“He exchange to Ar”: He at a flow rate of 0.63 L min⁻¹ exchanged to Ar at a flow rate of 0.21 L min⁻¹). However, these experiments showed similar fractionation indices, except for Cd. These suggest that the ablation and aerosol transport process are mostly responsible for the fractionation under these conditions.

Table 11 Operating conditions for laser ablation, ICP-MS and GED

Laser ablation		
Laser ablation system	LSX-500, Nd:YAG	GeoLas Q, ArF excimer
Wavelength	266 nm	193 nm
Pulse duration	6 ns	15 ns
Ablation frequency	10 Hz	10 Hz
Spot size	50 μm	80 μm
Laser fluence	13.8 J cm ⁻²	17.5 J cm ⁻²
Power density	2.3 GW cm ⁻²	0.9 GW cm ⁻²
Ablation time	4 min	4 min
Ablation mode	single hole drilling	single hole drilling
Sample	NIST 610	NIST 610

ICP-MS	
Instrument	PE Sciex ELAN 6100 DRC+
Nebulizer gas flow	0.95 – 1.05 L min ⁻¹
Auxiliary gas flow	0.75 L min ⁻¹
Plasma gas flow	17.5 L min ⁻¹
RF power	1350 W
Lens setting	autolens calibrated
Detector mode	dual (pulse counting and analogue mode)
Dwell time	10 ms
Scan mode	peak hopping

Gas mode	Ablation cell gas	Sample gas out (GED)
He without GED	He, 0.25 L min ⁻¹	-
He without GED	He, 0.63 L min ⁻¹	-
He exchange to Ar	He, 0.63 L min ⁻¹	Ar, 0.21 L min ⁻¹
Air exchange to Ar	Air, 0.25 L min ⁻¹	Ar, 0.21 L min ⁻¹

Influence of the ablation gas environment on elemental fractionation

Figure 39 and Figure 40 demonstrate the differences in fractionation caused by the ablation cell gases (He or air), while introducing argon only into the ICP. Fractionation indices determined for highly fractionating elements such as P, Zn, As, Ag, Cd, Sb, Au, Pb, Bi were higher for He in both experiments (193 nm and 266 nm) when compared to air. The results indicate that, elemental fractionation is rather influenced by the particle size distribution of the aerosol generated (affected by the laser wavelength¹³⁵) and the transport efficiency (affected by the properties of the carrier gas). The reason for the lower fractionation indices obtained using air as ablation cell gas may be related to the composition (higher oxide concentration) and size of particles generated and transported to the ICP-MS.

Mixed gas (He with air) experiments has not been tested until now, however in contrast to ref¹⁶¹, independent of the laser wavelength (193 or 266 nm), ablation and transport in air provided the lowest fractionation indices for most highly fractionating elements. This shows that the addition of high concentration of oxygen to the ablation gas or even ablation in air does not increase and rather reduce the fractionation when oxygen is not entering the plasma.

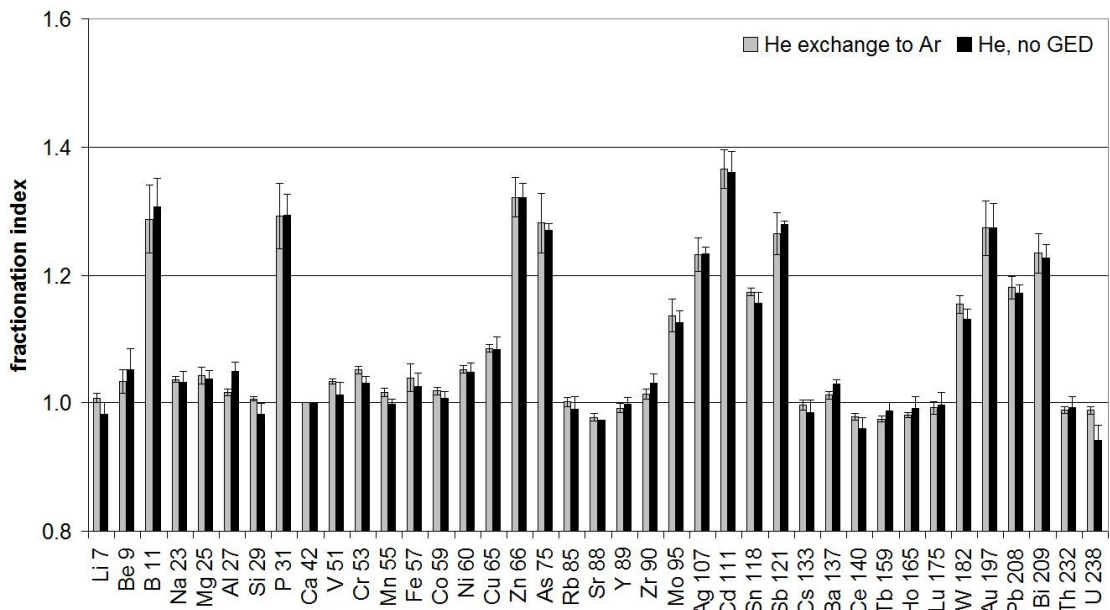


Figure 37 Fractionation indices calculated for the ablation of NIST 610 ($\lambda = 193$ nm, 80 μ m spot size, 10 Hz ablation frequency, 4 minutes time duration) in He.

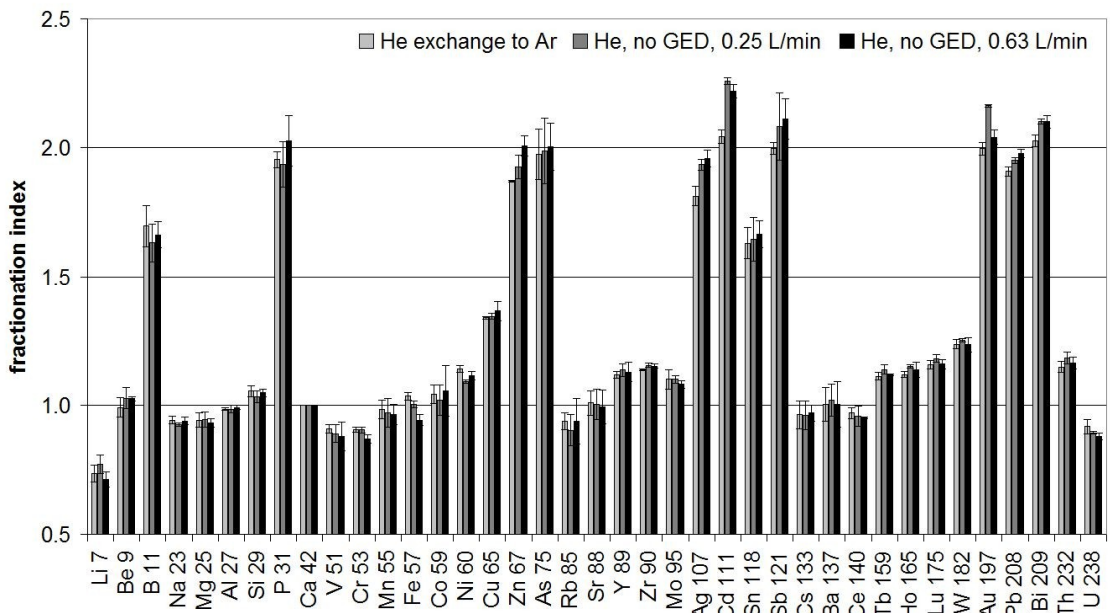


Figure 38 Fractionation indices calculated for the ablation of NIST 610 ($\lambda = 266$ nm, 50 μ m spot size, 10 Hz ablation frequency, 4 minutes time duration) in He.

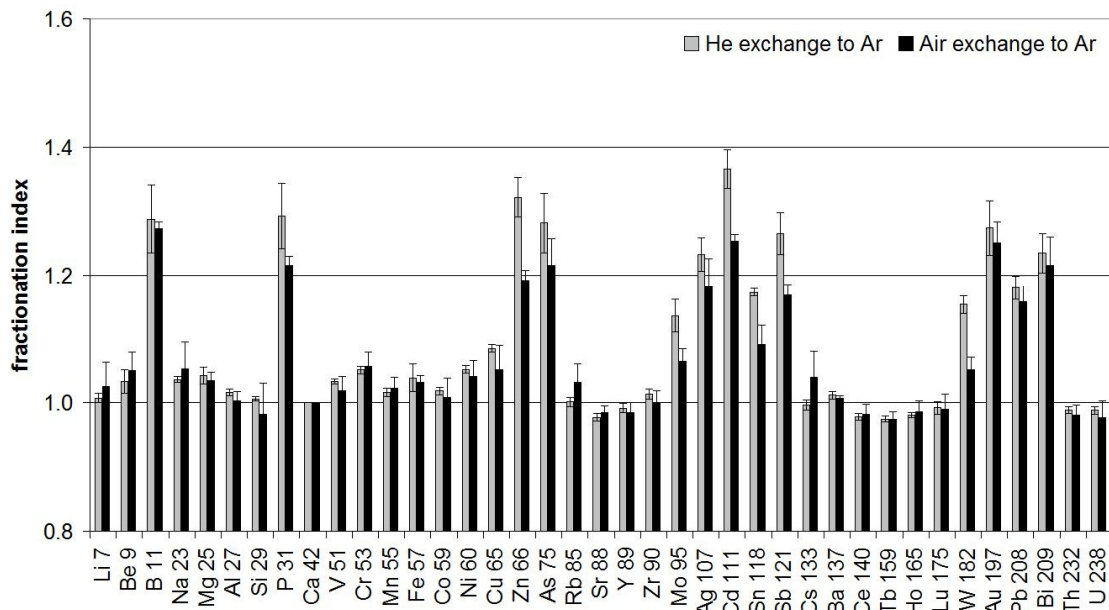


Figure 39 Fractionation indices calculated for the ablation of NIST 610 ($\lambda = 193$ nm, 80 μm spot size, 10 Hz ablation frequency, 4 minutes time duration) in He and air.

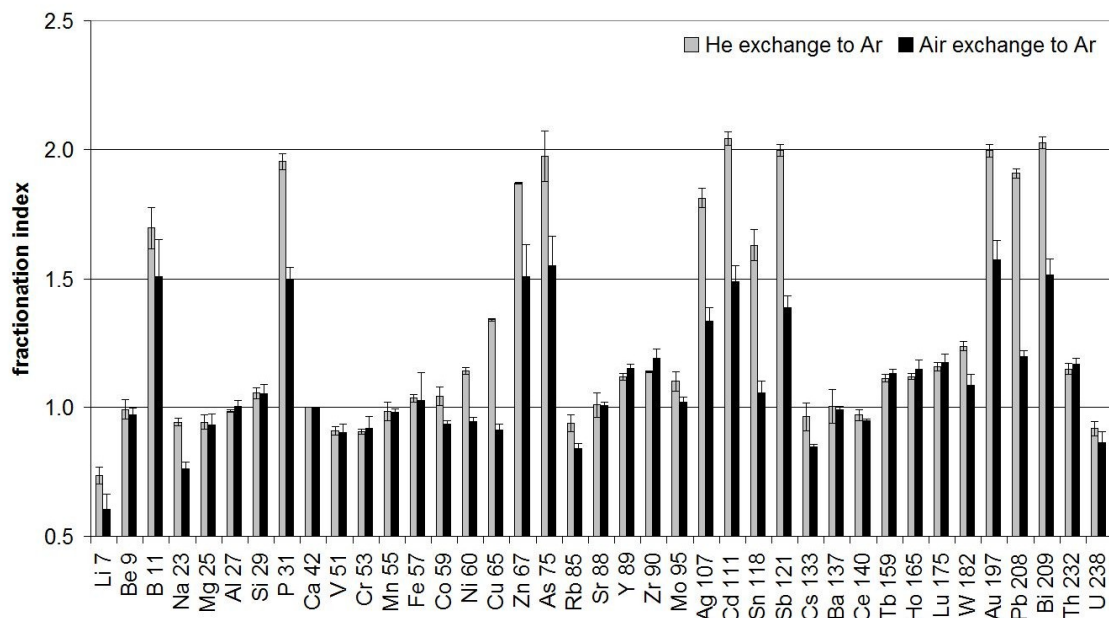


Figure 40 Fractionation indices calculated for the ablation of NIST 610 ($\lambda = 266$ nm, 50 μm spot size, 10 Hz ablation frequency, 4 minutes time duration) in He and air.

The temporal intensity ratios (Figure 41) for Pb/Ca and Pb/U are plotted together with the count rates acquired for these analytes during ablation in helium or air. In case of ablation in He, the transient ratio starts to increase after 100 s of ablation (i.e. 1000 laser pulses). In contrast, when ablating in air a less pronounced increase in the transient ratios can be observed. The results suggest that under the given flow rate of air a more representative sampling (ablation, particle generation) and aerosol transport take place, which lead to lower fractionation. Additionally, the particle size distribution was more uniform in air in comparison to He over ablation time (Chapter 4.4, Figure 46).

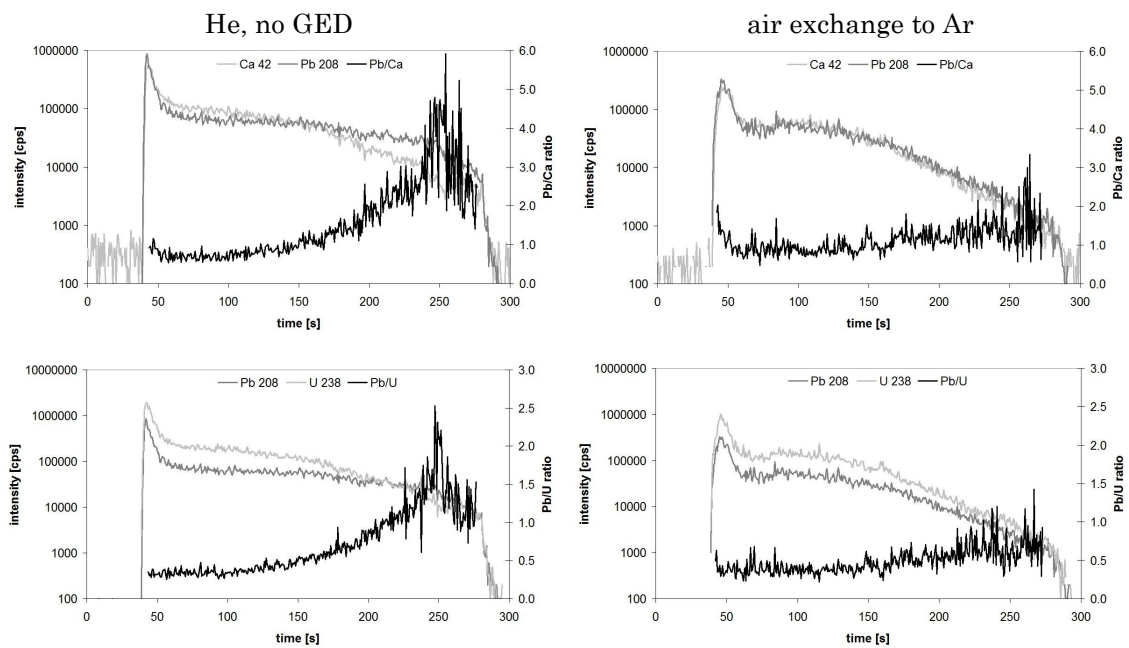


Figure 41 Transient signals of ^{42}Ca , ^{208}Pb , ^{238}U and the temporal intensity ratio of $^{208}\text{Pb} / ^{42}\text{Ca}$ and $^{208}\text{Pb} / ^{238}\text{U}$ during the ablation of NIST 610 ($\lambda = 266 \text{ nm}$, $50 \mu\text{m}$ spot size, 10 Hz ablation frequency, 4 minutes time duration) in He (left side) and in air (right side).

4.4 Comparison of aerosol particle sizes generated in He, Ar and air

Particle sizes were compared for laser aerosols generated in various gas atmospheres. A silicate glass NIST SRM 610 was ablated using single hole drilling mode by an ArF excimer laser system (GeoLas C, MicroLas, Göttingen, Germany) operating at a wavelength of 193 nm. The operating condition of the laser system was kept constant during the experiments. A spot size of 120 μm was ablated using an ablation frequency of 4 Hz at an energy density of 21 J cm^{-2} . Particle size distributions of the aerosols generated were determined by a laser diffraction based optical particle counting device (HSLAS, Particle Measuring Systems, Denver, CO, USA) in the size range of 0.067-0.95 μm . It must be stated that the performance of the particle counter was not completely adequate, since severe service maintenance was performed on the old instrument before the experiments. Moreover, the particle counter provides no information on the differentiation between individual particles and agglomerates during the measurements. Furthermore, the data obtained for channels 7 and 17 related to 0.0975 μm and 0.195 μm sizes were interpolated using the data obtained for the former and the latter channels owing to misleading information provided by the device. Therefore, the results of these experiments are for information only, and can not be handled as fully reliable data. Prior to the measurements, the aerosol was diluted to avoid overloading of the detector by a bucket wheel-type device (MD19-li, Matter Engineering AG, Wohlen, Switzerland). For data evaluation, the applied dilution factors were taken into account to correct for the aerosol density decrease.

Figure 42 indicates the differences in particle size distribution of the aerosol generated in various gas environments. A difference can be observed between He and both Ar and air. The size range of in He generated particles is significantly narrower, while the presence of particles in the size range of 0.2 - 1 μm is more pronounced in case of Ar and air. The characteristic curve between 67 - 100 nm may be influenced by the operation of the particle counter and cannot be fully interpreted. This indicates that the aerosol generated in air and Ar consists of more small particles (< 100 nm) in contrast to aerosols generated in He. It can be assumed that the density difference of the gases has an influence on these changes. The number of particles generated in air and Ar in the size fractions of < 90 nm and > 155 nm with respect to the total amount of aerosol generated in both gases are similar (Figure 43). In aerosols generated in Ar a slightly higher presence (2 – 3 %) of larger particles (> 200 nm) can be observed, while the aerosols generated in air are rich in particles in the

size range of 97-135 nm. In general, 99 % of the total aerosol consisted of particles smaller than 150 nm in case of He, while this fraction was reduced to 87 % and 92 % for ablation in Ar and air, respectively.

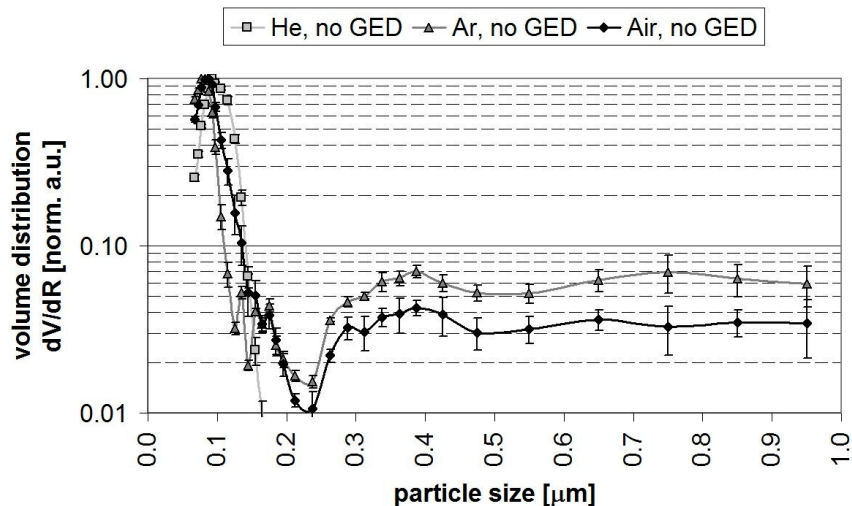


Figure 42 Comparison of particle size distributions (normalized to arbitrary units) generated in He, Ar and air at a flow rate of 0.25 L min⁻¹. The aerosol was not transported through the gas exchanger during the experiments.

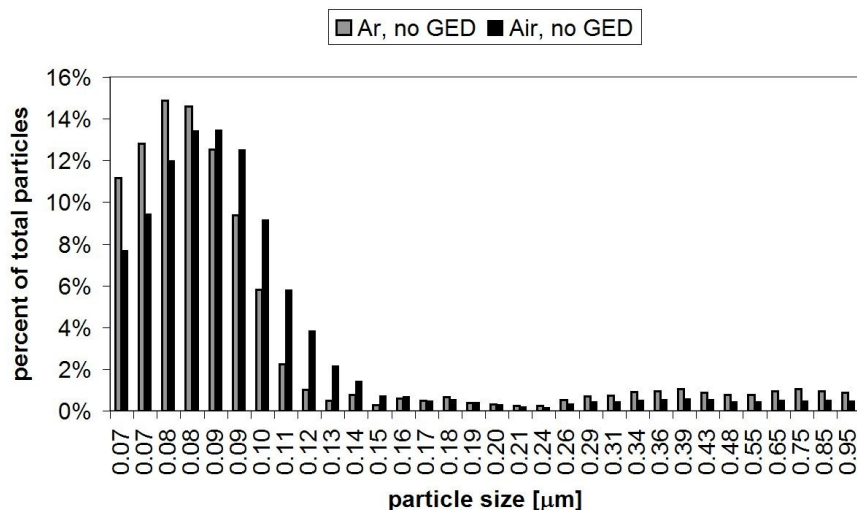


Figure 43 Comparison of particle size distributions obtained for Ar and air without transporting the aerosol through the GED.

The PSD measurements indicate that the gas exchange process do not significantly influence or change the size of the particles reaching the ICP and is not responsible for coagulation of particles (Figure 44 and 45). However, when comparing He exchange to Ar (Figure 44) or air exchange to Ar (Figure 45) it becomes visible that the signal response by the particle counter is dependent on the gas density and when the aerosol is introduced in Ar into the particle counter, the signal response is higher for small particle sizes.

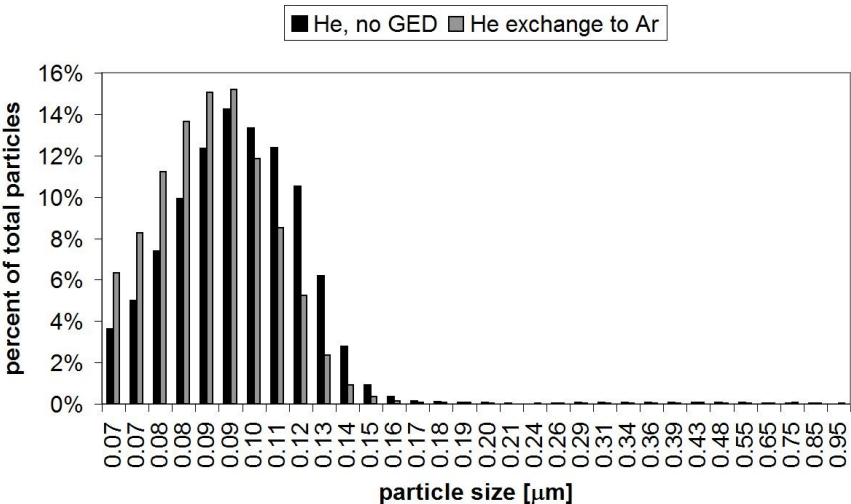


Figure 44 Influence of the gas exchange process on the particle size distribution using He as carrier gas.

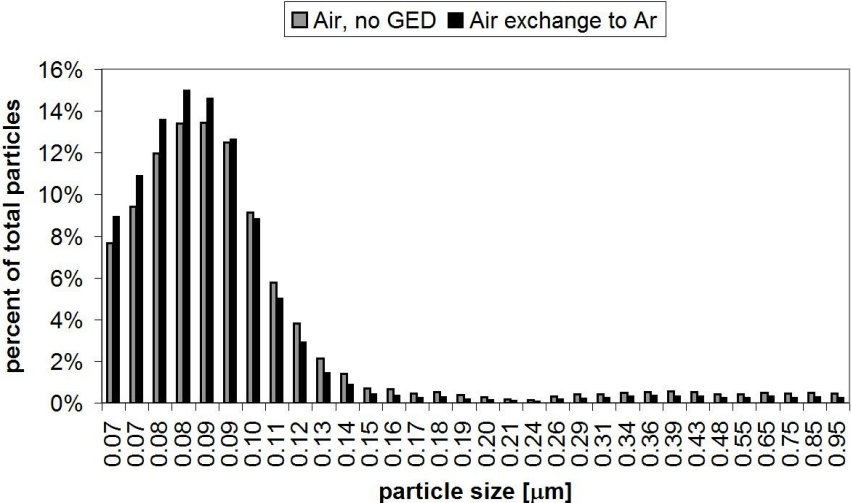


Figure 45 Influence of the gas exchange process on the particle size distribution using air as carrier gas.

Concerning the transient change in PSD it was found that while the PSD of the generated aerosol in air and Ar were not dramatically different over an approximately 2 minutes continuous laser ablation, severe changes were observed when using He. The integration time of the particle counter used for the experiments was 30 s and transient data were collected three times (3 x 30 s), which are plotted in Figure 46. In He after approximately 2 minutes ablation, the aerosol mostly consisted of particles smaller than 200 nm only, while larger particles (0.2 – 1.0 μm) were only present close to the ablation threshold. This implies that for Ar and air aerosols with more constant particle size distributions are formed during single hole drilling ablations as shown for 480 laser pulses.

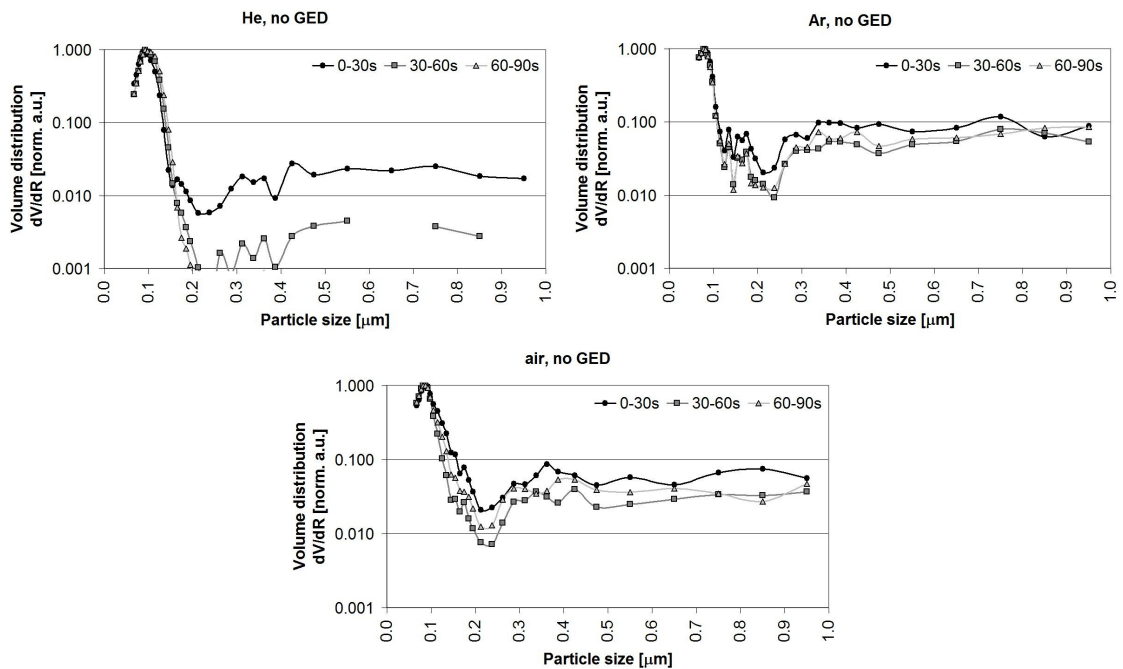


Figure 46 Temporal changes in particle size distribution of aerosols generated in He, Ar and air. Data acquisition was performed in steps of 30 s (n=3).

Results of PSD measurements are similar to information collected by visual observation of the generated aerosols. Visual investigation of aerosols was carried out by collecting particles on membrane filters to perform Scanning Electron Microscopy (SEM) studies (Microscopy centre, ETH Zurich, Dr. F. Krumeich). The SEM images were collected by a Zeiss Leo Gemini 1530 FEG instrument operating at a low acceleration voltage of 1 kV to obtain detailed images using secondary ion detection. Secondary electrons that are ejected from the orbitals of specimen atoms by inelastic scattering interactions with beam electrons can provide information about morphology and surface topography. Figure 47 indicates that the aerosol produced in helium consist of tiny particles forming agglomerates having a

'fluffy' structure¹⁰¹. No spherical particles were visually found beside the agglomerates. Moreover, no visual difference was found between the aerosol structures and particle sizes when exchanging He to Ar (in close agreement with data shown in Figure 44).

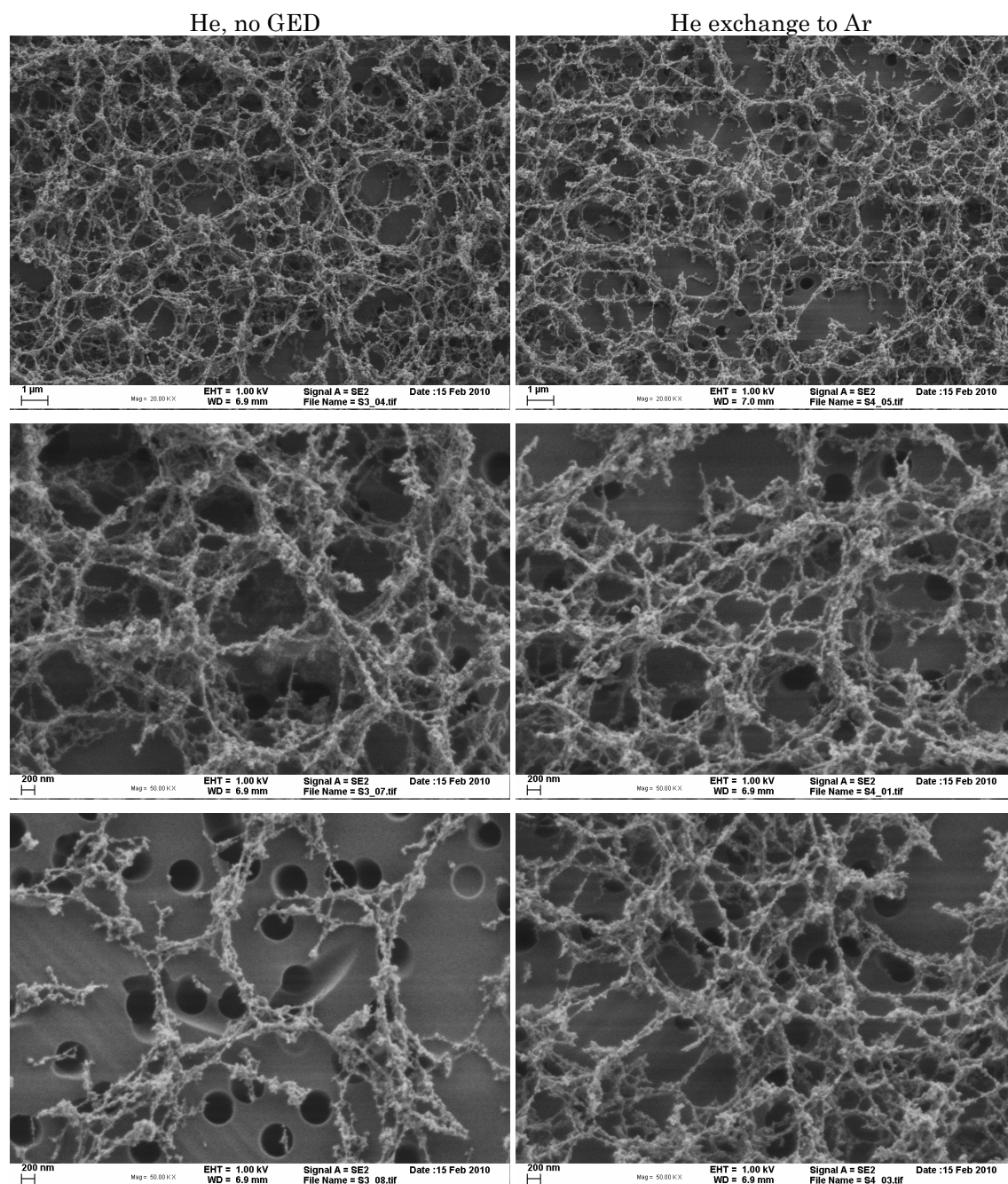


Figure 47 Scanning electron microscope images obtained for aerosols generated from NIST 610 in helium without gas exchange (left) and with exchange to Ar (right).

Aerosols generated in Ar (Figure 48) showed spherical particles in size up to approximately 1 μm and 'high density agglomerate centers' beside the same cotton-like aerosol structure as it was observed for He. For aerosols generated in ambient air (Figure 49) the typical cotton-like structures were changed to smaller structures with shorter 'fragments'. Here, spherical particles were also found rarely in a size range of a few hundred nm. By exchanging air to Ar no visual difference was found in the aerosol structures and particle sizes, which is in agreement with Figure 45 based on the data obtained with the optical particle counter.

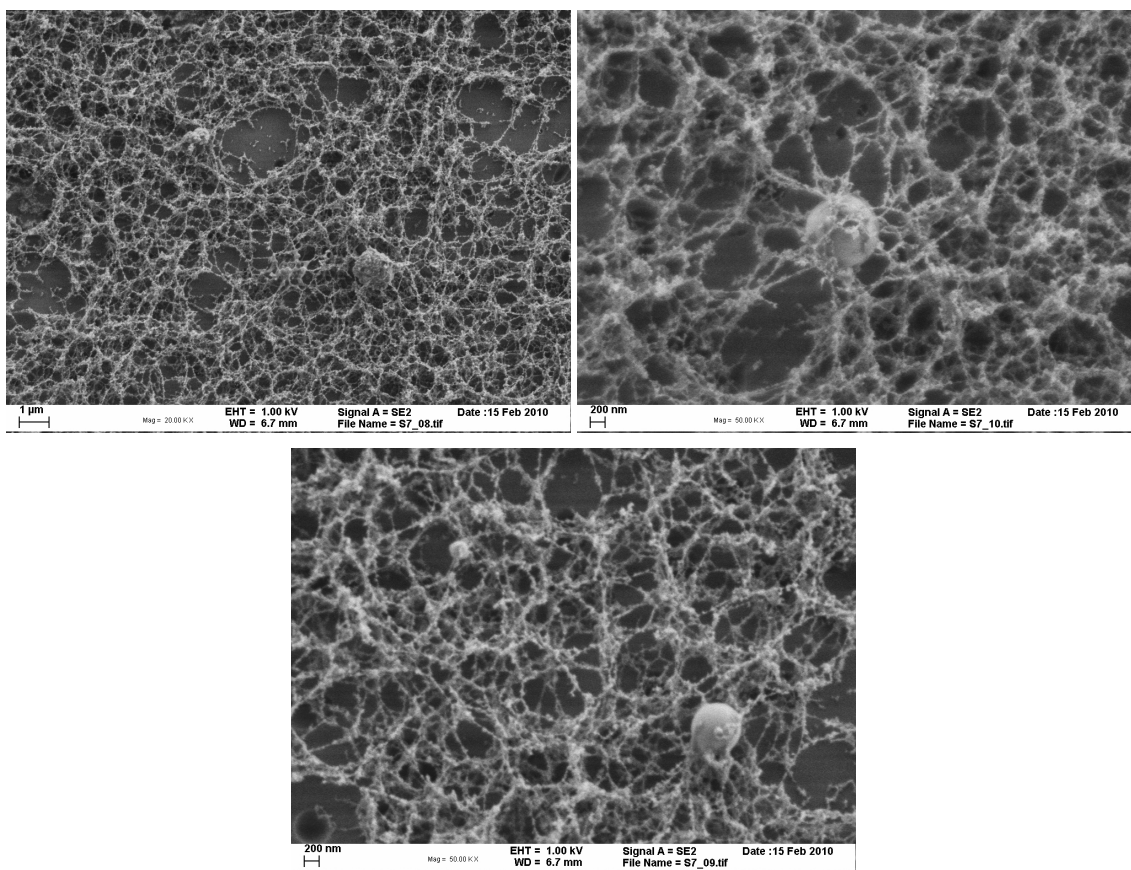


Figure 48 Scanning electron microscope images obtained for aerosols generated from NIST 610 in argon without introducing the aerosols into the gas exchange device.

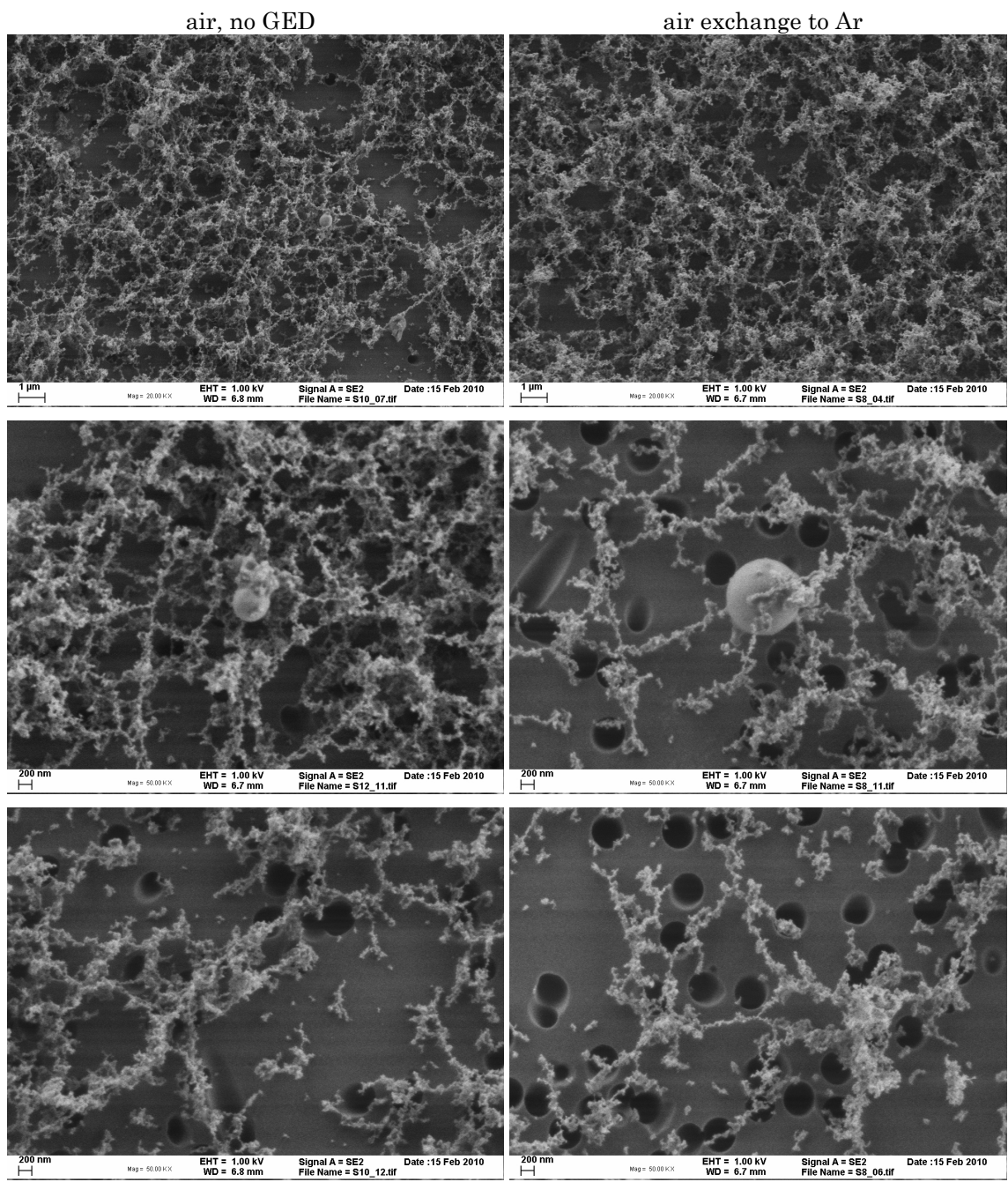


Figure 49 Scanning electron microscope images obtained for aerosols generated from NIST 610 in air without gas exchange (left) and with exchange to Ar (right).

4.5 Investigation of ion diffusion within the ICP

The influence of various aerosol carrier gases such as helium, nitrogen, hydrogen, neon has been studied in terms of transport efficiency, signal response, fractionation and particle size distribution^{135,191,68,102,198,131}. The most promising gas was found to be helium, since it provided higher transport efficiency than argon and reduced the particle deposition significantly around the crater^{102,191}. Therefore, enhanced sensitivity, lower background count rates and improved limits of detection have been observed^{191,102}. The enhanced sensitivity can be caused by both higher aerosol transport efficiency and the presence of helium within the ICP. The particle undergoes vaporization, atomization and ionization within the plasma, and these complex processes are influenced by the gas introduced into the ICP. Parameters, such as gas kinetic temperature, electron number density and electron temperature are representing the physical properties of the plasma^{199,200}, which are influenced by gases other than argon. Gas kinetic temperature is considered to be the most important parameter for vaporization and atomization. Electron temperature and number density rather influence the degree of ionization. All these parameters are depending on the power supplied to the plasma (RF power) and on the type of gases introduced and their flow rates. Furthermore, gas kinetic temperature influences ion kinetic energies after expansion in the vacuum interface, which affects the extent of ion transmission through the ion optics and mass spectrometer¹⁹². It was reported that helium significantly contributes to increased gas temperatures, while it has a less pronounced effect on the electron temperature and number density¹³¹. On the other hand, the presence of helium within the ICP has been reported to be a potential drawback, since the generated ions within the plasma may undergo more severe diffusion than in pure argon¹¹. Since the ion diffusion is inversely proportional to mass, light elements are undergoing more severe diffusion than heavy elements²⁰¹. It has been demonstrated that the use of helium for LA contribute to a more uniform vaporization of particles within the ICP and cause a larger radial ion spread, which reduces the number of ions transmitted and detected by the mass spectrometer¹¹. This loss is compensated by an improved vaporization due to a higher central channel gas temperature within the ICP and a faster removal of material from the vapor cloud around the particle¹¹. The obtained radial and axial ion intensity distribution profiles within the ICP were interpreted, however, the extent of ion diffusion losses versus enhanced gas temperature influencing vaporization was impossible to compare¹¹.

4.5.1 Evaluation of radial ion profiles obtained using He or Ar as carrier gases

The influence of helium on the plasma conditions may depend on the amount of gas entering the ICP. In the study demonstrated by Wang et. al.¹¹, the experiments were performed using 1.3 L min⁻¹ helium gas flow rate, which contributes to fast transport of the laser generated aerosol into the ICP and stable transient signals. Our current experimental setup including a gas exchange device, theoretically, capable to perform experiments to investigate mass dependent ion diffusion^{11,201} losses was based on experiments focusing on helium exchange to argon in front of the ICP. However, the experiments were carried out at significantly lower carrier gas flow rates, since the maximum gas flow rate of argon leaving the GED is limited to 0.21 L min⁻¹.

Vertical ion distribution profiles were investigated and compared when using He or Ar as aerosol carrier gases. Two sets of experiments were performed, either using a 266 nm or 193 nm laser. The ion signal recording was carried out on an Agilent 7500cs quadrupole ICP-MS optimized prior to the experiments. The experimental conditions are summarized in Table 12.

To evaluate radial ion distribution, each point plotted indicated in the figures represent background corrected 70 s long signals generated by single hole drilling ablation performed at an ablation frequency of 10 Hz. Figure 50 illustrates the obtained profiles using 193 nm and 266 nm LA with various gas combinations. The obtained radial ion profiles are not symmetric, since the torch-box gas exhaust connection of the ICP-MS drag the gas towards the negative axis of the translation stage of the torch. The right side of the profiles of the intensity maxima clearly indicate a mass dependent radial ion spread. Since diffusion is inversely proportional to mass, light ions are undergoing a more severe diffusion (i.e. radial spread) in the plasma than heavier ions. The figure indicates that radial ion profiles are broader for 193 nm than for 266 nm. This can be explained by the particle size distribution of the aerosol generated by the different laser wavelengths. As demonstrated in ref¹³⁷, the amount of material ablated is smaller for 193 nm LA than for 266 nm. However, the particle size distribution is shifted to smaller particle sizes in case of 193 nm LA, especially when helium is used as aerosol carrier gas^{88,135,137}. The more complete vaporization of particles leads to a more efficient ion generation within the ICP¹⁰⁵. The generated ions therefore represent a slightly broader radial distribution than the ions generated from significantly larger particles in case of 266 nm LA. Though, no significant differences were found when comparing the radial ion distribution when introducing He into the ICP in

contrast when Ar only is present in the plasma. The reason for the observed similarities in radial ion profiles might be the minor contribution of He in the total gas flow entering the central channel of the ICP. The gas flow rates in this study are limited by the gas exchange device, which provide 0.21 L min⁻¹ outlet gas flow rate (He exchanged to Ar) to transport the aerosol to the ICP. This flow rate was taken as a degree of measure in the experiments, thus for the measurements without GED, He and Ar gas flow rates were set to closely identical gas flow rates.

Table 12 Operating conditions for laser ablation, ICP-MS and GED

	LA-ICP-MS combination 1	LA-ICP-MS combination 2
Laser ablation		
Laser ablation system	LSX-500, Nd:YAG	GeoLas C, ArF excimer
Wavelength	266 nm	193 nm
Pulse duration	6 ns	15 ns
Ablation frequency	10 Hz	10 Hz
Spot size	50 μm	60 μm
Laser fluence	12.7 J cm ⁻²	24.8 J cm ⁻²
Ablation time	70 s	70 s
Ablation mode	single hole drilling	single hole drilling
Sample	NIST 610	NIST 610
ICP-MS		
Instrument	Agilent 7500cs	Agilent 7500cs
Nebulizer gas flow	1.00 L min ⁻¹ (He is carrier gas), 0.95 L min ⁻¹ (Ar is carrier gas or He exchange to Ar)	1.05 L min ⁻¹ (He is carrier gas), 0.95 L min ⁻¹ (Ar is carrier gas or He exchange to Ar)
RF power	1400 W	1400 W
Sampling depth	3.0 mm	3.0 mm
Torch-X	0.7 mm	1.0 mm
Torch-Y	monitored	monitored
Lens – extract1	5.7 V	4.6 V
Lens – extract2	-160.0 V	-184.0 V
Omega bias-cs	-38 V	-42 V
Omega lens-cs	9.0 V	10.2 V
P/A factors	tuned	Tuned
Reaction cell mode	OFF	OFF
Gas mode		
	Ablation cell gas	Sample gas out (GED)
He without GED	He, 0.25 L min ⁻¹	-
Ar without GED	He, 0.25 L min ⁻¹	-
He exchange to Ar	He, 0.63 L min ⁻¹	Ar, 0.21 L min ⁻¹

The comparison of the obtained radial profiles with profiles reported by Wang et. al.¹¹ is shown in Figure 51. The profiles compared for 266 nm LA using Ar as carrier gas indicate a significant difference between the two experiments. Nevertheless, both experiments were performed on the same ICP-MS instrument, there is a great difference between the gas flow rates used. In the study of Wang et. al.¹¹ Ar, at a flow rate of 1.25 L min⁻¹, was passed through the ablation cell providing a stable and rapid transport of aerosol into the ICP (Table 13).

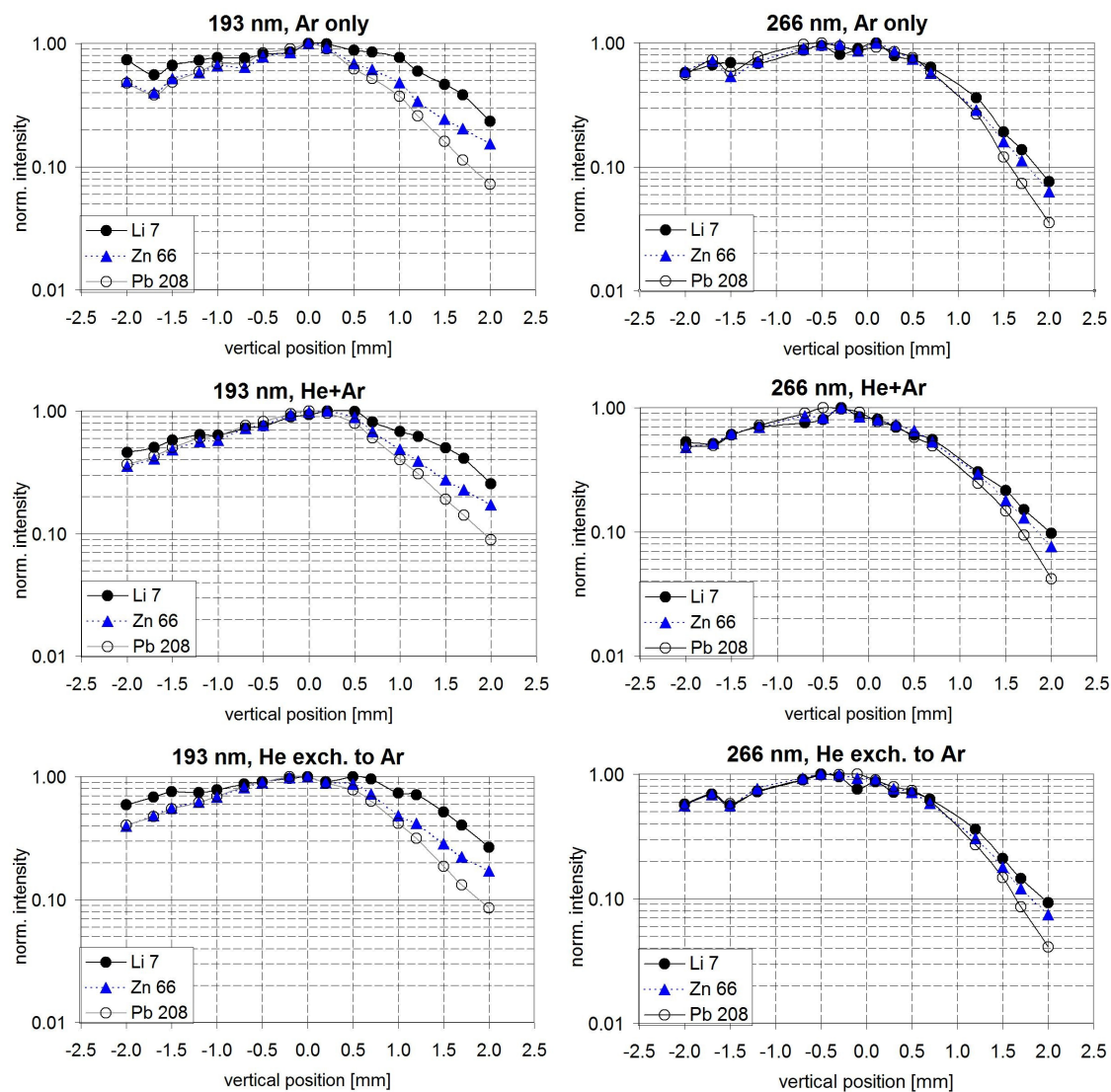


Figure 50 Comparison of radial ion signal profiles obtained for ${}^7\text{Li}$, ${}^{66}\text{Zn}$, ${}^{208}\text{Pb}$ at a constant sampling depth of 3.0 mm. Laser ablation sampling was carried out at wavelengths of 193 nm and 266 nm using Ar (top) or He (middle and bottom) as aerosol carrier gas and represent ion diffusion profiles for Ar only (top and bottom) and He admixed with Ar (middle) within the ICP.

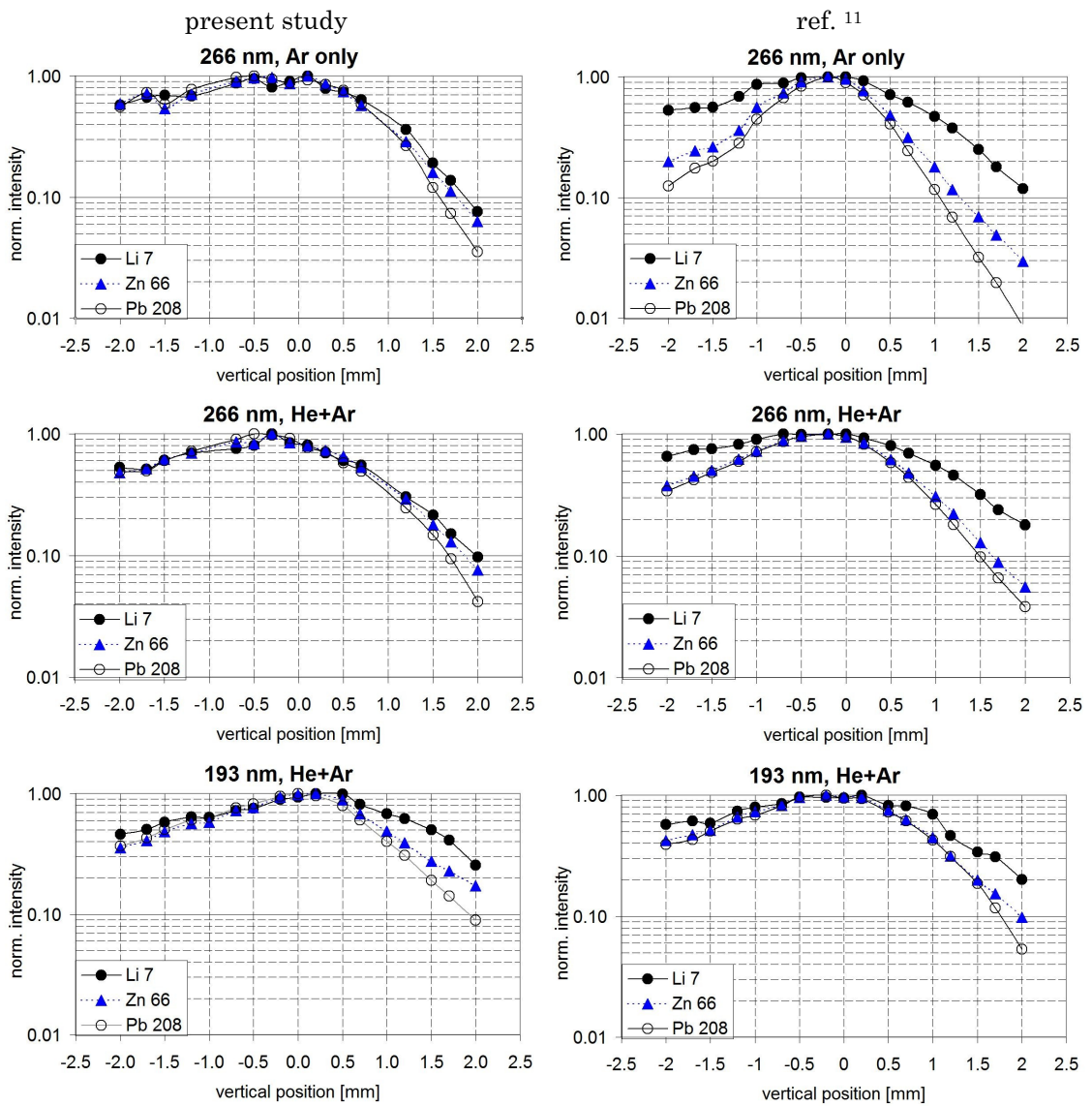


Figure 51 Comparison of radial ion signal profiles obtained for ${}^7\text{Li}$, ${}^{66}\text{Zn}$, ${}^{208}\text{Pb}$ at a constant sampling depth of 3.0 mm to profiles reported in ref.¹¹. Laser ablation sampling was carried out at wavelengths of 266 nm and 193 nm using Ar (top) or He (middle and bottom) as aerosol carrier gas and represent ion diffusion profiles for Ar only (top) and He admixed with Ar (middle and bottom) within the ICP.

Table 13 Operating conditions for laser ablation, ICP-MS used by Wang et. al. in ref ¹¹

	LA-ICP-MS combination 1	LA-ICP-MS combination 2
Laser ablation		
Laser ablation system	LSX-200, Nd:YAG	GeoLas C, ArF excimer
Wavelength	266 nm	193 nm
Pulse duration	4 ns	15 ns
Ablation frequency	10 Hz	10 Hz
Spot size	50 μm	63 μm
Laser fluence	7 J cm ⁻²	7 J cm ⁻²
Ablation time	60 s	60 s
Ablation mode	single hole drilling	single hole drilling
Sample	NIST 610	NIST 610
ICP-MS		
Instrument	Agilent 7500cs	Agilent 7500cs
Nebulizer gas flow	0.7 L min ⁻¹ (He is carrier gas), 0 L min ⁻¹ (Ar is carrier gas)	0.7 L min ⁻¹ (He is carrier gas), 0 L min ⁻¹ (Ar is carrier gas)
RF power	1400 W	1400 W
Sampling depth	3.0 mm	3.0 mm
Lens – extract1	4.2 V	4.2 V
Lens – extract2	-103 V	-103 V
Omega bias-cs	-48 V	-48 V
Omega lens-cs	8.2 V	8.2 V
P/A factors	tuned	tuned
Reaction cell mode	OFF	OFF
Carrier gas		Ablation cell gas
He		He, 1.3 L min ⁻¹
Ar		Ar, 1.25 L min ⁻¹

In case of the present study the flow rate of Ar carrier gas was limited to 0.21 L min⁻¹, which may provide lower transport efficiency. In front of the injector, Ar nebulizer gas was added and the total Ar gas flow entering the ICP was 1.2 L min⁻¹, while in case of ref ¹¹ no nebulizer gas flow was added to the 1.25 L min⁻¹ Ar. When using He as carrier gas, the obtained profiles were more similar to that shown by Wang et. al, however the gas flow rates were significantly different between the two studies. In ref¹¹ 1.3 L min⁻¹ He was admixed with 0.7 L min⁻¹ Ar in front of the torch of the ICP. The experiment in this study was performed using 0.21 L min⁻¹ He admixed with 1 L min⁻¹ or 1.05 L min⁻¹ Ar in case of 266 nm and 193 nm experiments, respectively. The high gas flow rates may shift the zones (preheating zone, initial radiation zone, normal analytical zone²⁰¹) slightly closer to the sampler cone, thus the sampling depth may be slightly reduced. The higher gas flow rate in the center of the ICP might lead to a higher velocity of ions and shorter residence time, especially if small sampling depth is used.

Under these operating conditions in the present study, severe ion diffusion in the presence of helium was not measured, which suggests that a minor contribution of helium in the total carrier gas entering the ICP does not induce more severe diffusion of ions than observed in Ar only within the ICP.

4.5.2 Studies on mass dependent ion intensity changes when exchanging He to Ar

In parallel to radial ion profile investigations, experiments to determine mass dependent ion intensity changes were carried out based on the exchange of helium to argon. By maintaining the high transport efficiency provided by helium, ion signals may be enhanced when Ar only is present in the ICP if diffusion is reduced.

The operating conditions of the ICP-MS and laser system applied in this study are summarized in Table 14. The difference in operating conditions of the ICP-MS when using different gas combinations (Ar only in the ICP or He admixed with Ar in the ICP) is indicated by the influence of the Ar nebulizer gas flow rate on sensitivity. The obtained data on background corrected count rates integrated for 70 s single hole drilling ablations carried out using different Ar nebulizer gas flow rates in the range of 0.7-1.3 L min⁻¹ were plotted to visualize the results. The influence of the nebulizer gas flow on sensitivity is shown in Figure 52.

Table 14 Operating conditions for laser ablation, ICP-MS and GED

Laser ablation		
Laser ablation system	GeoLas Q, ArF excimer	
Wavelength	193 nm	
Pulse duration	15 ns	
Ablation frequency	10 Hz	
Spot size	60 μm	
Laser fluence	22.5 J cm ⁻²	
Ablation time	70 s	
Ablation mode	single hole drilling	
Sample	NIST 610	
ICP-MS		
Instrument	PE Sciex ELAN 6100 DRC+	
Auxiliary gas flow	0.8 L min ⁻¹	
Plasma gas flow	17.5 L min ⁻¹	
RF power	1380 W	
Lens setting	autolens calibrated	
Detector mode	dual (pulse counting and analogue mode)	
Dwell time	10 ms	
Scan mode	peak hopping	
Gas mode	Ablation cell gas	Sample gas out (GED)
He without GED	He, 0.25 L min ⁻¹	-
Ar without GED	Ar, 0.25 L min ⁻¹	-
He through GED	He, 0.28 L min ⁻¹	He, 0.25 L min ⁻¹
He exchange to Ar	He, 0.63 L min ⁻¹	Ar, 0.21 L min ⁻¹
Air exchange to Ar	compressed air, 0.25 L min ⁻¹	Ar, 0.21 L min ⁻¹

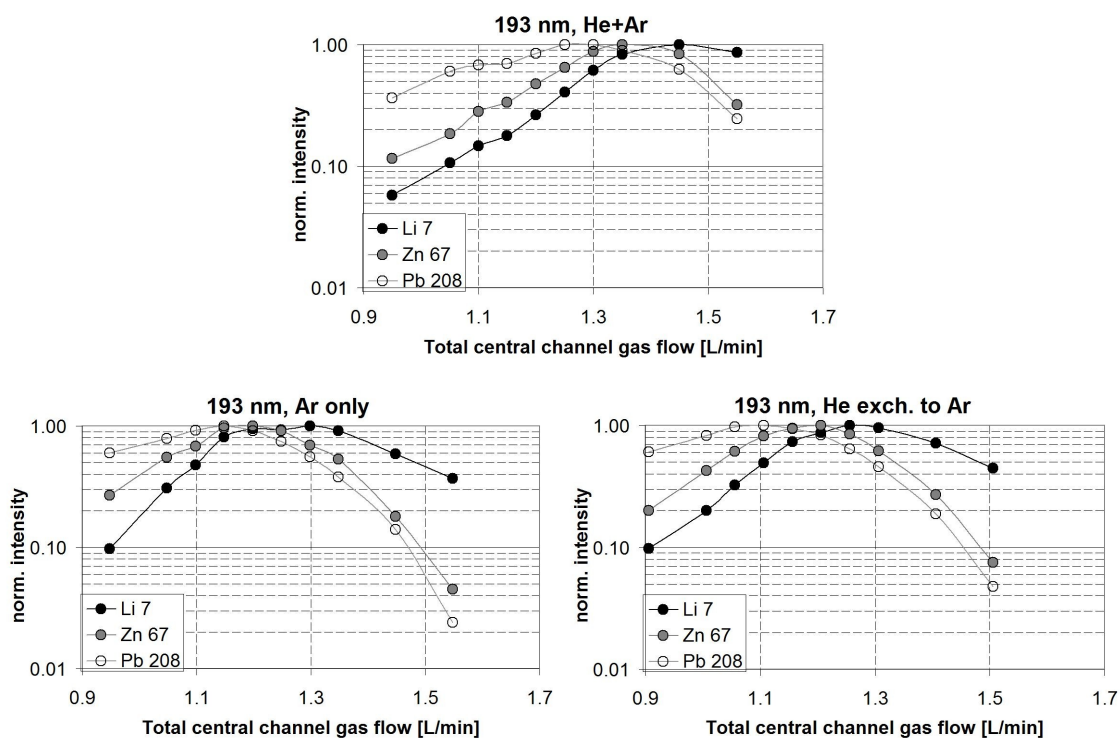


Figure 52 Signal intensity of Li, Zn and Pb in dependence on the total central channel gas flow rate entering the ICP. Laser ablation sampling was carried out at a wavelength of 193 nm using He (top and bottom right) or Ar (bottom left) as aerosol carrier gas and represent ion diffusion profiles for He admixed with Ar (top) and Ar only (bottom left and right) within the ICP.

Efficient exchange of helium by Ar is indicated by the closely identical sensitivity vs. central channel gas flow rate patterns to that observed when using Ar as aerosol carrier gas. While the patterns are very similar for gas combinations supplying Ar only into the ICP, they become significantly different when introducing He also into the plasma. Data on U^+/Th^+ intensity ratio, oxide formation and a list of elements showing maximum sensitivity at individual nebulizer gas flow rates are summarized in Table 15. While adding more Ar merged with the aerosol carrier gas into the central channel of the ICP, the ion sensitivities are reaching a maximum at different flow rates. This difference is in relation with the gas temperature (higher gas flow provides lower temperature), sampling depth (higher gas flow provides reduced sampling depth), residence time (higher gas flow increases velocity and decreases residence time), melting point and the 1st ionization potential of the elements contained in the particles. It is clearly visible that higher nebulizer gas flow rates ($>1.0 \text{ L min}^{-1} \text{ Ar}$) correspond to increasing U^+/Th^+ ratios. U and Th represent high 1st IP elements with relatively high melting points and are monitored to provide information on vaporization, atomization and ionization driven changes within the ICP²⁰². Moreover, since

higher gas flows contribute to lower gas temperature, the oxide formation also increases. While these changes are highly undesired, it is remarkable that certain elements such as Li, Be, B have intensity maximum at these highly ‘over tuned’ conditions (1.2 – 1.3 L min⁻¹ Ar when using He as carrier gas). The higher gas flow rate needed for maximum sensitivity for these light elements can be explained by the reduced ion diffusion when the sampling depth is decreased. However, the high melting point and high ionization potential of Be and B would suggest a later zone within the plasma providing the highest sensitivity. The presence of helium within the central channel of the plasma contributes to better heat conductivity and this shifts the region of the greatest ionization on a tangential axis within the ICP.

Table 15 U⁺/Th⁺ intensity ratio, oxide formation and a list of elements showing maximum sensitivity obtained for individual nebulizer gas flow rates when introducing He admixed with Ar (‘He, no GED’) or Ar only (‘He exchange to Ar’) into the ICP

Nebulizer gas flow	0.7	0.8	0.85	0.9	0.95	1.0	1.05	1.1	1.2	1.3
He, no GED (He = 0.25 L/min)										
Total gas flow	0.95	1.05	1.10	1.15	1.20	1.25	1.3	1.35	1.45	1.55
U ⁺ /Th ⁺	1.1	1.1	1.1	1.1	1.2	1.3	1.4	1.6	2.0	2.4
ThO ⁺ /Th ⁺	0.1 %	0.1 %	0.1 %	0.1 %	0.1 %	0.2 %	0.3 %	0.5 %	1.0 %	3.6 %
	-	-	Au	-	-	Y, Zr, Ba, La, Cr, Pr, Tb, Ho, Tm, Lu, Ta, W, Tl, Pb, Th, U	Ca, Ti, Cr, Mn, Fe, Co, Ni, Cu, Rb, Sr, Mo, Sn, Cs, Bi	Na, Mg, Al, Si, V, Zn, Ga, As, Ag, Cd, Sb	Li, Be, P	B
He exchange to Ar (Ar = 0.21 L/min)										
Total gas flow	0.91	1.01	1.06	1.11	1.16	1.21	1.26	1.31	1.41	1.51
U ⁺ /Th ⁺	1.1	1.2	1.3	1.4	1.5	1.6	1.7	1.7	1.9	2.1
ThO ⁺ /Th ⁺	0.1 %	0.1 %	0.2 %	0.3 %	0.3 %	0.3 %	0.4 %	0.6 %	0.6 %	1.0 %
	-	Au	Y, Zr, Ba, La, Ce, Pr, Tb, Ho, Tm, Lu, Ta, W, Th	Ca, Ti, Fe, Co, Ni, Cu, Sr, Mo, Sn, Cs, Tl, Pb, Bi, U	Al, V, Cr, Mn, Ga, Rb, Ag, Cd, Sb	Mg, Si, Zn, As	Li, Be, Na, P	B	-	-

To overcome the sensitivity differences caused by altered operating conditions of the ICP when different gas combinations are used, data on sensitivity for optimum conditions and individual element sensitivity maxima were compared. The background corrected count rates of transient signals obtained at each nebulizer gas flow setting were abundance normalized and the sensitivity [cps/ppm] was calculated for every element taking the certified element concentration in NIST 610¹⁹⁶ into account. The nebulizer gas flow selected for the ‘*optimum conditions*’ provided the highest sensitivity for most of the elements

measured and an oxide formation of less than 0.5 % based on ThO^+/Th^+ (e.g. neb. gas flow: 1.0 L min^{-1} in case of 'He, no GED'; and neb. gas flow: 0.9 L min^{-1} in case of 'He exchange to Ar', Table 15). The '*maximum sensitivity*' of each individual element was selected from the entire measurement. In the figures the ratio of both the data obtained at 'optimum conditions' and the 'maximum sensitivities' are compared.

Results on the influence of exchanging helium to argon

The influence of exchanging helium to argon would theoretically lead to excitation conditions not influenced by gases other than Ar within the ICP, while maintaining the high aerosol transport efficiency provided by He from the ablation cell. Diminishing the influence of helium on ICP conditions by exchanging He to Ar should lead to enhanced sensitivity if ion diffusion is reduced¹¹. In this case, the enhancement would show mass dependence. However, the investigated radial ion profiles within this study do not indicate severe diffusion in case of a minor contribution of helium in the central channel gas flow of the ICP (Chapter 4.5.1).

By mapping the ICP-MS sensitivity response as a function of nebulizer gas flow rate the attainable sensitivity provided by different gas combinations was compared. The obtained sensitivity for optimized ICP operating conditions and the individual element sensitivity maxima are compared in Figure 53. The sensitivity response curves are typical with indications on diffusion and space charge effects (higher sensitivity for heavier masses due to better transmission of heavier ions through the cones and ion optics), and degree of ionization (high 1st ionization potential for Be, B, P, As, Au) and vaporization (Y, La, Ta) related differences of elements. Since the optimum conditions generally do not provide maximum sensitivity for light elements (Li, Be, B) as shown in Table 15, the plot with individual element sensitivity maxima indicates significantly higher sensitivity for these elements. Moreover, the optimum ICP conditions indicate enhanced sensitivity for B, P, Zn, As when exchanging He to Ar. An example for the comparison of the sensitivity obtained for B and As at optimum conditions and their maximum sensitivity attainable is shown in Table 16. The results indicate that if helium is not present in the ICP, the region of the greatest ionization is shifted on a tangential axis caused by the applied nebulizer gas flow rates. Nevertheless, since in both cases He was used as ablation gas atmosphere, the particle sizes remain unchanged, therefore the vaporization of particles are kept very similar and complete. Hence, the maximum sensitivities obtained are not significantly different (within 10 %). The ratio of the sensitivities (Figure 54) clearly indicates the differences in the highest sensitivity zone shifts for various elements. The obtainable sensitivity when exchanging helium to argon is approximately 20 % lower for most elements in contrast to the aerosol directly introduced into the ICP in He. The loss in

sensitivity may be caused by aerosol loss within the GED and by altered ICP operating conditions (gas temperature).

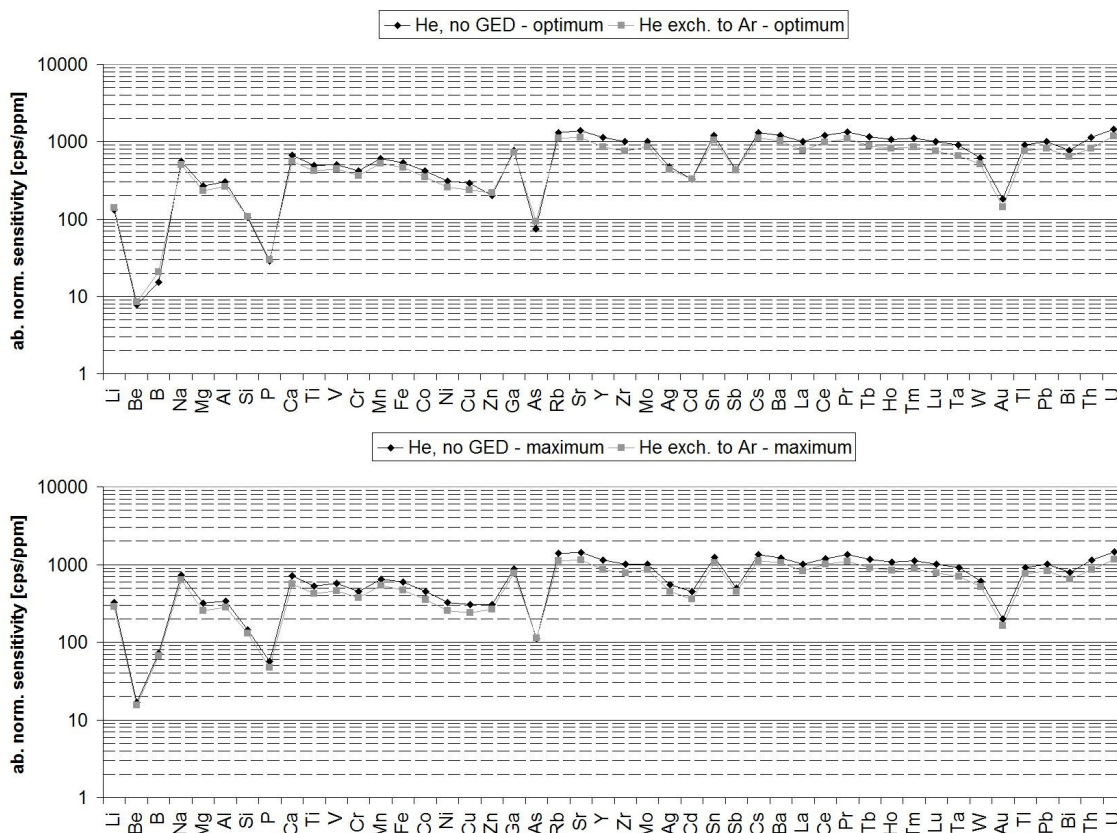


Figure 53 Comparison of element sensitivities for optimum ICP operating conditions and individual element sensitivity maxima obtained when introducing the aerosol in helium into the ICP versus exchanging helium to argon.

Table 16 Comparison of B and As sensitivities for He and He exchange to Ar experiments based on the conditions shown in Table 15

	Boron		Arsenic	
	Optimum ICP conditions	Maximum sensitivity	Optimum ICP conditions	Maximum sensitivity
He, no GED				
Sensitivity [cps/ppm]	15.1	72.8	74.2	111.4
Neb. gas flow rate [L/min]	1.0	1.3	1.0	1.1
U ⁺ /Th ⁺	1.3	2.4	1.3	1.6
ThO ⁺ /Th ⁺	0.2 %	3.6 %	0.2 %	0.5 %
He exchange to Ar				
Sensitivity [cps/ppm]	20.6	66.0	92.5	113.7
Neb. gas flow rate [L/min]	0.9	1.1	0.9	1.0
U ⁺ /Th ⁺	1.4	1.7	1.4	1.6
ThO ⁺ /Th ⁺	0.3 %	0.6 %	0.3 %	0.3 %
Difference	↑ 36 %	↓ 9 %	↑ 25 %	↑ 2 %

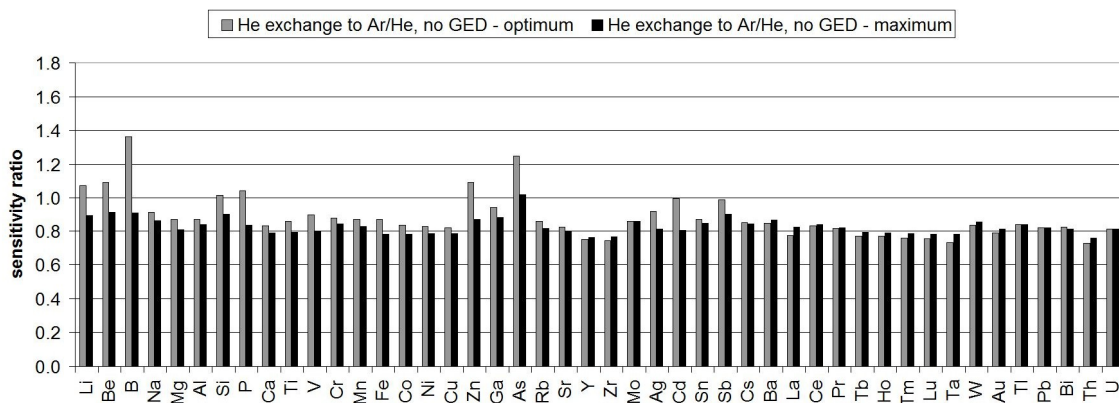


Figure 54 Comparison of sensitivity ratios obtained when exchanging helium to argon in contrast when the aerosol is directly introduced into the ICP in helium.

Results indicating aerosol loss within the gas exchange device

During experiments, a loss of aerosol within the GED was observed based on the recorded signal intensities by the ICP-MS when introducing the aerosol into the gas exchanger. The extent of aerosol loss was investigated by passing the aerosol in helium through the GED (without exchanging it to Ar) in comparison to transporting the aerosol in He directly into the ICP-MS from the ablation cell. In the case when helium is introduced into the GED, without turning the sweep gas on, a temporal loss of He gas flow is observed, which is caused by migration of helium through the membrane. This process is slowing down until the whole gas converter cell is filled by helium. After several minutes, the loss of helium gas flow rate is greatly reduced (approximately 0.28 L min⁻¹ He inlet gas flow rate vs. 0.25 L min⁻¹ He outlet gas flow rate; Table 14). The obtained differences in sensitivity with or without passing the aerosol through the gas exchanger are indicated in Figure 55. The figure indicates that severe differences in sensitivity when comparing optimum operating conditions with maximum sensitivity are not found, since in both cases the aerosol is introduced in helium into the ICP. However, the sensitivity obtained when passing the aerosol through the gas exchanger is generally lower by 20 % in contrast when the generated aerosol is directly introduced into the ICP-MS. This reduction in sensitivity may only be related to aerosol loss by 20 % within the GED.

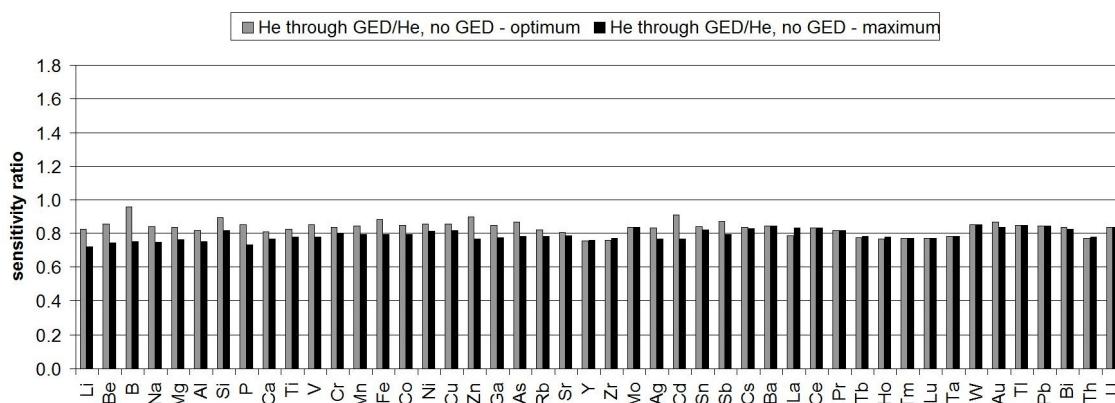


Figure 55 Comparison of sensitivity ratios obtained when passing the aerosol in helium through the GED in contrast when the aerosol is directly introduced into the ICP. The ratios indicate an approximately 20 % loss of aerosol within the GED.

Comparing the influence of helium exchange to argon to transporting the aerosol in He through the GED

To overcome the loss of aerosol when introducing the aerosol into the GED (Figure 55), another comparison was made (Figure 56). In this case a mass dependent trend in sensitivity can be observed, namely approximately 20 % higher sensitivity for low mass elements (e.g. Li, Be, B etc.) in contrast to heavy elements (e.g. Pb, Bi, U, etc.). This might indicate reduced ion diffusion when He is not present in the ICP, however this observation is highly suffering from non-reproducibility. Moreover, certain elements, such as P, Zn, Ga, As, Sb were found to be outliers from the trend as it was also observed in Figure 54 and are influenced by the altered ICP conditions.

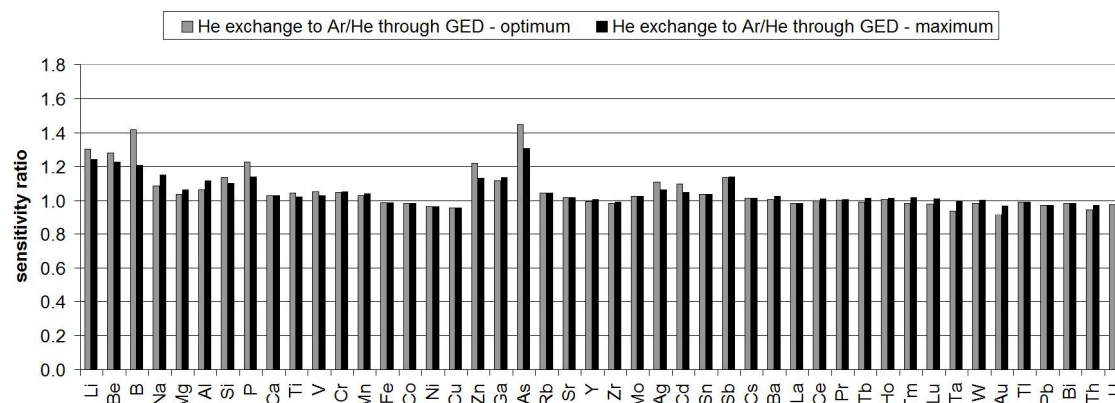


Figure 56 Comparison of sensitivity ratios obtained when exchanging helium to argon in contrast when the aerosol is passed through the GED in helium without gas exchange.

4.6 Application of GED to remove gas impurities from the transport system

As demonstrated in Chapter 2, gas impurities entering the carrier gas from the transport system may have significant influence on plasma conditions. The gas impurities entering the ICP were a function of tube material and length (i.e. surface area in contact with the gas). To demonstrate that the gas exchange device is capable to maintain stable ICP conditions by removing gas impurities and water vapor from the carrier gas, moreover to confirm that the observed sensitivity changes were caused by gas impurities, gas exchange experiments were performed to verify these processes. Nylon tubes (SMC, i.d. 4 mm) in a length of 1 and 10 m were connected to the transport system upstream of the ablation cell. The same experimental setup as shown in Figure 16 was used and the gas exchange device was connected between the ablation cell and the ICP-MS only in the case when the carrier gas was exchanged. All other tubes in the entire setup consisted of high purity Tygon tubing (Tygon 2275). Constant He gas flow rate (0.63 L/min) through the nylon tubes and the ablation cell was maintained during the entire experiment. The ICP conditions were optimized before both experiments (Table 17).

Table 17 Operating conditions for laser ablation, ICP-MS and GED

Laser ablation				
Laser ablation system	GeoLas Q, ArF excimer			
Wavelength	193 nm			
Pulse duration	15 ns			
Ablation frequency	10 Hz			
Spot size	60 μm			
Laser fluence	20 J cm^{-2}			
Ablation time	70 s			
Ablation mode	single hole drilling			
Sample	NIST 610			
ICP-MS				
Instrument	PE Sciex ELAN 6100 DRC+			
Auxiliary gas flow	0.8 L min^{-1}			
Plasma gas flow	17.5 L min^{-1}			
RF power	1380 W			
Lens setting	autolens calibrated			
Detector mode	dual (pulse counting and analogue mode)			
Dwell time	10 ms			
Scan mode	peak hopping			
Gas mode	Tubes upstream of ablation cell	Ablation cell gas	Sample gas out (GED)	ICP neb. gas flow
He without GED	Nylon (SMC) 1 m or 10 m long	He, 0.63 L min^{-1}	GED not connected	Ar, 0.9 L min^{-1}
He exchange to Ar	Nylon (SMC) 1 m or 10 m long	He, 0.63 L min^{-1}	Ar, 0.21 L min^{-1}	Ar, 1.0 L min^{-1}

Gas impurities significantly affect ICP operating conditions by enhancing sensitivity, altering intensity ratios, changing oxide formation and causing increased background count rates by polyatomic ion formation¹⁷⁶. These changes were more significant when using longer tubes. Figure 57 indicates intensity enhancement when directly introducing He into the ICP-MS passing through the 10 m long nylon tube in contrast to 1 m. Intensity enhancement factors and element dependence was found to be very similar to changes observed in Figure 17 caused by the PVC tubes. Furthermore, Figure 57 demonstrates that by removing the impurities from the gas stream by gas exchange, stable ICP operating conditions and constant oxide formation can be obtained.

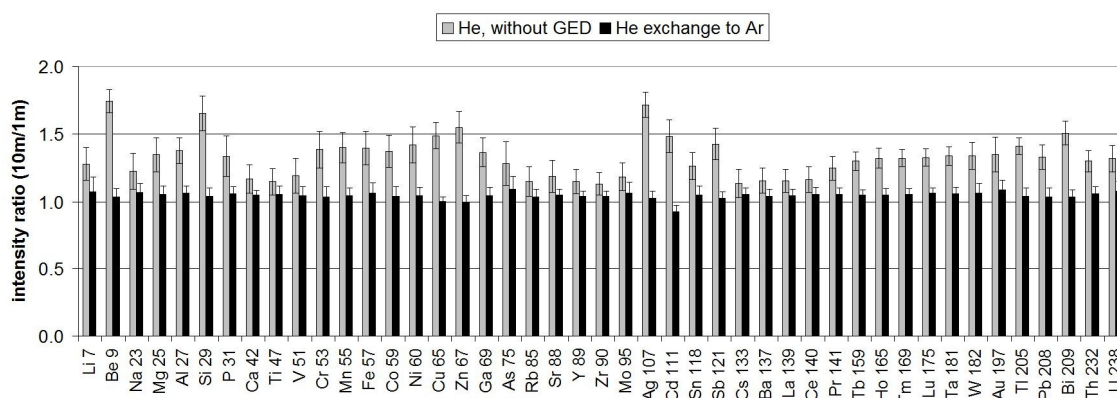


Figure 57 Intensity ratios observed using 10 m and 1 m long nylon tubes connected upstream of the ablation cell. The results indicate that gas impurities from the nylon tube material causing significant intensity enhancement in the ICP-MS. By removing these impurities by the gas exchange process, ICP operating conditions become stable. Uncertainty is expressed as \pm standard deviation. Oxide formation based on ThO^+/Th^+ without gas exchange: 0.27 % (1 m nylon tube), 1.27 % (10 m nylon tube), with gas exchange: 0.24 % (1 m nylon tube), 0.25 % (10 m nylon tube).

The comparison of the background count rates obtained for various gas conditions is shown in Figure 58. Analytes indicated in the figures are affected by polyatomic ion formation within the plasma. The higher background count rates are clearly visible when changing between 1 m and 10 m long nylon tube without using the gas exchanger. In case of gas exchange, significant differences in polyatomic ion formation are not observed confirming that the undesired impurities from the tubes are removed and not entering the ICP. Some of the potential hydrogen and oxygen based polyatomic interferences influencing several m/z are summarized in Table 18.

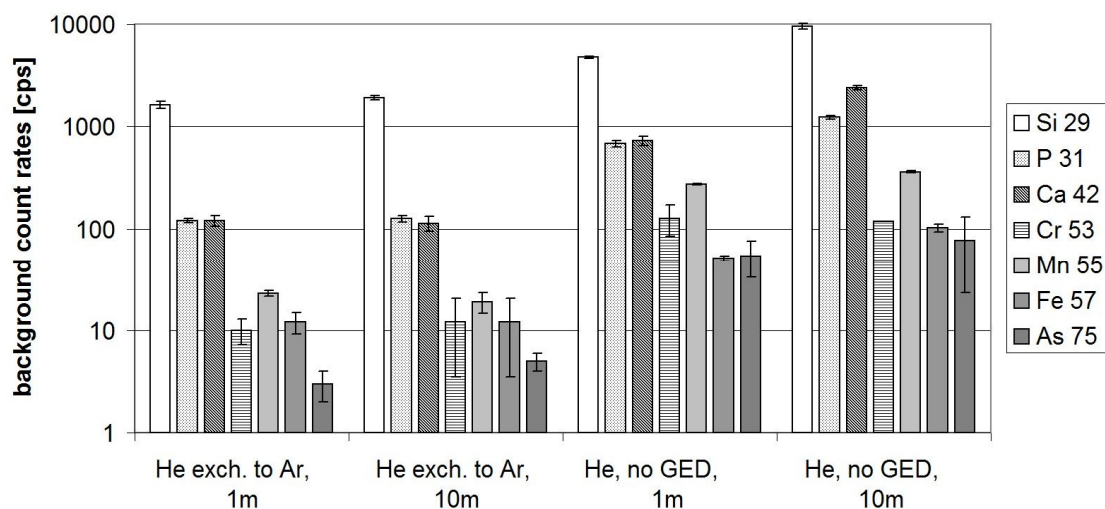


Figure 58 The obtained background count rates do not indicate severe differences when the gas impurities are removed from the gas stream by the GED. In contrast, impurities from the longer nylon tube (10 m) entering the ICP are causing higher background count rates.

Table 18 Potential hydrogen and oxygen based polyatomic interferences on m/z 29, 31, 42, 53, 55, 57, 75

m/z	Potential polyatomic interferences
29	$^{13}\text{C}^{16}\text{O}$, $^{12}\text{C}^{17}\text{O}$, $^{12}\text{C}^{16}\text{O}^1\text{H}$, $^{14}\text{N}_2^1\text{H}$
31	$^{15}\text{N}^{16}\text{O}$, $^{14}\text{N}^{17}\text{O}$, $^{14}\text{N}^{16}\text{O}^1\text{H}$, $^{12}\text{C}^{18}\text{O}^1\text{H}$, $^{15}\text{N}_2^1\text{H}$
42	$^{40}\text{Ar}^1\text{H}_2$,
53	$^{13}\text{C}^{40}\text{Ar}$, $^{36}\text{Ar}^{16}\text{O}^1\text{H}$
55	$^{38}\text{Ar}^{16}\text{O}^1\text{H}$
57	$^{40}\text{Ar}^{17}\text{O}$, $^{40}\text{Ar}^{16}\text{O}^1\text{H}$
75	$^{38}\text{Ar}^{36}\text{Ar}^1\text{H}$, $^{40}\text{Ar}^{17}\text{O}^{18}\text{O}$, $^{40}\text{Ar}^{17}\text{O}_2^1\text{H}$

4.7 Direct liquid ablation in ambient air using aerosol suction

The aerosol suction approach¹⁸⁹ was also tested on liquid samples. In this case, as demonstrated in Chapter 3.3.3, a micro-diaphragm pump drags the air and the laser generated aerosol into the tube inlet, which is placed relatively close to the laser spot. The pump carries the aerosol together with the gas into the gas exchanger and further into the ICP. Direct liquid ablation has been reported as an alternative calibration strategy for laser aerosols¹⁷⁴. It was demonstrated that laser generated aerosols from diluted standard stock solutions using a 20 μm laser spot size can provide detection limits as low as 0.1 ng/g, moreover matrix and fractionation effects are greatly reduced. These experiments were carried out using an ArF excimer laser operating at a wavelength of 193 nm¹⁷⁴.

In the current study, direct liquid ablation was also tested for the aerosol suction approach using a Ti-sapphire femtosecond laser ablation system (Legend, Coherent Inc., Santa Clara, CA, USA) operating at its fundamental wavelength of approximately 800 nm providing a pulse duration of less than 150 fs. The absorption coefficient of water (approximately 0.03 cm^{-1}) at this NIR wavelength is similar to that of the deep UV used in ref¹⁷⁴. Nevertheless, the femtosecond laser system provides a freely adjustable frequency in the range of 1-1000 Hz, which is a great advantage over the ArF excimer laser systems to increase the mass transport to the ICP-MS.

Obtained sensitivity and limits of detection as a function of ablation frequency

For the experiment a standard solution was prepared from various stock solutions. The stock solutions of ICP multi-element standard solution (Merck IV) and single element standard solutions (Merck and CPI International) were mixed and diluted to a nominal concentration of 5 mg/L using 1 % HNO_3 . In total 30 elements were included in the prepared solution, covering the entire mass range from m/z 7 – 238. Moreover, a 1 % HNO_3 blank solution was also prepared.

Limitations in the arrangement of the experimental setup

Since the ablation events caused severe sputtering of tiny liquid droplets containing dissolved elements and acid and may have caused damage and contamination of the focusing lens and the high reflection mirror, thus these components needed to be protected. For this purpose an ablation cell top was placed under the optical components. The liquid samples were filled in 100 μL Teflon beakers. The tube inlet was placed within a range of

maximum 3-4 mm from the liquid sample surface at an angle of 90°. The focal length of the laser and the applied cell top did not allow any further optimization of the angle of the tube inlet. Moreover, during laser ablation, sputtering droplets made the cell window wet, which might contribute to reduced transmission of laser energy onto the liquid surface. The solution surface was left open and was not covered. Covering of the liquid surface with a thin layer of plastic film (Parafilm)¹⁷⁴ caused instable signals. The tube inlet in the present experiment was a relatively small diameter PTFE tubing with an i.d. of 2 mm. Laboratory ambient air (continuously dust filtered by a high performance laminar flow box) had free access to the liquid samples and was used as aerosol carrier gas. The operating voltage of the diaphragm-pump was set to provide an air flow rate of 0.25 L min⁻¹, which was exchanged to argon within the gas exchanger.

Figure 59 shows typical transient signal structures acquired as a function of ablation frequency. A repetition rate of 50 Hz and 100 Hz provided stable signals, while frequencies of less than 50 Hz contributed to high relative uncertainty in the transient signals and frequencies of higher than 100 Hz generated a 'brute-force' ablation, causing well defined droplet formation on top of the liquid surface. Moreover, extreme droplet sputtering and strong vibration of the liquid within the container was observed. As a function of repetition rate, the obtained sensitivity and detection limits were plotted and are shown in Figure 60 and Figure 61, respectively.

The calculated limits of detection are based on the standard deviation of the blank solution (1% HNO₃) ablated, the determined sensitivity (Figure 60), and the number of data points included in the integration interval of the background (blank solution) and the signal (multi-element solution)¹⁸⁴. As Figure 61 indicates, all elements measured showed detection limits of less than 1 µg/g when using a laser repetition rate of 10 Hz only, except boron (below limits of detection). Detection limits for an ablation frequency between 200 Hz and 1 kHz are not dramatically different for the elements measured. The lowest detection limits for m/z > 115 for extreme ablation conditions (1 kHz) were lower than 1 ng/g.

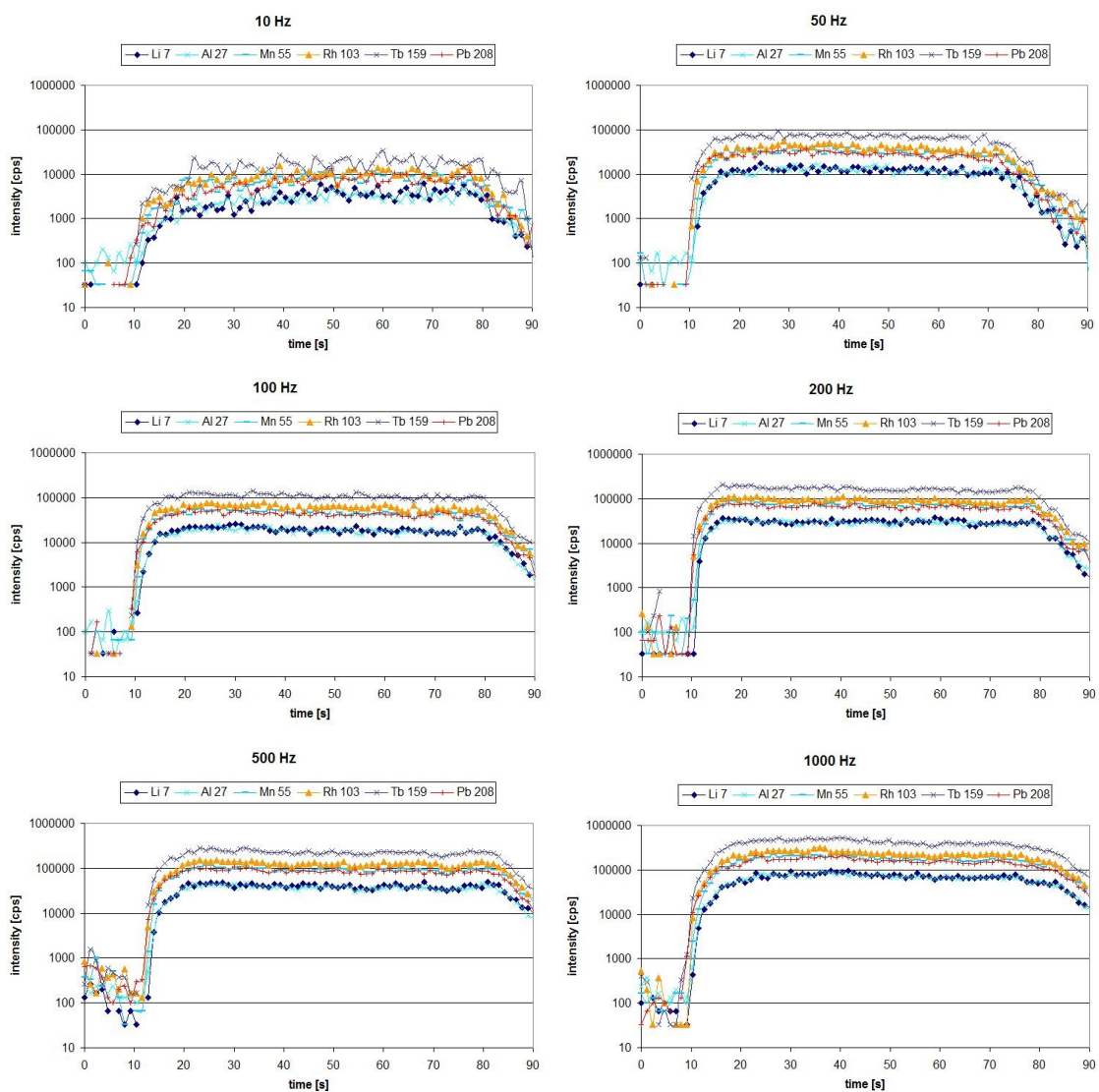


Figure 59 Transient signal structures obtained for direct liquid ablation in air and aerosol suction of a multi-element solution containing various elements at a nominal concentration of 5 mg/L. NIR-fs-LA was carried out with a spot size of approximately 100 μm , 1 mJ pulse energy, providing an energy density of 12.7 J/cm² and a power density of approximately 85 GW/cm². The ICP-MS dwell time was set to 30 ms to minimize the transient fluctuations of the signals generated by the diaphragm pump.

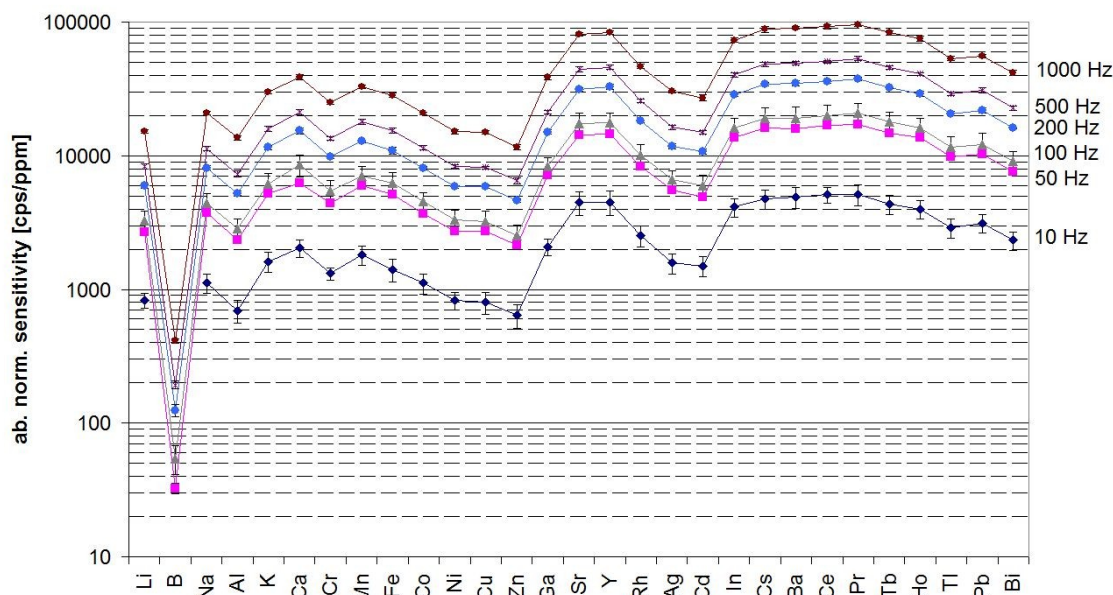


Figure 60 Abundance normalized sensitivity as a function of ablation frequency obtained for direct liquid ablation of a multi-element solution containing various elements at a nominal concentration of 5 mg/L. Measurement uncertainty is expressed as \pm standard deviation (n=3).

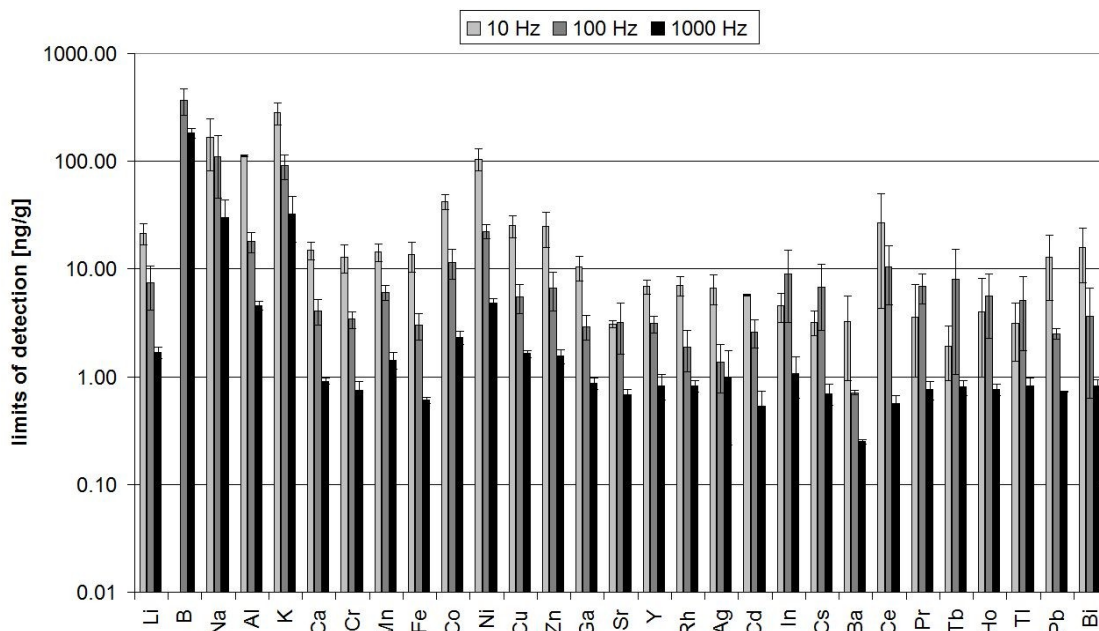


Figure 61 Limits of detection (ng/g) as a function of ablation frequency obtained for direct liquid ablation of a multi-element solution containing various elements at a nominal concentration of 5 mg/L. Measurement uncertainty is expressed as \pm one standard deviation (n=3).

Influence of a matrix load of up to 900 µg/g Na on element concentrations of 5 µg/g

Four multi-element solutions were prepared, such as described in the previous section containing various elements at a nominal concentration of 5 µg/g diluted by 1 % HNO₃. Single element solution of Na (NaNO₃) was added to the multi-element solutions as matrix and diluted from 1000 mg/L to 250 mg/L, 500 mg/L, 900 mg/L respectively in the solutions “B2”, “B3” and “B4”. The solution “B1” contained Na at 5 mg/L only and was treated as matrix free solution. Laser ablation events were carried out in spot ablation mode with an ablation frequency of 50 Hz. The dependence of the calculated element concentrations on Na concentration is summarized in Figure 62.

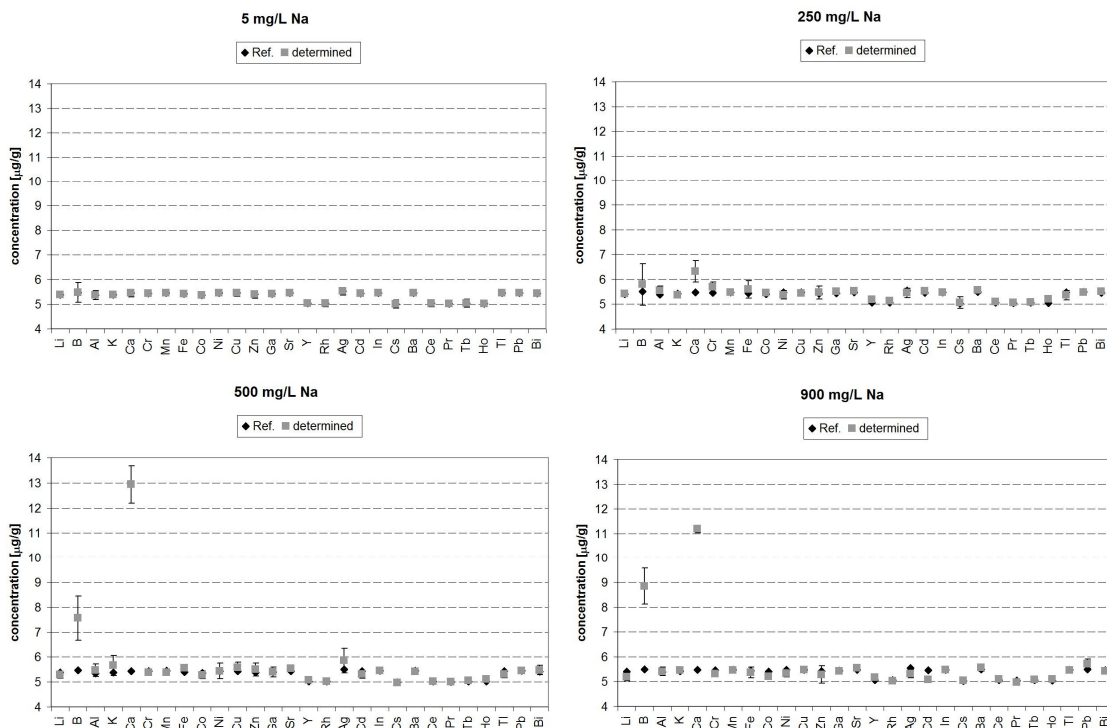


Figure 62 Calculated element concentrations using solution “B1” as external standard and ¹¹⁵In as internal standard. Measurement uncertainty is expressed as ± standard deviation (n=3).

Na matrix load of up to 900 mg/L (up to a factor of approximately 180 times higher concentration, than the analyte concentration) did not influence most element concentrations significantly. Differences were obtained for boron and calcium. Boron might be influenced by a doubly charged ion formation of Na⁺, however the 2nd ionization potential of Na is a factor of 1.5 higher than the 1st ionization potential of Ar. Therefore, this is

unlikely to be the cause of the difference. Potential polyatomic ion formation on m/z 11 is currently unknown. However, both boron (^{11}B) and calcium (^{42}Ca) might be influenced by the relatively low count rates acquired during signal acquisition owing to low sensitivity obtained for boron (32.6 ± 2.9 cps/ppm) and the low abundance of ^{42}Ca significantly influenced by a minor contribution of polyatomic ion formation (e.g. $^{23}\text{Na}^{18}\text{O}^1\text{H}$). In case of the solution 'B4' Cd was underestimated by 7 %.

Efficient gas exchange was monitored based on background count rates caused by polyatomic ion formation of the components of the solvent and on the oxide formation during ablation. Oxide formation based on $^{140}\text{Ce}^{16}\text{O}^+ / ^{140}\text{Ce}$ was measured to be 0.15 ± 0.1 %, which is more than an order of magnitude lower than typically measured for solution nebulization.

4.8 Conclusion

This chapter summarized the results of various experiments to study fundamental processes when performing online gas exchange. Ablation in air using the applied experimental conditions provided less pronounced temporal elemental fractionation over an extended ablation period. Moreover, the particle size fractions generated were more constant over time than in He. Optical particle counting experiments based on laser light scattering and scanning electron microscopy studies did not indicate severe changes in the aerosol structure and particle sizes generated by 193 nm LA when the aerosol was passed through the gas exchanger. In general, the structure of aerosols was different for the ablation in He, Ar and air. In He and Ar similar agglomerates with cotton-like structures were found, while in air the particle formation processes provided smaller structures and shorter fragments. Particle counting experiments indicated that the aerosols formed are consisting of 99 % (He), 87 % (Ar) and 92 % (air) of particles smaller than 150 nm for the ablation of NIST 610 using 193 nm. This suggests that the vaporization of particles within the ICP is most complete when ablating in He, while the fraction of large particles was the highest in case of the ablation in Ar. Since the gas exchange device allows the introduction of Ar at a constant purity into the ICP-MS, the plasma operating conditions are more constant and less influenced by gas impurities contaminating the carrier gas flow in dependence on the tube materials. In terms of ablation, humidity of air was found to play an important role for the determination of boron, while more than 40 other elements were not affected. The presence of water vapor within the ablation cell might contribute to the

formation of boron-hydrides, which are expected to be converted to boron-oxide. This process has been found to be different in case of samples containing boron at highly different concentrations. Furthermore, the early zone of the ICP providing the highest intensity for boron is partially inconsistent with the boiling point and ionization energy of elemental boron, which would suggest a later decomposition of boron in the plasma. Most likely, boron is vaporized as boron-oxide, which has a lower boiling point than elemental boron and showing the highest sensitivity at an early zone within the ICP, where diffusion is less pronounced. Radial ion profiles obtained in this study showed no influence of helium on ion spread within the ICP, which finding is inconsistent with data published in the literature. However, in these experiments the contribution of helium within the total gas flow entering the injector of the ICP was significantly lower and the comparison of the influence of various gases was limited by the relatively low outlet flow rate of the gas exchange device used.

The developed novel sampling approach utilizing ambient air for laser ablation and aerosol suction followed by gas exchange offers a viable alternative to analyze various solid and liquid samples using LA-ICP-MS without the need of an ablation cell and it opens numerous applications, which will be discussed in the following chapter.

5. Trace analysis of gold using new calibration materials

The content of this chapter was partially published in

J. Anal. At. Spectrom., 2009, ref.¹⁹⁴

Authors: R. Kovacs, S. Schlosser, S. P. Staub, A. Schmiderer, E. Pernicka and D. Günther

Characterization of calibration materials for trace element analysis and fingerprint studies of gold using LA-ICP-MS

and in

New technologies for Archaeology: Multidisciplinary investigations in Palpa and Nasca, Peru, Springer Verlag, 2009, ref.²⁰³

Authors: S. Schlosser, R. Kovacs, E. Pernicka, D. Günther, M. Tellenbach

Fingerprints in gold (*This work consists of equal contributions of the first and second author*)

5.1 Introduction

Laser ablation-inductively coupled plasma-mass spectrometry (LA-ICP-MS) is an attractive analytical technique for the determination of major, minor and trace elements in solid samples⁶³. The main advantages of LA-ICP-MS are high spatial resolution, reduced sample preparation time, low sample consumption, high sensitivity, low limits of detection, wide linear dynamic range, and elemental and isotopic information⁷². Wide range of applications give evidence of its potential, and studies from geology, biology, and environmental and material sciences are currently the dominating applications^{72,94}. Besides the multi-elemental analysis of bulk materials, one of the growing applications is fingerprinting, e.g. in gemstones⁷¹, gold²⁰⁴, cannabis crops²⁰⁵ and forensic objects²⁰⁶. A qualitative method performed on gold using LA-ICP-MS has been first reported by Watling and has been solely based on the relative intensities of a number of elements, which were used for provenance identification of gold samples²⁰⁴. Since that initial work, a number of studies using trace element fingerprinting for gold provenance have been reported^{207,208,209,210,211}. It is essential that the analytical method used for provenance investigations or for authenticity verifications of precious artifacts must be quasi non-destructive or require very small

amounts of sample. This requirement is fulfilled by laser ablation-ICP-MS^{71,212,213}. However, a major limitation of LA-ICP-MS is commonly attributed to the lack of suitable reference materials with similar matrix composition to the sample, which makes the quantitative analysis difficult and partially explains the qualitative approach reported in the literature. For gold analysis using laser ablation, six solid gold-matrix based reference materials exist from NIST (CRM FAU6-11). These contain up to 16 trace elements in the concentration range between 1 and 100 mg kg⁻¹. These elements are As, Bi, Cr, Cu, Fe, Mg, Mn, Ni, Pb, Pd, (Pt and Si occasionally), Sn, Ti, Zn and Ag. However, Ag may occur more than three orders of magnitude higher in concentration in various gold objects. Unfortunately, none of these reference materials are commercially available anymore. Furthermore, the list of elements does not cover the entire range of elements of interest for provenance studies of gold artifacts. The elements, which are also of major interest in gold fingerprint studies include Cd, Ir, Os, Rh, Ru, Sb, Se, Te, and W. The six platinum group elements can be applied as a useful tool to distinguish between different gold types of archaeological objects, since these cannot be affected by contamination during burial. For authenticity verifications a major role can be attributed to Cd, because this can be used as an indicator for modern gold types. Therefore, calibration materials, which provide access also for these elements would be required for the analysis of gold artifacts.

To overcome some of the limitations caused by the lack of appropriate solid reference materials, solution standards utilized for calibration have already attracted particular attention and have been widely applied in a number of analytical studies^{165,171,172,214}. The nebulized calibration solutions are commonly desolvated before entering the ICP in order to reduce oxide formation and the probability of polyatomic interferences^{16,17}. In contrast it has also been reported that the application of wet instead of desolvated aerosols improves accuracy for the analysis of silicate glass, polyethylene and metal alloys²¹⁵. Such comparison of solution calibration between wet and dry (desolvated aerosol) plasma conditions using fs-LA-ICP-MS has been recently reported²¹⁶. Solution calibration has also been applied in a study on trace element investigations in Celtic gold coins. However, it has been shown that a prepared multi-element solution with unstable element concentrations leads to inaccurate analysis²¹⁷.

This study contributes to an extensive archaeological provenance investigation on Pre-Columbian gold artifacts being carried out at CEZA, Mannheim. For trace element analysis and fingerprint studies of various gold objects using LA-ICP-MS, two solid gold samples were produced by Norddeutsche Affinerie AG, Hamburg, Germany (later on referred to as NA1 and NA2). These two samples provide access to more elements (Ti, Cr, Mn, Fe, Co, Ni, Cu, Zn, As, Se, Pd, Cd, Sn, Sb, Te, Pt, Pb, Bi) in a wide concentration range of up to 1200 mg kg⁻¹ and contain Ag as a major element (1 % and 5.4 % in NA1 and NA2 respectively).

These materials were thoroughly characterized with respect to element composition and distribution using LA-ICP-MS and finally applied as calibration materials for the analysis of gold artifacts. The analyses were carried out using solution calibration and matrix-matched solid calibration. The solution calibration was performed using three synthetic solutions to obtain a calibration curve. The calibration solutions were prepared taking the chemical compatibility of the elements into account. The solid calibration was accomplished using two NIST gold CRMs (FAU7 and FAU10). The results of the analyses carried out on the new calibration materials were furthermore compared to the element concentration values based on digestion and solution analysis by ICP-OES provided by the manufacturer.

5.2 Experimental

The measurements under ‘dry plasma conditions’ were performed using an ELAN 6100 DRC II quadrupole ICP-MS instrument (Perkin Elmer SCIEX, Thornhill, Canada). The solution calibration performed under ‘wet plasma conditions’ was carried out using a double focusing magnetic sector field ICP-MS instrument (Element2, Thermo Finnigan, Bremen, Germany) operated in high resolution mode to diminish the influence of potential polyatomic interferences caused by the solvent. The liquid aerosol produced by a self aspirating concentric PFA microflow nebulizer ($100 \mu\text{L min}^{-1}$) in combination with a cyclonic spray chamber was mixed with the laser generated aerosol transported in He in front of the injector of the ICP using a glass Y-piece. During the entire analysis a 1.5 % hydrochloric acid blank was nebulized into the plasma to maintain stable wet plasma conditions. Desolvation of the nebulized solutions in front of the injector of the ICP was also tested, however some elements (Sn, Sb, Te) were significantly affected by depletion during desolvation process. When operating the ICP-MS under ‘dry’ plasma conditions, the laser generated aerosol transported in helium was mixed with argon (nebulizer gas) with a glass mixing bulb in front of the injector. The laser sampling was carried out in single hole drilling mode using either a solid-state Nd:YAG nanosecond laser operating at 213 nm (LSX-213, CETAC Technologies, Omaha, NE, USA) or a Ti-sapphire-based femtosecond laser ablation system (Legend, Coherent Inc., Santa Clara, CA, USA) operating at its third harmonic ($\sim 265 \text{ nm}$)⁸⁰. Prior to the analysis the ICP-MS was optimized for sensitivity, while keeping the oxide formation low ($< 0.5 \%$ for ‘dry’ plasma conditions based on ThO^+/Th^+ when ablating NIST SRM 610). The operating conditions of the ICP-MS instruments and the laser ablation systems are summarized in Table 19. The data acquisition started with the measurement of 30 s of the blank followed by approximately 50

s of signal acquisition from a single crater ablation. For quantification, Cu was selected as the internal standard. The data reduction and the signal integration were carried out using the standard procedure as described in reference¹⁸⁴.

Table 19 Operating conditions of ICP-MS and laser ablation systems

ICP-MS		
Instrument	PE Sciex ELAN DRC II	Thermo Finnigan Element2
Nebulizer gas flow	0.95 L min ⁻¹	0.83 L min ⁻¹
Auxiliary gas flow	0.95 L min ⁻¹	0.75 L min ⁻¹
Plasma gas flow	18 L min ⁻¹	16 L min ⁻¹
RF power	1480 W	1350 W
Torch position	manually adjusted (X and Y positions)	X: 4.50 mm, Y: 3.00 mm, Z: -4.80 mm
Lens settings	auto lens on	extr.: -2000.0 V, Focus: -739.1 V, X-deflection: 0.80 V, Y-deflection: 7.50 V, Shape: 140.32 V; High resolution lenses: Quad1: 0.81 V, Quad2: - 2.00 V, Focus Quad1: 0.50 V
Detector mode	dual	dual
Dwell time	10 ms	10 ms
Scan mode	peak hopping	E-scan
Laser ablation		
LA system	LSX-213, Nd:YAG	Ti-sapphire-based fs-LA
Wavelength	213 nm	~ 265 nm
Pulse length	4 ns	< 150 fs
Ablation frequency	5 Hz	10 Hz
Spot size	50 μm	~ 80 μm
Laser fluence	13.7 J cm ⁻²	3.6 J cm ⁻²
Carrier gas flow	1.0 L min ⁻¹ He	1.0 L min ⁻¹ He

Reagents, calibration solutions and reference materials

Preparation of standard solutions. The calibration solutions were prepared using single element standard solutions (1000 mg L⁻¹, MERCK, CPI International). Three solutions were prepared containing all selected elements in different concentration to perform matrix-matched solution calibration. Since the matrix was gold and silver, the dilution and mixing of the element standards had to be considered carefully in order to avoid instability or precipitation (e.g. AgCl) of the elements in the final solution. The preparation of one calibration solution containing all desired elements with diluted HNO₃ was inappropriate because mixing Ag with other element standards containing HCl would cause depletion of Ag concentration. Furthermore, the stability of Au in HNO₃ is weaker than in HCl. Therefore, Ag was transferred into a chloro-complex [AgCl_x^{1-x}] by mixing Ag with concentrated HCl. The Ag-chloro-complex was then mixed with the element standard solutions and diluted using 1.5 % HCl prepared from sub-boiled hydrochloric-acid and ultra high purity water (Milli-Q, Millipore). The stability of the standards was monitored over

time by solution nebulization ICP-MS. Three calibration solutions were prepared in PP vials with element concentrations of 20, 50 and 100 $\mu\text{g L}^{-1}$, while the concentration of Cu, Ag and Au were kept constant at 50 $\mu\text{g L}^{-1}$, 1.5 mg L^{-1} and 10 mg L^{-1} respectively. The composition of the calibration solutions and the isotopes measured are summarized in Table 20.

Table 20 Elements, concentrations of the solution standards used for calibration and isotopes included in the measurement protocol

Element	Isotopes measured	Solution 1 [mg L^{-1}]	Solution 2 [mg L^{-1}]	Solution 3 [mg L^{-1}]
Ti	47, 48	0.02	0.05	0.1
Cr	52, 53	0.02	0.05	0.1
Mn	55	0.02	0.05	0.1
Fe	56, 57	0.02	0.05	0.1
Co	59	0.02	0.05	0.1
Ni	58, 60	0.02	0.05	0.1
Cu	63, 65	0.05	0.05	0.05
Zn	66-68	0.02	0.05	0.1
As	75	0.02	0.05	0.1
Se	77, 78	0.02	0.05	0.1
Pd	105, 106	0.02	0.05	0.1
Ag	107, 109	1.5	1.5	1.5
Cd	111	0.02	0.05	0.1
Sn	118, 119	0.02	0.05	0.1
Sb	121, 123	0.02	0.05	0.1
Te	126, 128	0.02	0.05	0.1
Pt	194, 195	0.02	0.05	0.1
Au	197	10	10	10
Pb	208	0.02	0.05	0.1
Bi	209	0.02	0.05	0.1

Solid calibration. Additional investigation of the produced gold calibration materials was performed using two NIST solid gold CRMs. FAU7 (NIST 8053) and FAU10 (NIST 8062) fine gold block reference materials were used for validation of the quantification carried out using solution calibration. The element composition of the reference materials is indicated in Table 21.

5.3 Results and discussion

Selection of analytes for analysis. Quadrupole-based ICP-MS instruments are often used for fast transient data acquisition, and the selection of isotopes before analyzing gold objects is crucial. The most influential polyatomic interferences may originate from the formation of oxides and argides (e.g. ^{99}Ru : $^{63}\text{Cu}^{36}\text{Ar}$; ^{101}Ru : $^{63}\text{Cu}^{38}\text{Ar}$, $^{65}\text{Cu}^{36}\text{Ar}$; ^{103}Rh : $^{65}\text{Cu}^{38}\text{Ar}$, $^{63}\text{Cu}^{40}\text{Ar}$; ^{105}Pd : $^{65}\text{Cu}^{40}\text{Ar}$; ^{111}Cd : $^{95}\text{Mo}^{16}\text{O}$, ^{121}Sb : $^{105}\text{Pd}^{16}\text{O}$; ^{147}Sm : $^{107}\text{Ag}^{40}\text{Ar}$, ^{123}Sb and ^{123}Te : $^{107}\text{Ag}^{16}\text{O}$), which cannot be resolved with this type of mass spectrometer. Therefore, when performing qualitative analysis the extent of potential polyatomic interferences must be taken into account and most of the given polyatomic interferences can be circumvented by selecting the suitable isotopes. However, some of these interferences can only be resolved using reaction cell technology²¹⁸ in combination with a quadrupole-ICP-MS.

5.3.1 Evaluation of the solid calibration materials

Two solid gold calibration materials produced for this study (NA1, NA2) were analyzed by LA-ICP-MS using solution and solid calibration approaches. For solid calibration either a Ti-sapphire-based femtosecond laser ablation system or a solid-state Nd:YAG nanosecond laser ablation system were applied, while for solution calibration only the femtosecond laser system was used. To verify that the prepared solutions are suitable for calibration, FAU7 and FAU10 (NIST 8053 and NIST 8062) solid gold CRMs were analyzed for validation. A comparison of the determined concentration values versus the certified values (NIST) is shown in Figure 63 and summarized in detail in Table 21.

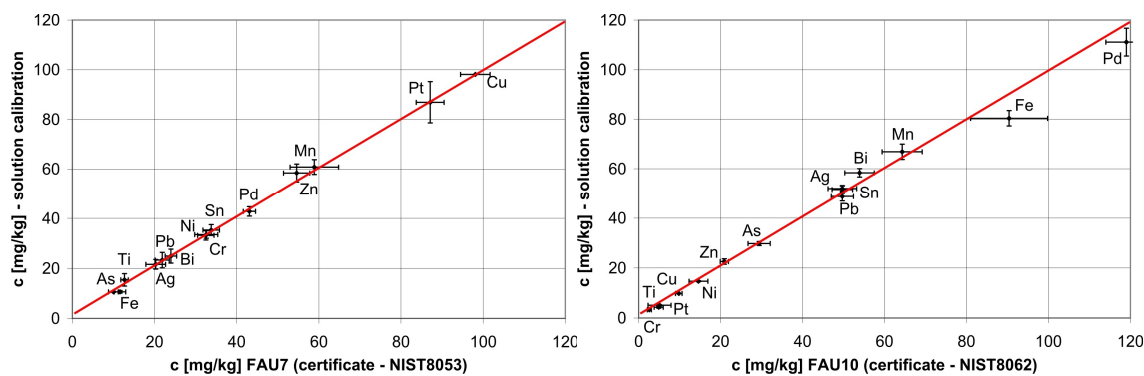


Figure 63 Comparison of the results obtained using solution calibration with the certified values of FAU7 and FAU10.

Table 21 Reference values in comparison to the determined concentrations (mg kg⁻¹) of FAU7 (NIST 8053), FAU10 (NIST 8062), NA1 and NA2 using solution calibration and Cu as internal standard ('wet' plasma conditions). Sampling was carried out using femtosecond laser ablation (n=6)

	FAU7				FAU10				NA1			NA2		
	REF.		Solution cal.		REF.		Solution cal.		REF. ^a	Solution cal.		REF. ^a	Solution cal.	
	AVG	SD	AVG	SD	AVG	SD	AVG	SD	AVG	AVG	SD	AVG	AVG	SD
Ti	12.7	0.9	15.4	2.5	2.6	0.5	3.26	0.09		2.28	0.03		3.96	0.20
Cr	32.6	2.8	33.5	1.5	4.9	1.1	3.94	0.23	9	10.5	0.2	25	27.5	0.3
Mn	58.9	5.9	60.8	3.0	64.3	4.9	66.9	3.1	7	7.73	0.19	62	62.5	1.6
Fe	11.6	1.4	10.6	0.5	90.4	9.4	80.4	3.1	34	43.4	0.5	806	989	8
Co									10	10.7	0.2	124	114	2
Ni	32.5	2.0	33.2	1.9	14.6	2.3	15.3	0.8	48	53.0	0.8	1092	1102	8
Cu	98.1	3.6	98.1	-	9.8	0.8	9.8	-	99	99	-	1062	1062	-
Zn	54.6	3.2	58.4	3.6	20.9	1.0	22.6	1.1	11	12.4	0.9	114	111	2
As	10.0	1.2	10.6	0.2	29.4	2.7	29.8	0.8	43	45.7	2.2	112	106	5
Se									10	10.2	1.3	114	103	6
Pd	43.1	1.5	42.8	1.9	119	5	111	6	55	58.7	0.8	1112	1096	24
Ag	20.3	2.4	21.6	1.9	49.7	3.5	52.0	1.1	1%	0.9%	0.1%	5.45%	5.4%	0.4%
Cd									10	11.8	0.5	82	104	3
Sn	33.8	2.0	35.3	2.2	49.7	2.5	51.6	1.7	50	53.2	0.8	773	1114	6
Sb									9	12.1	0.6	102	111	2
Te									10	11.1	1.5	112	106	8
Pt	87.1	3.4	86.9	8.3	5.1	2.8	5.1	0.2	58	68.0	4.0	1152	1119	66
Pb	21.9	1.7	23.3	3.1	49.7	2.7	48.7	1.8	9	11.5	1.5	90	108	2
Bi	24.0	1.4	24.9	2.8	53.9	3.6	58.4	1.7	9	11.1	1.2	100	110	3

^a information values based on digestion and solution analysis by ICP-OES provided by the manufacturer (RSD \approx 2 %)

The solution calibration of the ICP-MS and femtosecond-laser sampling provided precise (< 5 %) and accurate (< 8 %) concentrations for most of the elements in FAU7 and FAU10. Major deviations were observed for Ti (21-27 %) and Fe (9-11 %) in both samples and Cr (12 %) in case of FAU10 when compared to the certified values. However, all the uncertainties of the measured and certified values are overlapping each other, except Ti in case of NA2. The applicability of solution calibration was confirmed on the majority of elements using FAU7 and FAU10. Therefore, the same calibration was performed for the analysis of NA1 and NA2. For the calculations, Cu was used as internal standard. Cu concentration values provided by the manufacturer were confirmed using the 100 % normalization approach (data not shown). Our results in comparison to the information values provided by the manufacturer show significant deviations for certain elements. For most elements, these deviations were found to be up to 15 % and 10 % for NA1 and NA2, respectively. The most

significant difference (31 %) was found for Sn in NA2, while the deviation was only 6 % in case of NA1. In both samples, the calculated concentrations of Cd were 15 % and 21 % higher than the information values for NA1 and NA2 respectively. A higher deviation was also found for Fe (with approximately 20 %). However, the determined results were not influenced by counting statistics, since the limits of detection were lower than 1 mg kg⁻¹ for all elements in all four analyses (FAU7, FAU10, NA1, NA2). Since discrepancy was found between the LA-ICP-MS results and the information values, further measurements using NA2 as external standard for the analysis of NA1 were performed. The obtained deviations are summarized in Figure 64A and 64B. Figure 64A shows the difference between the determined concentrations and the information values for NA1 when using NA2 for calibration. In Figure 64B NA2 was quantified using NA1 for calibration. The results show that deviations of up to 36 % were detected in case of NA1, with the highest deviations obtained for Sn, Pt, Se, Co and Bi. For NA2 deviations of up to 26 % were detected, with the highest deviations obtained for the same elements, indicating that inaccurate information values are given for NA1 and NA2. Finally, using the element concentration values determined using solution calibration for NA1 and NA2, the quantification of the two solid calibration materials improved (Figure 64C and 64D) for most of the elements except Se and Sb.

To confirm our results obtained by solution calibration, solid calibration using FAU7 and FAU10 was also performed using 'dry' plasma conditions. The results obtained for the individual measurements are summarized in Table 22 and 23. In general, fs and ns-LA provided similar results and significant differences were not found between the element concentrations determined using the two lasers. The uncertainties were found to be lower in most cases when the analysis was performed using the femtosecond laser system. For illustration, analyte transient signals acquired using femto- and nanosecond lasers are shown in Figure 65. The advantageous utilization of femtosecond laser ablation for ablation of metals, i.e. less heat transfer into the sample, smaller particle sizes, more complete vaporization of particles within the ICP has been reported and should therefore provide smoother signals²¹⁹. This can be partially confirmed when ablating gold. During ablation of FAU7 and FAU10 however, spikes in the intensity profiles were recorded exclusively for both Ag isotopes. These spikes occurred not consistently and their origin is currently unknown. Therefore, the Cu to Ag ratios were calculated and every signal deviating more than 3 times the standard deviation of the ratio was rejected from the analysis. Signals of other elements were found to be stable.

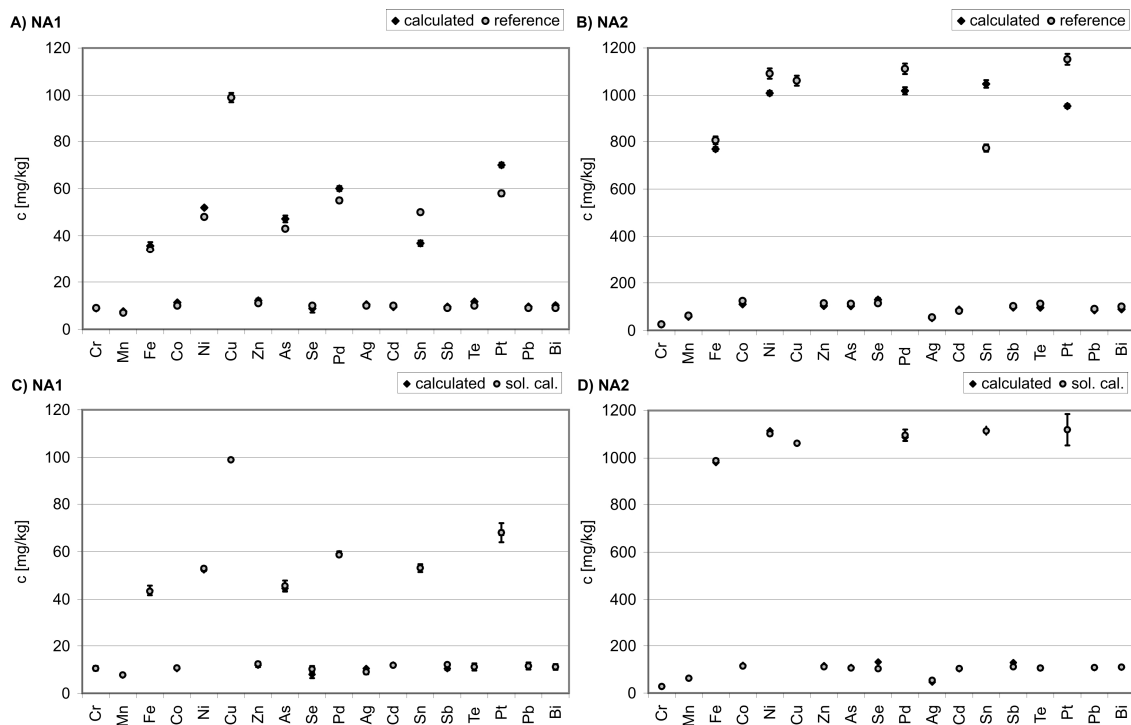


Figure 64 Cross validation of NA1 and NA2. For quantification of NA1, NA2 was applied as external standard. The calculation of the element concentration values was performed using either the information values of NA2 (Fig. A) or the determined values (Fig. C) using solution calibration. For quantification of NA2, NA1 was applied as external standard. The calculation of the element concentration values was performed using either the information values of NA1 (Fig. B) or the determined values (Fig. D) using solution calibration. The concentration of Ag was calculated in mg kg^{-1} and divided by 10000 to include it in the graphs.

Solution and solid calibration approaches provided similar results for both samples. The largest deviations were found for Ti and Cr, while the deviation for the other elements remained below 10 %. Concerning the major element Ag, the 5.4 wt% content was confirmed using both calibration techniques for NA2. In case of NA1, less than 10 % deviation was found for Ag when comparing the two calibration methods. Considering the uncertainty propagation when using solid reference materials for quantification of solids in comparison to solution based calibration for solid samples it can be stated that the solution calibration is the most promising approach to quantify the micro-heterogeneity within solids.

Table 22 Determined concentrations (mg kg⁻¹) of NA1 using FAU7 and FAU10 as calibration standards and Cu as internal standard ('dry' plasma conditions). Sampling was carried out using either femtosecond or nanosecond laser ablation (n=4)

	FAU7_fs-LA		FAU7_ns-LA		FAU10_fs-LA		FAU10_ns-LA	
	AVG	SD	AVG	SD	AVG	SD	AVG	SD
Ti	1.7	0.1	1.7	0.2	1.5	0.1	1.4	0.1
Cr	9.5	0.4	9.3	2.1	13.3	0.6	10.2	2.3
Mn	7.1	0.3	6.9	0.7	7.2	0.3	6.7	0.7
Fe	45.2	2.1	51.0	5.3	48.8	2.2	49.2	6.7
Ni	52.2	0.6	52.4	2.6	53.6	0.6	51.9	2.6
Cu	99		99		99		99	
Zn	10.2	0.7	12.5	6.3	11.0	0.8	13.0	6.6
As	42.5	1.3	48.2	2.5	44.9	1.3	42.9	2.2
Pd	59.2	1.0	58.7	3.1	63.2	1.1	60.3	3.2
Ag	1.00%	0.01%	1.01%	0.03%	1.04%	0.02%	1.00%	0.03%
Sn	49.5	1.5	49.7	2.3	51.8	1.6	50.5	2.4
Pt	65.0	0.9	64.7	5.1	65.4	0.9	66.7	5.3
Pb	10.6	0.5	10.0	1.2	12.0	0.5	11.1	1.3
Bi	10.7	0.8	10.4	1.4	10.7	0.8	10.6	1.5

Table 23 Determined concentrations (mg kg⁻¹) of NA2 using FAU7 and FAU10 as calibration standards and Cu as internal standard ('dry' plasma conditions). Sampling was carried out using either femtosecond or nanosecond laser ablation (n=4)

	FAU7_fs-LA		FAU7_ns-LA		FAU10_fs-LA		FAU10_ns-LA	
	AVG	SD	AVG	SD	AVG	SD	AVG	SD
Ti	3.4	0.1	3.8	0.3	3.0	0.1	3.1	0.3
Cr	26.7	0.4	26.5	0.7	37.6	0.5	29.1	0.7
Mn	58.0	0.4	56.5	1.9	59.0	0.4	55.3	1.8
Fe	1022	11	1243	69	1102	12	1133	63
Ni	1098	10	1074	22	1127	10	1065	22
Cu	1062		1062		1062		1062	
Zn	96.0	3.2	108	7	115	4	110	7
As	101	2	118	4	107	2	105	3
Pd	1097	16	1076	29	1171	17	1106	29
Ag	5.2%	0.1%	5.5%	0.1%	5.4%	0.1%	5.5%	0.1%
Sn	1037	16	1069	11	1085	16	1086	11
Pt	1071	9	1069	29	1076	9	1102	30
Pb	99.3	4.3	106	4	112	5	118	5
Bi	106	6	110	3	106	6	112	3

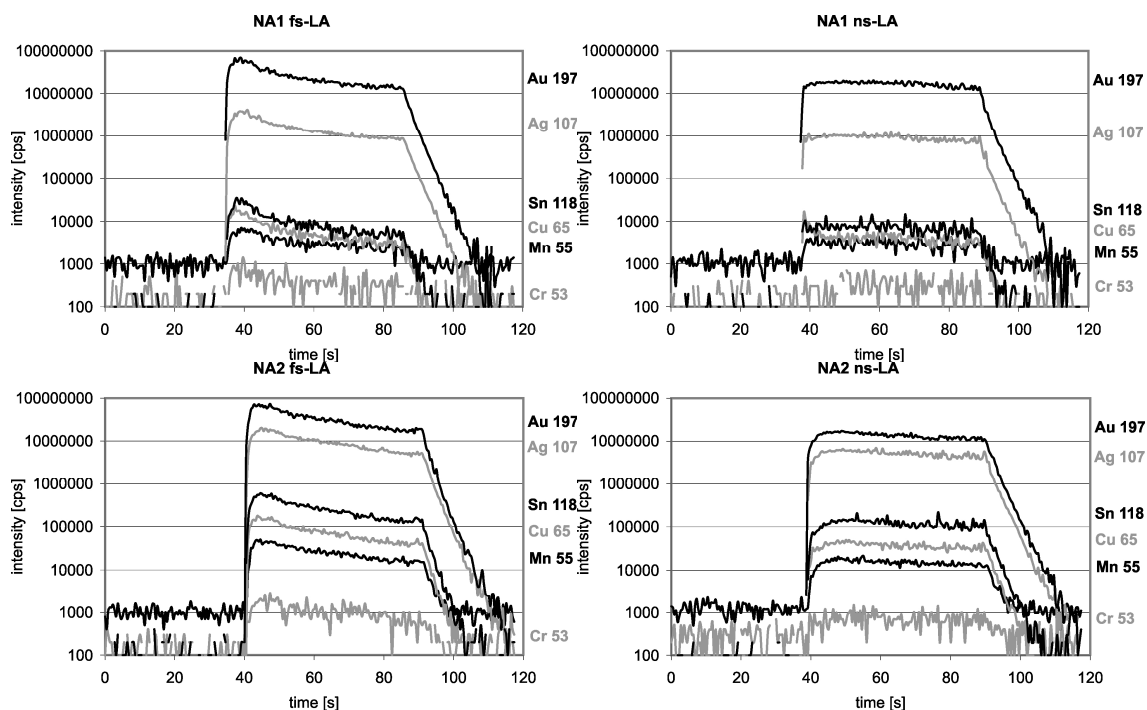


Figure 65 Typical transient signal structures of six analytes when ablating NA1 and NA2 using femtosecond- (10 Hz) and nanosecond- (5 Hz) laser ablation systems ('dry' plasma conditions).

5.3.2 Quantitative analysis of various gold objects

The two calibration materials offer well suitable list of elements for quantitative analyses of gold objects. In our laboratory a number of gold analyses were carried out using LA-ICP-MS, which provides a quasi non-destructive way to investigate major, minor and trace element concentrations within the valuable gold objects. The obtained information on chemical composition and the trace element fingerprint of the objects can contribute to full characterization of gold objects in terms of authenticity and provenance. Furthermore, the comparison of the determined composition of various sampling locations over the sample surfaces may provide indications for production processes and tools involved, moreover it contributes to the differentiation of the base metal used to produce the individual parts of objects.

These investigations were performed using a solid-state Nd:YAG laser system operating at a wavelength of 266 nm with a pulse duration of approximately 5 ns and a quadrupole-ICP-MS instrument (ELAN 6100 DRC II) used for transient signal acquisition. As a function of object size, a closed cylindrical ablation cell in volume of approximately 35 cm³ (Figure 66),

and an open-design ablation cell (Figure 67-68) were applied. The open-design cell was placed onto the sample surface and tightly sealed using a shapeable, plastic material (Blu Tack, Bostik Ltd.). Since the sealing process caused microscopic surface contamination, only a limited number of analyses were performed on large sized samples. Furthermore, the sealing process might cause damage on fragile samples. The recently developed novel sampling approach based on atmospheric sampling and aerosol suction could provide a very suitable alternative for the analysis of such large objects (Chapter 3).

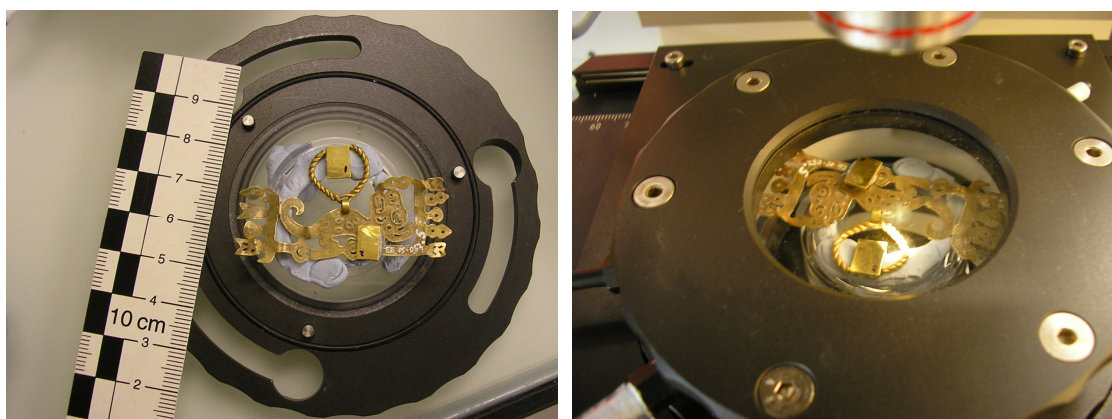


Figure 66 The application of closed ablation cells with sufficient space to accommodate sample(s) and solid calibration materials.

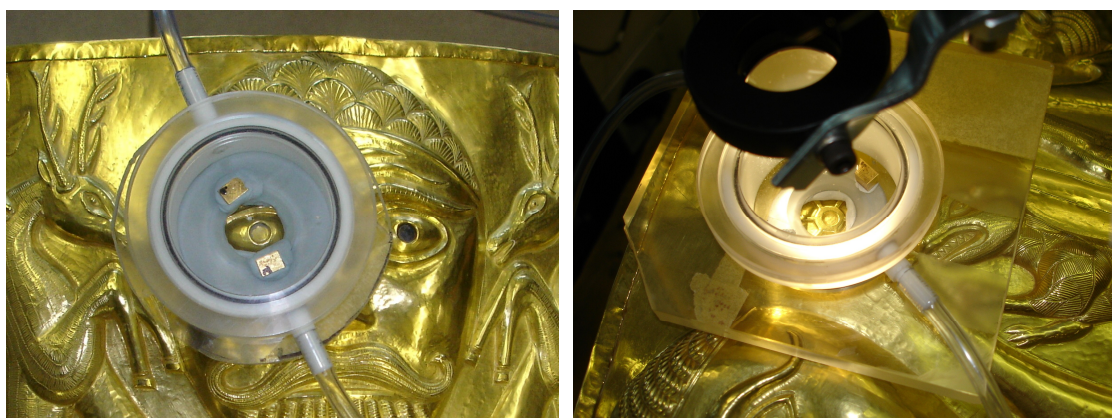


Figure 67 The application of ablation cells with an aperture on the bottom for the analysis of large objects. The analyzed object depicted is a large gold cauldron found in the Chiemsee, Germany in 2001.

Investigation of gold ornaments and deposit samples deriving from early Peruvian cultures

Gold artifacts from one of the largest collections worldwide of Chavín gold objects were investigated. The Ebnöther Collection²²⁰, a private collection donated to the town museum of Schaffhausen, Museum zu Allerheiligen Schaffhausen, Switzerland owns 36 objects that include crowns, pectorals, ear plugs, nose ornaments and finger rings, which can typologically be assigned without doubt to the Chavín and Cupisnique cultures. These cultures were typical of northern Peru in the period of about 900 B.C. – 200 B.C. The numerous nose ornaments part of the Ebnöther Collection could be assigned by W. Alva to a site called Cerro Corbacho, Zaña valley, north Peru²²¹. Most of the objects from the Ebnöther Collection are supposed to derive from a looted archaeological site (Cerro Corbacho) on the Peruvian north coast. For this reason they are of particular interest for the provenance study focusing on the earliest Peruvian gold metallurgy, having its beginnings in the early first millennium B.C. Numerous objects including a pectoral, nose ornaments, finger rings and necklace beads were analyzed. Furthermore, some geological gold samples from the Petersen Collection, (Pontificia Universidad Católica del Perú, Lima) were also included in our study.

A prerequisite for the analysis of these precious objects is a very low sample destruction, which needs to be compromised with the required limits of detection. Thus, laser ablation events were performed in single hole drilling mode using 50 µm crater diameter and an ablation frequency of 4 Hz for 45 s to apply the lowest possible destruction to the samples, while obtaining sufficient data for data analysis (Figure 68, Table 24). Each individual object part was sampled 3 to 4 times to ensure representative sampling. Before signal acquisition, the possible contamination from the sample surface was removed by approximately 20 laser shots. Pre-ablation was performed on all objects samples but not on the native gold deposits, because of the limited thickness of the grains. All matrix elements were measured and were taken into account for the calculation of the element concentrations. The signals of Ag and Au major elements were recorded by changing the mass resolution from 0.8 amu to 0.4 amu (so-called custom resolution) to reduce the signal intensities²²². Data evaluation was performed using the 100 % normalization procedure as described in reference¹⁶³. This approach can only be applied when all constituents of a sample can be analyzed and allows therefore the quantification of samples using the entire matrix as internal standard. The acquired signals of the elements for many of the gold artifacts were mostly stable. However, spikes (generally caused by large particles) were often observed in the signals of trace elements. These spikes occurred not consistently (not for all isotopes of an element). Therefore, highly deviating signal intensities (more than a factor of 10 higher than the average count rates) were rejected from the analysis.

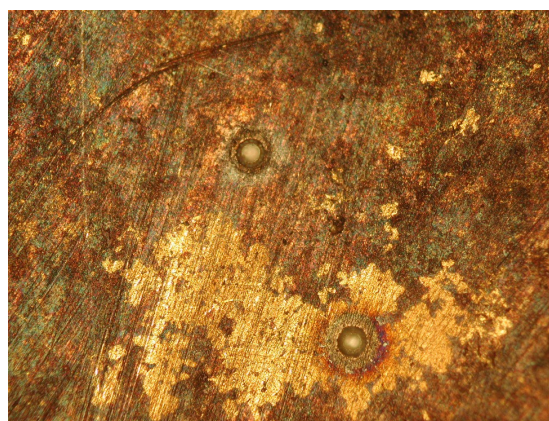
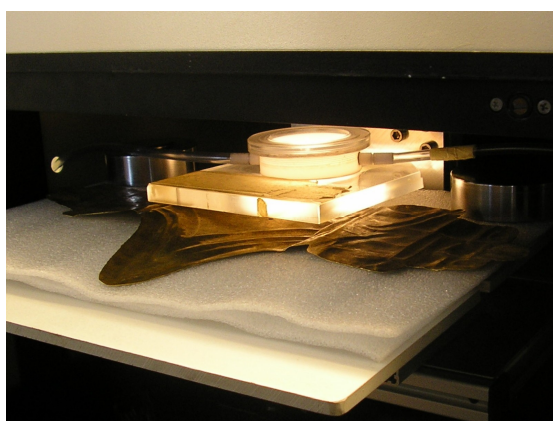


Figure 68 The analysis of a cruciform pectoral (EBN15020, Ebnöther Collection, Museum zu Allerheiligen Schaffhausen, Switzerland) using an open design ablation cell, and laser generated craters using 50 μm spot size on the surface of the object.

Table 24 Determined composition and trace element content of the suspension ring of a nose ornament (EBN15020)

	c [wt%]			c [$\mu\text{g g}^{-1}$]																
	Cu	Ag	Au	Ti	Cr	Mn	Fe	Co	Ni	Zn	As	Se	Pd	Cd	Sn	Sb	Te	Pt	Pb	Bi
Base plate																				
AVG	2.5	38.5	58.9	0.9	0.4	1.6	81	0.3	1.0	8	0.7	4	10	0.3	2.0	0.4	3	19	10	1.9
RSD%	8	0.3	0.1	23	-	47	93	-	65	6	3	-	11	26	79	44	10	1	5	10

The composition of the analyzed objects summarized in this chapter is based on the quantification using NA2 gold calibration material as external standard and the information on element composition of NA2 determined by solution calibration (Table 21).

Photographs of the analyzed samples are shown in Figure 68 and Figures A. 1 – A. 11. The determined, detection limit filtered major, minor and trace element concentrations are summarized in Table 24 and Tables A. 1 - 17. The detection limits were calculated for each analyte and each measurement run based on ref ¹⁸⁴.

The analysis of the objects revealed that the major constituents of the artifacts, Cu (1.2 – 5.6 %), Ag (17.8 – 49.8 %) and Au (46 – 80.4 %), varied to a great extent. The increased amount of Cu and Ag can be attributed to treatment procedures during production of the objects. The trace elements, Cr, Co, Ni, As were in most cases not detected, while low concentrations (few $\mu\text{g g}^{-1}$) for Mn, Cd, Sn, Sb, Te, and Bi were determined. All of the analyzed objects show high concentrations of Pd (up to $59 \mu\text{g g}^{-1}$) and Pt (up to 0.25 %). It was found that some objects, composed of more parts, were produced from different gold varieties. An example is the nose ornament (Figure A. 6), where the difference between pendant and suspension ring was predicted based on the color. This was confirmed by the LA-ICP-MS analysis, which demonstrated that the suspension ring has a different major element composition and trace element pattern than the pendant and connecting ring (Table A. 8). Deposit samples (Figure A. 11, Table A. 17) consist mainly of Au and Ag, and it is assumed that Cu is present in the gold objects as contamination, which occurred during the treatment processes.

The information obtained from these analyses are a part of an ongoing archaeological investigation on the provenance of Peruvian gold artifacts²⁰³.

Investigation of a gold figurine using NA2 solid calibration material

A gold figurine (Figure 69) was analyzed by LA-ICP-MS to determine the composition and trace element distribution of its various parts. The gold object investigated weighs 24 g and has a height of 7.3 cm. As observed from the front, the left foot is broken off. Its architecture and the technical production are described in detail in ref.²²³. It was reported that the figurine is in relation with the Islamic world and it dates back to the 11th – 12th century A.D. based on its stylistic features. The figurine is completely made by using granulation technique. The framework consists of tiny tubes that are connected to the sheet metal. The end of these tubes forms a ring consisting of six gold granules. The object is damaged at several locations.



Figure 69 Side-view and front-view of the gold figurine.

Quantitative LA-ICP-MS analyses were performed on the broken off foot. The investigations were performed using a laser system operating at a wavelength of 213 nm and a quadrupole-ICP-MS instrument (ELAN 6100 DRC II). During analysis all matrix elements were measured and were taken into account for the calculation of element concentrations. Data evaluation was performed using the 100 % normalization procedure as described in ref.¹⁶³. For the determination of element concentrations, the NA2 gold calibration material was applied as external standard.

Table 25 Determined composition and trace element content of various parts (granules, n=3; joints, n=3; base metal 1, n=6; base metal 2, n=5) of the gold figurine

		c [wt%]			c [$\mu\text{g g}^{-1}$]											
		Cu	Ag	Au	Mn	Fe	Co	Ni	Zn	As	Pd	Sn	Sb	Pt	Pb	Bi
Granules	AVG	7.0	15.1	77.2	44	4630	2.5	75	100	74	20	180	42	120	560	8
	RSD%	6	3	0.2	40	10	9	9	10	4	14	8	13	11	9	7
Joints	AVG	7.9	17.3	74.4	13	2640	2.0	88	62	16	23	210	47	120	740	7
	RSD%	17	6	2	63	73	31	25	55	57	17	47	48	22	62	59
Base metal 1	AVG	6.7	15.8	77.1	16	2710	1.2	59	62	52	20	180	42	120	570	7
	RSD%	4	5	1	21	22	15	7	27	47	5	17	10	6	9	14
Base metal 2	AVG	5.8	18.7	75.2	3	740	0.9	57	41	52	18	470	56	92	1080	8
	RSD%	13	6	1	9	5	26	10	11	44	6	25	5	8	16	7

The obtained results are summarized in Table 25. Additionally, elements such as Cr, Ti, Se, Cd, Te were also quantified, however these elements were below limits of detection. The granules (Figure 70), solder joints and the metal framework (referred to as 'base metal') were analyzed within 17 runs in total. The analyses of the metal framework were performed two times, once from the top of the sample (base metal 1) and from the bottom of the sample (base metal 2, Figure 70).

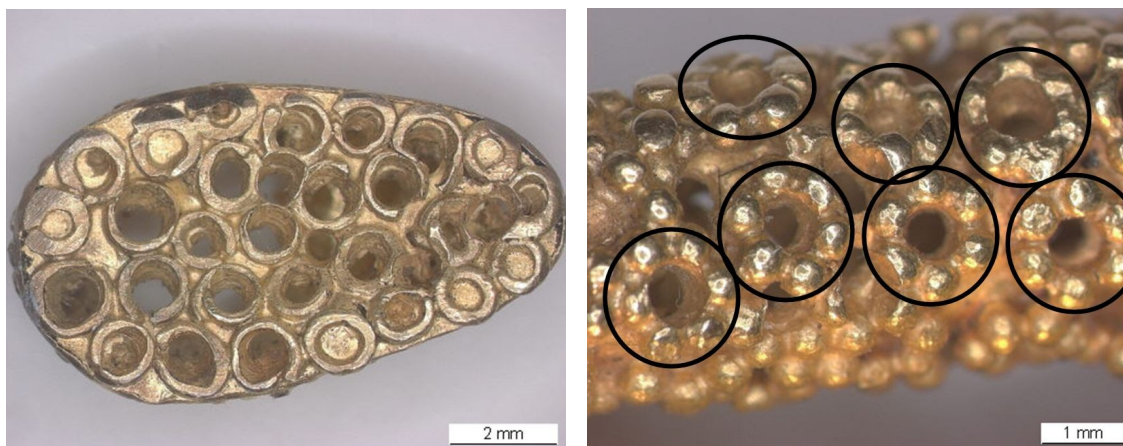


Figure 70 Bottom of the foot (left) and the soldered granules forming groups (right).

The granules and the base metal 1 showed lower silver concentration than the solder joints and base metal 2. The copper content within the solder joints was only slightly higher (< 1 %) than in the rest of the metal. The Pb concentration was found to increase in parallel with the increasing Ag concentration. The composition of base metal 2 differs from the composition of other parts indicated by the significantly different Ag, Cu, Au, Mn, Fe, Sn and Pb content.

The determined data contributes to a thorough investigation of the gold figurine with respect to its age, production circumstances and historical background.

5.4 Conclusion

Two gold calibration materials (NA1 and NA2) were investigated using fs- and ns-LA-ICP-MS. Owing to an extended list of elements and a wide concentration range within these materials, they are well suited for fingerprint studies of archaeological gold objects. The studies on the NA1 and NA2 gold materials included solution and solid calibration strategies. The applicability of solution calibration as a promising alternative calibration approach for the analysis of gold using LA-ICP-MS was confirmed. This calibration approach allows quantification of as many elements as needed for a thorough characterization of an unknown gold object. Furthermore, it allows minimizing the uncertainty contribution from the calibration. The deviation between the results and the certificate was 4-8 % for most elements when analyzing FAU7 and FAU10 NIST CRMs. Precision was found to be better than the error bars given in the certificate, which demonstrates that femtosecond-laser ablation is well suitable for gold ablation. When performing solid calibration using FAU7 and FAU10, the uncertainties of the determined element concentration values were lower when applying femtosecond laser, however ns- and fs-laser ablation systems provided similar results. Solution and matrix matched solid calibration techniques demonstrated that solution calibration and direct solid calibration provided concentration values for the two materials NA1 and NA2, which agree better than concentrations determined after digestion of the gold samples, as provided by the manufacturer.

For the investigation of various gold objects, such as the Pre-Columbian gold artifacts, the two characterized gold calibration materials (NA1 and NA2) provided an appropriate selection of elements. The obtained fingerprints allow further statistical data evaluation on the origin of gold used for production of jewelry or archaeological objects and will contribute to the investigation of raw material treatment processes used for the production of the gold objects. Moreover, the obtained data can also contribute to the differentiation of modern and historical gold types.

6. Conclusions and outlook

6.1 Conclusions

The investigations presented in this work provide insights into past drawbacks, solutions and new capabilities of laser ablation sampling coupled to ICP-MS. Owing to the incompatibility of air with the Ar plasma gas in the ICP, laser ablation sampling was restricted to the application of an inert (Ar, He) well sealed gas atmosphere. Since the gas composition of the ICP strongly affects vaporization, atomization and ionization processes, the use of constant high purity gases is preferred. Even small amount gas additions (e.g. H₂, N₂) affect plasma conditions resulting in significantly altered signal intensity and therefore, changed intensity ratios (analyte vs. internal standard) as it has been widely demonstrated in the literature. The extreme ‘sensitivity’ characteristics of the ICP even for the introduction of gas impurities were demonstrated in the present work. Beside the numerous factors affecting the performance of LA-ICP-MS, the material of tubes used for gas supply to the ablation cell and for carrying the aerosol to the ICP-MS was shown to be an additional important factor to be considered. Owing to the permeability of various tube materials, the tiny amount of gas (H₂, O₂) and water (H₂O) molecules may enter the carrier gas flow by the tube degassing process. Since the degassing is time dependent and the ICP conditions are gas composition dependent, a drift in sensitivity can be observed until the degassing components reach a constant minimum. Consequently, tube material was found to be a potential source of drift, which can affect the total uncertainty budget, as demonstrated by Luo et. al.¹⁷⁹. Fluoropolymer (e.g. FEP, PTFE, PFA) and copper tubes can be a suitable choice for gas supply owing to their low permeability and hydrophobicity. Suitable tube materials for aerosol transport are non-electrostatic, hydrophobic, the least permeable to ambient gases and water and preferably flexible.

In the general LA-ICP-MS experimental setup, the gas in which the ablation is performed is transported into the ICP. Therefore, the ablation and ICP induced changes affected by the kind of gas can not be separated. However, this work describes a novel laser ablation sampling method, which utilizes a gas exchange device capable to online exchange various gases (e.g. air) to Ar while keeping the laser generated aerosols in the gas phase passing the device. An advantage of the gas exchange is that the concentration of gases other than Ar is decreased to a very high extent. Subsequently, as demonstrated the gas exchanger is capable to remove gas impurities entering the gas flow from the inner surface of the tubes. Thus, stable ICP operating conditions are maintained owing to the constant purity of argon

entering the plasma. With the application of the gas exchanger in the experimental setup, laser ablation sampling can be carried out in ambient air, thus air tightness and tightly sealed ablation cells are not representing a prerequisite any more. Performing laser ablation sampling without the use of an ablation cell was demonstrated to offer high flexibility in terms of the direct analysis of solid samples independently of surface geometry and sample size. In the present work, complete aerosol sampling was not achieved, however the aerosol sucked by the tube inlet directed to the ablation crater was representative with respect to the composition of the analyzed samples. The particle size distribution of the aerosol generated in air was found to contain large, spherical particles up to 1 μm in diameter, such as Ar. However, the majority (92 %) of the aerosol consisted of particles smaller than 150 nm, which can be successfully vaporized within the ICP. Moreover, the particle deposition around the crater was slightly reduced when using air in contrast to Ar. Scanning electron microscopy and optical particle counting experiments did not indicate significant change of particle sizes when the aerosol was introduced into the gas exchange device. The novel atmospheric sampling approach was tested for quantitative analysis of various solid materials and represents a potential alternative for the analysis of large objects.

Additionally, this work demonstrated the characterization of two new gold calibration materials (NA1 and NA2) using fs- and ns-LA-ICP-MS in terms of element composition. Liquid calibration performed for the analysis of laser generated aerosols of NA1 and NA2 was found to be a viable alternative for accurate quantification of element concentrations within the gold calibration materials. This approach provided accuracy and precision in the order of 8 % and 5 %, respectively. The validation of the quality of the data was carried out using NIST 8053 and 8062. The obtained element concentrations within NA1 and NA2 using liquid calibration were confirmed by performing solid calibration using NIST 8053 and 8062 as calibration standards.

For the analysis of gold samples, the two solid calibration materials and the combination of dry plasma conditions and fast scanning quadrupole ICP-MS instruments may offer the most suitable combination. Generally the application of liquid calibration limits the attainable detection limits owing to the higher background count rates influenced by the presence of water within the ICP. In this study, therefore, a double focusing sector field ICP-MS instrument was used, operating in high resolution mode to resolve the polyatomic interferences. Performing desolvation may lead to element dependent loss (e.g. Sn, Sb, Te) from the solution standards and makes the calibration unsuitable.

The applicability of the two calibration materials was confirmed on various gold samples and provided appropriate selection of elements as required for archaeological studies.

Furthermore, their composition was closely matrix-matched to the unknown samples, which improved the precision and accuracy.

6.2 Outlook

The quantitative results achieved using the developed atmospheric sampling approach are encouraging, however it did not provide a complete aerosol sampling. Currently, an ideal position of the tube inlet with respect to the ablation crater can not be given. Therefore, aerosol expansion and suction need to be investigated in more detail. Aerosol visualization experiments utilizing light scattering are required to determine the optimum position of the tube inlet. To improve aerosol suction efficiency, beside adjusting laser parameters such as pulse energy, repetition rate and optimum position of the tube inlet, the performance of aerosol suction needs to be improved. Since the flow rate of air in the present setup is limited to 0.25 L min^{-1} determined by the gas exchange device, a high performance gas exchanger providing flow rates of up to 1 L min^{-1} is required and could contribute to more efficient aerosol suction. To perform such a technical improvement on the device, parameters affecting the gas exchange process (pore size, porosity, membrane length, partial pressure difference) need to be studied further and optimized. Alternatively, thinner membrane and optimized partial pressure difference within the gas converter cell might contribute to faster gas exchange. The reduction of the diameter and length of the annular membrane might contribute to faster aerosol washout and faster signal response by the ICP-MS. Although, the reduction of the latter parameters would reduce the volume of the central channel, the porosity of the membrane and the number of gas converter cells might be increased. Besides, to decrease the loss of aerosol within the gas exchanger, the pore size needs to be reduced from the current 100 nm. In fact, gas converter cells connected in parallel fully optimized for the highest performance might be significantly improve the system capabilities (gas velocity, aerosol washout speed, particle recovery). In case of potential production limitations of such silica membranes, technical solutions and analytical performance required must be compromised.

Further improved aerosol entrainment into the transport tube might also be realized with the application of a small ablation cell top (small diameter cell window on a plastic ring having an outlet on its top part) capturing the aerosol generated. Since the developed atmospheric sampling method has no requirements on the sample size and geometry, it can be a useful alternative for the analysis of large art and archeological objects. Furthermore, beside the elemental analyses performed on various solid samples, studies aiming isotope ratio determinations using LA-MC-ICP-MS utilizing aerosol suction are already in progress. Preliminary results indicate that this sampling method is well suited also for

isotopic determination and might be applied for the first time as a quasi non-destructive, non-contact approach for the analysis of objects of any size and shape.

This study indicates that the requirements for ablation cells (e.g. ablation gas purity, cell size and air tightness, aerosol dispersion and washout characteristics) can be overcome and the suction of the generated aerosol can also provide similar accuracy and precision such as the application of a closed ablation cell.

The future of LA-ICP-MS depends on the understanding of the various fundamental processes involved. The current limitations of the technique, e.g. elemental fractionation, particle size dependent vaporization and matrix dependence for quantification need to be studied in more detail to improve the capabilities of LA-ICP-MS. As shown in this study, with the application of air, a more stable particle size distribution was generated over time providing reduced elemental fractionation. By studying the particle forming processes during ablation in more detail, laser induced fractionation might be further reduced and improving stoichiometry of ablated and transported particles might contribute to better precision and accuracy and less dependence on matrix-matching in terms of quantification²²⁴. Furthermore in the future of LA-ICP-MS, the principle of the novel sampling method might be considered in the design of hand-held micro laser sampling systems equipped with a micro-plasma based ICP-MS for on site direct analysis of objects difficult to transport or highly valuable, such as those objects analyzed in the present work. In terms of lower detection limits, the detection efficiency of the ICP-MS might be improved by the development and optimization of ion funnels that directly focus the ions into the mass spectrometer and reduce the extent of space charge effects. Moreover, the recently developed fully simultaneous SF-ICP-MS instruments based on a Mattauch-Herzog configuration are expected to further improve the capabilities of LA-ICP-MS in terms of accuracy, precision, detection limits and less spectral interferences and are assumed to make an impact in a growing number of applications.

In terms of applications, geological studies most likely continue to remain the major area for LA-ICP-MS with respect to fluid inclusion analyses^{225,226,227} and geochronology^{228,229}, while the number of environmental^{230,231} and forensic^{232,233,234} applications are expected to be continuously increasing in the future.

7. Appendix

7.1 Quantitative results of Peruvian gold samples



Figure A. 1 Finger rings (EBN15010.01-03), Ebnöther Collection, Museum zu Allerheiligen Schaffhausen, Switzerland.

Table A. 1 Determined composition and trace element content of three finger rings (EBN15010.01, EBN15010.02, EBN15010.03)

	c [wt%]			c [$\mu\text{g g}^{-1}$]																
	Cu	Ag	Au	Ti	Cr	Mn	Fe	Co	Ni	Zn	As	Se	Pd	Cd	Sn	Sb	Te	Pt	Pb	Bi
EBN15010.01																				
AVG	4.4	49.8	45.8	0.3	0.9	2.0	87	0.4	-	95	-	-	43	0.9	0.8	-	1.8	600	17	1.8
RSD%	6	2	2	-	-	40	39	-	-	19	-	-	3	-	35	-	83	12	8	15
EBN15010.02																				
AVG	3.4	36.8	59.7	0.8	3	2.0	160	-	1.0	26	-	21	47	0.25	1.2	0.25	0.4	1090	6	0.6
RSD%	10	7	4	54	-	47	72	-	-	38	-	-	11	47	63	26	-	13	32	54
EBN15010.03																				
AVG	3.1	36.8	60.0	3	1.2	2.3	140	-	0.4	33	-	1.8	44	0.08	1.9	0.4	1.4	780	8	0.7
RSD%	7	2	1	-	15	39	52	-	57	64	-	-	7	-	34	32	35	9	57	18



Figure A. 2 Finger ring (EB15044, left) and nose ring (EBN15036, right), Ebnöther Collection, Museum zu Allerheiligen Schaffhausen, Switzerland.

Table A. 2 Determined composition and trace element content of various parts of a finger ring (EB15044)

	c [wt%]			c [$\mu\text{g g}^{-1}$]																
	Cu	Ag	Au	Ti	Cr	Mn	Fe	Co	Ni	Zn	As	Se	Pd	Cd	Sn	Sb	Te	Pt	Pb	Bi
Back, nostril																				
AVG	1.9	22.9	75.1	-	-	1.7	150	-	0.9	25	-	-	39	-	2.0	3	1.0	1470	7	4
Back, neck																				
AVG	1.9	22.1	75.9	-	-	3	190	0.19	1.3	22	-	1.4	39	0.5	2.1	2.1	1.1	1370	7	4
Back, ear																				
AVG	1.8	21.2	76.9	-	-	1.7	89	-	1.2	20	-	6	39	0.5	1.6	2.4	2.2	1310	8	5
Band shaped ring																				
AVG	2.0	24.0	73.9	-	-	2.3	160	0.23	0.6	20	-	-	24	0.25	2.4	3	1.0	690	6	4

Table A. 3 Determined composition and trace element content of various parts of a nose ring (EBN15036)

	c [wt%]			c [$\mu\text{g g}^{-1}$]																
	Cu	Ag	Au	Ti	Cr	Mn	Fe	Co	Ni	Zn	As	Se	Pd	Cd	Sn	Sb	Te	Pt	Pb	Bi
Loop shaped end																				
AVG	2.1	33.3	64.4	-	0.6	1.4	68	-	-	18	-	8	28	0.16	8	0.3	0.7	900	3	0.8
Middle wire																				
AVG	2.8	32.3	64.8	-	1.3	2.5	190	-	-	34	-	-	26	0.09	2.5	1.2	-	800	4	1.06
Outer wire, end																				
AVG	2.2	31.9	65.7	-	-	1.5	120	-	-	27	-	9	24	-	4	0.6	2.3	930	2.4	0.5



Figure A. 3 Necklace (EB15-027.01), Ebnöther Collection, Museum zu Allerheiligen Schaffhausen, Switzerland.

Table A. 4 Determined composition and trace element content of various parts of beads analyzed (EB15-027.01A, EB15-027.01B)

	c [wt%]			c [$\mu\text{g g}^{-1}$]																
	Cu	Ag	Au	Ti	Cr	Mn	Fe	Co	Ni	Zn	As	Se	Pd	Cd	Sn	Sb	Te	Pt	Pb	Bi
Solder (.01A)																				
AVG	3.7	33.6	62.5	-	0.4	0.4	29	-	-	9	0.5	5	30	0.16	0.20	0.11	2.3	810	6	0.7
RSD%	7	5	2	-	-	17	51	-	-	73	-	-	1	32	56	-	12	4	8	12
One hemisphere (.01A)																				
AVG	2.7	34.7	62.4	0.5	0.22	-	19	-	0.3	4	0.6	7	40	0.14	0.3	-	2.4	1250	4	0.3
RSD%	10	1	0.3	22	-	-	43	-	-	83	-	52	3	8	51	-	26	6	12	30
Other hemisphere (.01A)																				
AVG	2.5	35.6	61.8	0.6	0.5	0.5	52	-	-	5	-	6	39	0.15	0.18	0.07	2.5	1170	3	0.22
RSD%	5	1	0.6	51	63	-	-	-	-	62	-	-	5	62	26	3	16	9	14	38
Solder (.01B)																				
AVG	3.6	31.3	65.0	4	1.8	4	210	-	0.4	20	-	1.2	38	-	1.4	0.21	0.9	1010	6	0.3
RSD%	8	9	4	40	-	25	12	-	4	52	-	-	7	-	39	17	21	20	6	33
One hemisphere (.01B)																				
AVG	3.4	31.3	65.2	-	4	2.1	81	-	0.3	15	-	15	43	0.14	1.3	0.19	1.2	1050	6	0.4
RSD%	9	8	4	-	40	-	28	-	10	45	-	-	4	38	16	54	69	9	9	19
Other hemisphere (.01B)																				
AVG	3.1	32.1	64.6	0.5	4	3	69	-	-	24	-	6	42	0.3	1.1	0.11	0.7	1030	5	0.3
RSD%	6	6	3	-	-	-	9	-	-	24	-	36	7	48	25	-	12	16	10	12



Figure A. 4 Necklace (EB15853), Ebnöther Collection, Museum zu Allerheiligen Schaffhausen, Switzerland.

Table A. 5 Determined composition and trace element content of two beads (EB15853B, EB15853D)

	c [wt%]			c [$\mu\text{g g}^{-1}$]																	
	Cu	Ag	Au	Ti	Cr	Mn	Fe	Co	Ni	Zn	As	Se	Pd	Cd	Sn	Sb	Te	Pt	Pb	Bi	
Solder (EB15853B)																					
AVG	2.9	28.7	68.2	9	1.0	9	450	0.3	1.3	25	1.4	4	34	0.19	0.6	0.20	1.8	950	7	0.4	
RSD%	9	2	1	38	43	42	72	30	80	28	15	14	8	72	8	74	29	13	12	17	
One hemisphere (EB15853B)																					
AVG	2.6	29.0	68.2	2.5	0.5	3	210	0.22	0.4	25	0.9	10	36	0.07	0.7	0.19	1.8	1150	6	0.3	
RSD%	3	3	1	88	19	131	59	13	-	11	-	40	2	33	20	17	26	4	2	8	
Other hemisphere (EB15853B)																					
AVG	2.6	29.2	67.9	25	1.7	36	1520	1.6	3	32	4	3	36	0.15	1.0	2.2	2.3	1150	8	0.4	
RSD%	3	5	2	78	53	51	43	37	81	10	19	-	5	32	34	155	33	6	26	12	
Bead (EB15853D)																					
AVG	5.6	21.3	72.8	12	-	5	570	-	0.7	36	-	7	59	0.14	1.3	0.18	1.1	2080	110	0.13	
RSD%	3	4	1	45	-	28	79	-	12	30	-	30	3	61	54	23	77	4	11	15	



Figure A. 5 Round bead (EBN15032, left) and nose ornament (EBN15040, right), Ebnöther Collection, Museum zu Allerheiligen Schaffhausen, Switzerland.

Table A. 6 Determined composition and trace element content of various parts of a round bead (EBN15032)

	c [wt%]			c [$\mu\text{g g}^{-1}$]																
	Cu	Ag	Au	Ti	Cr	Mn	Fe	Co	Ni	Zn	As	Se	Pd	Cd	Sn	Sb	Te	Pt	Pb	Bi
Solder																				
AVG	2.8	24.7	72.4	0.7	-	4	200	-	-	25	-	5	34	0.20	1.9	5	0.4	1240	6	1.2
RSD%	18	1	1	-	-	8	12	-	-	42	-	-	13	9	12	15	-	19	31	5
One hemisphere																				
AVG	2.8	23.5	73.6	1.1	1.1	4	120	0.3	0.9	27	-	-	34	0.19	1.9	7	1.2	1270	5	1.5
RSD%	6	3	1	-	77	71	48	-	21	10	-	-	15	47	13	21	18	11	43	25
Other hemisphere																				
AVG	2.6	22.9	74.3	1.7	0.5	3	130	0.13	0.25	20	-	-	32	0.3	1.8	6	0.5	1100	8	1.3
RSD%	6	1	0.3	-	-	37	45	13	-	18	-	-	12	64	11	10	45	20	83	13

Table A. 7 Determined composition and trace element content of two parts of a nose ornament (EBN15040)

	c [wt%]			c [$\mu\text{g g}^{-1}$]																
	Cu	Ag	Au	Ti	Cr	Mn	Fe	Co	Ni	Zn	As	Se	Pd	Cd	Sn	Sb	Te	Pt	Pb	Bi
Suspension ring																				
AVG	2.2	24.0	73.7	1.9	0.6	7	290	0.24	0.6	47	6	6	46	0.23	1.2	1.6	1.6	1550	15	1.1
RSD%	6	8	3	85	49	21	15	28	45	3	11	-	12	44	16	2	41	15	26	23
Connecting ring																				
AVG	2.2	24.7	73.0	2.1	0.8	7	230	0.22	0.9	47	10	-	48	0.23	3	1.3	1.3	1690	14	1.0
RSD%	12	6	2	105	72	31	14	6	24	14	89	-	23	27	107	29	10	25	30	29



Figure A. 6 Nose ornaments (EB15-052.03, left; EBN15014, right), Ebnöther Collection, Museum zu Allerheiligen Schaffhausen, Switzerland.

Table A. 8 Determined composition and trace element content of three parts of a nose ornament (EB15-052.03)

	c [wt%]			c [$\mu\text{g g}^{-1}$]																
	Cu	Ag	Au	Ti	Cr	Mn	Fe	Co	Ni	Zn	As	Se	Pd	Cd	Sn	Sb	Te	Pt	Pb	Bi
Pendant																				
AVG	1.5	17.8	80.5	2.5	-	7	320	0.3	0.8	26	2.0	5	58	0.5	1.2	2.7	1.0	2390	36	1.5
RSD%	4	2	0.4	85	-	22	25	8	29	15	-	-	8	28	13	7	74	5	16	3
Connecting ring																				
AVG	1.6	17.7	80.4	2.1	-	9	330	0.3	0.9	34	3	7	57	0.3	1.3	3	2.1	2290	43	1.8
RSD%	16	4	1	6	-	45	41	34	61	30	-	50	27	47	41	42	39	24	23	18
Suspension ring																				
AVG	2.9	26.0	70.9	1.4	-	1.2	33	-	1.2	49	-	10	44	0.2	1.2	0.5	0.6	2040	5	0.4
RSD%	4	6	2	-	-	16	20	-	-	9	-	32	9	50	15	20	6	1	32	8

Table A. 9 Determined composition and trace element content of various parts of a nose ornament (EBN15014)

	c [wt%]			c [$\mu\text{g g}^{-1}$]																
	Cu	Ag	Au	Ti	Cr	Mn	Fe	Co	Ni	Zn	As	Se	Pd	Cd	Sn	Sb	Te	Pt	Pb	Bi
Back, broken head																				
AVG	2.9	37.9	59.1	-	-	-	-	-	-	33	-	-	28	0.11	3	0.8	1.5	890	15	2.2
Back, outer wire																				
AVG	3.6	39.3	57.0	0.5	-	0.5	41	-	-	13	-	-	23	0.13	1.4	0.6	1.3	750	14	3
Back, inner wire																				
AVG	3.0	38.7	58.2	4	-	1.2	62	-	-	13	-	3	25	0.06	1.2	0.3	0.6	850	10	1.5
Back, bonding part																				
AVG	3.9	38.5	57.5	0.8	-	0.9	14	-	-	19	-	-	29	0.3	1.1	0.6	0.9	930	9	1.4



Figure A. 7 Nose ornaments (EBN15015, left; EBN15016, right), Ebnöther Collection, Museum zu Allerheiligen Schaffhausen, Switzerland.

Table A. 10 Determined composition and trace element content of two parts of a nose ornament (EBN15015)

	c [wt%]			c [$\mu\text{g g}^{-1}$]																	
	Cu	Ag	Au	Ti	Cr	Mn	Fe	Co	Ni	Zn	As	Se	Pd	Cd	Sn	Sb	Te	Pt	Pb	Bi	
Connecting ring																					
AVG	2.7	21.9	75.3	0.7	-	1.8	69	-	0.5	27	-	-	34	0.3	0.8	0.7	0.9	1310	5	0.7	
RSD%	6	6	2	-	-	18	23	-	48	20	-	-	21	23	12	12	56	16	17	8	
Suspension ring																					
AVG	2.6	32.5	64.7	4	0.6	4	130	-	0.6	22	2.1	2.1	36	0.5	3	0.4	1.7	1360	6	0.9	
RSD%	6	4	2	31	-	21	27	-	39	42	-	-	8	25	17	9	27	10	51	20	

Table A. 11 Determined composition and trace element content of two parts a nose ornament (EBN15016)

	c [wt%]			c [$\mu\text{g g}^{-1}$]																	
	Cu	Ag	Au	Ti	Cr	Mn	Fe	Co	Ni	Zn	As	Se	Pd	Cd	Sn	Sb	Te	Pt	Pb	Bi	
Connecting ring																					
AVG	2.5	27.1	70.3	1.5	1.4	4	270	0.3	1.1	36	2.3	-	42	0.22	4	2.5	0.9	1610	12	1.3	
RSD%	3	2	1	50	-	14	24	16	14	13	32	-	4	39	7	3	20	6	20	17	
Suspension ring																					
AVG	2.2	22.7	74.8	-	1.8	3	200	0.4	1.1	30	1.7	9	56	0.5	5	2.2	1.6	2530	10	1.0	
RSD%	8	6	2	-	-	10	6	11	18	14	-	-	16	68	9	4	32	8	10	3	



Figure A. 8 Nose ornaments (EBN15017, left; EB15-052.04, right), Ebnöther Collection, Museum zu Allerheiligen Schaffhausen, Switzerland.

Table A. 12 Determined composition and trace element content of the suspension ring of a nose ornament (EBN15017)

	c [wt%]			c [$\mu\text{g g}^{-1}$]																
	Cu	Ag	Au	Ti	Cr	Mn	Fe	Co	Ni	Zn	As	Se	Pd	Cd	Sn	Sb	Te	Pt	Pb	Bi
Suspension ring																				
AVG	3.5	30.2	66.1	6	1.2	8	300	0.4	0.5	38	1.9	7	34	0.23	6	1.4	1.2	1400	19	1.8
RSD%	28	4	2	96	-	90	64	-	4	12	-	-	11	31	17	7	69	12	43	58

Table A. 13 Determined composition and trace element content of the various parts of a nose ornament (EB15-052.04)

	c [wt%]			c [$\mu\text{g g}^{-1}$]																
	Cu	Ag	Au	Ti	Cr	Mn	Fe	Co	Ni	Zn	As	Se	Pd	Cd	Sn	Sb	Te	Pt	Pb	Bi
Pendant																				
AVG	2.3	24.2	73.3	0.4	0.4	0.8	-	0.8	2.0	10	0.6	-	46	0.3	0.7	0.24	2.0	1760	5	0.25
RSD%	9	2	0.8	-	-	16	-	-	72	25	-	-	18	35	43	33	26	17	25	35
Suspension ring																				
AVG	2.5	26.3	71.0	-	1.0	1.7	54	0.3	0.3	16	0.8	-	39	0.3	1.7	0.4	2.3	1590	10	1.0
RSD%	13	2	1	-	87	48	46	-	77	30	-	-	5	30	77	46	4	2	95	15
Connecting ring																				
AVG	2.0	23.7	74.1	0.5	0.8	3	150	0.16	0.6	25	2.0	3	40	0.21	1.6	0.6	1.9	1480	9	0.4
RSD%	2	3	1	-	64	42	15	11	75	8	33	-	19	16	34	21	13	15	10	18



Figure A. 9 Nose ornament (EBN15039), Ebnöther Collection, Museum zu Allerheiligen Schaffhausen, Switzerland.

Table A. 14 Determined composition and trace element content of various parts of a nose ornament (EBN15039)

	c [wt%]			c [$\mu\text{g g}^{-1}$]																
	Cu	Ag	Au	Ti	Cr	Mn	Fe	Co	Ni	Zn	As	Se	Pd	Cd	Sn	Sb	Te	Pt	Pb	Bi
Suspension ring																				
AVG	2.3	43.2	54.3	1.1	-	0.9	69	-	-	15	-	3	29	0.24	0.6	0.14	0.9	940	4	0.4
RSD%	1	2	1	20	-	37	31	-	-	20	-	-	11	92	7	12	57	10	7	8
Connecting ring to stone pendant																				
AVG	2.4	42.7	54.8	-	1.1	0.8	37	-	0.3	20	-	4	27	0.22	0.5	0.13	1.0	890	6	0.5
RSD%	9	3	3	-	65	16	10	-	-	10	-	-	4	66	9	17	82	7	23	29
Connecting ring to gold pendant																				
AVG	2.4	42.8	54.7	1.6	-	1.1	33	-	1.0	19	1.6	9	30	0.3	0.5	0.14	0.8	930	7	0.5
RSD%	11	5	3	87	-	38	49	-	-	10	-	-	5	50	20	-	15	6	33	20
Gold pendant																				
AVG	2.2	31.4	66.3	1.5	0.4	3	250	0.5	-	42	1.9	-	28	0.21	2.0	0.7	0.7	940	6	0.7
RSD%	4	3	1	-	-	42	34	-	-	11	21	-	42	56	37	21	27	60	7	24



Figure A. 10 Nose ornament (EBN15038, left; EB15-052.05, right), Ebnöther Collection, Museum zu Allerheiligen Schaffhausen, Switzerland.

Table A. 15 Determined composition and trace element content of various parts of a nose ornament (EBN15038)

	c [wt%]			c [$\mu\text{g g}^{-1}$]																
	Cu	Ag	Au	Ti	Cr	Mn	Fe	Co	Ni	Zn	As	Se	Pd	Cd	Sn	Sb	Te	Pt	Pb	Bi
Suspension ring																				
AVG	2.6	30.5	66.7	0.8	1.4	1.4	73	-	-	15	-	-	28	0.18	1.3	0.12	0.6	940	3	0.25
RSD%	6	8	3	-	-	31	20	-	-	30	-	-	16	70	12	7	10	16	15	4
Connecting ring																				
AVG	2.5	29.0	68.3	0.9	0.9	0.7	52	-	0.6	13	-	-	34	0.08	0.8	0.4	0.7	1230	3	0.7
RSD%	5	3	2	-	-	16	19	-	-	26	-	-	12	-	18	20	46	11	23	24
Pendant																				
AVG	3.4	25.6	70.9	-	-	0.5	21	0.10	-	8	-	3	20	0.15	0.6	0.12	0.5	610	1.7	0.6
RSD%	11	16	6	-	-	16	62	-	-	23	-	-	4	-	25	35	64	11	4	14

Table A. 16 Determined composition and trace element content of various parts of a nose ornament (EB15-052.05)

	c [wt%]			c [$\mu\text{g g}^{-1}$]																
	Cu	Ag	Au	Ti	Cr	Mn	Fe	Co	Ni	Zn	As	Se	Pd	Cd	Sn	Sb	Te	Pt	Pb	Bi
Pendant																				
AVG	1.2	44.8	54.0	-	0.3	2.1	87	0.21	0.8	33	0.7	7	19	0.4	1.4	0.4	4	670	8	1.7
RSD%	9	1	1	-	-	68	117	-	56	45	7	57	16	42	24	38	25	8	22	10
Connecting ring																				
AVG	2.3	30.3	67.3	0.4	1.8	3	160	0.3	0.5	23	1.9	-	40	0.3	3	0.8	3	1650	7	1.4
RSD%	6	2	0.8	-	-	36	32	-	15	27	11	-	10	26	33	12	7	9	20	12
Suspension ring																				
AVG	2.0	21.7	76.1	0.9	0.6	3	130	-	0.9	30	-	9	36	0.3	4	0.7	1.8	1310	2.5	0.5
RSD%	7	1	0.3	10	4	54	44	-	27	32	-	60	12	90	29	38	25	10	18	32



Figure A. 11 Gold deposit samples (X19, top left; X26, top right; M395/Pa, bottom left; M395/Pb, bottom right), Petersen Collection, Pontificia Universidad Católica del Perú, Lima, Peru.

Table A. 17 Determined composition and trace element content of various deposit samples (X19, X26, M395/Pa, M395/Pb)

	c [wt%]		c [$\mu\text{g g}^{-1}$]																	
	Ag	Au	Ti	Cr	Mn	Fe	Co	Ni	Cu	Zn	As	Se	Pd	Cd	Sn	Sb	Te	Pt	Pb	Bi
X19																				
AVG	9.5	90.5	1.4	1.6	-	43	0.15	0.6	170	3	-	-	5	0.5	0.4	9	1.8	0.6	0.9	0.9
RSD%	2	0.2	-	25	-	95	9	29	6	33	-	-	47	72	16	8	-	25	72	84
X26																				
AVG	5.1	94.8	1.0	5	-	29	0.7	10	420	2.5	1.5	12	3	0.11	1.4	21	0.4	1.3	0.5	0.6
RSD%	1	0.1	-	127	-	27	-	133	8	23	-	44	52	-	59	17	-	58	91	10
M395/Pa																				
AVG	10.1	89.8	-	-	-	120	0.3	1.5	230	3	4	7	5	0.4	4	9	1.2	0.7	2.5	0.8
RSD%	2	0.2	-	-	-	100	5	67	7	114	30	28	12	46	158	11	30	64	62	29
M395/Pb																				
AVG	0.5	99.5	-	-	0.6	35	0.15	0.24	300	3	-	-	0.6	0.08	0.3	5	1.0	0.4	0.3	0.3
RSD%	2	0.01	-	-	-	54	-	43	27	56	-	-	49	86	73	28	71	26	85	48

7.2 Abbreviations

∅	diameter
λ	wavelength
μL	microliter
μm	micrometer
°C	centigrade
A.D.	Anno Domini
a.u.	arbitrary unit
AC	alternating current
amu	atomic mass unit
AVG	average
B.C.	Before Christ
bp.	boiling point
c.v.	certified value
CCD	charge coupled device
cm	centimeter
cm ²	square centimeter
cm ³	cubic centimeter
cps	counts per second
CRM	certified reference material
DC	direct current
DRC	dynamic reaction cell
DSI	direct sample insertion
e.g.	for example (exempli gratia)
ESA	electrostatic analyzer
et. al.	and co-workers (et alii)
etc.	and so on (et cetera)
ETV	electrothermal vaporization
eV	electron volt
FAAS	flame atomic absorption spectrometry
FEP	fluorinated ethylene-propylene
FES	flame atomic emission spectrometry
fs	femtosecond
FT	Fourier transform
g	gram

GC	gas chromatography
GED	gas exchange device
GFAAS	graphite furnace atomic absorption spectrometry
GW	giga-watt
h	hour
HG	hydride generation
HHPN	hydraulic high pressure nebulization
HR	high resolution
HV	high voltage
Hz	Hertz
i.d.	inner diameter
ICP	inductively coupled plasma
ICP-MS	inductively coupled plasma-mass spectrometry
ICP-OES	inductively coupled plasma-optical emission spectrometry
IP	ionization potential
IR	infrared
IT	ion trap
J	Joule
K	Kelvin
kg	kilogram
kV	kilovolt
L	liter
LA	laser ablation
LOD	limits of detection
m	meter
m/z	mass to charge ratio
M ²⁺	doubly charged ion
m ³	cubic meter
mbar	millibar
MC-MS	multicollector-mass spectrometer
MCN	micro-concentric nebulizer
MH	Mattauch-Herzog
MHz	mega-Hertz
min	minute
mJ	milli-Joule
mL	milliliter
mm	millimeter

mp.	melting point
MS	mass spectrometry, mass spectrometer
ms	millisecond
n	number of analysis
n _e	electron number density
ng	nanogram
NIR	near infrared
NIST	National Institute of Standards and Technology
nm	nanometer
ns	nanosecond
P/A factor	calibration between pulse counting and analogue detection modes
PFA	perfluoroalkoxy
PN	pneumatic nebulization
PP	polypropylene
ppb	parts per billion
ppm	parts per million
ppq	parts per quadrillion
PSD	particle size distribution
PTFE	polytetrafluoroethylene
PVC	polyvinyl chloride
Q-MS	quadrupole-mass spectrometer
R	resolution
RF	radio frequency
RSD	relative standard deviation
s	second
SD	standard deviation
SEM	scanning electron microscopy
SF-MS	sector field-mass spectrometer
SRM	standard reference material
TOF	time of flight
torr	~ 1mmHg (Torricelli)
USN	ultrasonic nebulization
UV	ultraviolet
V	volt
W	watt
wt%	weight percent
YAG	yttrium aluminium garnet

7.3 List of figures

Figure 1	Schematic diagram of a quadrupole ICP-MS, the ELAN 6000 ⁶ .	18
Figure 2	Schematic view of an Ar ICP in a Fassel torch ⁶ .	19
Figure 3	Calculated values for degree of ionization (%) of M ⁺ and M ²⁺ at $T_i = 7500$ K, $n_e = 1 \times 10^{15}$ cm ⁻³ . Elements marked by an asterisk yield significant amounts of M ²⁺ but partition functions are not available ^{15,18} .	21
Figure 4	Degree of ionization versus ionization energy for singly charged ions in the ICP ^{15,19} .	22
Figure 5	Transverse profiles of ions across the mouth of the plasma torch ¹⁵ .	23
Figure 6	ICP and sampling interface for ICP-MS ^{15,18} . A: torch and load coil; B: induction region; C: aerosol gas flow; D: initial radiation zone; E: normal analytical zone; F: sampler cone; G: skimmer cone; H: boundary layer of ICP gas deflected outside sampler; I: supersonic jet; J: ion lens.	24
Figure 7	Schematic diagram of quadrupole rods showing ion trajectory and applied voltages ¹⁵ .	25
Figure 8	Reverse Nier-Johnson geometry HR-ICP-MS ³⁷ .	26
Figure 9	Schematic diagram of a discrete dynode electron multiplier ⁶ .	27
Figure 10	Double pass spray chamber ¹⁵ .	29
Figure 11	A typical glass cyclonic spray chamber ⁵ .	29
Figure 12	Schematic view of a glass concentric nebulizer ⁵ .	30
Figure 13	Schematic setup of LA-ICP-MS ⁶⁵ .	32
Figure 14	Schematic view of the optical beam path performing beam homogenization for an ArF excimer laser operating at a wavelength of 193 nm in combination with a petrographic microscope ⁸³ .	34
Figure 15	Fractionation indices reported by Fryer et. al. for a total of 4 minutes continuous ablation of NIST 610 silicate glass normalized to Ca ¹⁴⁸ .	40
Figure 16	Schematic view of the experimental setup for the tube material studies. Plastic taps were applied to switch between different tubes without changing the carrier gas flow rate.	47
Figure 17	Enhancement in signal intensity using 5, 10, 20 m long PVC tubes normalized to 1 m. The tubes were applied as transport tubes. Laser ablation system: ArF excimer (GeoLas C, 94.5 μ m, 10 Hz, 3.2 J cm ⁻²). Measured oxide formation: 0.31 % (1 m), 0.44 % (5 m), 0.56 % (10 m), 1.06 % (20 m) based on ThO ⁺ /Th ⁺ .	49
Figure 18	Element-to-Ca ratios for 5, 10 and 20 m PVC tubes, normalized to the results obtained with 1 m long tube. The tubes were applied as transport tubes.	50
Figure 19	Differences in the He gas blank when using PVC tubes of 1, 2, 5, 10, 20 m downstream of the ablation cell (n=3, RSD \approx 1 %). The most significant differences in intensity were measured for argon-hydride (m/z 41) with a factor of 3.6, oxygen (m/z 16) with a factor of 3.3 and water (m/z 18) with a factor of 1.7 when comparing background intensities measured for a tube length of 20 m in contrast to 1 m. The increase in intensity of carbon	

(m/z 12) was 60 %, whereas the intensity of nitrogen (m/z 14) decreased by 30 %. Furthermore, a minor decrease of 4 % in the ion intensity of argon was also observed..... 50

Figure 20 Temporal changes of plasma composition when using 1 and 10 m long PVC tubes over a period of 4.5 hours. To plot the analytes to the same figure, the intensity of $^{12}\text{C}^+$ was divided by 10. 51

Figure 21 Correlation of the background intensity of $^1\text{H}^+$ and $^{16}\text{O}^+$ and the background corrected intensity obtained for $^{23}\text{Na}^+$, $^{29}\text{Si}^+$, $^{31}\text{P}^+$ and $^{66}\text{Zn}^+$ when using the 10 m PVC tube as transport tube (40 μm , 10 Hz). To plot the analytes to the same figure, the intensity of $^{23}\text{Na}^+$ and $^{29}\text{Si}^+$ was divided by 100 and 10, respectively..... 53

Figure 22 Element-to-Ca ratios for 10 m PVC tube normalized to the results obtained using 2 m long tube. The tubes were used upstream of the sample cell. Helium was applied as carrier gas and ultra high purity water was nebulized into the plasma. The oxide rate was determined for ThO^+/Th^+ and was 11.2 % for both tube lengths (2 m and 10 m). 53

Figure 23 Correlation between the abundance normalized sensitivity for Ag and the background count rates for $^{36}\text{Ar}^+$, $^{16}\text{O}^+$, $^{40}\text{Ar}^1\text{H}^+$ and $^1\text{H}^+$, using different tube material and length. Oxide formation based on ThO^+/Th^+ : 0.36 % (1 m PVC), 0.77 % (10 m PVC), 0.45 % (1 m nylon), 2.21 % (10 m nylon), 0.38 % (1 m Teflon), 0.43 % (10 m Teflon), 0.35 % (1 m copper), 0.35 % (9 m copper). Doubly-charged ion formation based on $^{42}\text{Ca}^{++}/^{42}\text{Ca}^+$: 0.29 % (1 m PVC), 0.45 % (10 m PVC), 0.36 % (1 m nylon), 0.67 % (10 m nylon), 0.35 % (1 m Teflon), 0.38 % (10 m Teflon), 0.37 % (1 m copper), 0.36 % (9 m copper). 54

Figure 24 Element-to-Ca ratios for the four tube materials. The calculated element ratios for a longer tube (10 m except copper 9 m) were normalized to the results obtained with 1 m long tube. The tubes were applied upstream of the ablation cell. 55

Figure 25 Correlation of the 1st ionization potential and the signal enhancement based on the data of Figure 2 (20 m PVC normalized to 1 m). 56

Figure 26 Atmospheric sampling approach. The laser generated aerosol is directly sucked by the tube directed relatively close (within 3 mm) to the ablated crater at an angle of either 90 ° or 45 °. 63

Figure 27 Sketch of the experimental setup of the novel sampling approach..... 63

Figure 28 Average background count rates for the closed cell configuration using various gases for aerosol transport. In the experiment assigned with “He without GED”, the gas exchange device was not connected to the transport system..... 65

Figure 29 Comparison of the abundance normalized sensitivity obtained using various carrier gases ($\lambda = 193$ nm, 60 μm spot size, 10 Hz ablation frequency, 20 J cm^{-2} energy density)..... 65

Figure 30 Light microscope images of craters generated by 150 laser pulses ($\lambda = 193$ nm, 60 μm spot size, 10 Hz ablation frequency, 21.6 J cm^{-2} energy density) on NIST 610 SRM with a magnification of 1000. During ablation the cell was flushed by Ar (left) or compressed air (right) at a flow rate of 0.25 L min^{-1} 66

Figure 31 Typical transient signals of six analytes of NA2 gold calibration material¹⁹⁴. Laser ablation sampling was performed in ambient air using the open cell configuration and 100 μm spot size, 4 Hz ablation frequency and a fluence of 8 J cm^{-2} at a wavelength of 213 nm. The ICP-MS dwell time was set to 50 ms per isotope. 67

Figure 32	Light microscope image of a crater generated by 120 laser pulses ($\lambda = 213$ nm, $50 \mu\text{m}$ spot size, 4 Hz ablation frequency, 12.0 J cm^{-2} energy density) on NA2 gold calibration material with a magnification of 1000. Laser ablation was carried out in laboratory ambient air at a flow rate of 0.25 L min^{-1}	68
Figure 33	Relative sensitivity of various elements within NIST 610 (silicate glass) and MBH-B22 (brass) obtained for the aerosol suction approach in contrast to in cell ablation.....	70
Figure 34	Transient signals of six analytes of MBH-B22 brass CRM. Laser ablation was performed in ambient air using the novel sampling approach and $50 \mu\text{m}$ spot size, 10 Hz ablation frequency, a fluence of 8 J cm^{-2} at a wavelength of 213 nm. The ICP-MS dwell time was set to 50 ms per isotope.....	72
Figure 35	Transient signals of various analytes during the ablation of NIST 610 ($\lambda = 193$ nm, $60 \mu\text{m}$ spot size, 10 Hz ablation frequency, 21.9 J cm^{-2} energy density) in compressed air (top) and ambient air (bottom).	78
Figure 36	Abundance normalized sensitivities calculated for the ablation of NIST 610 ($\lambda = 193$ nm, $60 \mu\text{m}$ spot size, 10 Hz ablation frequency, 21.9 J cm^{-2} energy density) in compressed air, laboratory ambient air and humid air. The sensitivity ratio of compressed air and ambient air indicates that only boron is affected by humidity changes in the ablation cell.....	79
Figure 37	Fractionation indices calculated for the ablation of NIST 610 ($\lambda = 193$ nm, $80 \mu\text{m}$ spot size, 10 Hz ablation frequency, 4 minutes time duration) in He.	83
Figure 38	Fractionation indices calculated for the ablation of NIST 610 ($\lambda = 266$ nm, $50 \mu\text{m}$ spot size, 10 Hz ablation frequency, 4 minutes time duration) in He.	83
Figure 39	Fractionation indices calculated for the ablation of NIST 610 ($\lambda = 193$ nm, $80 \mu\text{m}$ spot size, 10 Hz ablation frequency, 4 minutes time duration) in He and air.....	84
Figure 40	Fractionation indices calculated for the ablation of NIST 610 ($\lambda = 266$ nm, $50 \mu\text{m}$ spot size, 10 Hz ablation frequency, 4 minutes time duration) in He and air.....	84
Figure 41	Transient signals of ^{42}Ca , ^{208}Pb , ^{238}U and the temporal intensity ratio of $^{208}\text{Pb} / ^{42}\text{Ca}$ and $^{208}\text{Pb} / ^{232}\text{U}$ during the ablation of NIST 610 ($\lambda = 266$ nm, $50 \mu\text{m}$ spot size, 10 Hz ablation frequency, 4 minutes time duration) in He (left side) and in air (right side).	85
Figure 42	Comparison of particle size distributions (normalized to arbitrary units) generated in He, Ar and air at a flow rate of 0.25 L min^{-1} . The aerosol was not transported through the gas exchanger during the experiments..	87
Figure 43	Comparison of particle size distributions obtained for Ar and air without transporting the aerosol through the GED.....	87
Figure 44	Influence of the gas exchange process on the particle size distribution using He as carrier gas.	88
Figure 45	Influence of the gas exchange process on the particle size distribution using air as carrier gas.	88
Figure 46	Temporal changes in particle size distribution of aerosols generated in He, Ar and air. Data acquisition was performed in steps of 30 s (n=3).....	89
Figure 47	Scanning electron microscope images obtained for aerosols generated from NIST 610 in helium without gas exchange (left) and with exchange to Ar (right).....	90

Figure 48 Scanning electron microscope images obtained for aerosols generated from NIST 610 in argon without introducing the aerosols into the gas exchange device.	91
Figure 49 Scanning electron microscope images obtained for aerosols generated from NIST 610 in air without gas exchange (left) and with exchange to Ar (right).....	92
Figure 50 Comparison of radial ion signal profiles obtained for ${}^7\text{Li}$, ${}^{66}\text{Zn}$, ${}^{208}\text{Pb}$ at a constant sampling depth of 3.0 mm. Laser ablation sampling was carried out at wavelengths of 193 nm and 266 nm using Ar (top) or He (middle and bottom) as aerosol carrier gas and represent ion diffusion profiles for Ar only (top and bottom) and He admixed with Ar (middle) within the ICP.....	96
Figure 51 Comparison of radial ion signal profiles obtained for ${}^7\text{Li}$, ${}^{66}\text{Zn}$, ${}^{208}\text{Pb}$ at a constant sampling depth of 3.0 mm to profiles reported in ref. ¹¹ . Laser ablation sampling was carried out at wavelengths of 266 nm and 193 nm using Ar (top) or He (middle and bottom) as aerosol carrier gas and represent ion diffusion profiles for Ar only (top) and He admixed with Ar (middle and bottom) within the ICP.....	97
Figure 52 Signal intensity of Li, Zn and Pb in dependence on the total central channel gas flow rate entering the ICP. Laser ablation sampling was carried out at a wavelength of 193 nm using He (top and bottom right) or Ar (bottom left) as aerosol carrier gas and represent ion diffusion profiles for He admixed with Ar (top) and Ar only (bottom left and right) within the ICP.	100
Figure 53 Comparison of element sensitivities for optimum ICP operating conditions and individual element sensitivity maxima obtained when introducing the aerosol in helium into the ICP versus exchanging helium to argon.	103
Figure 54 Comparison of sensitivity ratios obtained when exchanging helium to argon in contrast when the aerosol is directly introduced into the ICP in helium.	104
Figure 55 Comparison of sensitivity ratios obtained when passing the aerosol in helium through the GED in contrast when the aerosol is directly introduced into the ICP. The ratios indicate an approximately 20 % loss of aerosol within the GED.	105
Figure 56 Comparison of sensitivity ratios obtained when exchanging helium to argon in contrast when the aerosol is passed through the GED in helium without gas exchange.	105
Figure 57 Intensity ratios observed using 10 m and 1 m long nylon tubes connected upstream of the ablation cell. The results indicate that gas impurities from the nylon tube material causing significant intensity enhancement in the ICP-MS. By removing these impurities by the gas exchange process, ICP operating conditions become stable. Uncertainty is expressed as \pm standard deviation. Oxide formation based on ThO^+/Th^+ without gas exchange: 0.27 % (1 m nylon tube), 1.27 % (10 m nylon tube), with gas exchange: 0.24 % (1 m nylon tube), 0.25 % (10 m nylon tube).	107
Figure 58 The obtained background count rates do not indicate severe differences when the gas impurities are removed from the gas stream by the GED. In contrast, impurities from the longer nylon tube (10 m) entering the ICP are causing higher background count rates.....	108
Figure 59 Transient signal structures obtained for direct liquid ablation in air and aerosol suction of a multi-element solution containing various elements at a nominal concentration of 5 mg/L. NIR-fs-LA was carried out with a spot size of approximately 100 μm , 1 mJ pulse energy, providing an energy density of 12.7 J/cm ² and a	

power density of approximately 85 GW/cm ² . The ICP-MS dwell time was set to 30 ms to minimize the transient fluctuations of the signals generated by the diaphragm pump.....	111
Figure 60 Abundance normalized sensitivity as a function of ablation frequency obtained for direct liquid ablation of a multi-element solution containing various elements at a nominal concentration of 5 mg/L. Measurement uncertainty is expressed as \pm standard deviation (n=3).....	112
Figure 61 Limits of detection (ng/g) as a function of ablation frequency obtained for direct liquid ablation of a multi-element solution containing various elements at a nominal concentration of 5 mg/L. Measurement uncertainty is expressed as \pm one standard deviation (n=3).....	112
Figure 62 Calculated element concentrations using solution “B1” as external standard and ¹¹⁵ In as internal standard. Measurement uncertainty is expressed as \pm standard deviation (n=3).....	113
Figure 63 Comparison of the results obtained using solution calibration with the certified values of FAU7 and FAU10.	122
Figure 64 Cross validation of NA1 and NA2. For quantification of NA1, NA2 was applied as external standard. The calculation of the element concentration values was performed using either the information values of NA2 (Fig. A) or the determined values (Fig. C) using solution calibration. For quantification of NA2, NA1 was applied as external standard. The calculation of the element concentration values was performed using either the information values of NA1 (Fig. B) or the determined values (Fig. D) using solution calibration. The concentration of Ag was calculated in mg kg ⁻¹ and divided by 10000 to include it in the graphs.	125
Figure 65 Typical transient signal structures of six analytes when ablating NA1 and NA2 using femtosecond- (10 Hz) and nanosecond- (5 Hz) laser ablation systems (‘dry’ plasma conditions).....	127
Figure 66 The application of closed ablation cells with sufficient space to accommodate sample(s) and solid calibration materials.	128
Figure 67 The application of ablation cells with an aperture on the bottom for the analysis of large objects. The analyzed object depicted is a large gold cauldron found in the Chiemsee, Germany in 2001.	128
Figure 68 The analysis of a cruciform pectoral (EBN15020, Ebnöther Collection, Museum zu Allerheiligen Schaffhausen, Switzerland) using an open design ablation cell, and laser generated craters using 50 μ m spot size on the surface of the object.....	130
Figure 69 Side-view and front-view of the gold figurine.	132
Figure 70 Bottom of the foot (left) and the soldered granules forming groups (right).....	133
Figure A. 1 Finger rings (EBN15010.01-03), Ebnöther Collection, Museum zu Allerheiligen Schaffhausen, Switzerland.	139
Figure A. 2 Finger ring (EB15044, left) and nose ring (EBN15036, right), Ebnöther Collection, Museum zu Allerheiligen Schaffhausen, Switzerland.	140
Figure A. 3 Necklace (EB15-027.01), Ebnöther Collection, Museum zu Allerheiligen Schaffhausen, Switzerland.	141

Figure A. 4	Necklace (EB15853), Ebnöther Collection, Museum zu Allerheiligen Schaffhausen, Switzerland...	142
Figure A. 5	Round bead (EBN15032, left) and nose ornament (EBN15040, right), Ebnöther Collection, Museum zu Allerheiligen Schaffhausen, Switzerland	143
Figure A. 6	Nose ornaments (EB15-052.03, left; EBN15014, right), Ebnöther Collection, Museum zu Allerheiligen Schaffhausen, Switzerland.....	144
Figure A. 7	Nose ornaments (EBN15015, left; EBN15016, right), Ebnöther Collection, Museum zu Allerheiligen Schaffhausen, Switzerland.....	145
Figure A. 8	Nose ornaments (EBN15017, left; EB15-052.04, right), Ebnöther Collection, Museum zu Allerheiligen Schaffhausen, Switzerland.....	146
Figure A. 9	Nose ornament (EBN15039), Ebnöther Collection, Museum zu Allerheiligen Schaffhausen, Switzerland.....	147
Figure A. 10	Nose ornament (EBN15038, left; EB15-052.05, right), Ebnöther Collection, Museum zu Allerheiligen Schaffhausen, Switzerland.....	148
Figure A. 11	Gold deposit samples (X19, top left; X26, top right; M395/Pa, bottom left; M395/Pb, bottom right), Petersen Collection, Pontificia Universidad Católica del Perú, Lima, Peru.	149

7.4 List of tables

Table 1	Distribution of ionization potentials (IP) among the elements for singly and doubly charged ions at 1 eV intervals. Adapted from refs ^{15,19}	22
Table 2	Operating conditions for laser ablation and ICP-MS.....	48
Table 3	Changing element-to-Ca intensity ratios as a function of time (individual data points are shown) and tube (PVC) length (40 μm , 10 Hz).....	52
Table 4	Operating conditions for ICP-MS, laser ablation systems and gas exchange device.....	62
Table 5	Gas flow rates applied for the measurements performed using various gases for laser ablation and aerosol transport. The measured oxide formation based on ThO^+/Th^+ is shown for the respective measurements.....	64
Table 6	Determined element concentrations and average detection limits ($\mu\text{g g}^{-1}$) for the analysis of NIST 8054 and NIST 8063 using NA2 as calibration standard and Cu as internal standard. The laser sampling was carried out in ambient air in a partially open ablation cell.....	69
Table 7	Analytical results and obtained detection limits for MBH-B22 treating as sample using MBH-B26 brass certified reference material as calibration standard and Cu as internal standard. The laser sampling was carried out in ambient air without using an ablation cell.....	71
Table 8	Analytical results and obtained detection limits for JK-37 steel turnings CRM treating as samples using ECRM-298-1 as calibration standard and Cr as internal standard. The laser sampling was carried out in ambient air without using an ablation cell.....	71
Table 9	Limits of detection (ng g^{-1}) as a function of ablation frequency (NIR-fs-LA) for direct liquid ablation in ambient air utilizing aerosol suction.....	76
Table 10	Melting and boiling points of boron, boron-oxide and boranes.....	79
Table 11	Operating conditions for laser ablation, ICP-MS and GED.....	82
Table 12	Operating conditions for laser ablation, ICP-MS and GED.....	95
Table 13	Operating conditions for laser ablation, ICP-MS used by Wang et. al. in ref ¹¹	98
Table 14	Operating conditions for laser ablation, ICP-MS and GED.....	99
Table 15	U^+/Th^+ intensity ratio, oxide formation and a list of elements showing maximum sensitivity obtained for individual nebulizer gas flow rates when introducing He admixed with Ar ('He, no GED') or Ar only ('He exchange to Ar') into the ICP.....	101
Table 16	Comparison of B and As sensitivities for He and He exchange to Ar experiments based on the conditions shown in Table 15.....	103
Table 17	Operating conditions for laser ablation, ICP-MS and GED.....	106

Table 18	Potential hydrogen and oxygen based polyatomic interferences on m/z 29, 31, 42, 53, 55, 57, 75	108
Table 19	Operating conditions of ICP-MS and laser ablation systems	120
Table 20	Elements, concentrations of the solution standards used for calibration and isotopes included in the measurement protocol	121
Table 21	Reference values in comparison to the determined concentrations (mg kg ⁻¹) of FAU7 (NIST 8053), FAU10 (NIST 8062), NA1 and NA2 using solution calibration and Cu as internal standard ('wet' plasma conditions). Sampling was carried out using femtosecond laser ablation (n=6).....	123
Table 22	Determined concentrations (mg kg ⁻¹) of NA1 using FAU7 and FAU10 as calibration standards and Cu as internal standard ('dry' plasma conditions). Sampling was carried out using either femtosecond or nanosecond laser ablation (n=4).....	126
Table 23	Determined concentrations (mg kg ⁻¹) of NA2 using FAU7 and FAU10 as calibration standards and Cu as internal standard ('dry' plasma conditions). Sampling was carried out using either femtosecond or nanosecond laser ablation (n=4).....	126
Table 24	Determined composition and trace element content of the suspension ring of a nose ornament (EBN15020)	130
Table 25	Determined composition and trace element content of various parts (granules, n=3; joints, n=3; base metal 1, n=6; base metal 2, n=5) of the gold figurine.....	133
Table A. 1	Determined composition and trace element content of three finger rings (EBN15010.01, EBN15010.02, EBN15010.03).....	139
Table A. 2	Determined composition and trace element content of various parts of a finger ring (EB15044).....	140
Table A. 3	Determined composition and trace element content of various parts of a nose ring (EBN15036)	140
Table A. 4	Determined composition and trace element content of various parts of beads analyzed (EB15-027.01A, EB15-027.01B).....	141
Table A. 5	Determined composition and trace element content of two beads (EB15853B, EB15853D)	142
Table A. 6	Determined composition and trace element content of various parts of a round bead (EBN15032)....	143
Table A. 7	Determined composition and trace element content of two parts of a nose ornament (EBN15040)	143
Table A. 8	Determined composition and trace element content of three parts of a nose ornament (EB15-052.03)	144
Table A. 9	Determined composition and trace element content of various parts of a nose ornament (EBN15014)	144
Table A. 10	Determined composition and trace element content of two parts of a nose ornament (EBN15015) ..	145
Table A. 11	Determined composition and trace element content of two parts a nose ornament (EBN15016)	145

Table A. 12	Determined composition and trace element content of the suspension ring of a nose ornament (EBN15017).....	146
Table A. 13	Determined composition and trace element content of the various parts of a nose ornament (EB15-052.04).....	146
Table A. 14	Determined composition and trace element content of various parts of a nose ornament (EBN15039).....	147
Table A. 15	Determined composition and trace element content of various parts of a nose ornament (EBN15038).....	148
Table A. 16	Determined composition and trace element content of various parts of a nose ornament (EB15-052.05).....	148
Table A. 17	Determined composition and trace element content of various deposit samples (X19, X26, M395/Pa, M395/Pb).....	149

7.5 References

- 1 R. S. Houk, V. A. Fassel, G. D. Flesch, H. J. Svec, A. L. Gray and C. E. Taylor, Inductively Coupled Argon Plasma As An Ion-Source For Mass-Spectrometric Determination Of Trace-Elements, *Anal. Chem.*, 1980, **52**, 2283.
- 2 D. A. Solyom, O. A. Gron, J. H. Barnes and G. M. Hieftje, Analytical capabilities of an inductively coupled plasma Mattauch-Herzog mass spectrometer, *Spectrochim. Acta B*, 2001, **56**, 1717.
- 3 L. Moens, F. Vanhaecke, J. Riondato and R. Dams, Some figures of merit of a new double focusing inductively coupled plasma mass spectrometer, *J. Anal. At. Spectrom.*, 1995, **10**, 569.
- 4 D. Günther, H. P. Longerich and S. E. Jackson, A New Enhanced Sensitivity Quadrupole Inductively-Coupled Plasma-Mass Spectrometer (ICP-MS), *Canadian Journal of Applied Spectroscopy*, 1995, **40**, 111.
- 5 S. J. Hill, Inductively Coupled Plasma and its Applications, Blackwell, 2007
- 6 A. Montaser, Inductively Coupled Plasma Mass Spectrometry, *Wiley-VCH*, 1988
- 7 R. Hermann and C. T. J. Alkemade, Chemical Analysis by Flame Photometry, 2nd ed., Interscience Publishers, New York, 1983
- 8 B. Welz and M. Sperling, Atomic Absorption Spectrometry, Wiley-VCH, Weinheim, 1999
- 9 J. M. Mermet and E. Poussel, ICP emission spectrometers - 1995 analytical figures of merit, *Appl. Spectrosc.*, 1995, **49**, A 12.
- 10 K. L. Linge and K. E. Jarvis, Quadrupole ICP-MS: Introduction to Instrumentation, Measurement Techniques and Analytical Capabilities, *Geostandards and Geoanalytical Research*, 2009, **33**, 445.
- 11 Z. Wang, B. Hattendorf and D. Günther, Vaporization and ionization of laser ablation generated aerosols in an inductively coupled plasma mass spectrometer - implications from ion distribution maps, *J. Anal. At. Spectrom.*, 2006, **21**, 1143.
- 12 E. H. Evans and J. J. Giglio, Interferences in inductively coupled plasma mass-spectrometry - a review, *J. Anal. At. Spectrom.*, 1993, **8**, 1.
- 13 H. P. Longerich, Oxychlorine ions in inductively coupled plasma mass spectrometry - effect of chlorine speciation as Cl⁻ and ClO₄⁻, *J. Anal. At. Spectrom.*, 1993, **8**, 439.
- 14 H. Niu and R. S. Houk, Fundamental aspects of ion extraction in inductively coupled plasma mass spectrometry, *Spectrochim. Acta B*, 1996, **51**, 779.
- 15 K. E. Jarvis, A. L. Gray and R. S. Houk, Handbook of Inductively Coupled Plasma Mass Spectrometry, Blackie & Son, 1992

-
- 16 H. S. Niu, K. Hu and R. S. Houk, Langmuir probe measurements of electron-temperature and electron-density behind the skimmer of an inductively coupled plasma mass-spectrometer, *Spectrochim. Acta B*, 1991, **46**, 805.
 - 17 A. Goldwasser and J. M. Mermet, Contribution of the Charge-Transfer Process to the Excitation Mechanisms in Inductively Coupled Plasma Atomic Emission-Spectroscopy, *Spectrochimica Acta Part B-Atomic Spectroscopy*, 1986, **41**, 725.
 - 18 R. S. Houk, Mass-Spectrometry of Inductively Coupled Plasmas, *Anal. Chem.*, 1986, **58**, A97.
 - 19 A. R. Date and A. L. Gray, Applications of Inductively Coupled Plasma, *Blackie, Glasgow*, 1989
 - 20 D. J. Douglas and J. B. French, An improved interface for inductively coupled plasma-mass spectrometry (ICP-MS), *Spectrochim. Acta B*, 1986, **41**, 197.
 - 21 J. A. Olivares and R. S. Houk, Ion sampling for inductively coupled plasma mass-spectrometry, *Anal. Chem.*, 1985, **57**, 2674.
 - 22 D. J. Douglas and J. B. French, Gas-dynamics of the inductively coupled plasma mass- spectrometry interface, *J. Anal. At. Spectrom.*, 1988, **3**, 743.
 - 23 W. N. Radicic, J. B. Olsen, R. V. Nielson, J. H. Macedone and P. B. Farnsworth, Characterization of the supersonic expansion in the vacuum interface of an inductively coupled plasma mass spectrometer by high-resolution diode laser spectroscopy, *Spectrochim. Acta B*, 2006, **61**, 686.
 - 24 S. D. Tanner, Space-charge in ICP-MS - calculation and implications, *Spectrochim. Acta, Part B*, 1992, **47**, 809.
 - 25 G. R. Gillson, D. J. Douglas, J. E. Fulford, K. W. Halligan and S. D. Tanner, Nonspectroscopic Interelement Interferences In Inductively Coupled Plasma Mass-Spectrometry, *Anal. Chem.*, 1988, **60**, 1472.
 - 26 A. R. Date and A. L. Gray, Plasma source-mass spectrometry using an inductively coupled plasma and a high-resolution quadrupole mass filter, *Analyst*, 1981, **106**, 1255.
 - 27 N. Bradshaw, E. F. H. Hall and N. E. Sanderson, Inductively coupled plasma as an ion-source for high-resolution mass-spectrometry, *J. Anal. At. Spectrom.*, 1989, **4**, 801.
 - 28 C. B. Douthitt, The evolution and applications of multicollector ICPMS (MC-ICPMS), *Anal. Bioanal. Chem.*, 2008, **390**, 437.
 - 29 A. N. Halliday, D. C. Lee, J. N. Christensen, W. Yi, C. M. Hall, C. E. Jones, D.-A. H. Teagle, A. J. Walder and P. A. Freedman, I.C.P. magnetic sector multicollector mass spectrometry and its applications to geochemistry, *Mineralogical Magazine*, 1994, **58A**, 366.
 - 30 M. Balcerzak, An overview of analytical applications of time of flight-mass spectrometric (TOF-MS) analyzers and an inductively coupled plasma-TOF-MS technique, *Anal. Sci.*, 2003, **19**, 979.
-

-
- 31 P. P. Mahoney, G. Q. Li and G. M. Hieftje, Laser ablation inductively coupled plasma mass spectrometry with a time of flight mass analyser, *J. Anal. At. Spectrom.*, 1996, **11**, 401.
- 32 D. W. Koppenaal, C. J. Barinaga and M. R. Smith, Performance Of An Inductively Coupled Plasma Source Ion Trap Mass Spectrometer, *J. Anal. At. Spectrom.*, 1994, **9**, 1053.
- 33 K. E. Milgram, F. M. White, K. L. Goodner, C. H. Watson, D. W. Koppenaal, Barinaga, CJ, B. H. Smith, J. D. Winefordner, A. G. Marshall, R. S. Houk and J. R. Eyler, High resolution inductively coupled plasma fourier transform ion cyclotron resonance mass spectrometry, *Anal. Chem.*, 1997, **69**, 3714.
- 34 R. Thomas, Beginner's guide to ICP-MS - Part VI - The mass analyzer, *Spectroscopy*, 2001, **16**, 44.
- 35 A. N. Halliday, D. C. Lee, J. N. Christensen, M. Rehkamper, W. Yi, X. Z. Luo, C. M. Hall, C. J. Ballentine, T. Pettke and C. Stirling, Applications of multiple collector-ICPMS to cosmochemistry, geochemistry, and paleoceanography, *Geochim. Cosmochim. Acta*, 1998, **62**, 919.
- 36 L. Moens and N. Jakubowski, Double-focusing mass spectrometers in ICPMS, *Anal. Chem.*, 1-4-1998, **70**, 251A.
- 37 U. Giessmann and U. Greb, High resolution ICP-MS - a new concept for elemental mass spectrometry, *Fresenius J. Anal. Chem.*, 1994, **350**, 186.
- 38 R. Thomas, A beginner's guide to ICP-MS part X - Detectors, *Spectroscopy*, 2002, **17**, 34.
- 39 E. A. Kurz, Channel Electron Multipliers, *Am.*, 1979, **11**, 67.
- 40 J. G. Timothy and R. L. Bybee, Performance-Characteristics of High-Conductivity Channel Electron Multipliers, *Rev. Sci. Instrum.*, 1978, **49**, 1192.
- 41 A. N. Eaton, R. C. Hutton, P. Belton and D. Gregson, Extended dynamic range ICP-MS; elemental analysis from ppb to percent, *Chem. Geol.*, 1988, **70**, 174.
- 42 N. Onda, A new approach to extending the dynamic range in inductively coupled plasma-mass spectrometry, *Tohoku Journal of Experimental Medicine*, 1996, **178**, 91.
- 43 E. K. Potter, C. H. Stirling, M. B. Andersen and A. N. Halliday, High precision Faraday collector MC-ICPMS thorium isotope ratio determination, *Int. J. Mass Spectrom.*, 2005, **247**, 10.
- 44 A. Sanz-Medel (ed.), *Flow Analysis with Atomic Spectrometric Detectors*, Elsevier, Amsterdam, 1999
- 45 S. Maillefer, C. R. Lehr and W. R. Cullen, The analysis of volatile trace compounds in landfill gases, compost heaps and forest air, *Appl.*, 2003, **17**, 154.
- 46 D. Kremer, G. Ilgen and J. Feldmann, GC-ICP-MS determination of dimethylselenide in human breath after ingestion of Se-77-enriched selenite: monitoring of in-vivo methylation of selenium, *Anal. Bioanal. Chem.*, 2005, **383**, 509.
-

-
- 47 E. M. Krupp, C. Johnson, C. Rechsteiner, M. Moir, D. Leong and J. Feldmann, Investigation into the determination of trimethylarsine in natural gas and its partitioning into gas and condensate phases using (cryotrapping)/gas chromatography coupled to inductively coupled plasma mass spectrometry and liquid/solid sorption techniques, *Spectrochim. Acta B*, 2007, **62**, 970.
- 48 M. J. Powell, D. W. Boomer and R. J. Mcvicars, Introduction of Gaseous Hydrides Into An Inductively Coupled Plasma Mass-Spectrometer, *Anal. Chem.*, 1986, **58**, 2864.
- 49 X. Wang, M. Viczian, A. Lasztity and R. M. Barnes, Lead Hydride Generation for Isotope Analysis by Inductively Coupled Plasma Mass Spectrometry, *J. Anal. At. Spectrom.*, 1988, **3**, 821.
- 50 M. Janghorbani and B. T. G. Ting, Comparison of Pneumatic Nebulization and Hydride Generation Inductively Coupled Plasma Mass-Spectrometry for Isotopic Analysis of Selenium, *Anal. Chem.*, 1989, **61**, 701.
- 51 J. W. Olesik and L. C. Bates, Characterization of aerosols produced by pneumatic nebulizers for inductively coupled plasma sample introduction - effect of liquid and gas flow rates on volume based drop size distributions, *Spectrochim. Acta B*, 1995, **50**, 285.
- 52 R. H. Scott, V. A. Fassel, R. N. KNISELEY and D. E. Nixon, Inductively Coupled Plasma-Optical Emission Analytical Spectrometry - Compact Facility for Trace Analysis of Solutions, *Anal. Chem.*, 1974, **46**, 75.
- 53 B. L. Sharp, Pneumatic Nebulizers and Spray Chambers for Inductively Coupled Plasma Spectrometry - A Review .1. Nebulizers, *J. Anal. At. Spectrom.*, 1988, **3**, 613.
- 54 B. L. Sharp, Pneumatic Nebulizers and Spray Chambers for Inductively Coupled Plasma Spectrometry - A Review .2. Spray Chambers, *J. Anal. At. Spectrom.*, 1988, **3**, 939.
- 55 P. W. J. M. Boumans Ed., Fundamental Aspects of Aerosol Generation and Transport, Inductively Coupled Plasma Emission Spectroscopy, Part II. , Wiley, New York, 1987
- 56 A. Montaser and D. W. Golightly Eds., Liquid Sample Introduction into Plasmas, Inductively Coupled Plasmas in Analytical Atomic Spectrometry, 2nd ed. , VCH, New York, 1992
- 57 F. Vanhaecke, M. Vanholderbeke, L. Moens and R. Dams, Evaluation of a commercially available microconcentric nebulizer for inductively coupled plasma mass spectrometry, *J. Anal. At. Spectrom.*, 1996, **11**, 543.
- 58 V. Karanassios and G. Horlick, A computer-controlled direct sample insertion device for inductively coupled plasma mass-spectrometry, *Spectrochim. Acta B*, 1989, **44**, 1345.
- 59 D. Günther, S. E. Jackson and H. P. Longerich, Laser ablation and arc/spark solid sample introduction into inductively coupled plasma mass spectrometers [Review], *Spectrochim. Acta B*, 15-3-1999, **54**, 381.
- 60 D. W. Golightly, A. Montaser, B. L. Smith and A. F. Dorrzapf, Spark Ablation Inductively Coupled Plasma Spectrometry for Analysis of Geologic Materials, *Talanta*, 1989, **36**, 299.
-

-
- 61 F. Vanhaecke, M. Resano and L. Moens, Electrothermal vaporisation ICP-mass spectrometry (ETV-ICP-MS) for the determination and speciation of trace elements in solid samples - A review of real-life applications from the author's lab, *Anal. Bioanal. Chem.*, 2002, **374**, 188.
- 62 A. L. Gray, Solid sample introduction by laser ablation for inductively coupled plasma source-mass spectrometry, *Analyst*, 1985, **110**, 551.
- 63 N. S. Mokgalaka and J. L. Gardea-Torresdey, Laser ablation inductively coupled plasma mass spectrometry: Principles and applications, *Applied Spectroscopy Reviews*, 2006, **41**, 131.
- 64 D. Günther, Laser-ablation inductively-coupled plasma mass spectrometry, *Anal. Bioanal. Chem.*, 2002, **372**, 31.
- 65 D. Günther and B. Hattendorf, Solid sample analysis using laser ablation inductively coupled plasma mass spectrometry, *Trend. Anal. Chem.*, 2005, **24**, 255.
- 66 R. E. Russo, X. L. Mao and O. V. Borisov, Laser ablation sampling, *Trend. Anal. Chem.*, 1998, **17**, 461.
- 67 M. Odegard and M. Hamester, Preliminary investigation into the use of a high resolution inductively coupled plasma-mass spectrometer with laser ablation for bulk analysis of geological materials fused with $\text{Li}_2\text{B}_4\text{O}_7$, *Geostand. Newsl.*, 1997, **21**, 245.
- 68 T. Hirata and R. W. Nesbitt, U Pb isotope geochronology of zircon: Evaluation of the laser probe inductively coupled plasma mass spectrometry technique, *Geochim. Cosmochim. Acta*, 1995, **59**, 2491.
- 69 J. S. Becker and H. J. Dietze, Determination of trace elements in geological samples by laser ablation inductively coupled plasma mass spectrometry, *Fresenius J. Anal. Chem.*, 1999, **365**, 429.
- 70 T. J. Shepherd and S. R. Chenery, Laser ablation ICP-MS elemental analysis of individual fluid inclusions; an evaluation study, *Geochim. Cosmochim. Acta*, 1995, **59**, 3997.
- 71 M. Guillon and D. Günther, Quasi 'non-destructive' laser ablation-inductively coupled plasma-mass spectrometry fingerprinting of sapphires, *Spectrochim. Acta B*, 2001, **56**, 1219.
- 72 S. F. Durrant, Laser ablation inductively coupled plasma mass spectrometry: achievements, problems, prospects, *J. Anal. At. Spectrom.*, 1999, **14**, 1385.
- 73 J. Sneddon and Y. I. Lee, Lasers in analytical atomic spectrometry - An overview, *Spectr. Letters*, 1997, **30**, 1417.
- 74 P. Arrowsmith, Laser ablation of solids for elemental analysis by inductively coupled plasma mass-spectrometry, *Anal. Chem.*, 1987, **59**, 1437.
- 75 Y. Huang, Y. Shibata and M. Morita, Micro laser ablation-inductively coupled plasma-mass spectrometry. 1. Instrumentation and performance of microlaser ablation system, *Anal. Chem.*, 1993, **65**, 2999.
-

-
- 76 S. Chenery and J. M. Cook, Determination of rare-earth elements in single mineral grains by laser ablation microprobe inductively coupled plasma-mass spectrometry - preliminary-study, *J. Anal. At. Spectrom.*, 1993, **8**, 299.
- 77 T. E. Jeffries, S. E. Jackson and H. P. Longerich, Application of a frequency quintupled Nd:YAG source ($\lambda = 213$ nm) for laser ablation inductively coupled plasma mass spectrometric analysis of minerals, *J. Anal. At. Spectrom.*, 1998, **13**, 935.
- 78 S. E. Jackson, H. P. Longerich, G. R. Dunning and B. J. Freyer, The application of laser-ablation microprobe; inductively coupled plasma-mass spectrometry (LAM-ICP-MS) to in situ trace-element determinations in minerals, *Can. Mineral.*, 1992, **30**, Part 4, 1049.
- 79 M. Guillong, I. Horn and D. Günther, Capabilities of a homogenized 266 nm Nd : YAG laser ablation system for LA-ICP-MS, *J. Anal. At. Spectrom.*, 2002, **17**, 8.
- 80 J. Koch, M. Wälle, J. Pisonero and D. Günther, Performance characteristics of ultra-violet femtosecond laser ablation inductively coupled plasma mass spectrometry at similar to 265 and similar to 200 nm, *J. Anal. At. Spectrom.*, 2006, **21**, 932.
- 81 R. E. Russo, X. L. Mao, J. J. Gonzalez and S. S. Mao, Femtosecond laser ablation ICP-MS, *J. Anal. At. Spectrom.*, 2002, **17**, 1072.
- 82 F. Poitrasson, X. L. Mao, S. S. Mao, R. Freydier and R. E. Russo, Comparison of ultraviolet femtosecond and nanosecond laser ablation inductively coupled plasma mass spectrometry analysis in glass, monazite, and zircon, *Anal. Chem.*, 2003, **75**, 6184.
- 83 D. Günther, R. Frischknecht, C. A. Heinrich and H. J. Kahlert, Capabilities of an Argon Fluoride 193 nm excimer laser for laser ablation inductively coupled plasma mass spectrometry microanalysis of geological materials, *J. Anal. At. Spectrom.*, 1997, **12**, 939.
- 84 P. Telouk, E. F. Rose-Koga and F. Albarede, Preliminary results from a new 157 nm laser ablation ICP-MS instrument: New opportunities in the analysis of solid samples, *Geostandards Newsletter-the Journal of Geostandards and Geoanalysis*, 2003, **27**, 5.
- 85 C. Leloup, P. Marty, D. Dallava and M. Perdereau, Quantitative analysis for impurities in uranium by laser ablation inductively coupled plasma mass spectrometry: Improvements in the experimental setup, *J. Anal. At. Spectrom.*, 1997, **12**, 945.
- 86 F. Bea, P. Montero, A. Stroh and J. Baasner, Microanalysis of minerals by an excimer UV-LA-ICP-MS system, *Chem. Geol.*, 22-11-1996, **133**, 145.
- 87 I. Horn, D. Günther and M. Guillong, Evaluation and design of a solid-state 193 nm OPO-Nd : YAG laser ablation system, *Spectrochim. Acta B*, 2003, **58**, 1837.
- 88 M. Guillong, I. Horn and D. Günther, A comparison of 266 nm, 213 nm and 193 nm produced from a single solid state Nd : YAG laser for laser ablation ICP-MS, *J. Anal. At. Spectrom.*, 2003, **18**, 1224.
-

-
- 89 J. Gonzalez, X. L. Mao, J. Roy, S. S. Mao and R. E. Russo, Comparison of 193, 213 and 266 nm laser ablation ICP-MS, *J. Anal. At. Spectrom.*, 2002, **17**, 1108.
- 90 H. P. Longerich, D. Günther and S. E. Jackson, Elemental fractionation in laser ablation inductively coupled plasma mass spectrometry, *Fresenius J. Anal. Chem.*, 1996, **355**, 538.
- 91 P. M. Outridge, W. Doherty and D. C. Gregoire, The formation of trace element enriched particulates during laser ablation of refractory materials, *Spectrochim. Acta B*, 1996, **51**, 1451.
- 92 H. R. Kuhn and D. Günther, Elemental fractionation studies in laser ablation inductively coupled plasma mass spectrometry on laser-induced brass aerosols, *Anal. Chem.*, 2003, **75**, 747.
- 93 J. Koch, A. von Bohlen, R. Hergenroder and K. Niemax, Particle size distributions and compositions of aerosols produced by near-IR femto- and nanosecond laser ablation of brass, *J. Anal. At. Spectrom.*, 2004, **19**, 267.
- 94 R. E. Russo, X. L. Mao, H. C. Liu, J. Gonzalez and S. S. Mao, Laser ablation in analytical chemistry - a review, *Talanta*, 2002, **57**, 425.
- 95 A. J. G. Mank and P. R. D. Mason, A critical assessment of laser ablation ICP-MS as an analytical tool for depth analysis in silica-based glass samples, *J. Anal. At. Spectrom.*, 1999, **14**, 1143.
- 96 S. A. Darke and J. F. Tyson, Interaction of laser-radiation with solid materials and its significance to analytical spectrometry - a review, *J. Anal. At. Spectrom.*, 1993, **8**, 145.
- 97 X. L. Mao and R. E. Russo, Observation of plasma shielding by measuring transmitted and reflected laser pulse temporal profiles, *Appl. Phys. A - Mater.*, 1997, **64**, 1.
- 98 X. L. Mao, W. T. Chan, M. Caetano, M. A. Shannon and R. E. Russo, Preferential vaporization and plasma shielding during nano second laser ablation, *Appl. Surf. Sci.*, 1996, **96-8**, 126.
- 99 R. Hergenroder, Laser-generated aerosols in laser ablation for inductively coupled plasma spectrometry, *Spectrochim. Acta B*, 2006, **61**, 284.
- 100 K. Niemax, Laser ablation - reflections on a very complex technique for solid sampling, *Fresenius J. Anal. Chem.*, 2001, **370**, 332.
- 101 H. R. Kuhn and D. Günther, The agglomeration state of nanosecond laser-generated aerosol particles entering the ICP, *Anal. Bioanal. Chem.*, 2005, **383**, 434.
- 102 S. M. Eggins, L. P. J. Kinsley and J. M. G. Shelley, Deposition and element fractionation processes during atmospheric pressure laser sampling for analysis by ICP-MS, *Appl. Surf. Sci.*, 1998, **129**, 278.
- 103 R. Glaus, R. Kägi, F. Krumeich and D. Günther, Phenomenological studies on structure and elemental composition of nanosecond and femtosecond laser-generated aerosols with implications on LA-ICP-MS, *Spectrochim. Acta, Part B, submitted*, 2010
-

-
- 104 H. R. Kuhn and D. Günther, Laser ablation-ICP-MS: particle size dependent elemental composition studies on filter-collected and online measured aerosols from glass, *J. Anal. At. Spectrom.*, 2004, **19**, 1158.
- 105 H. R. Kuhn, M. Guillong and D. Günther, Size-related vaporisation and ionisation of laser-induced glass particles in the inductively coupled plasma, *Anal. Bioanal. Chem.*, 2004, **378**, 1069.
- 106 H. R. Kuhn, J. Koch, R. Hergenroder, K. Niemax, M. Kalberer and D. Günther, Evaluation of different techniques for particle size distribution measurements on laser-generated aerosols, *J. Anal. At. Spectrom.*, 2005, **20**, 894.
- 107 D. B. Aeschliman, S. J. Bajic, D. P. Baldwin and R. S. Houk, High-speed digital photographic study of an inductively coupled plasma during laser ablation: comparison of dried solution aerosols from a microconcentric nebulizer and solid particles from laser ablation, *J. Anal. At. Spectrom.*, 2003, **18**, 1008.
- 108 J. Koch, S. Schlamp, T. Rosgen, D. Fliegel and D. Günther, Visualization of aerosol particles generated by near infrared nano- and femtosecond laser ablation, *Spectrochim. Acta B*, 2007, **62**, 20.
- 109 J. Koch, M. Walle, S. Schlamp, T. Rosgen and D. Günther, Expansion phenomena of aerosols generated by laser ablation under helium and argon atmosphere, *Spectrochim. Acta B*, 2008, **63**, 37.
- 110 J. Koch, M. Walle, R. Dietiker and D. Günther, Analysis of laser-produced aerosols by inductively coupled plasma mass spectrometry: Transport phenomena and elemental fractionation, *Anal. Chem.*, 2008, **80**, 915.
- 111 M. Thompson, J. E. Goulter and F. Sieper, Laser ablation for the introduction of solid samples into an inductively coupled plasma for atomic-emission spectrometry, *Analyst (London)*, 1981, **106**, 32.
- 112 J. W. Carr and G. Horlick, Laser Vaporization of Solid Metal Samples Into An Inductively Coupled Plasma, *Spectrochimica Acta Part B-Atomic Spectroscopy*, 1982, **37**, 1.
- 113 T. Ishizuka and Y. Uwamino, Inductively coupled plasma emission-spectrometry of solid samples by laser ablation, *Spectrochim. Acta B*, 1983, **38**, 519.
- 114 P. Arrowsmith and S. K. Hughes, Entrainment and transport of laser ablated plumes for subsequent elemental analysis, *Appl. Spectrosc.*, 1988, **42**, 1231.
- 115 T. Mochizuki, A. Sakashita, H. Iwata, T. Kagaya, T. Shimamura and P. Blair, Laser ablation for direct elemental analysis of solid samples by inductively coupled plasma mass-spectrometry, *Anal. Sci.*, 1988, **4**, 403.
- 116 L. Moenkeblankenburg, M. GACKLE, D. Gunther and J. Kammel, Processes of Laser Ablation and Vapor Transport to the ICP, *Plasma Source Mass Spectrometry*, 1990, **85**, 1.
- 117 D. Bleiner and D. Günther, Theoretical description and experimental observation of aerosol transport processes in laser ablation inductively coupled plasma mass spectrometry, *J. Anal. At. Spectrom.*, 2001, **16**, 449.
-

-
- 118 C. C. Garcia, H. Lindner and K. Niemax, Transport efficiency in femtosecond laser ablation inductively coupled plasma mass spectrometry applying ablation cells with short and long washout times, *Spectrochim. Acta B*, 2007, **62**, 13.
- 119 E. F. Cromwell and P. Arrowsmith, Fractionation effects in laser ablation inductively coupled plasma mass spectrometry, *Appl. Spectrosc.*, 1995, **49**, 1652.
- 120 J. Koch, I. Feldmann, N. Jakubowski and K. Niemax, Elemental composition of laser ablation aerosol particles deposited in the transport tube to an ICP, *Spectrochim. Acta B*, 2002, **57**, 975.
- 121 E. L. Gurevich and R. Hergenroder, A simple laser ICP-MS ablation cell with wash-out time less than 100 ms, *J. Anal. At. Spectrom.*, 2007, **22**, 1043.
- 122 J. Pisonero, D. Fliegel and D. Günther, High efficiency aerosol dispersion cell for laser ablation-ICP-MS, *J. Anal. At. Spectrom.*, 2006, **21**, 922.
- 123 H. Lindner, D. Autrique, J. Pisonero, D. Gunther and A. Bogaerts, Numerical simulation analysis of flow patterns and particle transport in the HEAD laser ablation cell with respect to inductively coupled plasma spectrometry, *J. Anal. At. Spectrom.*, 2010, **25**, 295.
- 124 D. Monticelli, E. L. Gurevich and R. Hergenroder, Design and performances of a cyclonic flux cell for laser ablation, *J. Anal. At. Spectrom.*, 2009, **24**, 328.
- 125 J. Koch, G. Schaldach, H. Berndt and K. Niemax, Numerical simulation of aerosol transport, *Anal. Chem.*, 2004, **76**, 130A.
- 126 D. Bleiner and A. Bogaerts, Computer simulations of laser ablation sample introduction for plasma-source elemental microanalysis, *J. Anal. At. Spectrom.*, 2006, **21**, 1161.
- 127 Z. C. Hu, Y. S. Liu, S. Gao, S. H. Hu, R. Dietiker and D. Gunther, A local aerosol extraction strategy for the determination of the aerosol composition in laser ablation inductively coupled plasma mass spectrometry, *J. Anal. At. Spectrom.*, 2008, **23**, 1192.
- 128 D. Asogan, B. L. Sharp, C. J. P. O'Connor, D. A. Green and R. W. Hutchinson, An open, non-contact cell for laser ablation-inductively coupled plasma-mass spectrometry, *J. Anal. At. Spectrom.*, 2009, **24**, 917.
- 129 H. Reinhardt, M. Kriews, H. Miller, O. Schrems, C. Ludke, E. Hoffmann and J. Skole, Laser ablation inductively coupled plasma mass spectrometry: a new tool for trace element analysis in ice cores, *Fresenius J. Anal. Chem.*, 2001, **370**, 629.
- 130 J. Feldmann, A. Kindness and P. Ek, Laser ablation of soft tissue using a cryogenically cooled ablation cell, *J. Anal. At. Spectrom.*, 2002, **17**, 813.
- 131 N. N. Sesì, A. Mackenzie, K. E. Shanks, P. Y. Yang and G. M. Hieftje, Fundamental studies of mixed-gas inductively coupled plasmas, *Spectrochim. Acta B*, 1994, **49**, 1259.
- 132 R. S. Houk, A. Montaser and V. A. Fassel, Mass-Spectra and Ionization Temperatures in An Argon-Nitrogen Inductively Coupled Plasma, *Appl. Spectrosc.*, 1983, **37**, 425.
-

-
- 133 A. Montaser and R. L. Vanhoven, Mixed-Gas, Molecular-Gas, and Helium Inductively Coupled Plasmas for Analytical Atomic Spectrometry - A Critical-Review, *Crc Critical Reviews in Analytical Chemistry*, 1987, **18**, 45.
- 134 P. Schramel and L. Q. Xu, Further Investigation of An Argon-Hydrogen Plasma in ICP-Spectroscopy, *Fresenius Zeitschrift fur Analytische Chemie*, 1984, **319**, 229.
- 135 I. Horn and D. Günther, The influence of ablation carrier gasses Ar, He and Ne on the particle size distribution and transport efficiencies of laser ablation-induced aerosols: implications for LA-ICP-MS, *Appl. Surf. Sci.*, 2003, **207**, 144.
- 136 D. Gunther and C. A. Heinrich, Enhanced sensitivity in laser ablation-ICP mass spectrometry using helium-argon mixtures as aerosol carrier - Plenary lecture, *J. Anal. At. Spectrom.*, 1999, **14**, 1363.
- 137 I. Horn, M. Guillong and D. Günther, Wavelength dependant ablation rates for metals and silicate glasses using homogenized laser beam profiles - implications for LA-ICP-MS, *Appl. Surf. Sci.*, 2001, **182**, 91.
- 138 A. P. K. Leung, W. T. Chan, X. L. Mao and R. E. Russo, Influence of gas environment on picosecond laser ablation sampling efficiency and ICP conditions, *Anal. Chem.*, 15-11-1998, **70**, 4709.
- 139 F. G. Smith, D. R. Wiederin and R. S. Houk, Argon xenon plasma for alleviating polyatomic ion interferences in inductively coupled plasma mass-spectrometry, *Anal. Chem.*, 1991, **63**, 1458.
- 140 M. Guillong and C. A. Heinrich, Sensitivity enhancement in laser ablation ICP-MS using small amounts of hydrogen in the carrier gas, *J. Anal. At. Spectrom.*, 2007, **22**, 1488.
- 141 S. F. Durrant, Feasibility of improvement in analytical performance in laser ablation inductively coupled plasma-mass spectrometry (LA-ICP-MS) by addition of nitrogen to the argon plasma, *Fresenius J. Anal. Chem.*, 1994, **349**, 768.
- 142 I. Rodushkin, P. Nordlund, E. Engstrom and D. C. Baxter, Improved multi-elemental analyses by inductively coupled plasma-sector field mass spectrometry through methane addition to the plasma, *J. Anal. At. Spectrom.*, 2005, **20**, 1250.
- 143 P. Heitland and J. A. C. Broekaert, Addition of small amounts of helium and hydrogen to the working gases in slurry nebulization inductively coupled plasma atomic emission spectrometry for the analysis of ceramic powders, *J. Anal. At. Spectrom.*, 1997, **12**, 981.
- 144 N. Shibata, N. Fudagawa and M. Kubota, Effects of hydrogen mixed with argon carrier gas in electrothermal vaporization inductively coupled plasma mass-spectrometry, *Spectrochim. Acta B*, 1992, **47**, 505.
- 145 J. P. Matousek and J. M. Mermet, The Effect of Added Hydrogen in Electrothermal Vaporization Inductively-Coupled Plasma-Atomic Emission-Spectrometry, *Spectrochim. Acta B*, 1993, **48**, 835.
- 146 H. Louie and S. Y. P. Soo, Use of nitrogen and hydrogen in inductively coupled plasma mass-spectrometry, *J. Anal. At. Spectrom.*, 1992, **7**, 557.
-

-
- 147 D. Beauchemin and J. M. Craig, Investigations on mixed-gas plasmas produced by adding nitrogen to the plasma gas in ICP-MS, *Spectrochim. Acta B*, 1991, **46**, 603.
- 148 B. J. Fryer, S. E. Jackson and H. P. Longerich, Design, operation and role of the laser ablation microprobe coupled with an inductively coupled plasma mass spectrometer (LAM-ICP-MS) in the earth sciences, *Can. Mineral.*, 1995, **33**, 303.
- 149 D. Figg and M. S. Kahr, Elemental fractionation of glass using laser ablation inductively coupled plasma mass spectrometry, *Appl. Spectrosc.*, 1997, **51**, 1185.
- 150 C. A. Morrison, D. D. Lambert, R. J. S. Morrison, W. W. Ahlers and I. A. Nicholls, Laser ablation inductively coupled plasma-mass spectrometry - an investigation of elemental responses and matrix effects in the analysis of geostandard materials, *Chem. Geol.*, 1995, **119**, 13.
- 151 S. Chenery, A. Hunt and M. Thompson, Laser ablation of minerals and chemical differentiation of the ejecta, *J. Anal. At. Spectrom.*, 1992, **7**, 647.
- 152 J. G. Williams and K. E. Jarvis, Preliminary assessment of laser ablation inductively coupled plasma mass-spectrometry for quantitative multielement determination in silicates, *J. Anal. At. Spectrom.*, 1993, **8**, 25.
- 153 H. C. Liu, O. V. Borisov, X. L. Mao, S. Shuttleworth and R. E. Russo, Pb/U fractionation during Nd : YAG 213 nm and 266 nm laser ablation sampling with inductively coupled plasma mass spectrometry, *Appl. Spectrosc.*, 2000, **54**, 1435.
- 154 T. E. Jeffries, N. G. Pearce, W. T. Perkins and A. Raith, Chemical fractionation during infrared and ultraviolet laser ablation inductively coupled plasma mass spectrometry: Implications for mineral microanalysis, *Analytical Communications*, 1996, **33**, 35.
- 155 M. Guillong and D. Günther, Effect of particle size distribution on ICP-induced elemental fractionation in laser ablation-inductively coupled plasma-mass spectrometry, *J. Anal. At. Spectrom.*, 2002, **17**, 831.
- 156 M. Guillong, H. R. Kuhn and D. Günther, Application of a particle separation device to reduce inductively coupled plasma-enhanced elemental fractionation in laser ablation-inductively coupled plasma-mass spectrometry, *Spectrochim. Acta B*, 2003, **58**, 211.
- 157 X. L. Mao, A. C. Ciocan and R. E. Russo, Preferential vaporization during laser ablation inductively coupled plasma atomic emission spectroscopy, *Appl. Spectrosc.*, 1998, **52**, 913.
- 158 O. V. Borisov, X. L. Mao, A. Fernandez, M. Caetano and R. E. Russo, Inductively coupled plasma mass spectrometric study of non- linear calibration behavior during laser ablation of binary Cu- Zn Alloys, *Spectrochim. Acta B*, 1999, **54**, 1351.
- 159 P. Goodall, S. G. Johnson and E. Wood, Laser ablation inductively coupled plasma atomic emission spectrometry of a uranium zirconium alloy: Ablation properties and analytical behavior, *Spectrochim. Acta B*, 1995, **50**, 1823.
- 160 D. J. Figg, J. B. Cross and C. Brink, More investigations into elemental fractionation resulting from laser ablation inductively coupled plasma mass spectrometry on glass samples, *Appl. Surf. Sci.*, 1998, **129**, 287.
-

-
- 161 J. Kosler, H. P. Longerich and M. N. Tubrett, Effect of oxygen on laser-induced elemental fractionation in LA-ICP-MS analysis, *Anal. Bioanal. Chem.*, 2002, **374**, 251.
- 162 I. Kroslakova and D. Gunther, Elemental fractionation in laser ablation-inductively coupled plasma-mass spectrometry: evidence for mass load induced matrix effects in the ICP during ablation of a silicate glass, *J. Anal. At. Spectrom.*, 2007, **22**, 51.
- 163 A. M. Leach and G. M. Hieftje, Methods for shot-to-shot normalization in laser ablation with an inductively coupled plasma time-of-flight mass spectrometer, *J. Anal. At. Spectrom.*, 2000, **15**, 1121.
- 164 V. Kanicky and J. M. Mermet, Use of a single calibration graph for the determination of major elements in geological materials by laser ablation inductively coupled plasma atomic emission spectrometry with added internal standards, *Fresenius J. Anal. Chem.*, 1999, **363**, 294.
- 165 D. Günther, H. Cousin, B. Magyar and I. Leopold, Calibration studies on dried aerosols for laser ablation inductively coupled plasma mass spectrometry, *J. Anal. At. Spectrom.*, 1997, **12**, 165.
- 166 A. Raith and R. C. Hutton, Quantitation methods using laser ablation ICP-MS .1. analysis of powders, *Fresenius J. Anal. Chem.*, 1994, **350**, 242.
- 167 V. R. Bellotto and N. Miekeley, Improvements in calibration procedures for the quantitative determination of trace elements in carbonate material (mussel shells) by laser ablation ICP-MS, *Fresenius J. Anal. Chem.*, 2000, **367**, 635.
- 168 R. D. Evans, P. M. Outridge and P. Richner, Applications of laser ablation inductively coupled plasma mass spectrometry to the determination of environmental contaminants in calcified biological structures, *J. Anal. At. Spectrom.*, 1994, **9**, 985.
- 169 D. Günther, A. Von Quadt, R. Wirz, H. Cousin and V. J. Dietrich, Elemental analyses using laser ablation-inductively coupled plasma-mass spectrometry (LA-ICP-MS) of geological samples fused with $\text{Li}_2\text{B}_4\text{O}_7$ and calibrated without matrix-matched standards, *Mikrochim. Acta*, 2001, **136**, 101.
- 170 H. F. Falk, B. Hattendorf, K. Krenkelrothensee, N. Wieberneit and S. L. Dannen, Calibration of laser-ablation ICP-MS. Can we use synthetic standards with pneumatic nebulization?, *Fresenius J. Anal. Chem.*, 1998, **362**, 468.
- 171 C. Pickhardt, J. S. Becker and H. J. Dietze, A new strategy of solution calibration in laser ablation inductively coupled plasma mass spectrometry for multielement trace analysis of geological samples, *Fresenius J. Anal. Chem.*, 2000, **368**, 173.
- 172 J. S. Becker, C. Pickhardt and H. J. Dietze, Determination of trace elements in high-purity platinum by laser ablation inductively coupled plasma mass spectrometry using solution calibration, *J. Anal. At. Spectrom.*, 2001, **16**, 603.
- 173 D. P. Baldwin, D. S. Zamzow and A. P. Dsilva, Aerosol mass measurement and solution based standard additions for quantitation in Laser Ablation Inductively Coupled Plasma Atomic Emission Spectrometry, *Anal. Chem.*, 1994, **66**, 1911.
-

-
- 174 D. Günther, R. Frischknecht, H. J. Muschenborn and C. A. Heinrich, Direct liquid ablation: a new calibration strategy for laser ablation ICP-MS microanalysis of solids and liquids, *Fresenius J. Anal. Chem.*, 1997, **359**, 390.
- 175 F. Boue-Bigne, B. J. Masters, J. S. Crighton and B. L. Sharp, A calibration strategy for LA-ICP-MS analysis employing aqueous standards having modified absorption coefficients, *J. Anal. At. Spectrom.*, 1999, **14**, 1665.
- 176 R. Kovacs and D. Gunther, Influence of transport tube materials on signal response and drift in laser ablation-inductively coupled plasma-mass spectrometry, *J. Anal. At. Spectrom.*, 2008, **23**, 1247.
- 177 A. M. Leach and G. M. Hieftje, Factors affecting the production of fast transient signals in single shot laser ablation inductively coupled plasma mass spectrometry, *Appl. Spectrosc.*, 2002, **56**, 62.
- 178 J. Venable and J. A. Holcombe, Peak broadening from an electrothermal vaporization sample introduction source into an inductively coupled plasma, *Spectrochim. Acta B*, 2001, **56**, 1431.
- 179 Y. Luo, S. Gao, H. P. Longerich, D. Günther, S. Wunderli, H. L. Yuan and X. M. Liu, The uncertainty budget of the multi-element analysis of glasses using LA-ICP-MS, *J. Anal. At. Spectrom.*, 2007, **22**, 122.
- 180 S. F. Durrant, Alternatives to all-argon plasmas in inductively coupled plasma mass spectrometry (ICP-MS) - an overview [review], *Fresenius J. Anal. Chem.*, 1993, **347**, 389.
- 181 J. W. H. Lam and G. Horlick, A comparison of Argon and mixed gas plasmas for Inductively Coupled Plasma Mass-Spectrometry, *Spectrochim. Acta B*, 1990, **45**, 1313.
- 182 Z. C. Hu, S. Gao, D. Günther, S. G. Hu, X. M. Liu and H. L. Yuan, Direct determination of tellurium in geological samples by inductively coupled plasma mass spectrometry using ethanol as a matrix modifier, *Appl. Spectrosc.*, 2006, **60**, 781.
- 183 C. O. Connor, B. L. Sharp and P. Evans, On-line additions of aqueous standards for calibration of laser ablation inductively coupled plasma mass spectrometry: theory and comparison of wet and dry plasma conditions, *J. Anal. At. Spectrom.*, 2006, **21**, 556.
- 184 H. P. Longerich, S. E. Jackson and D. Günther, Laser ablation inductively coupled plasma mass spectrometric transient signal data acquisition and analyte concentration calculation, *J. Anal. At. Spectrom.*, 1996, **11**, 899.
- 185 Modern Plastics Encyclopedia, McGraw Hill, 1988
- 186 Permeability and other film properties of plastics and elastomers, Plastics Design Library, 1995
- 187 Polymer data Handbook, Oxford University Press, Inc., 1999
- 188 J. D. Venable and J. A. Holcombe, Signal enhancements produced from externally generated 'carrier' particles in electrothermal vaporization-inductively coupled plasma mass spectrometry, *Spectrochim. Acta B*, 14-7-2000, **55**, 753.
-

-
- 189 R. Kovacs, K. Nishiguchi, K. Utani and D. Gunther, Development of direct atmospheric sampling for laser ablation-inductively coupled plasma-mass spectrometry, *J. Anal. At. Spectrom.*, 2010, **25**, 142.
- 190 D. Autrique, A. Bogaerts, H. Lindner, C. C. Garcia and K. Niemax, Design analysis of a laser ablation cell for inductively coupled plasma mass spectrometry by numerical simulation, *Spectrochimica Acta Part B-Atomic Spectroscopy*, 2008, **63**, 257.
- 191 D. Günther and C. A. Heinrich, Enhanced sensitivity in laser ablation-ICP mass spectrometry using helium-argon mixtures as aerosol carrier - Plenary lecture, *J. Anal. At. Spectrom.*, 1999, **14**, 1363.
- 192 Z. Wang, B. Hattendorf and D. Günther, Analyte response in laser ablation inductively coupled plasma mass spectrometry, *J. Am. Soc. Mass Spectr.*, 2006, **17**, 641.
- 193 K. Nishiguchi, K. Utani and E. Fujimori, Real-time multielement monitoring of airborne particulate matter using ICP-MS instrument equipped with gas converter apparatus, *J. Anal. At. Spectrom.*, 2008, **23**, 1125.
- 194 R. Kovacs, S. Schlosser, S. P. Staub, A. Schmiderer, E. Pernicka and D. Gunther, Characterization of calibration materials for trace element analysis and fingerprint studies of gold using LA-ICP-MS, *J. Anal. At. Spectrom.*, 2009, **24**, 476.
- 195 A. F. Holleman and E. Wiberg, *Lehrbuch der Anorganischen Chemie*, Walter de Gruyter, Berlin, 1995
- 196 N. J. G. Pearce, W. T. Perkins, J. A. Westgate, M. P. Gorton, S. E. Jackson, C. R. Neal and S. P. Chenery, A compilation of new and published major and trace element data for NIST SRM 610 and NIST SRM 612 glass reference materials, *Geostand. Newsl.*, 1997, **21**, 115.
- 197 H. Wiltsche, L. Flamigni and D. Günther, Spatially resolved plasma diagnostics with indications on temperature dependence of the ICP, *unpublished*, 2010
- 198 S. F. Durrant, Multi-elemental analysis of environmental matrices by laser ablation inductively coupled plasma mass spectrometry, *Analyst*, 1992, **117**, 1585.
- 199 R. S. Houk and N. Praphairaksit, Dissociation of polyatomic ions in the inductively coupled plasma, *Spectrochim. Acta B*, 2001, **56**, 1069.
- 200 D. A. Wilson, G. H. Vickers and G. M. Hieftje, Ionization temperatures in the inductively coupled plasma determined by mass-spectrometry, *Appl. Spectrosc.*, 1987, **41**, 875.
- 201 F. Vanhaecke, R. Dams and C. Vandecastelle, Zone Model As An Explanation for Signal Behavior and Non-Spectral Interferences in Inductively-Coupled Plasma-Mass Spectrometry, *J. Anal. At. Spectrom.*, 1993, **8**, 433.
- 202 B. Hattendorf, C. Latkoczy and D. Günther, Laser ablation-ICPMS, *Anal. Chem.*, 2003, **75**, 341A.
- 203 S. Schlosser, R. Kovacs, E. Pernicka, D. Günther and M. Tellenbach, Fingerprints in gold, *New technologies for Archaeology: Multidisciplinary investigations in Palpa and Nasca, Peru*; eds. M. Reindel, G. Wagner, Springer Verlag, 2009, 409.
-

-
- 204 R. J. Watling, H. K. Herbert, D. Delev and I. D. Abell, Gold fingerprinting by laser ablation inductively coupled plasma mass spectrometry, *Spectrochim. Acta B*, 1994, **49**, 205.
- 205 R. J. Watling, Sourcing the provenance of cannabis crops using inter-element association patterns 'fingerprinting' and laser ablation inductively coupled plasma mass spectrometry, *J. Anal. At. Spectrom.*, 1998, **13**, 917.
- 206 R. J. Watling, B. F. Lynch and D. Herring, Use of laser ablation inductively coupled plasma mass spectrometry for fingerprinting scene of crime evidence, *J. Anal. At. Spectrom.*, 1997, **12**, 195.
- 207 B. Grigorova, S. Anderson, J. de Bruyn, W. Smith, K. Stulpner and A. Barzev, The AARL gold fingerprinting technology, *Gold Bulletin*, 1998, **31**, 26.
- 208 A. Gondonneau and M. F. Guerra, The circulation of precious metals in the Arab Empire: The case of the Near and the Middle East, *Archaeometry*, 2002, **44**, 573.
- 209 M. F. Guerra, A. Gondonneau and J. N. Barrandon, South American precious metals and the European economy: A scientific adventure in the Discoveries time, *Nucl. Instr. and Meth. B*, 1998, **138**, 875.
- 210 M. F. Guerra, C. O. Sarthre, A. Gondonneau and J. N. Barrandon, Precious metals and provenance enquiries using LA-ICP-MS, *Journal of Archaeological Science*, 1999, **26**, 1101.
- 211 P. M. Outridge, W. Doherty and D. C. Gregoire, Determination of trace elemental signatures in placer gold by laser ablation inductively coupled plasma-mass spectrometry as a potential aid for gold exploration, *J. Geochem. Explor.*, 1998, **60**, 229.
- 212 W. Devos, C. Moor and P. Lienemann, Determination of impurities in antique silver objects for authentication by laser ablation inductively coupled plasma mass spectrometry (LA-ICP-MS), *J. Anal. At. Spectrom.*, 1999, **14**, 621.
- 213 D. Talib, R. L. Ma, C. W. Mcleod and D. Green, Multielement analysis of modern and ancient coins using diamond lapping film and laser ablation CP mass spectrometry, *Canadian Journal Of Analytical Sciences And Spectroscopy*, 2004, **49**, 156.
- 214 L. Halicz and D. Günther, Quantitative analysis of silicates using LA-ICP-MS with liquid calibration, *J. Anal. At. Spectrom.*, 2004, **19**, 1539.
- 215 C. O'Connor, B. L. Sharp and P. Evans, On-line additions of aqueous standards for calibration of laser ablation inductively coupled plasma mass spectrometry: theory and comparison of wet and dry plasma conditions, *J. Anal. At. Spectrom.*, 2006, **21**, 556.
- 216 M. Walle, J. Koch and D. Gunther, Analysis of brass and silicate glass by femtosecond laser ablation inductively coupled plasma mass spectrometry using liquid standard calibration, *J. Anal. At. Spectrom.*, 2008, **23**, 1285.
- 217 C. Bendall, The application of trace element and isotopic analyses to the study of celtic gold coins and their metal sources, 2003, Dissertation, Johann Wolfgang Goethe University, Frankfurt, Germany.
-

-
- 218 P. R. D. Mason and W. J. Kraan, Attenuation of spectral interferences during laser ablation inductively coupled plasma mass spectrometry (LA-ICP-MS) using an rf only collision and reaction, *J. Anal. At. Spectrom.*, 2002, **17**, 858.
- 219 D. C. Perdian, S. J. Bajic, D. P. Baldwin and R. S. Houk, Time-resolved studies of particle effects in laser ablation inductively coupled plasma-mass spectrometry, *J. Anal. At. Spectrom.*, 2008, **23**, 336.
- 220 M. Ebnöther, Vom Toten Meer zum Stillen Ozean, Vom Toten Meer zum Stillen Ozean, Sammlung Ebnöther, Museum zu Allerheiligen Schaffhausen, Verlag Gerd Hatje, Ostfildern-Ruit, 1999
- 221 W. Alva, Orfebrería del Formativo. In: Lavalle JA (ed) Oro del Antiguo Perú. Colección arte y tesoros del Perú, 1992, 116.
- 222 C. A. Heinrich, T. Pettke, W. E. Halter, M. Aigner-Torres, A. Audetat, D. Günther, B. Hattendorf, D. Bleiner, M. Guillong and I. Horn, Quantitative multi-element analysis of minerals, fluid and melt inclusions by laser-ablation inductively-coupled-plasma mass- spectrometry, *Geochim. Cosmochim. Acta*, 2003, **67**, 3473.
- 223 A. Shalem, A note on a unique Islamic golden figurine, *Iran*, 2002, **40**, 173.
- 224 C. C. Garcia, H. Lindner and K. Niemax, Laser ablation inductively coupled plasma mass spectrometry-current shortcomings, practical suggestions for improving performance, and experiments to guide future development, *J. Anal. At. Spectrom.*, 2009, **24**, 14.
- 225 M. Guillong, C. Latkoczy, J. H. Seo, D. Gunther and C. A. Heinrich, Determination of sulfur in fluid inclusions by laser ablation ICP-MS, *J. Anal. At. Spectrom.*, 2008, **23**, 1581.
- 226 D. Günther, B. Hattendorf and A. Audetat, Multi-element analysis of melt and fluid inclusions with improved detection capabilities for Ca and Fe using laser ablation with a dynamic reaction cell ICP-MS, *J. Anal. At. Spectrom.*, 2001, **16**, 1085.
- 227 B. Stoffell, J. J. Wilkinson and T. E. Jeffries, Metal transport and deposition in hydrothermal veins revealed by 213nm UV laser ablation microanalysis of single fluid inclusions, *American Journal of Science*, 2004, **304**, 533.
- 228 A. Cocherie and M. Robert, Laser ablation coupled with ICP-MS applied to U-Pb zircon geochronology: A review of recent advances, *Gondwana Res.*, 2008, **14**, 597.
- 229 J. Kosler, Laser ablation ICP-MS - a new dating tool in Earth science, *Proceedings of the Geologists Association*, 2007, **118**, 19.
- 230 S. F. Durrant and N. I. Ward, Recent biological and environmental applications of laser ablation inductively coupled plasma mass spectrometry (LA-ICP-MS), *J. Anal. At. Spectrom.*, 2005, **20**, 821.
- 231 A. M. Ghazi, Laser ablation ICP-MS: A new elemental and isotopic ratio technique in environmental forensic investigation, *Environ. Forensics*, 2005, **6**, 7.
- 232 S. Becker, M. Dücking, P. Watzke and W. Stoecklein, Laser ablation in forensic glass analysis: The use of matrix matched standards for quantitative float glass analysis, *Forensic Sci. Int.*, 2003, **136**, 361.
-

-
- 233 S. Montero, J. R. Almirall, A. Hobbs, L. Morris and S. Gross, Sample introduction of materials of forensic interest using laser ablation for inductively coupled plasma mass spectrometry analysis of metals, *Abstr. Pap. Amer. Chem. Soc.*, 2002, **223**, 127.
- 234 R. J. Watling, Novel application of laser ablation inductively coupled plasma mass spectrometry in forensic science and forensic archaeology, *Spectroscopy*, 1999, **14**, 16.

7.6 Curriculum Vitae

Personal data:

Name: Robert Kovacs
Date of birth: 06.10.1981
Place of birth: Debrecen, Hungary
Nationality: Hungarian

Education:

1988-1996 Szoboszlói Street Primary School, Debrecen, Hungary
1996-2000 Mihály Fazekas High School (spec. in Biology), Debrecen, Hungary
2000-2005 Student in Environmental Science, University of Debrecen,
Faculty of Natural Sciences, Debrecen, Hungary
2004 Certificate in radiation protection (extended level), Quality X-Ray Ltd.,
Debrecen, Hungary
2004-2005 Diploma student at Department of Inorganic and Analytical Chemistry,
University of Debrecen
2005 Diploma in Environmental Science (M.Sc., spec. in Chemistry)
2006-2010 PhD student in Analytical Chemistry, Research group of Prof. D. Günther,
Laboratory of Inorganic Chemistry, ETH Zurich, Zurich, Switzerland

Teaching experience:

2005 Laboratory courses in Spectrophotometry for undergraduate students in
Pharmaceutical Sciences, Department of Inorganic and Analytical
Chemistry, University of Debrecen
2005 Laboratory courses in Atomic Absorption Spectrometry for undergraduate
students in Chemistry, Department of Inorganic and Analytical Chemistry,
University of Debrecen
2007-2010 Laboratory courses in LA-ICP-MS for undergraduate students in Chemistry
and Interdisciplinary Sciences, D-CHAB, ETH Zurich
